LBL-13588
c.2

# Lawrence Berkeley Laboratory
UNIVERSITY OF CALIFORNIA

## Materials & Molecular Research Division

RECEIVED
LAWRENCE
BERKELEY LABORATORY
MAR 21 1983
LIBRARY AND
DOCUMENTS SECTION

# A MÖSSBAUER SPECTROMETRY STUDY OF Fe-Ni-X ALLOYS

Brent Thomas Fultz
(Ph.D. Thesis)

November 1982

TWO-WEEK LOAN COPY

*This is a Library Circulating Copy which may be borrowed for two weeks. For a personal retention copy, call Tech. Info. Division, Ext. 6782.*

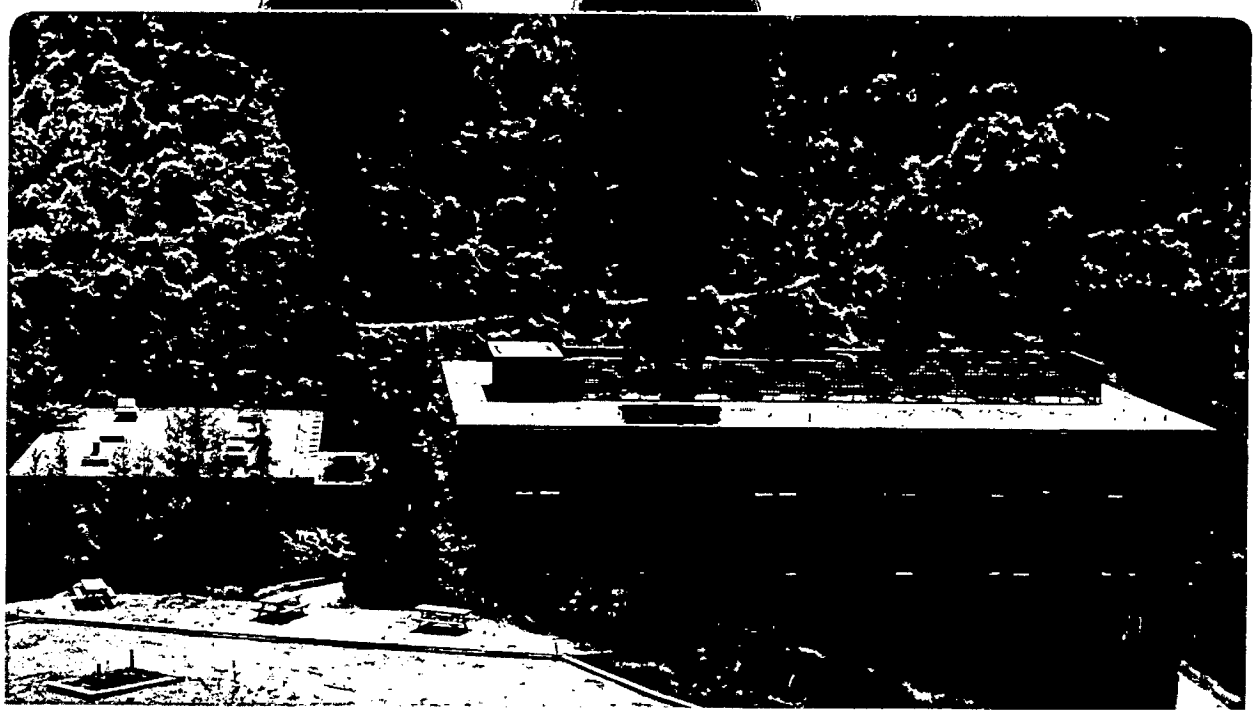

LBL-13588
c.2

Prepared for the U.S. Department of Energy under Contract DE-AC03-76SF00098

## DISCLAIMER

This document was prepared as an account of work sponsored by the United States Government. While this document is believed to contain correct information, neither the United States Government nor any agency thereof, nor the Regents of the University of California, nor any of their employees, makes any warranty, express or implied, or assumes any legal responsibility for the accuracy, completeness, or usefulness of any information, apparatus, product, or process disclosed, or represents that its use would not infringe privately owned rights. Reference herein to any specific commercial product, process, or service by its trade name, trademark, manufacturer, or otherwise, does not necessarily constitute or imply its endorsement, recommendation, or favoring by the United States Government or any agency thereof, or the Regents of the University of California. The views and opinions of authors expressed herein do not necessarily state or reflect those of the United States Government or any agency thereof or the Regents of the University of California.

LBL-13588

# A MÖSSBAUER SPECTROMETRY STUDY OF Fe-Ni-X ALLOYS

By

Brent Thomas Fultz
(Ph.D. Thesis)

Lawrence Berkeley Laboratory
University of California
Berkeley, California 94720

November 1982

This work was supported by the Director, Office of Energy Research, Office of Basic Energy Science, Materials Science Division of the U.S. Department of Energy under Contract Number DE-AC03-76SF00098.

# A MÖSSBAUER SPECTROMETRY STUDY OF Fe-Ni-X ALLOYS

**Brent Thomas Fultz**

## ABSTRACT

The Mössbauer effect was used for obtaining microstructural and microchemical information about two-phase tempering of Fe-9Ni alloys. Methods for microchemical analysis required substantial development work. Mössbauer spectra from many high purity materials with known compositions and thermomechanical processings were obtained in a thorough "calibration" program. Martensite solute concentration changes were then determined from Mössbauer spectra obtained after tempering.

This thesis attempts to cover the fundamental background material underlying the use of the Mössbauer effect for chemical analysis of ternary Fe-9Ni-1X alloys. A picture of electronic effects around solute atoms is presented in order to justify a semi-phenomenological model of linear response of hyperfine magnetic field perturbations to magnetic moments. Some formal development of this model allowed estimates of hyperfine structure to be made for non-dilute binary and ternary alloys. The temperature-dependent effects of Ni solutes on the shapes of Mössbauer peaks from binary Fe-9Ni alloys are analyzed within this model. The effects of ternary "X" solutes on Mössbauer spectra of Fe-9Ni-X alloys are also successfully estimated. Because hyperfine magnetic field perturbations at $^{57}$Fe nuclei near Ni atoms were found to have anisotropic components, changes in the lattice magnetization interfered with the methods of chemical analysis until the lattice magnetizations were "locked" with an applied magnetic field. Sensitive difference spectrum procedures were eventually developed so that ±0.03% concentration changes of many ternary solutes in

martensite could be measured. Ni concentrations of ±0.1% could also be detected.

The austenite formed by a nucleation and growth mechanism. Ni, Mn, Cr, and Si were found to segregate to the austenite. The addition of ternary solutes to a Fe-9Ni matrix had substantial effects on the rate of austenite formation and its stability against the martensite transformation. The austenite phase boundary was found to move towards lower Ni concentrations as some ternary solutes segregated to the austenite. The relative diffusivity of Ni versus that of the other solutes was largely responsible for determining the balance of solute concentrations in the austenite. Especially for lower tempering temperatures, the temperature dependence of the number of nucleation sites had a major influence on the kinetics of austenite precipitation.

## ACKNOWLEDGMENTS

I believe that the completeness, and even the logical consistency of the present research topic demanded this large experimental, theoretical, and literary effort. The burdens of the experimental and theoretical work, and the agony of writing about them, have extended beyond myself to many people around me, and my feelings of gratitude extend to all people who have patiently tolerated and helped this onerous undertaking.

Prof. J. W. Morris, Jr. supervised this research; without his generous support and occasional guidance this project would not have been accomplished. His patience has been proved through the course of this work in a way that should dispel some common misconstructions about him. I find it difficult to imagine how this Ph.D. thesis, or another like it, could be completed outside his research group without substantially more difficulty.

The patience of my family and friends, especially Colleen O'Hara and Esther D. Fultz, also helped me complete this work. In the earlier stages when the end was nowhere in sight, I was fortunate to acquire some of their faith in the ultimate success of the outcome, a faith which was deeper than my own.

The Department of Materials Science and Mineral Engineering of the University of California, Berkeley, and the Materials and Molecular Research Division of the Lawrence Berkeley Laboratory, showed less patience, but their positions can be understood in the light of their current cost consiousness, and I am grateful for the opportunity of working for them.

"High technology" was employed to produce this document. Jeanne Shull composed the main text with its equations on the U. C. Berkeley UNIX system. I am especially grateful for her effort because working with UNIX was an educational experience for both of us. Incidentally, this page and most of the pages 284-346 were printed by impact printers on

Z-80 microcomputer systems.

I am grateful to J. I. Kim for many important discussions and his collaborative STEM work -- we still have some important unfinished business that I hope will be revived soon. Discussions with other senior colleagues, in particular C. K. Syn, S. K. Hwang, S. Wen, M. Hong, K. M. Chang, and other colleagues H. J. Kim, D. E. Wedge, T. Mohri, I. W. Wu, D. Dietderich, G. M. Chang, Y. H. Kim, L. T. Summers, and G. Fior, have helped me to develop many of the ideas in the present work.

I thank Prof. L. H. Schwartz for useful advice regarding some early experimental data. His original attempts at chemical analysis of 9Ni steel inspired the direction of this work. I have also been fortunate to have had brief, but disproportionately useful conversations with other workers in the field of Mössbauer spectroscopy, especially R. A. Levy and M. Eibschütz.

John Holthuis provided the technical expertise for the preparation of the high purity materials. I am also grateful to W. Wong and H. Riebe for their help with machine shop techniques.

Nippon Kokan Kabushiki supplied the commercial 9Ni steel for the present research. Only a small amount of metal was needed for Mössbauer spectrometry, but our concurrent mechanical properties testing and microstructural characterization work helped point to some of the interesting problems.

The Office of Naval Research provided some funding for the initial construction of the Mössbauer spectrometer. O. N. R. supported me during much of my previous work on phase analysis development.

All original work reported in this thesis was supported by the Director, Office of Energy Research, Office of Basic Energy Science, Materials Science Division of the U. S. Department of Energy under Contract # DE-AC03-76SF00098.

# Table of Contents


I. Introduction ..... 1

II. The Physical Metallurgy of 9Ni Steel ..... 10

III. Basic Theory of the Mössbauer Effect ..... 20

A. The Origin of the Mössbauer Effect ..... 20

B. Mössbauer Spectrometry ..... 24

C. Hyperfine Fields ..... 27

1. The Isomer Shift ..... 28

2. The Nuclear Electric Quadrupole Effect ..... 31

2. The Hyperfine Magnetic Field Effects ..... 32

IV. Phenomenology of Solute-Induced Perturbations of $^{57}$Fe Hyperfine Magnetic Fields ..... 36

A. Additive Hyperfine Magnetic Field Perturbations and their Probabilities ..... 36

B. General Features of Previous Work ..... 39

C. Dilute Alloys ..... 43

D. Inhomogeneous Solutions ..... 47

E. Ni Composition Analysis ..... 51

F. Anisotropic Hyperfine Magnetic Field Perturbations ..... 54

G. Localized Isomer Shifts ..... 56

V. Sources of Hyperfine Magnetic Fields at Nuclei ..... 58

A. Perspective and Introduction ..... 58

B. Classical Contributions: $H_{MAC}, H_{DIP}, H_{ORB}$ ..... 61

C. The Fermi Contact Interaction ..... 62

D. Exchange; Core Polarization: $H_{CORE}$ ..... 63

E. Conduction Electron Polarization: $H_{CEP}$ ..... 68

1. First Order Perturbation Theory ..... 68

2. Friedel Theory ..... 71

3. R.K.K.Y. Theory ..... 72

4. Cross-Terms and Other Considerations ..... 76

F. Outer Electron Polarization: $H_{OV}$ ..... 89

G. Electron Bonding Polarization: $H_{COV}$ ..... 92

H. Interband Mixing: $H_{HYB}$ ..... 94

I. Coulomb Correlation Corrections ..... 98

VI. Models and Calculations of $\{\Delta H_i^X\}$ and $\{\Delta i_i^X\}$ in Fe-X and Fe-Ni-X Alloys ..... 102

A. Early Models ..... 103

B. Linear Response of Hyperfine Magnetic Fields to Magnetic Moments ..... 112

C. Linear Response in Binary Alloys ..... 117

D. A Compromise Treatment of Linear Response in Non-Dilute Binary Alloys ..... 129

E. A Compromise Treatment of Linear Response in Non-Dilute Ternary Alloys ..... 136

VII. Experimental ..... 144

A. Materials and Specimen Preparation ..... 144

B. X-ray Diffractometry and Analytical Scanning Transmission Elec-

tron Microscopy ..... 148

C. Radiation Source ..... 151

D. Detectors ..... 152

E. The Doppler Drive and Mechanical Vibrations ..... 157

F. The Computer System ..... 159

G. Tempering Experiments in the Vacuum Furnace ..... 161

H. Magnet ..... 166

I. Spectrometer Performance and Operation ..... 167

VIII. Data Processing ..... 173

A. Corrections for Doppler Drive Performance ..... 173

B. Procedures for Stripping Peaks and Differencing Spectra ..... 176

1. Austenite Analysis ..... 176

2. Difference Spectrum Procedures ..... 180

3. Other Data Processing Procedures ..... 187

C. Thickness Distortion Corrections ..... 189

IX. Experimental Results ..... 196

A. Chemical Analysis Development ..... 196

1. Ni Analysis ..... 196

2. X Analysis in Fe-Ni-X ..... 201

B. Tempering Experiments ..... 205

1. Kinetics of Austenite Formation ..... 206

2. Kinetics of Solute Segregation ..... 207

C. Anisotropic Hyperfine Magnetic Field Perturbations around Ni Atoms at 18°C ..... 210

X. Discussion ..... 213

A. Electronic Effects ..... 213

1. Electron Transfer and Magnetic Moment Perturbations ..... 213

2. The Shape of Mössbauer Peaks from Fe-10Ni ..... 227

3. Changes in $\{f(r_j)\}$ with Ni Concentration ..... 232

4. The Temperature Dependence of $\{\Delta H_i^{Ni}\}$ ..... 236

5. Anisotropy of Hyperfine Magnetic Fields: Martensite Magnetic Anisotropy and Temperature Dependence ..... 240

B. Ferrous Metallurgy ..... 248

1. Time-Temperature -Transformation Characteristics of the $\alpha' \rightarrow \gamma$ Reaction ..... 248

2. Equilibrium Austenite Precipitation in Ternary Alloys ..... 254

3. Ni-X Covalent Bonding ..... 258

4. Solute-Vacancy Binding and Isomer Shifts ..... 261

5. Austenite Nucleation: Mechanical History and Solute Effects ..... 266

6. Thermal Stability of Austenite: Effects of Ternary Solutes ..... 269

7. Mössbauer Spectrometry in Physical Metallurgy ..... 271

XI. Conclusions and Summary ..... 275

A. Chemical and Phase Analysis ..... 275

B. Electronic Structure ..... 277

C. Metallurgy of Fe-Ni Alloys ..... 280

D. Miscellaneous ..... 281

Appendix A* Moments of Binomial Distribution ..... 283

References ..... 284

Figure Captions ..... 300

Figures ..... 306

Table I. Alloy Elements of "9Ni" Steel ..... 15

Table II. The Magnetic Sextet of $^{57}$Fe Mössbauer Peaks ..... 33

Table III. Some Hyperfine Magnetic Field Perturbations at $^{57}$Fe Nuclei Near Solute Atoms ..... 41

Table IV. General Screening Considerations ..... 81

Chart 1 ..... 118

Table V. Some Important Magnetic Moment Combinations for Fe-X Alloys ..... 121

Table VI. $N_S^X$ for Fe-Ni-X Alloys ..... 203

Table VII. Moments of the Binomial Distribution for 14 Trials ..... 231a

Table VIII. Austenite Thermal Stabilities ..... 270

# CHAPTER I

# INTRODUCTION

The Mössbauer effect in $^{191}$Ir was discovered and correctly interpreted by Rudolf Mössbauer in 1957 [1-3]. As explained in Chapter III, the Mössbauer effect involves a nuclear $\gamma$-ray resonance with a remarkably large Q (the ratio of transition energy to line width). In the 1960's this feature led to elegant experiments which measured the gravitational red shift [4,5], effects of acceleration on photon energies [6], and effects due to phase and intensity modulation of $\gamma$-rays [7,8]. The large Q of the nuclear resonance mostly reflects the smallness of the energy uncertainty of the nuclear excited state. Mössbauer used the energy width of the excited state and the uncertainty principle to determine the lifetime of the excited state of $^{191}$Ir [1]. Other nuclear properties such as the nuclear spins, the nuclear electric quadrupole moment, and changes in the nuclear radius during excitation, can be measured with Mössbauer effect experiments. These nuclear properties are manifested through their "hyperfine interactions" (the subject of Chapter V) with electric and magnetic fields at the nucleus. However, these properties intrinsic to the nucleus are independent of the environment around the nucleus. Now, over 20 years after the discovery of the Mössbauer effect, the nuclear properties are known constants. Consequently, for experiments in materials science the Mössbauer nucleus can be used as a *probe* of known characteristics that measures properties of its immediate environment.

Some general features of the Mössbauer effect make it well-suited for materials science investigations. It is a fortunate coincidence that the nucleus which exhibits the most observable Mössbauer effect has 26 protons. This nucleus, $^{57}$Fe, accounts for 2.2% of all iron in nature. Therefore all materials of interest in ferrous metallurgy are filled with numerous probe nuclei which are

chemically identical to all other Fe nuclei. Isotopic enrichment of specimens with $^{57}Fe$ is usually unnecessary. Two other convenient features of the Mössbauer effect deserve mention. 1.) In spite of the high energy of the $\gamma$-rays used, their momentum transfers are small, so obtaining a Mössbauer spectrum from a specimen does not alter its chemical or structural properties. 2.) The simple geometrical arrangements of Mössbauer spectrometers and the constant properties of the probe nuclei facilitate many types of *in-situ* experiments. For example, in the present work many Mössbauer spectra were obtained at 500°C.

Besides the obvious requirement that the material being studied must contain the Mössbauer isotope, other general features of Mössbauer spectrometry can affect its applicability to problems in materials science. In practice it takes about 10 hours to obtain a full Mössbauer spectrum of good quality. This can be an important limitation for kinetics experiments. Intensity problems also require that a Mössbauer spectrum is obtained from a large, macroscopic ($>0.01 cm^2$) area of material that includes at least $10^{18}$ $^{57}Fe$ nuclei. Although the energy spread associated with the Mössbauer effect is impressively small ($\approx 10^{-8}$ eV), chemical and crystallographic effects on Mössbauer spectra, developed through hyperfine interactions, can be even smaller. This energy spread (linewidth) can then be a disadvantage because it limits the amount of information available in a Mössbauer spectrum. Nevertheless, this lack of resolution is often not a serious problem, and in the present work it allows for simplified interpretations of data on ternary solute concentrations.

Often the biggest difficulty involving an application of Mössbauer spectrometry to a problem in materials science is the small amount of previous work that is applicable to the problem. In comparison to other experimental techniques of materials science, there have been relatively few Mössbauer spec-

trometry investigations of metallurgical phenomenon. In too many of these investigations, a well-known metallurgical reaction was observed to cause changes in Mössbauer spectra, and these qualitative results constituted a publication which "demonstrated the power of Mössbauer spectrometry for investigating this metallurgical reaction". Granted, there is a need for such demonstration experiments, even if their interpretations of the Mössbauer spectra or the metallurgical reactions are incorrect. However, after nearly 20 years of applications of the Mössbauer effect to problems of physical metallurgy, there is an even greater need for credible attempts at systematic Mössbauer studies of metallurgical problems. In addition to supplying information that can help explain particular metallurgical phenomena, such systematic investigations can supply "standards" information which will be of direct value both for further work in materials science, and for furthering the understanding of the hyperfine structure seen in Mössbauer spectrometry. Motivation for such comprehensive Mössbauer spectrometry investigations of metallurgical phenomena must come from the interesting properties of the materials themselves, in conjunction with the unique features of Mössbauer spectrometry. The investigator must wear the hats of both a "materials scientist" and a "Mössbauer spectroscopist".

A review of previous studies of metallurgical problems by Mössbauer spectrometry is beyond the scope of this work. Several reviews have appeared recently on this subject [9-15], older reviews may also be helpful [16-19]. However, descriptions of a few previous experiments are helpful for providing an introductory flavor of how Mössbauer spectrometry was used to obtain phase and chemical analysis information from Fe-Ni-X alloys.

Phase analysis is one of the most straightforward applications of Mössbauer spectrometry to problems in materials science. Phase analyses of

materials first involve the identification of which pattern of peaks in a Mössbauer spectrum corresponds to which phase. Intensity measurements are then correlated to the amount of each phase present. The absolute intensities of the patterns of peaks can be measured, or the relative fraction of $^{57}Fe$ in each phase can be determined by comparing the relative intensities of peaks from all phases. Martensite (bcc), austenite (fcc), and carbide phases are interest in studies of 9Ni steel.

Mössbauer spectrometry analysis of retained austenite contents in carbon and alloy steels is well-developed. Marcus et al. [20] studied the effect of heat treatments on the austenite content of stainless steel. Other workers pointed out complicating factors in this sort of analysis [21]. Comparisons with x-ray diffractometry measurements of austenite content were carried out later [22-25], and vindicated the earlier work. These studies showed that Mössbauer spectrometry is a more reliable technique than x-ray diffractometry for measuring austenite contents of ferritic low alloy steels, especially when these materials have low austenite contents and significant crystallographic textures. Mössbauer spectrometry is reliable in heavily deformed materials where quantitative x-ray diffractometry is impossible; it has been used to study the transformation of retained austenite near fracture surfaces of 9Ni and 6Ni steel [26-28].

Carbides have been the subject of a number of studies by Mössbauer spectrometry [29-36]. Unlike the retained austenite in low alloy steels, the common carbide phases are ferromagnetic, and their absorption intensity is spread into sextets of isolated peaks. This reduces the sensitivity of the Mössbauer technique to the presence of carbides, although with good experimental data the presence of less than one percent of carbides can be measured quantitatively. Such measurements have been used to follow the decomposition of retained

austenite into carbides during tempering of AISI 4340 steel [35].

Chemical concentration analysis of a ferromagnetic phase in an alloy steel is less straightforward than the previous examples of phase analyses, and requires high quality experimental data.. Solute atoms alter the hyperfine fields at $^{57}Fe$ nuclei near them, and these effects cause small shifts in spectral peaks. The observed hyperfine structure that results from these solutes can often be correlated to the solute concentration for non-concentrated, disordered alloys. Chapter IV describes the phenomenology that was used to interpret the hyperfine structure observed in the following examples of previous work. The solute concentration is a major factor in this phenomenology, so a phenomenological interpretation of the hyperfine structure may be used to determine unknown solute concentrations of appropriate alloy systems. It is, of course, prudent to first establish that this phenomenology is applicable to each new combination of solute atom and host alloy.

Successful early studies of $Fe_2Mo$ precipitation in binary Fe-6Mo alloys by Marcus et al. [37,38] showed that the growth of a Mössbauer peak attributable to $Fe_2Mo$ occurred simultaneously with changes in the hyperfine structure of the bcc matrix. Their analysis of the bcc hyperfine structure did not assume a disordered solution of Mo in Fe, and it gave the curious result that Fe atoms in a quenched Fe-6Mo alloy have 50% more single Mo neighbors, and 50% fewer pairs of Mo neighbors, than would be expected in a disordered solution. A more careful and systematic Mössbauer spectrometry study by Asano [39] later found no evidence for non-random order in Fe-Mo alloys. My own treatment of the Marcus et al. data assumes a disordered alloy, and yields fine agreement between the amount of Mo depleted from the matrix and the amount of Mo tied up in $Fe_2Mo$ precipitates. Similar hyperfine structure was seen in Fe-Ni-Co-Mo maraging steel [20], and the loss of Mo from the matrix was also evident during

a Ni-Mo precipitation reaction in this material.

Very small scale composition fluctuations are inherent to spinodal decomposition reactions, and Mössbauer spectrometry has been successfully used to study spinodal decomposition in a Fe-Cr-Co alloy [40]. In this material the hyperfine structure is primarily due to Cr atoms that are near $^{57}$Fe nuclei. Using the phenomenology described in Chapter IV, the hyperfine structure was simulated by assuming that the Cr concentration profile was a growing 3-dimensional sinusoid. Good agreement between simulated and experimental data was found.

Studies of hyperfine structure in binary Fe-X alloys are of interest in themselves, and many have been performed without any intent to develop methods for solute concentration analysis. Nevertheless, a characterization of how the observed hyperfine structure depends on the solute concentration is an integral part of such studies. As discussed in Chapter IV, a fairly good consensus has been reached regarding the phenomenology of the $^{57}$Fe hyperfine structure around certain solutes. Such "calibration" work has shown that the hyperfine structure can be a good measure of the alloy composition; in a Fe-3Mn alloy Vincze and Campbell [41] found that a phenomenological analysis of the hyperfine structure determined the Mn concentration to within a few tenths of a percent. An important result of such studies of hyperfine structure is that interpretations of hyperfine structure are least ambiguous for dilute ($\approx$1%) alloys. Consequently, the quantitative analysis of solute concentrations is most reliable for dilute alloys.

The problem with a tool for accurate chemical analysis of dilute alloys is that dilute alloys form a small class of materials which are usually metallurgically boring -- rather few phase transformations or ordering reactions occur in them. However, in the previous examples of Mo precipitation in Fe-Ni-Co-Mo

alloys and the spinodal decomposition of Fe-Cr-Co alloys, it is important to note that the prominent hyperfine structure was due to Mo and Cr solutes; the Ni and Co solutes evidently had much smaller effects on the hyperfine structure. This feature of hyperfine structure suggests that accurate chemical analysis methods for dilute solute concentrations may be of more general use in materials science. In starting the present work it was hoped that the presence of Ni would have only a small effect on the hyperfine structure due to dilute concentrations of "X" solutes in Fe-9Ni-1X alloys. This turned out to be largely true, and much of this thesis work involved determining dilute X solute concentrations in Fe-9Ni-1X alloys by methods that work well for dilute, binary Fe-X alloys. The presence of Ni was, of course, necessary for the metallurgically interesting austenite formation to occur. Furthermore, it was later found that Ni concentration changes of the martensite could also be measured with at least semi-quantitative success.

The analysis of small ternary solute concentrations in the martensite of 9Ni steel was also a goal of a previous study by Kim and Schwartz [26]. They obtained data showing a satellite peak in Mössbauer spectra of 9Ni steel, and observed that this peak decreased in intensity after about 10 hours of tempering. Unfortunately, they did not undertake a systematic study of the effects of X solutes on Mössbauer spectra of Fe-9Ni-1X alloys, and they attributed this satellite peak to $^{57}$Fe nuclei that are near carbon atoms. The systematic experimental study reported here proves that this interpretation is incorrect. An electronic model used in the present work also helps to justify the interpretation of the "X satellite" in Fe-9Ni-1X alloys. An outline of how this electronic model is developed is deferred to the first section of Chapter V.

A plethora of apparently diverse concepts and data is relevant to the use of the Mössbauer effect for chemical analysis of 9Ni steel. Chapter II of this thesis

presents a physical metallurgy background of 9Ni steel, with emphasis on the effect of retained austenite on its low temperature mechanical properties. The need to measure the amount of austenite and its solute concentrations is discussed, and problems with other experimental techniques are mentioned. Chapter III serves to explain the basic physics of the Mössbauer effect. Chapter IV develops the phenomenological model of additive hyperfine magnetic field perturbations, a model which has found extensive application in materials science, although frequently without any fundamental justification. Chapter V describes the basic electronic mechanisms whereby solute atoms can affect the hyperfine magnetic fields at neighboring $^{57}$Fe nuclei. Chapter VI reviews models of $^{57}$Fe hyperfine magnetic field perturbations due to solutes in dilute and non-concentrated Fe-X alloys. The success of this model (the "model of linear response of hyperfine magnetic fields to magnetic moments") in accounting for the hyperfine structure of dilute binary alloys is discussed. This model is formally extended to include non-concentrated binary alloys and ternary alloys such as Fe-9Ni-1X. Qualitative estimates of the hyperfine structure in these alloys are reserved for the discussion in Chapter X.A. Chapter X.A. also uses the model of linear response to discuss the observed dependences of hyperfine structure on temperature. Chapter X.B. interprets the metallurgical data on austenite precipitation kinetics and solute segregation to the austenite. Some miscellaneous and qualitative metallurgical results are also discussed. Experimental methods, including a novel "locking" of lattice magnetizations during spectrum collection, are described in Chapter VII. Data analysis procedures and a description of experimental results are covered in Chapters VIII and IX, respectively. Conclusions are summarized in Chapter XI.

It should be mentioned that the experimental data in the figures are arranged in a coherent sequence. After some introductory figures, the

sequence begins with an early hunt for carbon effects on Mössbauer spectra, followed by a Ni and X solute "calibration program", early tempering experiments, magnetic anisotropy experiments, later tempering experiments, and finally data on the metallurgical properties of austenite in 9Ni steel and Fe-9Ni-1X alloys. The figures are effectively a chapter in themselves, and may later prove to be the most valuable part of this entire thesis.

# CHAPTER II

## THE PHYSICAL METALLURGY OF 9Ni STEEL

From a cryogenic structural engineering standpoint, ferritic steels have three salient features. The first positive attribute of ferritic steels is their high strength, which becomes even greater at lower temperatures. Secondly, ferritic steels have low levels of alloy additions and are rather inexpensive. The general negative attribute of ferritic steels is the temperature dependence of their resistance to crack propagation. At "high" temperatures near room temperature, their notch toughness is usually good. However, as the temperature is reduced to a temperature characteristic of each material, its toughness begins to drop. It falls to a low value known as the "lower shelf toughness", which is again fairly temperature-independent over a range of low temperatures. The lower shelf toughness can be more than an order of magnitude smaller than the "upper shelf toughness", and since the transition from the upper shelf to the lower shelf can occur over only a few tens of degrees C, this ductile-to-brittle transition is a major engineering concern. Consequently, the central problem in the design of ferritic alloys for cryogenic service has been the suppression of the ductile-to-brittle-transition temperature* (DBTT), which hopefully is a goal attainable without any significant sacrifice of either strength or economy.

Since the early 1900's, Ni has been recognized as an alloy element beneficial to the low temperature toughness of ferritic steels [42,43]. In 1932 Sergeson [44] reported data on the low temperature impact toughness of 2-5% Ni steels, and these materials were accepted for service to -100°C by the American Society for Testing of Materials in the 1930's. The International Nickel Com-

* The DBTT is defined as the temperature at which the notch toughness of the material is the average of the upper shelf and lower shelf toughnesses.

pany developed 9Ni steel in 1942. All these ferritic Ni steels are initially given austenitizing treatments, followed by a rapid cooling to form a martensitic microstructure. It is well-known that the addition of Ni serves to increase the hardenability of steels [45-48] by suppressing the formation of (large-grained) proeutectoid ferrite. The martensite that is formed is fine-grained and reasonably ductile. Grain refinement is an effective means of suppressing the DBTT of ferritic alloys [49-51]. In recent work with 9Ni [52] and 12Ni [53,54] alloys, increasing the "grain refinement" was shown to be beneficial for further suppression of the DBTT.

In the development of 9Ni steel it was recognized that a tempering at 570°C was particularly beneficial to its low temperature notch toughness [55,56]. The suppression of the DBTT achieved in 2-5% Ni steels after tempering is usually very small, from 0 to -10°C [43]. However, for 9Ni steel the suppression of the DBTT after tempering can be as large as -100°C to -200°C. Early workers correlated this difference in tempering response to the austenite that is retained in 9Ni steel after tempering [55,56]. For Fe-9Ni, 570°C is in the $\alpha+\gamma$ two-phase region of the equilibrium Fe-Ni phase diagram (see Fig. 1a), and some formation of austenite is therefore expected during tempering. Some of this austenite that is retained at room temperature is seen along martensite lath boundaries in the transmission electron micrograph of Figure 2.

C. W. Marschall et al. [57,58] performed a systematic study of the effects of different tempering treatments on the Charpy toughness of 9Ni steel at 77K. They correlated these data to the amount of austenite present at room temperature, and the amount present at room temperature after quenching the steel to 77K. They found that it was necessary for the austenite to be thermally stable with respect to the martensite transformation if good cryogenic toughness is to be obtained. Tempering for less than 10 hours at temperatures below

600°C was found to be especially effective in producing large amounts of stable austenite. Higher tempering temperatures and longer tempering times were found to be deleterious to both austenite retention and cryogenic notch toughness.

While the importance of the thermal stability of retained austenite was realized by the work of Marschall et al., an understanding of the austenite stability against the martensite transformation during mechanical deformation remained elusive for the next 15 years. Ōoka et al. [59,60] prepared an alloy with a composition predicted for the retained austenite in 9Ni steel, based on equilibrium phase diagrams. They found the material to be austenitic, and this austenite appeared stable against the martensite transformation during fracture. A fractographic examination of 9Ni steel broken below the DBTT led Kron et al. [61] to suggest that brittle fracture was promoted by austenite which transformed to martensite during mechanical deformation. Mechanical stability was listed as an essential feature of the austenite in a cryogenic 6Ni steel developed by Nagashima et al. [62,63]. The mechanical stability of the austenite in 6Ni steel during fracture was indicated by transmission electron micrographs taken by Haga [64], which showed austenite particles near the fracture surface of impact specimens that were constrained to break in a very brittle manner.

However, although these observations suggested that a mechanically stable and ductile austenite interfered with the extension of a crack tip, all such hypotheses were dispelled by 1978, largely on the basis of backscatter Mössbauer spectrometry data [26,27] and fracture profile TEM work [28]. No austenite was found near the fracture surfaces of 6Ni or 9Ni steels subjected to a wide variety of heat treatments and testing conditions. The austenite apparently transformed to martensite in the plastic zone ahead of the crack tip

[27], so the austenite itself cannot serve to blunt a crack tip. Instead, it is necessary to consider how the process of the $\gamma \rightarrow \alpha'$ transformation, and how the consequent fresh martensite particles, may play a role in the fracture process. It has been suggested [65] that the dilatation associated with the $\gamma \rightarrow \alpha'$ transformation in the plastic zone may serve to reduce the stress intensity at the crack tip. However, the small dilatation and the small amount of austenite involved would provide only a small reduction in stress intensity. The material would also have to be fairly ductile to begin with, so that there would be a large plastic zone.

J. W. Morris, Jr. et al. [66] proposed a mechanism whereby thermally stable retained austenite particles transform during deformation to martensite particles that effectively grain-refine the microstructure. In 9Ni steel it is observed that the effective grain size is larger than the width of individual martensite laths because packets of laths exhibit a cooperative cleavage. In the Morris mechanism the common cleavage plane of a packet of martensite laths is shortened when *thermally stable* austenite transforms in response to the local stress to a martensite particle with a different crystallographic orientation than its neighbors. On the other hand, experimental evidence suggests that *thermally unstable* austenite transforms to a martensite particle with the same crystallographic orientation as its neighbors, and does not interfere with the cooperative cleavage of the packet of martensite laths. The Morris mechanism is called into question by a scanning electron fractography study by Yamada [67], who observed that the presence of thermally stable austenite in 9Ni steel had no effect on the cleavage facet size. Instead, Yamada attributes the beneficial effect of retained austenite to a grain boundary adhesion effect, where a temper embrittlement inherent to the martensite matrix is reduced by interlath austenite. Presumably the fresh martensite formed from this inter-

lath austenite during deformation is also beneficial to adhesion.

There may be important consequences of the tempering, or of the austenite, on the properties of the martensite matrix itself. For instance, recovery of microstresses and defect structures of the martensite laths are expected during tempering, but this is expected in 2-5% Ni steels, too, for which there is little benefit of tempering. The $\gamma \rightarrow \alpha'$ transformation will also serve to effect changes in the martensite microstructure. The plastic strains associated with this transformation of interlath austenite will surely change the nature of the interface between the martensite laths, and may even cause plastic deformation in these neighboring laths. So far neither of these changes of the martensite matrix have been related to the systematics of the cryogenic mechanical properties of 9Ni steel.

It is important to note that these mechanisms involving the martensite microstructure, the mechanisms of Morris and Yamada, and possibly even other unconceived mechanisms are not mutually exclusive. Perhaps they all have some significance for cryogenic mechanical properties. Even if definitive evidence is eventually found to support one of these mechanisms, this evidence will probably not rule out the importance of the other mechanisms. It is this author's opinion that there is no immediate prospect for a complete understanding of the mechanism(s) behind the large suppression of the DBTT that occurs after tempering 9Ni steel.

Nevertheless, it is the hope for an eventual understanding of this beneficial effect of tempering that provided the initial motivation for the present research. A comprehensive approach towards such an understanding should probably include a systematic program of mechanical properties tests. Such work is not reported here*. The present research was mostly limited to the

* The author has performed a parallel study of Charpy impact testing to determine the DBTT of a series of isothermally tempered 9Ni steel specimens. A second parallel x-ray

study of basic characteristics of austenite formation during the tempering of 9Ni alloys.

At the start of the present research there was no reliable data on the solute concentration of the austenite. It was believed that thermal stability of the austenite against the martensite transformation depended on its solute content to some extent; it had often been suggested (without experimental proof) that the austenite formed at temperatures above 600°C has too little Ni to remain stable at low temperatures. The further commercial additions of Mn, Cr, Si, and C to the alloy may also serve to affect the austenite stability, as well as the process of its formation. (see Table I.)

**TABLE I**

Alloy Elements of "9 Ni" Steel (w/o)

| Fe | Ni | Mn | Si | Cr | C | P | S |
|---|---|---|---|---|---|---|---|
| Bal. | 9.1 | .50 | .20 | .17 | .06 | .004 | .004 |

Based on inconclusive x-ray measurements of austenite lattice parameters, Marschall et al. attributed the austenite stability entirely to its solute chemistry [58]. Their data suggested that the austenite initially forms with a high C concentration, and as Ni diffuses into the austenite its C content is reduced and it becomes less stable. In this way, Ni will destabilize the austenite. They further hypothesized that the martensite becomes embrittled by the presence of C while the material also suffers from the effects of a thermally unstable austenite. Although the data of Marschall et al. is ambiguous, the possibility that the austenite composition is changing during tempering is intriguing because it implies a non-equilibrium process of austenite formation, which may allow the

diffractometry study of microstrains and particle sizes of the austenite and the martensite was also carried out. Certain trends in the Charpy data correlated better with the x-ray data than with the solute segregation data reported in this thesis. The results of these two parallel studies will be reported elsewhere.

alloy designer some additional freedom to control the austenite stability.

During the course of the present research, some solute concentration data from scanning transmission electron microscopy (STEM) studies of the austenite formed during tempering was reported for a Fe-6Ni commercial alloy [49,68], a Fe-9Ni commercial alloy [69], and binary and ternary Fe-Ni alloys [70-72]. The austenite in the Fe-Ni binary alloys was reported to have a Ni concentration in accordance with the equilibrium Fe-Ni phase diagram. However, the austenite in the commercial steels always had a lower Ni concentration that predicted by the equilibrium Fe-Ni phase diagram. In addition, the Ni content of these commercial alloys apparently increased with tempering time, implying a non-equilibrium process of austenite formation. However, these STEM studies did not attempt systematic measurements of the austenite composition as a function of tempering time and temperature. The simple and reliable methods of specimen preparation for Mössbauer spectrometry appeared to be convenient for a study of the evolution of the austenite composition.

At the beginning of the present research it was hoped that C concentration changes of the martensite could be determined by Mössbauer spectrometry, as claimed by Kim and Schwartz [25]. The C concentration of 9Ni steel has been shown to be particularly important in determining the thermal stability of retained austenite, and probably in determining the kinetics of its formation [73]. In addition, carbides have been observed in 6Ni steel after it was slowly cooled following austenitization [74], and such carbides apparently affected the formation of austenite. Because the low energy x-rays from C cannot be detected in STEM, Mössbauer spectrometry appeared to be especially useful at the time. However, early in the course of this work it became clear that Mössbauer spectrometry was ineffective for measuring the small C concentration changes in the martensite. Instead, like STEM, Mössbauer spectrometry

was effective in supplying data on Ni and "X" (Mn, Cr, Si) solute concentrations, but the effects of the "X" solutes could not be individually resolved in the Mössbauer spectra.

Mössbauer spectrometry techniques were used to simultaneously provide quantitative information on the amount of austenite which had formed, and the loss of Ni and X solutes from the martensite. This combination of phase and chemical analysis information proved valuable in understanding the process of austenite formation. Changes in the average austenite composition with tempering time and temperature were determined. The type of mechanism(s) involved in the process of austenite formation could also be determined. For instance, if the austenite formed by a diffusionless transformation followed by a diffusional solute enrichment, the relationship between the kinetics of solute segregation and the kinetics of austenite formation will be different from the proportional relationship expected if the austenite precipitated with its equilibrium solute concentration. The phase and chemical information that was obtained also served to supply evidence about the importance of the different solute diffusivities (see Fig. 1b) in determining the composition of the austenite.

Since the austenite is at best metastable at room temperature, high temperature measurements are required for reliable determinations of the kinetics of austenite formation. A hot-stage (vacuum furnace) was constructed for the Mössbauer spectrometer, and was used to provide the only reliable data which has yet been reported on the amount of austenite actually formed by tempering. The amount of austenite that had transformed to martensite upon cooling to room temperature was also determined. Unfortunately, there were difficulties in obtaining chemical composition information at high temperatures.

Most experimental measurements of the chemical composition of retained austenite in 9Ni steel are hampered by the small size of the austenite. The only

"well-known" metallurgical technique with adequate spatial resolution for these measurements is STEM. The width of the area analyzed in STEM is, however, comparable to the thickness of the specimen foil. Chemical concentration data taken by Romig and Goldstein [70-72] at points along a line normal to a $\gamma-\alpha'$ interface indicate a practical resolution limit of several hundred angstroms. Even this fine resolution may be insufficient for quantitative chemical analysis of some austenite particles with a dimension less than 1000 Å. Since the austenite particles are especially small after short tempering times, the apparent increase in austenite solute concentration with increasing tempering time, observed by J. I. Kim with STEM, may be due to spatial resolution problems with his specimens and equipment.

For its type of average chemical concentration analysis, Mössbauer spectrometry has effectively no spatial resolution limitation. The $^{57}Fe$ nucleus provides chemical composition information regarding its nearest neighbor atoms -- this is almost the smallest spatial dimension that has meaning for chemical concentration analysis. However, this information is averaged over all martensite crystals. In this respect the average local chemistry information provided by Mössbauer spectrometry is complementary to the less local, but not averaged, chemical composition information provided by STEM. Another advantage of having STEM analyses of austenite compositions was that they provided a check on the Mössbauer spectrometry data. This seemed desirable because Mössbauer spectrometry may be considered an unproven technique for chemical analysis. So although a study of chemical composition changes on an even finer scale may be considered a more elegant metallurgical application of Mössbauer spectrometry, the virtual impossibility of corroborating such measurements would be a disadvantage. The present work should provide firmer groundwork for the use of Mössbauer spectrometry in measuring finer scale

solute concentration changes in the future.

# CHAPTER III

# BASIC THEORY OF THE MÖSSBAUER EFFECT

## A. The Origin of the Mössbauer Effect.

In an analogy to atomic excited states, nuclei have excited states that may be described by quantum numbers for energy and spin, for example. I use the Mössbauer effect as a mechanism for exciting a $^{57}$Fe nucleus in the specimen material from its ground state to its first excited state. This excitation occurs by the absorption of a $\gamma$-ray emitted from a decaying $^{57}$Fe nucleus in the radiation source material. The mechanism is subtle; many aspects of a resonant $\gamma$-ray emission and absorption have no clear analogs in classical physics. One such aspect of the Mössbauer effect is the extraordinary accuracy of the $\gamma$-ray energy (about 1 part in $10^{14}$ ) required in order to resonantly excite a nucleus in the absorber material. A classical nucleus recoils after emitting a $\gamma$-ray, and the amount of the excited state energy given to the outgoing $\gamma$-ray will be reduced by this recoil energy. A freely recoiling $^{57}$Fe nucleus will emit a $\gamma$-ray with only 99.999999998% of the energy difference between the nuclear excited state and the nuclear ground state, and this accuracy is insufficient ($10^4$ times too sloppy) to excite a resonance in an absorber nucleus. A variety of techniques can be used to compensate for this recoil energy [75-80], but they are clumsy in comparison to the Mössbauer effect.

In the Mössbauer effect, the nucleus which emits (or absorbs) a $\gamma$-ray does not recoil freely, and the crystal containing this nucleus recoils as a unit. The recoil momentum is transferred directly to the entire crystal without first setting up lattice vibrational modes which involve the motion of only the emitting nucleus and a few of its neighbors. The $\gamma$-ray energy is reduced by the small recoil energy of the entire crystal, and no energy is consumed in exciting new lattice vibrations. When identical bullets are fired with nearly the same velocity

from a small pistol and from a heavy rifle, the recoil energy will be much less for the rifle. The energy of the "kick" of the rifle will be a fraction of that of the pistol, and this fraction will be equal to the ratio of their masses. In the same way, the recoil energy of an entire crystal is $\approx 10^{-23}$ times as large as that of a single nucleus. This trivial dissipation of energy allows the $\gamma$-ray energy to be sufficiently accurate to resonantly excite an absorber nucleus, provided that the absorber nucleus also does not recoil freely. A calculation of the probability of such a "recoilless" $\gamma$-ray emission by a nucleus in a crystal [1,81-86] is now outlined.

Let us start with an excited nucleus with its internal nuclear coordinates $\{\eta_{ex}\}$ in a crystal lattice whose initial state is described by the coordinates $\{\alpha_i\}$. The set $\{\alpha_i\}$ and time, $t$, describe the positions of the atoms (or more precisely the positions of the heavy nuclei) in the crystal by specifying the state of the lattice vibrational modes. After the $\gamma$-ray is emitted, the internal nuclear coordinates are $\{\eta_g\}$ and the lattice coordinates are $\{\alpha_f\}$. By Fermi's second golden rule the probability, $P$, of this emission process is proportional to the square of the transition matrix element:

$$P \propto |\langle \eta_g \alpha_f | H' | \eta_{ex} \alpha_i \rangle|^2 \qquad \text{III-1}$$

$H'$ is the interaction hamiltonian responsible for the decay of the excited nuclear state and the transfer of the $\gamma$-ray momentum to the lattice. The extremely short range of nuclear forces ensures independence between the motions of the center of mass of our nucleus in the crystal, and changes in the internal degrees of freedom of this nucleus. $H'$ is hence a product of two commuting sub-hamiltonians:

$$H' = H_N \, H_{CM} \quad ; \quad [H_N, H_{CM}] = 0 \, . \qquad \text{III-2a,b}$$

$H_N$ acts on $\eta$ , and $H_{CM}$ involves the position of the center of mass of the decaying nucleus, $X$, in the transfer of the recoil momentum to the lattice. Equation

III-2b allows us to express our state function $|\eta\alpha>$ as the product $|\eta>|\alpha>$. Equation III-1 becomes:

$$P \propto |<\eta_g|H_N|\eta_{ex}>|^2 \, |<\alpha_f|H_{CM}|\alpha_i>|^2 . \qquad \text{III-3}$$

The nuclear factor in equation III-3 is a constant and is independent of anything outside the decaying nucleus; we need consider only the lattice factor to explain the existence of the Mössbauer effect. We start by considering the one-dimensional functional form of $H_{CM}$, which we try to express as a Fourier series in a space coordinate $x$:

$$H_{CM}(x) = \sum_{k_i} a_k e^{ik_i x} . \qquad \text{III-4}$$

In correspondence with classical mechanics, the forms of quantum mechanical equations are invariant under Galilean transformations [81,87,88], where momentum and position coordinates are $p'$ and $x'$ for the moving observer. So if we proceed to Galilean transform our operator, $H_{CM}(x,t)$, with respect to the lattice state functions, $|\alpha(\textit{includes } X),t>$, the lattice matrix element of equation III-3 must be unchanged. In our Galilean transformation we apply both the momentum translation operator, $e^{-i\frac{x}{\hbar}mv}$ (since $p' = p - mv$), and the position translation operator, $e^{-ik\cdot vt}$ (since $x' = x - vt$), to $H_{CM}$; $v$ is the velocity of the new reference frame with respect to the old one, $m$ is the nuclear mass, and $\hbar$ is Planck's constant. If $H_{CM}$ involves more than one $k_i$ in equation III-4, these terms will require different operators for their position translation, and the new $H'_{CM}$ will not equal $H_{CM}$ times a phase factor of modulus unity. Hence the probability for $\gamma$-ray emission, $P$, will only be invariant for a moving observer if there is but one term in the Fourier series for $H_{CM}$. When we work with translations in momentum space where:

$$H_{CM}(k) = \sum_{x_j} a_{x_j} e^{-ikx_j},$$

then the momentum operators will likewise give trouble unless there is only one

term in this series for $H_{CM}(k)$. Momentum conservation requires that this one term be the $k_i = k_\gamma$ and $x_j = X$ term, where $\hbar k_\gamma$ is the $\gamma$-ray momentum. The probability of a $\gamma$-ray emission which changes the lattice state from $\alpha_i$ to $\alpha_f$ is now:

$$P_{fi} = \frac{|<\alpha_f|e^{ik_\gamma X}|\alpha_i>|^2}{\sum_{<\alpha_f|} |<\alpha_f|e^{ik_\gamma X}|\alpha_i>|^2} \quad . \qquad \text{III-5}$$

We have now normalized by the relative probability of all such possible transitions. However, the closure, $\sum_{<\alpha_f|} |\alpha_f><\alpha_f| = 1$, ensures that the denominator of equation III-5 equals 1.

The Mössbauer effect is observable because the probability of a $\gamma$-ray emission in which the lattice coordinates are unchanged,

$$P_{ii} = |<\alpha_i|e^{ik_\gamma X}|\alpha_i>|^2 \quad , \qquad \text{III-6}$$

is sufficiently large. $P_{ii}$ is the probability of a $\gamma$-ray emission without the generation of phonons for which only the recoil energy of the entire crystal $\left(\frac{(\hbar k_\gamma)^2}{10^{23} \cdot m}\right)$ will detract from the $\gamma$-ray energy.

In order to evaluate equation III-6, we must adopt a form for the lattice vibrational modes. For an Einstein solid in its ground state, equation III-6 becomes:

$$P_{ii} = \int_{-\infty}^{\infty} \left(\frac{m\omega}{\pi\hbar}\right)^{\frac{1}{4}} e^{-\frac{m\omega X^2}{2\hbar}} e^{ik_\gamma X} \left(\frac{m\omega}{\pi\hbar}\right)^{\frac{1}{4}} e^{-\frac{m\omega X^2}{2\hbar}} dX \, ,$$

which is the Fourier transform of a Gaussian function. This gives the result:

$$P_{ii} = e^{-k_\gamma^2 <X^2>} \quad . \qquad \text{III-7}$$

The Mössbauer effect occurs most efficiently when low energy $\gamma$-rays are emitted from nuclei which are tightly bound in a solid. If we adopt the Debye model and include a distribution of lattice vibrational frequencies, equation III-7 is still basically valid, but this calculation yields [1,81,86]:

$$P_{ii} = \exp - \left\{ \frac{6R}{k_B \vartheta} \left[ \frac{1}{4} + \left( \frac{T}{\vartheta} \right)^2 \int_0^{\frac{\vartheta}{T}} \frac{x}{e^x - 1} dx \right] \right\}. \qquad \text{III-8}$$

$R \equiv \frac{(\hbar k_\gamma)^2}{2m}$ is a recoil energy, $k_B$ is Boltzmann's constant, $T$, is temperature, and $\vartheta$ is the Debye temperature. Equation III-8 is useful for estimating how the efficiency of the Mössbauer effect decreases with temperature.

**B. Mössbauer Spectrometry**

All spectrometries involve the measurement of an "intensity" as a function of energy. In Mössbauer spectrometry the number of nuclear transitions in the absorber material (caused by the Mössbauer effect) is measured as the energy of the emitted $\gamma$-ray is shifted over a small range. All of the interesting information in our work comes from the distribution and relative intensities of the $\gamma$-ray absorptions as a function of the energy shift; our interest is in how this absorption profile differs for different absorber materials. The total intensity of the Mössbauer effect (proportional to $P_{ii}$) was, in fact, maintained as constant as was experimentally possible when studying different specimens.

The $\gamma$-ray energy shift can be accomplished in two ways. Mechanical motion of the radiation source with a velocity, $+V$, towards the absorber increases the $\gamma$-ray frequency in the absorber's reference frame. There is hence a change, $\Delta E$, in the $\gamma$-ray energy, $E_\gamma$, which is:

$$\Delta E = \frac{V}{c} E_\gamma .$$

A 1 mm/sec velocity will shift the energy of our 14.41 keV $\gamma$-ray from a $^{57}$Fe nucleus by $4.8 \times 10^{-8}$ eV. The second means of changing the $\gamma$-ray energy comes from a relativistic effect associated with the thermal vibrations of source and absorber nuclei [4,5,89]. Although these vibrations are averaged out over the relatively long times associated with nuclear decays and excitations, their energy is changed during a recoilless emission because the mass of the

decaying nucleus changes by $\frac{-E_\gamma}{c^2}$ when it loses energy to the $\gamma$-ray. So even though the phonon occupation numbers do not change during a recoilless emission, the phonon energy is increased by the fraction $\frac{-E_\gamma}{mc^2}$, which is energy lost from the $\gamma$-ray. If the absorber is hotter than the source, the absorption spectrum will be shifted to lower energies by the amount:

$$\Delta E = -\frac{1}{2}\frac{<V_{vibr}^2>}{c^2}E_\gamma \ ,$$

where $<V_{vibr}^2>$ is the mean squared thermal velocity.

We now predict with surprising accuracy the lineshape of the simplest Mössbauer spectrum from a monochromatic* source and a monochromatic absorber. It is now necessary to consider the nuclear factor which we left back in equation III-3. In a recoilless emission, the $\gamma$-ray energy distribution is the same as the energy distribution of the excited state of the source nucleus. The spread in energy of this excited state is determined by the lifetime of the excited nuclear state through the $\Delta E \Delta t \cong \hbar$ uncertainty relationship. There are several known processes which operate in parallel to drain probability density out of the excited nuclear state. The largest rate of decay is associated with internal conversion processes in which the nuclear energy is used to eject an atomic electron or x-ray. If internal conversion processes occur $\alpha$ times more frequently than $\gamma$-ray emissions, the total initial probability for decay of the excited state per unit time, $\frac{\Gamma'}{\hbar}$, will be more rapid than would be predicted by the nuclear factor of equation III-3.

$$\frac{\Gamma'}{\hbar} = (1 + \alpha)\ \frac{E_\gamma}{\hbar}\ |<\eta_g\,|\,H_N\,|\,\eta_{ex}>|^2 \ .$$

All known decay processes predict that the rate of decay of the excited nuclear

* All $^{57}Fe$ nuclei in a monochromatic source emit $\gamma$-rays with identical energy distributions.

state will be proportional to the remaining probability density in the excited state. The time dependence of the excited state probability is hence $e^{\frac{-\Gamma}{\hbar}t}$, and the excited state wavefunction goes as $e^{-\frac{\Gamma}{2\hbar}t}$. The Fourier transform of this exponential time dependence gives a Lorentzian energy dependence for the excited state. Expressing energy in terms of the velocity of the radiation source, and with $\Gamma \equiv \Gamma(\frac{c}{E_\gamma})$, we have for the $\gamma$-ray lineshape, $S(V)$:

$$S(V) = \frac{1}{\pi} \frac{\left(\frac{\Gamma}{2}\right)}{\left(\frac{\Gamma}{2}\right)^2 + (V - V_o)^2} . \qquad \text{III-9}$$

which is normalized such that:

$$\int_{-\infty}^{\infty} S(V)dV = 1 .$$

The energy dependence of the excited nuclear state of a monochromatic absorber is also a Lorentzian function of the same breadth. The *observed* lineshape will be the convolution of the source and absorber lineshapes. The convolution of two Lorentzian functions, each with half-width $\frac{\Gamma}{2}$, is again a Lorentzian function, but with a half-width $\Gamma$. After receiving some known corrections, the observed Mössbauer peaks from pure Fe metal were fit with a Lorentzian function to the best accuracy I could expect with my experimental data. This prediction of a Lorentzian lineshape for a Mössbauer peak obtained with a monochromatic source and absorber is a surprisingly accurate and clearly useful result.

The cross section for $\gamma$-ray absorption at the resonance energy, $\sigma_o$, can be determined from first principles [90,91] to be $2.5\times10^{-18}$ cm$^2$ for 14.41 keV $\gamma$-ray absorption by a $^{57}$Fe nucleus. There is a natural isotopic fraction of $^{57}$Fe, $\alpha$, of 0.022, and with a respectable value of $P_{ii}$ from equation III-8 of 0.75, we can

predict that a mean scattering length of $3.0\times10^{-4}$ cm would be characteristic of iron metal at room temperature, if it were monochromatic. We could obtain a Mössbauer spectrum experimentally by counting the number of $\gamma$-rays which traverse a foil specimen of about this thickness. Such a transmission geometry experiment measures dips in the count rate for $\gamma$-ray energies near resonance. Alternatively, we could count $\gamma$-rays which are re-emitted by the specimen following resonant absorptions within this characteristic distance near its surface. Such experiments that are designed to count backscatter radiation would exhibit higher count rates near resonance energies. Internal conversion radiations (6.3 keV x-rays or 5.6 keV electrons) may also be counted in order to obtain a Mössbauer spectrum, but all data for this thesis used transmitted or backscattered 14.41 keV $\gamma$-rays. Excellent agreement between features resolved in backscatter and transmission Mössbauer spectra was found (see Fig. 9), but the main body of my work used transmission Mössbauer spectra for reasons of efficiency, as described in Chapter VII.

**C. Hyperfine Fields**

"Hyperfine structure" was first cbserved around the turn of the century [92,93] in early atomic spectroscopy work using optical interferometry. W. Pauli [94] first suggested that these tiny fractional changes in optical wavelengths (about 1 part in $10^5$) were caused by perturbations of *electron* energy levels arising from an interaction between an electron magnetic moment and the nuclear spin. Several mechanisms for magnetic and electrostatic perturbations of electron energy levels due to interactions with nuclei were discovered and explained by atomic spectroscopists before 1940 [95].

Hyperfine interactions are the source of all information obtained in this Mössbauer spectrometry study. However, in contrast to optical spectrometry, in Mössbauer spectrometry the useful infcrmation comes from the perturbations

of *nuclear* energy levels arising from interactions with atomic electrons. There are three hyperfine interactions in Mössbauer spectrometry: (1) the isomer shift (a nuclear electric monopole effect), (2) the nuclear electric quadrupole effect, and (3) the hyperfine magnetic field effect. The origin of these three perturbations and some general mechanisms for producing them are described in this section. Emphasis is placed on hyperfine magnetic fields, since these are the most valuable source of metallurgical information from ferromagnetic iron alloys. For example, the phase analysis of Fe-Ni alloys is based simply on the presence or absence of a hyperfine magnetic field at $^{57}$Fe nuclei in martensite or austenite, respectively.

**1. The Isomer Shift**

The nuclear charge extends over a finite radius, and thus overlaps electron wavefunctions which are nonvanishing near $r=0$. The Coulomb interaction energy of a finite nucleus with such an interpenetrating electron perturbs the nuclear energy levels by about $+10^{-4}$ eV with respect to a point nucleus (see Fig. 3). Since the observed nuclear transition energy is the difference between the nuclear ground and excited state energies, if the Coulomb interaction is to affect the transition energy, there must be a difference between the nuclear charge density for the excited state, $\rho_{ex}(r)$, and that of the ground state, $\rho_g(r)$. The electron wavefunction, $\psi(r)$, itself does not depend on the internal nuclear coordinates. Furthermore, it is necessary that $\psi(r) = \psi(0)$ over the small dimension of the nuclear charge, because a change in $\psi(r)$ over such a short distance would require a huge kinetic energy for the electron. The Coulomb interaction energy between the electrons and the excited nucleus (with subscripts $e$ and $n$, respectively; $e$ is also the electronic charge) is:

$$E_{ex} = -e^2 \int_0^\infty \int_0^\infty \frac{|\psi(0)|^2 \rho_{ex}(r_n)}{|r_e - r_n|} d^3r_e d^3r_n \, .$$

The integral:

$$-\int_0^\infty \frac{e\rho_{ex}(r_n)}{|r_e - r_n|} d^3 r_n$$

is a potential which goes as $\frac{-Ze}{r_e}$ for $r_e$ greater than the nuclear radius, $r_n^{max}$. So if we consider the charge of the nucleus in shells* of different $r_n'$, the potential from each shell will be the $\frac{-Ze}{r_e}$ of a point nucleus from $r = \infty$ to $r = r_n'$, but will remain at the constant value $\frac{-Ze}{r_n'}$ for $r_e < r_n'$. The Coulomb interaction of each shell with the electron density will be less negative than it would be if the same nuclear charge were located at the origin. This net potential energy difference is:

$$+ \frac{2}{3}\pi Z e^2 (r_n')^2 |\psi(0)|^2 .$$

The net potential from an arbitrary radial distribution of nuclear charge can be constructed as a sum of these shell potentials weighted by the nuclear charge distribution, $\rho(r)$. This procedure serves to extract the second moment, $\langle r_n^2 \rangle$, from $\rho_{ex}(r)$, so the change in Coulomb interaction energy of the excited state with respect to a point nucleus will be:

$$E_{ex} = \frac{2}{3}\pi Z e^2 \langle r_{nex} \rangle^2 |\psi(0)|^2 .$$

With a similar expression for the ground state energy change, we have the change in energy of the nuclear transition known as the isomer shift [83,96,97]:

$$E_{ex} - E_g = \frac{2}{3}\pi Z e^2 |\psi(0)|^2 (\langle r_{nex}^2 \rangle - \langle r_{ng}^2 \rangle) . \qquad \text{III-10}$$

Only the $|\psi(0)|^2$ factor will change for different absorber materials; the nuclear charge distribution does not sense the chemical state of the absorber. The isomer shift thus serves to reveal changes in the electron density in the nucleus, i.e. changes in $|\psi(0)|^2$. For small $r$ the radial dependence of hydrogenic

* We mean "spherical shells", which do not imply a "shell model" for the nucleus itself.

wavefunctions goes as $r^l e^{\frac{-2r}{na_0}}$, where $n$ is the principal quantum number and $l$ is the angular momentum quantum number. Only $l = 0$ wavefunctions are non-vanishing at $r = 0$, so only electrons in $s$ states are directly responsible for the isomer shift*. The observed isomer shifts in $^{119}$Sn Mössbauer spectrometry correlate straightforwardly to changes in the number $5s$ valence electrons in Sn compounds.

Using equation III-10 for a straightforward correlation of $^{57}$Fe isomer shifts to changes in $|\psi_{4s}(0)|^2$ from $4s$ valence electrons is only possible for a series of iron compounds with the same number of $3d$ electrons. For example, in a series of compounds with the $3d^6\,4s^x$ configuration [97], the $^{57}$Fe isomer shifts decrease the energy of the nuclear transition as the number of $4s$ valence electrons increase. This agrees with equation III-10 because $\langle r_{nex}\rangle - \langle r_{ng}\rangle = -0.001\langle r_{ng}\rangle$. However, the $3d$ electrons have major shielding effects on the radial distributions of $3s$ electrons and other $s$ electrons; the addition of one $3d$ electron to an iron compound serves to reduce the $s$ electron density at the nucleus by nearly the amount that the addition of one $4s$ electron will increase $|\psi_{4s}(0)|^2$. Since $|\psi(0)|^2 = \sum_{n=1}^{4} |\psi_{ns}(0)|^2$, we must recognize the possibility that two compounds with the same isomer shift may have a substantially different balance of $3d$ and $4s$ electrons.

In alloys, not all $^{57}$Fe nuclei will experience the same isomer shift. $^{57}$Fe nuclei may experience increased or decreased isomer shifts depending on their proximity to the solute atoms. The effect of these localized isomer shifts on the shape of Mössbauer peaks is described in section IV-F. In this study the small isomer shifts were not so valuable for chemical analysis as they were for eluci-

* $p$ electrons become nonvanishing at $r = 0$ in atoms heavier than iron due to relativistic effects.

dating details of local electron spin polarization effects. It was the local electron spin polarizations which were of most value for chemical analysis, and the local isomer shifts were of value in unraveling them, as described in Chapters V, VI and X.

**2. The Nuclear Electric Quadrupole Effect.**

$^{57}$Fe nuclei in either the excited state or the ground state do not have spherical charge distributions. The excited state has a spin $I = \frac{3}{2}$ and the shape of a prolate (cigar shaped) ellipsoid. This charge distribution gives the nucleus an electric quadrupole moment. When placed in an external electric field, an electric quadrupole moment interacts with the electric field gradient to perturb the energy of the nuclear excited state. In the simplest case the electric field gradient direction defines the z axis. The $I = \frac{3}{2}$ excited state may choose the orientations $I_z = \frac{+3}{2}, \frac{+1}{2}, \frac{-1}{2}$, or $\frac{-3}{2}$ along this axis, but the inversion symmetry of an ellipsoid of charge requires that each pair $\frac{+3}{2}, \frac{-3}{2}$ and $\frac{+1}{2}, \frac{-1}{2}$ of orientations has the same interaction energy with an electric field gradient. The $^{57}$Fe ground state of $I = \frac{1}{2}$ can have only one interaction energy. Therefore two nuclear transition energies, due to $(I = \pm\frac{3}{2} \rightarrow I = \pm\frac{1}{2})$ and $(I = \pm\frac{1}{2} \rightarrow I = \pm\frac{1}{2})$, would be expected in this simplest case (see Fig. 3).

However, in pure iron with cubic symmetry no electric field gradient is possible at a $^{57}$Fe nucleus. Magnetostriction removes this cubic symmetry, but its resulting nuclear electric quadrupole effect is barely measurable [98,99]. Additionally, in ferromagnetic alloys of iron the z-axis is determined by the direction of the hyperfine magnetic field because the interaction of $I_z$ with this mag-

netic field is by far the dominant perturbation of the nuclear energy levels. So although the presence of a solute atom as a nearest neighbor to a $^{57}$Fe nucleus breaks the cubic symmetry, the electric field gradient direction (which is along the direction of separation between the $^{57}$Fe nucleus and the neighboring solute atom) does not generally bear any predictable relationship to the magnetically defined z-axis. In this case only a general broadening, and no net shift is expected in the hyperfine magnetic field splitting of the Mössbauer absorption peaks due to the electric quadrupole effect.

### 3. The Hyperfine Magnetic Field Effects.

This subsection explains the origin of the basic hyperfine magnetic field perturbation which gives a six peak spectrum from $^{57}$Fe nuclei in ferromagnetic iron alloys [83,100-102] We then describe factors which influence the relative intensities of these six peaks. The interaction energy of the nuclear magnetic moment, $\mu$ , with the magnetic hyperfine field, H *, is $\mu \cdot$H. The nuclear spin quantum number, $I$, is related to the nuclear magnetic moment by the nuclear magneton, $\mu_N$, times a gyromagnetic ratio $g_1$ for the excited state, and $g_0$ for the nuclear ground state. In our ferromagnetic martensite the interaction energy $\mu \cdot \mathbf{B}$ is by far the largest perturbation which lifts the degeneracy of nuclear states with differing components of nuclear spin. Therefore it is the component of nuclear spin along the magnetic field direction, $\hbar \mathbf{I}_z$, which is quantized in units of $\hbar$. For the $^{57}$Fe excited state with $I = \frac{3}{2}$ we have the set of $I_z = \{\frac{-3}{2}, \frac{-1}{2}, \frac{+1}{2}, \frac{+3}{2}\}$, and the set for the ground state is $I_z = \{\frac{-1}{2}, \frac{+1}{2}\}$, since the ground state spin is known to have $\mathbf{I} = \frac{1}{2}$. The nuclear decay is known to proceed by magnetic dipole (M1) radiation, so there exists a selection rule

*We use H to represent the hyperfine magnetic field in order to conform to conventional usage, not because we are dealing with the magnetic intensity vector.

whereby $I_z$ may only change by -1, 0, or +1 in the nuclear transition. Consequently we have only six different transition energies (see Fig. 3) which are shifted from an unperturbed energy by the amounts shown in Table II.

**TABLE II**

The Magnetic Sextet of $^{57}$Fe Mössbauer Peaks

| Peak Designation (of Fig. 3) | $I_z \rightarrow I_z$ ground → excited | Energy Shift | $\vartheta$ Dependence |
|---|---|---|---|
| 1 | -1/2 -> -3/2 | $(-\frac{3}{2}\lvert g_1\rvert - \frac{1}{2}g_o)\mu_N H$ | $\frac{3}{16}(1+\cos^2\vartheta)$ |
| 2 | -1/2 -> -1/2 | $(-\frac{1}{2}\lvert g_1\rvert - \frac{1}{2}g_o)\mu_N H$ | $\frac{4}{16}(\sin^2\vartheta)$ |
| 3 | -1/2 -> +1/2 | $(+\frac{1}{2}\lvert g_1\rvert - \frac{1}{2}g_o)\mu_N H$ | $\frac{1}{16}(1+\cos^2\vartheta)$ |
| 4 | +1/2 -> - 1/2 | $(-\frac{1}{2}\lvert g_1\rvert + \frac{1}{2}g_o)\mu_N H$ | $\frac{1}{16}(1+\cos^2\vartheta)$ |
| 5 | +1/2 -> +1/2 | $(+\frac{1}{2}\lvert g_1\rvert + \frac{1}{2}g_o)\mu_N H$ | $\frac{4}{16}(\sin^2\vartheta)$ |
| 6 | +1/2 -> +3/2 | $(+\frac{3}{2}\lvert g_1\rvert + \frac{1}{2}g_o)\mu_N H$ | $\frac{3}{16}(1+\cos^2\vartheta)$ |

$|H| > 300$ kG for $^{57}$Fe nuclei in our Fe-Ni martensites, and since $g_0 = -1.75g_1$, absorption peaks 3 and 4 of Fig. 3 are well-removed from the zero Doppler shift energy. On the other hand, the magnetically unperturbed absorption peak from $^{57}$Fe nuclei in the paramagnetic austenite lies near the zero Doppler shift energy (see Fig. 10). The austenite peak is hence well-resolved from all peaks of the magnetically split martensite spectrum. The method of phase analysis in this work determines the fraction of $^{57}$Fe nuclei in the austenite phase by taking the ratio of the area of the austenite peak to the total area of all peaks in the Mössbauer spectrum. Small corrections for differences in the resonance efficiencies of austenite and martensite, nonlinear absorption effects (thickness distortion), and chemical composition differences (which make the

vol.% of austenite different from the at.% of austenite) are discussed in Chapter VIII.

These six magnetically split absorption peaks differ in their net intensities averaged over all $\gamma$-ray propagation directions. As an example we calculate the total probability for transition no. 3 of Table II. By the Wigner-Eckart theorem we know that the matrix element responsible for the magnetic dipole nuclear transition will depend only on the inner product of the bra* ${}_n\langle\frac{3}{2},\frac{+1}{2}|$ for the nucleus in its excited state, and the ket $|\frac{1}{2},\frac{-1}{2}\rangle_n\,|1,1\rangle_\gamma$ for the nucleus in its ground state plus a $\gamma$-ray†. This inner product is the definition of the Clebsch-Gordon coefficient, $\langle j,m\,|m_1,m_2\rangle = \langle\frac{3}{2},\frac{1}{2}|-\frac{1}{2},1\rangle$, which equals $\sqrt{\frac{1}{3}}$, so the relative total probability that a nuclear absorption will be an $I_z = \frac{-1}{2} \rightarrow I_z = \frac{+1}{2}$ (type no. 3) absorption is $\frac{1}{3}$. Proceeding this way for the other five nuclear transitions, we find overall (angle-averaged) relative intensities of 3:2:1:1:2:3 for the six magnetically split absorption lines, in order of increasing energy.

The relative intensities of the six magnetically split absorption peaks also depend on the angle, $\vartheta$, between the magnetically defined z-axis and the direction of the $\gamma$-ray travel. We now argue the plausibility for the observed dependences of the six absorption probabilities of unpolarized $\gamma$-rays on the angle $\vartheta$. Two of the absorption peaks involve the change $\Delta I_z = 0$. Since the total z component of angular momentum is conserved in the nuclear transition, the absorbed $\gamma$-ray must have a zero z-component of angular momentum. The $\Delta I_z = 0$ transitions may be thought to arise from energy absorption by a mag-

* We use a notation for the nuclear state vector of $|I,I_z\rangle_n$, and an analogous $|j_1 j_z\rangle_\gamma$ for the spin quantum numbers of the $\gamma$-ray.
† In this example the $\gamma$-ray must be polarized along the z-axis (i.e. $j_z = 1$) in order to conserve the z component of angular momentum.

netic dipole which oscillates parallel to the z-axis. $\gamma$-rays which travel in the x-y plane must have their magnetic polarization along the z-axis in order to be absorbed. There will be no absorption of $\gamma$-rays which travel along the z-axis because they cannot sustain polarization along the z-axis. The maximum absorption in a $\Delta I_z = 0$ transition occurs for $\gamma$-rays in the x-y plane, and the angular dependence of this absorption is found to go as $\sin^2\vartheta$ (see Table II) for unpolarized $\gamma$-rays.

The combined excitation of one magnetic dipole oscillating along the x-axis and a second magnetic dipole oscillating 90 ° out of phase along the y-axis absorbs circularly polarized $\gamma$-rays travelling along the z-axis. Such a pair of dipoles is responsible for the four $\Delta I_z = \pm 1$ nuclear transitions. Although the maximum absorption in the $\Delta I_z = \pm 1$ transitions is for $\gamma$-rays travelling along the z-axis, there is still an absorption of linearly polarized $\gamma$-rays travelling along the x-axis (or y-axis) due to the excitation of a dipole oscillation along the y-axis (or x-axis). The intensity of the $\Delta I_z = \pm 1$ transitions go as $1 + \cos^2\vartheta$ (see Table II) for unpolarized $\gamma$-rays.

Peaks 1 and 6, and the other pair of $\Delta I_z = \pm 1$ absorptions, peaks 3 and 4, exhibit the same dependence of absorption probability on $\vartheta$, and a constant intensity ratio of 3:1. The nonlinear thickness distortion corrections described in Chapter VIII can hence be checked or calibrated by comparing the integrated intensities of these peaks.

# CHAPTER IV

# PHENOMENOLOGY OF SOLUTE-INDUCED PERTURBATIONS IN $^{57}$Fe HYPERFINE MAGNETIC FIELDS

## A. Additive Hyperfine Magnetic Field Perturbations and their Probabilities.

As early as 1961 Flinn and Ruby [103] observed extra peaks in Mössbauer spectra from ferromagnetic Fe-Al alloys. They attributed these peaks to $^{57}$Fe nuclei which neighbored Al atoms. In early work by Stearns [104] with ordered $Fe_3Si$ alloys, the observed spectra were decomposed into six line sub-spectra from $^{57}$Fe nuclei with different Si atom coordinations. The present section first describes the work of Wertheim, et al. [105], which substantially systematized the observed $^{57}$Fe hyperfine structure in Mössbauer spectra of many binary Fe-X alloys. In their work it was first assumed that when one solute atom (of an element "X") is located in the first nearest neighbor (1 n.n) shell of an $^{57}$Fe nucleus, this $^{57}$Fe nucleus will experience a perturbed hyperfine magnetic field of $H = H_0 + \Delta H_1^X$. In a very dilute alloy, $H_0$ is the hyperfine magnetic field at a $^{57}$Fe nucleus in pure iron, and is -330 kG*. To be more specific, let $\Delta H_1^X = +33$kG. A $^{57}$Fe nucleus with one solute atom in its 1n.n. shell will still give a six line absorption spectrum as outlined in Table II. However, this 10% reduction in the magnitude of the hyperfine magnetic field at the $^{57}$Fe nucleus causes a 10% reduction in the energy separation of its absorption peaks. In a dilute Fe-X alloy only a few $^{57}$Fe nuclei will experience this 10% reduction in $H$. The majority of $^{57}$Fe nuclei which have no solute nearest neighbors will provide a strong six peak spectrum nearly characteristic of pure iron, which we call the main "unperturbed" peaks. However, the observed Mössbauer spectrum from dilute Fe-X alloys will also include a sextet of "satellite" peaks due to those $^{57}$Fe

* The origin of the sign convention is explained in section V-D.

nuclei which have one solute atom in their 1 n.n. shell. These satellite peaks will lie on the low Doppler shift energy side of each "unperturbed" main peak (their velocities will be 10% closer to the center of the Mössbauer spectrum than the unperturbed main peaks). Other satellite intensities may require consideration. A similar, but smaller, $\Delta H_2^X$ was also assumed by Wertheim, et al. for the perturbation due to one solute atom in the 2n.n. shell, but individual hyperfine magnetic field perturbations due to solute atoms in 3n.n. and more distant shells were neglected.

Early studies of hyperfine magnetic field effects in Fe-X alloys did not use dilute solutions. In non-dilute solutions we must expect significant probabilities of finding more than one solute atom in a given nearest neighbor shell. If we assume that hyperfine magnetic field perturbations are additive, then if the $n_1$ solute atoms are in the 1n.n. shell and $n_2$ solute atoms are in the 2n.n. shell of a $^{57}$Fe nucleus, its hyperfine magnetic field will be:

$$H^X(n_1,n_2) = H_o + n_1\,\Delta H_1^X + n_2\,\Delta H_2^X\,.$$

More generally:

$$H^X(\{n_j\}) = H_o + \sum_{j=1}^{J} n_j\,\Delta H_j^X\,. \qquad \text{IV-1}$$

Equation IV-1 is the mathematical manifestation of assuming additivity of the $^{57}$Fe hyperfine magnetic field perturbations from individual solute neighbors in each nearest neighbor shell. It forms the phenomenological basis for the dependence of the hyperfine magnetic field on solute atom configurations around a $^{57}$Fe nucleus. We have considered only $J$ nearest neighbor shells explicitly (Wertheim, et al. used two), but $H_o$ may exhibit some dependence on solute concentration due to less localized (i.e. beyond the $J$ n.n. shell) magnetic polarization effects. This is included by considering $H_o$ to be weakly dependent on $c_X$.

It is also necessary to establish the relative numbers of each distinct arrangement of solute atoms around an iron atom in order to characterize the hyperfine structure observed in a Mössbauer spectrum. The probability of a solute atom in the $j^{th}$ nearest neighbor shell around an iron atom is directly related to the correlation functions used to define short-range-order coefficients. If there is inconsequential short range order in the alloy, as is apparently the case in this work, it is adequate to use a random solid solution model to predict the probability of each specific arrangement of solute atoms around a $^{57}$Fe nucleus--the probability of a specific set $\{n_j\}$. This model assigns the binomial probability *, $P(N_j,n_j,c_X)$, to the probability of finding $n_j$ atoms in the $j^{th}$ nearest neighbor shell which contains $N_j$ sites when the solute concentration is $c_X$. For substitutional solutes in the bcc structure the set $\{N_1,N_2,N_3 \cdots\}$ begins $\{8,6,12,24,8,6...\}$. If we consider perturbations due to solute atoms in only the first $J$ nearest neighbor shells of the bcc structure, the total probability of a nearest neighbor configuration with a specific set of shell occupancies, $\{n_j\}$, is $P_{\Sigma J}(\{N_j\},\{n_j\},c_X)$:

$$P_{\Sigma J}(\{N_j\},\{n_j\},c_X) = \prod_{j=1}^{J} P\ (N_j,n_j,c_X) \qquad \text{IV-2a}$$

$$P(N_j,n_j,c_X) \equiv \frac{N_j!}{(N_j - n_j)!\ n_j!} c_X^{n_j}(1 - c_X)^{N_j - n_j} \qquad \text{IV-2b}$$

It can be shown that the $P_{\Sigma J}$ are normalized:

$$\sum_{n_1=1}^{8} \sum_{n_2=1}^{6} \sum_{n_3=1}^{12} \cdots \sum_{n_J=1}^{N_J} P_{\Sigma J}\ (\{n_j\}\ ,c_X) = 1\ . \qquad \text{IV-2c}$$

Equations IV-2a,b give the probability of each set of nearest neighbor shell occupancies by X atoms, $\{n_j\}$, for a given $c_X$. Equation IV-2a is exact for a random solid solution. The approximation in the development was made in Eqn. IV-1 when the magnitudes of the hyperfine magnetic field perturbations were

* Note that the random probability of finding 3 solute atoms in the bcc 1n.n. shell is equal to the probability of 3 darts hitting a target in 8 tosses if the overall probability of each hit is c.

parameterized exclusively in terms of the sets $\{n_j\}$ and $\{\Delta H_j^X\}$. For my purposes, expressing the hyperfine magnetic field perturbation in terms of low order polynomials involving the $\{n_j\}$ is convenient for two reasons: 1) it works well enough to reduce the number of parameters necessary to account for the hyperfine magnetic field perturbation at a $^{57}$Fe nucleus surrounded by a complicated solute configuration, and 2) for random solid solutions we can determine the moments of the distribution of $^{57}$Fe hyperfine magnetic fields in terms of simple functions of low order moments of binomial probability distributions. Low order moments of binomial probability distributions are readily found; for example, see Table M in Chapter X.A. Especially convenient is the parameterization which assumes the simple additivity of equation IV-1. Despite the generally good success and popularity of these additive hyperfine magnetic field perturbations, the additivity assumption can become an approximation which deteriorates with increasing solute concentration. In Chapter VI it is shown how this error develops when the solute atom perturbations of the $^{57}$Fe hyperfine magnetic field are sensitive to the local environment of the solute atom itself. In Chapter X I discuss how this error largely accounts for why the skewness of the Fe-9Ni Mössbauer peaks differs qualitatively from the skewness predicted by the phenomenological nearest neighbor model with the additivity assumption. For the dilute concentrations of X solutes in Fe-9Ni-1X alloys, however, the low probability of having more than one X solute neighbor obviates the large errors associated with the additivity assumption. Some features of the phenomenological model of this Chapter IV are used for X element concentration analysis, but my method of Ni concentration analysis is not based on these results.

**B. General Features of Previous Work.**

Many Mössbauer spectrometry (and NMR spectrometry) experiments of the mid-1960's to the early 1970's [39,41,103-127] included the determination of the

set $\{\Delta H_j^X\}$ of equation IV-1 from experimental spectra. For example, the popular "two shell" data analysis procedure assumes that only $\Delta H_1^X$ and $\Delta H_2^X$ are significant (so J=2 in equations IV-1,2). The product $P(n_1,n_2,c_X) = P(8,n_1,c_X) \times P(6,n_2,c_X)$ is calculated for each of the 8×6 = 48 combinations of $n_1$ and $n_2$. The parameters $\Delta H_1$ and $\Delta H_2$ are fixed at trial values, and a sextet of Lorentzian peaks with intensity $P(n_1,n_2,c_X)$ is located at velocities predicted by equation IV-1 for $n_1$ and $n_2$. All 48 sextets of Lorentzians are then added together to generate a simulated spectrum. The simulated spectrum is compared with an experimentally measured spectrum from a random binary iron alloy with an X solute element concentration of $c_X$. The root mean square difference between the measured and simulated spectra is computed, and the parameters $\Delta H_1$ and $\Delta H_2$ are varied systematically until the minimum difference is found; these parameters are offered as $\Delta H_1^X$ and $\Delta H_2^X$.

Although many criticisms of the early Mössbauer work with Fe-X alloys were made by later workers, for the cases when the solute is Si or Cr there has been good agreement on the hyperfine magnetic field perturbations from solute atoms. The author's choices for these parameters are given in Table III. (Solutes more distant than the second nearest neighbor can be considered to produce only small distortions of the main "unperturbed" peak.)

| TABLE III | | |
|---|---|---|
| Some Hyperfine Magnetic Field Perturbations at $^{57}$Fe Nuclei near Solute Atoms (kG) | | |
| Solute | $\Delta H_1^X$ | $\Delta H_2^X$ |
| Mn | +23 | ~ 0 |
| Cr | +28 | +28 |
| Si | +26 | +10 |
| Ni* | -7 | -7 |

* No resolvable satellite structure; data were obtained from $<H^1>$ and 14 neighbor shell model at low $c_{Ni}$.

The additivity assumption of equation IV-1 is often vindicated experimentally for $c_X$ as large as 0.1. However, by working with dilute Fe-X solutions or with dilute X concentrations in Fe-Ni-X alloys as described below, I was able to avoid the additivity assumption entirely. I also avoided the effort involved in determining the sets of $\{\Delta H_j^X\}$ parameters by considering only the number of nearest neighbor shells which produced significant $\Delta H_j^X$ 's, and not the actual magnitudes of the $\Delta H_j^X$ 's.

The resolution of Mössbauer spectrometry, or lack of it, effectively determines the number of nearest neighbor shells at which a solute atom produces "significant" perturbations in $^{57}$Fe hyperfine magnetic fields. We define "insignificant" effects on the observed hyperfine structure as those due to remote solute atoms which result in small peak shifts that cannot be detected except perhaps as a broadening of the "unperturbed" absorption peak. If $\Delta H_j^X \leq 1.5$kG, no structure due to an X atom in the $j^{th}$ n.n. shell will be evident in absorption peaks 1 and 6 of my Mössbauer spectra from dilute Fe-X alloys. Hyperfine magnetic field perturbations due to solute atoms more remote than

those in the first few neighbor shells turn out to be insignificant for my experimental data. Unfortunately, if these insignificant nearest neighbor shells are considered when simulating an experimental spectrum, additional $\Delta H_j^X$ parameters will be introduced. This can only result in an improvement in the quality of fit to the experimental data. Non-unique and non-physical $\Delta H_j^X$ 's for distant nearest neighbor shells can be generated in this way. Vincze and Campbell [41] determined $X^2$ for the goodness of fit of their experimental Fe-X spectra to simulated spectra that were generated by using different numbers of significant $\Delta H_j^X$ parameters. They found that only $\Delta H_1^X$ and $\Delta H_2^X$ were meaningful for fitting their good quality Mössbauer data.

In work by Stearns [116] with Fe-Mn alloys, too many (five) nearest neighbor shells were used in the simulation of her experimental spectra, and an erroneous $\Delta H_2^{Mn}$ = +13.2kG and an erroneous $\Delta H_3^{Mn}$ = −6.6kG were reported. This example demonstrates the fallibility of the spectrum simulation procedure in a major way, but it is a fairly pathological example because the proposed satellite peaks due to 2n.n. and 3n.n. Mn atoms are on opposite sides of the main unperturbed absorption line. Note that there are 6 2n.n. sites which would provide a satellite peak at a 4% lower Doppler shift energy than the unperturbed peak, and 12 3n.n. sites which would provide a satellite peak at a 2% higher energy than the unperturbed peak. The average Doppler shift energy change will therefore be: $(-.04)\times 6 + (+.02)\times 12 = 0$. The addition of these satellites will hence have no effect on the first moment of the main unperturbed peak; only a composition dependent broadening of the main peak would occur due to these proposed 2n.n. and 3n.n. Mn satellites. We further note the suspicious decrease in $\Delta H_2^{Mn}$ and $\Delta H_3^{Mn}$ which Stearns found with higher Mn concentrations. This indicates that the broadening of the main peak was nearly composition-independent, and most likely due to problems with her experiment

or spectrum simulation technique.

**C. Dilute Alloys**

Beneath the processed experimental spectrum of a Fe-Mn alloy in Fig. 25 is a spectrum synthesized with significant hyperfine magnetic field perturbations assumed for Mn atoms in 1n.n. sites only. I did not attempt to determine $\Delta H_1^{Mn}$ by an iterative simulation procedure. I did, however, check to see that the satellite peak intensity was consistent with the binomial probability of finding one Mn atom in the 1n.n. shell. The ratio of satellite peak intensity to total peak intensity is seen to be quite close to the binomial probability $P(8,1,c_X=.0075)$. Since there are 8 sites in the 1n.n. shell, I believe the 1n.n. shell to be the only shell in which a Mn atom can effect a significant (-7%) hyperfine magnetic field perturbation at a $^{57}$Fe nucleus in a Fe-Mn alloy.

Dilute Fe-Cr alloys illustrate how hyperfine magnetic field perturbations due to Cr atoms in more than one significant nearest neighbor shell may be treated as one observable effect. It has been determined by many workers that $\Delta H_1^{Cr} \approx \Delta H_2^{Cr} \approx +26.5$kG, and Cr atoms in the 3n.n. and more distant shells produce much weaker effects. When $\Delta H_1 = \Delta H_2 \equiv \Delta H$, all combinations of $n_1$ and $n_2$ which give the same sum, $n = n_1 + n_2$, will predict the same hyperfine magnetic field, $H$, from equation IV-1. All combinations of $n_1$ and $n_2$ which give the same sum, $n$, will thus have degenerate nuclear energy levels; a single satellite peak will appear for each $n \cdot \Delta H$. In a random bcc solid solution we would expect the binomial probability for 14 trials, $P(14,n,c)$, to determine the net intensity of the satellite due to $n$ Cr atoms in either the 1n.n. or 2n.n. shell, since there are 14 sites in the two shells. This was used for the simulated Fe-Cr spectrum in Fig. 25. If we add up the degenerate, overlapping satellites with intensities predicted by the two shell ($J$=2) form of equation IV-2, we will also find the binomial probability, $P(14,n,c)$, because of an addition theorem* for binomial

* Equation IV-3 is obtained by binomial expanding the three factors in the equation,

coefficients:

$$\sum_{s=0}^{8}\sum_{r=0}^{6}\delta(r+s,i)\,\frac{8!6!c^{s+r}(1-c)^{8+6-r-s}}{(8-s)!s!(6-r)!r!} = \frac{14!}{(14-i)!i!}c^{i}\,(1-c)^{14-i}\,, \qquad \text{IV-3}$$

where $\delta(r+s,i)$ is the Kroeneker delta function ($\delta(i,i) = 1$; $\delta(i,k) = 0$ if $i \neq k$).

Besides giving a less ambiguous idea of the number of significant nearest neighbor sites at which a solute atom will perturb a $^{57}$Fe hyperfine magnetic field, the use of dilute solutions of Cr and Mn facilitates the interpretation of experimental spectra. First note the simplification of the binomial probability for small $c$:

$$\lim_{c\to 0} P(N,n,c) \equiv \lim_{c\to 0}\frac{N!}{(N-n)!n!}c^{n}(1-c)^{1-n} \approx \frac{1}{n!}(Nc)^{n} \text{ when } N \gg n\,. \qquad \text{IV-4}$$

The probability of finding 2 Mn atoms in the 1n.n. shell ($N$ = 8), or two Cr atoms in the (1+2)n.n. shell ($N$ = 14) is only the fraction $\frac{1}{2}Nc$ of the probability of finding one solute atom in that shell. The probability of each additional solute atom decreases by an additional factor of order $Nc$. When $c \leq .01$, effectively all of the observed satellite intensity will come from $^{57}$Fe nuclei with only one X solute neighbor in one of the $N^X$ significant nearest neighbor sites. For dilute solutions the additivity assumption of equation IV-1 is irrelevant.

Even for solute atoms which cause different hyperfine magnetic field perturbations at 1n.n. and 2n.n. $^{57}$Fe nuclei, the total intensity of all significant satellites may be a more practical experimental quantity than the individual satellites from one solute atom in each significant nearest neighbor shell. If all sites in the $J$ shells at which an X solute atom can provide a significant $^{57}$Fe hyperfine magnetic field perturbationare are combined, it is not possible to accurately synthesize all hyperfine structure in a Mössbauer spectrum of an Fe-X alloy (unless all $\Delta H_j^X$ are the same for all these $J$ significant shells).

---

$$[c+(1-c)]^{8}\,[c+(1-c)]^{6} = [c+(1-c)]^{14}\,,$$

and equating terms with equal powers of c.

However, the total intensity of the "X satellite" was the only quantitative information which could reliably be extracted from the broadened, unstructured satellites from the Fe-Ni-X alloys (X is Cr, Mn, Si, or C) used in this work. See Figures 26-28. As long as all significant $\Delta H_j^X$ have the same sign, as is apparently the case for Mn, Cr, and Si in this work, it is much simpler and more direct to work with only one composite nearest neighbor shell containing $N_s^X$ sites. Equation IV-3 shows that the composite satellite intensity will equal the total intensity from all the individual satellite peaks from all the significant nearest neighbor shells. For the rest of this thesis I refer to this composite satellite peak as the "X satellite" peak.

The ratio of the "X satellite" peak intensity, $I_s$, to the total absorption peak intensity, $I_t$, was determined from experimental data as described in Chapter VIII, and this ratio was used to determine $N_s^X$ for materials with known $c_X$. This "calibration procedure", which amounts to a determination of $N_s^X$, then allows the determination $c_X$ for materials with unknown X element composition:

$$\frac{I_s}{I_T} = N_s^X c_X \qquad \text{IV-5}$$

In equation IV-5 the total number of significant nearest neighbor sites, $N_s^X$, acts as an amplification factor to increase the visibility of solute atom effects on Mössbauer spectra. Mössbauer spectrometry is not equally sensitive to all solutes. As described later, the value of $N_s^{Cr}$ is 14, whereas C produces significant hyperfine magnetic field perturbations at only 6 neighboring sites. The satellite intensity in a Fe-9Ni-0.5 at.%Cr alloy will be $\frac{14}{6}$ times as intense as the satellite intensity from a Fe-9Ni-0.5 at.% C alloy. It is this "amplification" effect of $N_s^X$ which is largely responsible for the impressive sensitivity (<0.1 at.%) of Mössbauer spectrometry to solute concentration changes. A large calibration effort was invested in the determination of $N_s^X$ for each X solute atom of

interest in each Fe-Ni host of interest and at each temperature of interest. Such a systematic study is experimentally prudent. For instance, a change in $N_s^{Mn}$ from 8 to 14 was discovered for Fe-Ni-Mn alloys when the Ni content increases from 3 to 6 at.%.

In decomposing Mössbauer spectra from Fe-Ni-X alloys into a sextet of "X satellite" peaks and a sextet of unperturbed main absorption peaks, one can almost establish an operational definition of localized and delocalized hyperfine magnetic field perturbations. Changes in the position and width of the main "unperturbed" peaks are observed in Mössbauer spectra from Fe-X alloys, as noted by Wertheim, et al. and later workers. These energy shifts are more than an order of magnitude smaller than the shifts associated with the satellite peak and are approximately linear in solute concentration. Such translational shifts of the main absorption peaks are attributed to delocalized solute atom effects, e.g. [107]. If the main absorption peak were precisely translated in energy without any broadening, such a translation would accurately depict a uniform delocalized electronic disturbance around solute atoms; the different configurations of intermediate (i.e. 3n.n. to 6n.n.) solute atoms would not cause different shifts of the main absorption peak. Frequently both the shift and the broadening of the main absorption peaks are comparably small, and the small broadenings of the main absorption peaks may indicate that the hyperfine magnetic field disturbances due to solute atoms at intermediate distances are not uniform, but depend somewhat on the detailed configuration of these solute atoms. A clear dichotomy of these small main absorption peak changes into delocalized and localized effects is not feasible with Mossbauer data (however, see the detailed NMR data of Budnick et al. [123]). For my data it seems practical to simply define a delocalized effect as any effect involving solute atoms beyond the 2n.n. distance, so that the entire main absorption peak shift will

represent delocalized effects. For most purposes we can regard such delocalized solute effects on $^{57}Fe$ hyperfine magnetic fields as experimentally insignificant. Nevertheless, disturbances in the main absorption peak due to solute concentration changes were considered for calibration work where $c_X$ was varied from 0 to 1.25 at.%. Conveniently, in the chemical segregation studies of this thesis, $\Delta c_X$ was only a few tenths of a percent, and the proportionately smaller disturbances of the main absorption peaks could be ignored.

From previous work with Fe-Ni-X alloys [128,129] and from phase diagram work by others [70-72,130], I had no reason to suspect the presence of short-range-order in my materials. Some short-range-order will still allow the use of the random solid solution assumption with adequate accuracy. For example, in a dilute Fe-X alloy a 10-fold increase in the correlation function $f_{x,x}(r_{1n.n.})$ over its value for a random solid solution will produce only about a 10% effect on the ratio $\frac{I_s}{I_t}$. However, other correlations will also be changed in any ordering process which affects $f_{x,x}(r_{1n.n.})$ [131-133], so this example exaggerates the tolerance of the binomial probability to short range order. Nevertheless, in this work I found other experimental difficulties to be more troublesome than short-range-order (see section X.B.3.).

**D. Inhomogeneous Solutions.**

This chapter has now developed the relationship between satellite peak intensity and solute concentration for chemically homogeneous solutions, but in practice the martensite may not have a homogeneous solute concentration profile. In this section I estimate errors when determining the average solute concentration in an inhomogeneous alloy by using the preceding development of the phenomenological model of additive hyperfine magnetic field perturbations. If the binomial probabilities had a homogeneous first order property

such that $P(N,n,c)$ equaled $\frac{1}{\lambda}P(N,n,\lambda c)$, there would be no problems with concentration determinations of inhomogeneous solutions by measuring satellite intensities. In fact equation IV-5 has this homogeneous first order property, so we already know that at low solute concentrations there can be no problems with our concentration determinations.

The error in assuming a homogeneous solution becomes more significant with larger $c$. Consider an example with the 2n.n. shell model when an originally homogenized solute concentration becomes segregated into one region of martensite with a relative volume $\frac{1}{f}$ (where f > 1. Consequently, the solute concentration in this volume is increased by the factor $f$, and the rest of the martensite has no solute. Before this hypothetical solute segregation the total satellite intensity* is:

$$I_s = 1 - P(14,0,c)\,. \qquad \text{IV-6}$$

After segregation the satellite intensity will be:

$$I_s' = \frac{1}{f}[1 - P(14,0,fc)] \qquad \text{IV-7}$$

The difference between these two satellite intensities is:

$$I_s - I_s' = \frac{14 \cdot 13}{2} c^2(f - 1) + 0(c^3) \qquad \text{IV-8}$$

With equations IV-6 and -8, I find that when $c$=0.01 and $f$=2, the intensity of the satellite peak from the inhomogeneous alloy will be 0.93 times as large as the satellite peak from the homogeneous alloy. My method of chemical analysis would therefore underestimate the solute concentration of the segregated alloy by this fraction.

Consider an inhomogeneous Ni concentration caused by the martensite transformation of Ni-rich austenite formed during tempering. Assuming the

* In this section $I_s$ from a homogeneous solution and $I_s'$ from an inhomogeneous solution are already normalized by the total area of the absorption peak.

formation of 25% austenite with a Ni concentration of 20%, the remaining martensite would have its Ni concentration reduced from 9% to 6%. Using equation IV-6, the difference between the Fe-6Ni martensite spectrum and the Fe-9Ni martensite spectrum would be 1-1/2 times larger than the difference between the Fe-6Ni martensite spectrum and the spectrum of the inhomogeneous martensite (75% with 6% Ni and 25% with 20% Ni) produced when all the austenite had transformed. (This inhomogeneous martensite also has an average Ni concentration of 9%, however.) This example with its factor of 1-1/2 difference between difference spectrum intensities appears to agree well with the data of Fig. 41. However, the inappropriate use of equation IV-1 for concentrated Fe-Ni alloys, as discussed in Chapter VI, suggests that this good quantitative agreement is coincidental.

As suggested later, chemical inhomogeneities in the martensite will include diffusion profiles that develop as the solutes segregate to the austenite. The observed satellite intensity will be a sum of contributions from each composition of martensite weighted by the relative fraction of martensite with that composition, $D(c)$:

$$I_s' = \int_{c_1}^{c_2} D(c)\,[1 - P(14,0,c)]\,dc \qquad \text{IV-9}$$

where $c_1$ and $c_2$ are the minimum and maximum concentrations of solute in the martensite. It has not been possible to evaluate equation IV-11 by using $D(c)$ obtained from the solution to an appropriate diffusion problem. However, equation IV-9 has been evaluated for a one-dimensional concentration profile across a finite martensite crystal:

$$c(x) = c_0 - (c_0 - c_1)\,e^{-Bx}\,,$$

where $c_0$ is the initial concentration before diffusion (or the concentration at a large distance from the $\alpha'-\gamma$ interface). The parameter $B$ is such that the con-

centration rises to $c_2$ at the end of the crystal away from the $\alpha'-\gamma$ interface. The weight for each concentration, D(c), is obtained by normalizing the inverse spatial of the derivative of $c(X)$:

$$D(c) = \frac{1}{\ln\left(\frac{c_0 - c_1}{c_0 - c_2}\right)} \times \frac{1}{c_0 - c}, \qquad \text{IV-10}$$

With equation IV-10 in equation IV-9 we find, after expanding $(1-c)^{14}$ and integrating:

$$I_s^{\cdot} \simeq 1 - (1 - c_0)^{14} + \frac{14(1 - c_0)^{13}(c_1 - c_2)}{\ln\left(\frac{c_0 - c_1}{c_0 - c_2}\right)} \qquad \text{IV-11}$$

In obtaining equation IV-11 it is assumed that $1 - c_0 \gg c_0 - c_1$ and $1 - c_0 \gg c_0 - c_2$. This is equivalent to assuming that 1.) $c_0$ is small ($c_1$ and $c_2$ will be less than $c_0$ if the solute leaves the martensite), or 2.) for larger concentrations, $c_1$ and $c_2$ are nearly equal to $c_0$. In case no. 1, which is believed to apply to X element segregation from the martensite, it is found that equation IV-11 reduces to the satellite intensity of a homogeneous solution with an average solute concentration between $c_1$ and $c_2$. In case no. 2, which is believed to correspond better to Ni segregation from the martensite, equation IV-11 again reduces to the satellite intensity of a homogeneous solution with a solute concentration between $c_1$ and $c_2$.

Consider a concrete example of the exponential concentration profile for an X element solute. With the parameters $c_0 = 0.01$, $c_1 = 0.003$, and $c_2 = 0.009$, it is found that equation IV-6 will underestimate the actual average solute concentration by a factor of 0.93 when the satellite intensity predicted by equation IV-11 is used. Therefore this inhomogeneous X solute profile will have no significant effect on the accuracy of my method of finding the average X element concentration of martensite. Although the concept of a solute satellite is inappropriate at larger solute concentrations, for an example appropriate to Ni

the parameters $c_0 = 0.09$, $c_1 = 0.03$, and $c_2 = 0.08$ can be used to suggest that the homogeneous treatment of a Ni satellite intensity will underestimate the Ni concentration by a factor of 0.87. This is still a tolerable error, and the methods used here for Ni concentration analysis are not as fundamentally sound as the method of X element analysis anyhow, as explained in the next section.

In summary, the phenomenological model of additive hyperfine magnetic field perturbations is sensitive to inhomogeneities in solute concentration only when the additivity assumption is important and the inhomogeneities are large. At low solute concentrations when the additivity assumption is not important, we can conveniently use the approximate equation IV-5 for determining the solute concentration. Therefore, low solute concentrations are especially convenient from the chemical analysis standpoint because it is unnecessary to consider: 1.) the effect of inhomogeneities in the concentration profile, and 2.) the details of summing binomial probabilities. At higher solute concentrations, but when the changes in concentration are small (such as the case for Ni in this work), we need to consider effect no. 2, but not effect no. 1.

**E. Ni Composition Analysis**

In much of this thesis I consider the presence of Ni only as it affects Mössbauer absorptions from $^{57}$Fe nuclei which neighbor X solute atoms, where X is Mn, Cr, Si, or perhaps C. I argue that once the dependence of $N_s^{X*}$ on the Ni composition is determined, Mössbauer spectra of Fe-Ni-X alloys can yield information about the X concentration in the same phenomenological way as for Fe-X alloys. However, Ni atoms themselves produce perturbations in the hyperfine magnetic fields at $^{57}$Fe nuclei in Fe-Ni alloys. Some authors [41,113] have analyzed Fe-Ni Mössbauer spectra with equations IV-1 and -2 to find $\Delta H_1^{Ni} \approx \Delta H_2^{Ni} \geq -6.6$kG. This is a small perturbation in the hyperfine magnetic

field; satellite energy shifts at peaks nos. 1 and 6 will be smaller than the theoretical $^{57}$Fe Mössbauer linewidth by about a factor of 2. High resolution $^{57}$Fe spin echo NMR spectrometry at 1.35°K [123] has revealed structure on the high frequency side of the main 46.6 MHz NMR absorption line. For Ni chemical analysis of dilute Fe-Ni alloys we could fit satellite peaks to our data by using the set $\{\Delta H_j^{Ni}\}$ determined from NMR spectrometry, by using equation IV-2, and by relying on our faith that the unresolvable satellite structure is correct. Unfortunately, the specific neighbor shells responsible for the Ni satellites in NMR spectra are not as well established as for Mn, Cr, or Si satellite peaks. Additionally, Fe-9Ni is not a dilute solution of Ni in Fe; there is a 24% probability of 2 Ni atoms and a 10% probability of 3 Ni atoms being situated in the first two nearest neighbor shells around a $^{57}$Fe nucleus.

In a random Fe-Ni solid solution for which the additivity assumption of equation IV-1 is valid, we can calculate the mean hyperfine magnetic field perturbation, $<\Delta H>_J$, over J significant shells:

$$<\Delta H>_J = \sum_{n_1=0}^{N_1} \sum_{n_2=0}^{N_2} \cdots \sum_{n_J=0}^{N_J} P(N_1,n_1,c)\, P(N_2,n_2,c) \cdots P(N_J,n_J,c) \qquad \text{IV-12}$$

$$\times[n_1\Delta H_1 + n_2\Delta H_2 + \cdots + n_J\Delta H_j]\,.$$

Proceeding term by term with the factor in the square brackets we use the two relationships*:

$$\sum_{n=0}^{N} P(N,n,c) = 1 \qquad \text{IV-13a}$$

$$\sum_{n=0}^{N} n \cdot P(N,n,c) = Nc \qquad \text{IV-13b}$$

to show that:

$$<\Delta H>_J = [N_1\Delta H_1 + N_2\Delta H_2 + \cdots + N_J\Delta H_J]c\,. \qquad \text{IV-14}$$

* Equation IV-13a results from binomial expanding $[(1-c) + c]^N = 1$. To derive Eqn. 20b, note that the n=0 term vanishes, and substitute $N' = N - 1$ and $n' = n - 1$; see the footnote in section X.A.2.

So if the additivity assumption is valid, the first moment of the hyperfine magnetic field perturbation will be linear in $c$. Fig. 22 shows that $<\Delta H>_J$ is not linear in $c_{Ni}$ over the full composition range of 0 to 9% Ni. The set of $\Delta H_j^{Ni}$ parameters determined for dilute Fe-Ni solutions therefore cannot be used to accurately describe the shape of absorption peaks from an Fe-9Ni alloy. The failure of the phenomenological model of section IV.A. in predicting the shape of Mössbauer peaks from Fe-9Ni alloys is discussed in Chapters VI and X in the light of a less phenomenological model of linear response of hyperfine magnetic fields to magnetic moments. However, I did not attempt to develop the model of linear response to calculate the detailed shape of Mössbauer peaks from non-dilute Fe-9Ni alloys.

Although the data of Fig. 22 prevent the use of the additive hyperfine perturbation model for determining Ni concentration changes for Fe-Ni alloys with more than 6% Ni, the data suggest a phenomenological alternative method for Ni analysis. It can be shown that when a function $F(x)$ and its argument, $x$, are scaled by a factor $f$, the new function $fF(fx)$ has $n^{th}$ moments which are the same as the $n^{th}$ moments of $F(x)$ when multiplied by $f^n$. Fortunately Fig. 22 shows that the $n^{th}$ root of the $n^{th}$ moments* $<X^n>^{\frac{1}{n}}$, scale together linearly with the Ni composition over small composition ranges such as $0.07 \leq c_{Ni} \leq 0.09$. Since a peaked, continuous function can be determined from its moments, the absorption peaks from Fe-Ni alloys over this composition range must have the same functional form (i.e. the same shape), but are merely expanded in energy width by a factor $f$. For small $\Delta c_{Ni}$ this factor $f$ equals 1 minus a small term linear in $\Delta c_{Ni}$.

---

* Since $\lim_{A\to\infty} \int_{-A}^{A} x^{2n} \frac{1}{1-x^2}\, dx = \infty$ for $n \geq 1$, the second and fourth moments in Fig.22 (as well as the $0^{th}$, $1^{st}$, and $3^{rd}$) were determined numerically for some finite $A$.

So over a limited range of $\Delta c_{Ni}$, the absorption peaks from Fe-Ni alloys retain the same shape, but undergo a scale expansion which is linear in $\Delta c_{Ni}$. Now consider the arithmetical difference of two Mössbauer spectra from Fe-Ni alloys of slightly differing Ni compositions. Since the scale expansion is linear in $\Delta c_{Ni}$, it can be shown by a Taylor series argument that the height of the difference between peaks in the two spectra will also be linear in $\Delta c_{Ni}$. I have also verified the proportionality of difference spectrum height and scale expansion for a series of numerically computed Lorentzian curves with different mean positions and widths. This is the basis for my determination of Ni composition changes by measuring difference spectrum height. All that is necessary for calibration is the height of a peak in a difference spectrum of two Fe-Ni alloys of known composition. This calibration is provided by Figs. 13 and 14.

**F. Anisotropic Hyperfine Magnetic Field Perturbations.**

Equations IV-1 and -2 provide for the major systematics of local solute effects on $^{57}$Fe hyperfine magnetic fields. However, equation IV-1 considers all possible solute sites in a given nearest neighbor shell to be equivalent in their capacity for perturbation of the central $^{57}$Fe hyperfine magnetic field. Experiments with single crystals of Fe-Si [115], Fe-Cr [114], and Fe-Mo [39] have shown that this equivalence of sites in a particular nearest neighbor shell is not strictly true. In such single crystal experiments as conceived by Cranshaw [114,115], a saturating magnetic field is applied along known crystallographic directions of the specimen, and serves to align the $^{57}$Fe hyperfine magnetic fields antiparallel to the applied field direction (this alignment is described in the section V.D.). Mössbauer spectra obtained with different directions of applied magnetic field have revealed that there is a an anisotropic component to the hyperfine magnetic field perturbations around Si, Cr, and Mo atoms in pure iron. The hyperfine magnetic field perturbation of a $^{57}$Fe nucleus with one

Mo atom in its 2n.n. shell is not simply $1 \cdot \Delta H_2^{Mo}$, but now $\Delta H_2^{Mo} + \Delta D_2^{Mo}(3\cos^2\varphi - 1)$, where $\varphi$ is the angle between the hyperfine magnetic field direction and the vector connecting the $^{57}$Fe nucleus and the center (nucleus) of the Mo atom. There have been only a few experimental determinations of the sets $\{\Delta D_j^X\}$, but their elements appear to be on the order of 10% as large as the elements of $\{\Delta H_j^X\}$.

It was necessary to deal with the anisotropic nature of hyperfine magnetic field perturbations in this work because it was found that the magnetizations of the martensite crystals were reoriented after heat treating at temperatures above 350 °C. The distribution of angles $\varphi$ would hence change during heat treatments in an uncontrollable manner, and the magnitudes of these anisotropic effects therefore varied from spectrum to spectrum. The extent of this reorientation of the domain magnetizations could be estimated by comparing the intensity of a $\Delta I_z = \pm 1$ absorption (peaks 1, 3, 4, or 6) to the intensity of a $\Delta I_z = 0$ absorption (peaks 2 or 5). As described previously in section III.C.3., this intensity ratio will be representative of an average angle $\vartheta$ made by the hyperfine magnetic field direction and the direction of $\gamma$-ray propagation. Unfortunately, we cannot uniquely determine an average $\varphi$ from an average $\vartheta$. Nevertheless, when comparing Mössbauer spectra from two polycrystalline specimens it is reasonable to expect that the greater the difference in the ratio of intensity of peak 1 to peak 2, the greater will be the difference in the distribution of angles $\varphi$ in the two specimens, and the greater will be the difference in the anisotropic part of the hyperfine magnetic field perturbations for the two specimens. This correlation was discovered in the earlier series of tempering experiments; sudden apparent decreases in the Ni and X element content of the martensite occurred simultaneously with sudden decreases in the ratio of intensity of peak 2 to peak 1. Uncontrolled changes in anisotropic Ni perturba-

tions of the $^{57}$Fe hyperfine magnetic field were the major source of error in my earlier attempts to determine martensite chemistry changes during two-phase tempering.

No Fe-Ni single crystal experiments were undertaken in this work, so the set $\{\Delta D_j^{M}\}$ could not be positively determined. Instead, a novel experimental technique of always orienting the specimens in the same position in a saturating magnetic field was used for reproducibly controlling (i.e. "locking") the anisotropic hyperfine magnetic field perturbations. In these experiments the applied magnetic field forces the magnetization of each crystal in the polycrystalline specimen to lie antiparallel to the applied field direction. After a heat treatment the altered magnetic anisotropy of each crystal may favor a new magnetization direction, but the applied field forces its magnetization to lie along the same direction as the direction taken when the specimen was in the spectrometer before the heat treatment. As well as could be determined from the consistency of the chemical segregation data, and especially by the accurate 3:4:1:1:4:3 ratio of the six martensite peaks, the distribution of angles $\varphi$ in the specimens were quite reproducible from run to run. In this way the contribution of the anisotropic part of the hyperfine magnetic field perturbation could effectively be absorbed into the sets $\{\Delta H_j^{M}\}$ and $\{\Delta H_j^{X}\}$.

**G. Localized Isomer Shifts.**

The asymmetry of my Mössbauer spectra with respect to an inversion in Doppler shift energy is due entirely to isomer shift effects. Much of the "rigid translation" of the whole spectrum towards negative Doppler shift energy, $i_o$, is due to the different $|\psi(0)|^2$ of $^{57}$Fe nuclei in the Pd radiation source and the $|\psi(0)|^2$ of $^{57}$Fe nuclei in Fe metal. A uniform dependence of $|\psi(0)|^2$ on the total concentration of alloy elements (a nonlocal effect on $|\psi(0)|^2$) will produce merely a change in the total amount of this rigid translation. However, it is

possible for one X solute atom to produce a change $\Delta i_j^X$ in the isomer shift at only 1n.n. $^{57}$Fe nuclei; this is a local effect on $|\psi(0)|^2$. The particular sextet of satellite peaks associated with a configuration $\{n_j'\}$ of nearest neighbor solute atoms will translate upwards in energy (c.f. equation IV-1):

$$\Delta i^X(\{n_j'\}) = i_o + \sum_{j=1}^{J} n_j' \Delta i_j^X . \qquad \text{IV-15}$$

Since this sextet of satellites originates from hyperfine magnetic field perturbations around solute atoms, these isomer shift changes are caused by the same solute atom configurations which already produce significant hyperfine magnetic field perturbations. Equations IV-1 and -15 are generally combined to predict the positions of the satellite peaks in computer simulations of Mössbauer spectra. In the work with "X satellite peaks" from dilute solutions of X in Fe-Ni, I did not attempt to determine the set $\{\Delta i_j^X\}$ from my spectra. It was, however, evident how these localized isomer shifts affected the hyperfine structure. For example, the energy separation of the "X satellite" peak from the unperturbed main peak will be smaller for peak 6 than for peak 1 when the average local isomer shift is the same sign as the average local hyperfine magnetic field perturbation. Since the significant $\Delta H_j^{Ni}$ parameters are negative at 18°C, the significant $\Delta i_j^{Ni}$ parameters must also be negative in order to explain why peak no. 6 is narrower than peak no. 1 in a Fe-9Ni spectrum at 18°C.

# CHAPTER V

# SOURCES OF HYPERFINE MAGNETIC FIELDS AT NUCLEI

## A. Perspective and Introduction.

A rather large amount of background material underlies the application of Mössbauer spectrometry to studies of chemical composition changes in Fe-Ni-X martensites, so we pause here to reflect on the path taken and to illuminate the course of Chapters V and VI. The finite probability of recoilless $\gamma$-ray emissions and absorptions gives us a tool, the Mössbauer effect, to study very small shifts in nuclear energy levels. Useful and interesting shifts arise from interactions between the $^{57}$Fe nucleus and the effective magnetic field or electric potential in which it sits. Hyperfine interactions between the $^{57}$Fe nucleus and the *electrons* inside it are the important mechanisms for affecting the nuclear energy levels. Specifically, the electron spin density and the electron charge density in the nucleus are the most important sources of the hyperfine magnetic field splitting and the isomer shift, respectively. The periodicity of the electron wavefunctions in iron metal ensures that all $^{57}$Fe nuclei in pure iron will experience equivalent hyperfine interactions. However, a solute atom will disturb the electron charge and spin distribution in its vicinity by mechanisms described in this chapter. Chapter VI then describes how these mechanisms have been proposed to apply to the electrons in iron alloys in attempts to explain the chemical systematics of hyperfine field perturbations at $^{57}$Fe nuclei near solute atoms.

Electronic changes at a $^{57}$Fe nucleus near a solute atom can cause a significant change in the energy of $\gamma$-rays absorbed by that nucleus. In Chapter IV we operationally defined a "significantly perturbed" hyperfine magnetic field as an attribute of a $^{57}$Fe nucleus which gives a $\gamma$-ray absorption peak that can

be resolved experimentally from a main unperturbed absorption peak. This main peak is due to those $^{57}Fe$ nuclei which are beyond the "range" of the solute atom. The ratio of satellite peak intensity to the total absorption peak intensity is equal to the relative fraction of $^{57}Fe$ nuclei within the "range" of the solute atoms. When this "range" (determined as a number of nearest neighbor sites) is known and a random distribution of solute atoms is assumed, equations IV-2 or IV-5 can be used in the processing of experimental data to extract chemical composition information.

The hyperfine magnetic field at a $^{57}Fe$ nucleus originates from several electronic mechanisms which are to some extent interdependent and competing. It is convenient to express the total hyperfine magnetic field, $H$, as a sum of individual terms due to each mechanism, even though the specific electrons responsible for one mechanism are usually involved in other mechanisms. Different authors may choose different terms depending on whether they are oriented more towards the study of electronic structure or towards systematizing the hyperfine magnetic field perturbations at $^{57}Fe$ nuclei. In this work hyperfine magnetic field perturbations were used to count the arrangements of solute atoms around $^{57}Fe$ nuclei. This author was therefore oriented towards the systematics of hyperfine magnetic field perturbations at $^{57}Fe$ nuclei, and has chosen to express the total hyperfine magnetic field, $H$, as:

$$H = H_{CORE} + H_{COND} + H_{HYB} + H_{OV} + H_{COV} + H_{ORB} + H_{MAG} + H_{DIP} \qquad \text{V-1}$$

where the terms on the right hand side are arranged in rough order of decreasing importance for Fe-X alloys. The mechanisms responsible for each term are discussed in this chapter.

The working model later developed in Chapter VI groups the contributions to the $^{57}Fe$ hyperfine magnetic field so that the $^{57}Fe$ hyperfine magnetic field responds linearly to the magnetic moments in the alloy in three lumped contri-

butions: $H_L$, $H_{INL}$, and $H_{DNL}$. These three contributions are treated semi-phenomenologically, but they arise from groupings of the fundamental mechanisms described in the current chapter. This working model of linear response(s) of hyperfine magnetic field perturbations to magnetic moments is supported by the experimental systematics of hyperfine magnetic field perturbations of Fe-X alloys. This linear response model is a practical necessity because the contributions of all eight mechanisms described in this chapter cannot all be accurately estimated from fundamental considerations of electronic structure. Chapter VI develops this model for binary and ternary alloys, and formally predicts the changes expected for $^{57}$Fe hyperfine magnetic field perturbations due to neighboring X atoms when Ni is added to the matrix. In Chapter X this helps to justify, with some qualifications, the use of a method of X concentration analysis for Fe-Ni-X alloys, which is similar to the accepted method for Fe-X alloys described in Chapter IV. Other features such as temperature and composition dependences of the hyperfine magnetic field perturbations, and the shapes of Mössbauer peaks from Fe-Ni alloys, are also explained in Chapter X with this model.

Hyperfine magnetic field perturbations at $^{57}$Fe nuclei near solute atoms were used to monitor small solute concentration changes of Fe-Ni-X martensites in sequences of temperings. The absence of large hyperfine magnetic fields at $^{57}$Fe nuclei in the austenite allowed the determination of the amount of austenite formed during tempering. These two types of information, obtained simultaneously, enabled the identification of relationships between the kinetics of solute segregation and the kinetics of austenite precipitation. In particular, the solute concentration of the austenite was determined from this chemistry and phase information, and systematics of how the solute concentration of the austenite depended on tempering conditions and the original alloy composition

were explored.

**B. Classical Contributions:** $H_{MAG}, H_{DIP}, H_{ORB}$.

The relatively insignificant $H_{MAG}$, $H_{DIP}$, and $H_{ORB}$ contributions are the only hyperfine magnetic field contributions which can be understood as phenomena of classical electromagnetism. $H_{MAG}$ is due to the uniform magnetization of the specimen. The lattice magnetization, **M**, effects a classical magnetic field of $4\frac{\pi}{3}\mathbf{M}$. The magnetic return flux serves to reduce the magnetic field; this demagnetization is dependent on specimen geometry and the direction of **M**. (For examples see [134].) We also add into $H_{MAG}$ the hyperfine magnetic field contribution due to external magnetic fields applied to the specimen. For iron metal with no external applied fields, $H_{MAG} < +7kG$.

The classical $H_{DIP}$ contribution is caused by atomic dipole moments at nearest neighbor sites. In pure iron $H_{DIP}$ vanishes because of cubic symmetry. However, a solute atom with a magnetic moment differing from that of an iron atom by 1 $\mu_B$ will contribute ~ 1 kG to $H_{DIP}$ at a 1n.n. $^{57}$Fe nucleus. This small, orientation-dependent $H_{DIP}$ will be averaged out for Fe-X alloys with a random distribution of angles $\varphi$. Only a slight peak broadening will result.

$H_{ORB}$ arises from the atomic character of the 3*d* electrons around the $^{57}$Fe nucleus. Lattice effects in iron metal do not completely destroy the spherical symmetry otherwise seen by the Fe 3*d* wavefunctions, and electron orbital magnetic moments remain. A spin-orbit interaction involving the $^{57}$Fe nuclear spin and the unfilled 3*d* shell contributes an $H_{ORB}$ of +50 to +70 kG [106,135,136]. However, while this contribution to $H$ may be of substantial magnitude, it arises from electrons local to the $^{57}$Fe nucleus and often may not change significantly upon alloying. More importantly for iron atoms, an increase in the number of unpaired $3d\uparrow$ electrons will generate a small positive hyperfine magnetic field

contribution with $H_{ORB}$, but this will be overshadowed by the large negative contribution caused by core polarization, $H_{CORE}$, described in section V.D.

$H_{MAG}$, $H_{DIP}$, and $H_{ORB}$ may be understood with classical electromagnetism. Actual hyperfine magnetic fields in iron alloys are much larger than can be predicted from these three mechanisms. The other five contributions, $H_{CORE}$, $H_{COND}$, $H_{HYB}$, $H_{OV}$, and $H_{COV}$, do not originate as a classical magnetic flux density around an electric current, but depend on electron spin imbalances at a $^{57}$Fe nucleus through the Fermi contact interaction.

**C. The Fermi Contact Interaction.**

Using the Dirac theory for the electron, Fermi [137] and Fermi and Segrè [138,139] found a new term in the hamiltonian for the interaction of a single electron with a nucleus. This "Fermi contact term" is:

$$H_{FC} = \frac{-8\pi}{3} g_e \, g_N \, \mu_b \, \mu_N \, \mathbf{I}\cdot\mathbf{S} \, \delta(\mathbf{r}) \qquad \text{V-2}$$

Here **I** and **S** are spin operators which act on the nuclear and electron state functions, respectively; $\mu_B$ is the Bohr magneton, $g_e$ is the electron gyromagnetic ratio, $\mu_N$ and $g_N$ are the respective nuclear constants defined in section III.C.3. When this $H_{FC}$ acts on the state function of our system of nucleus and electron, we can identify the effective hyperfine magnetic field which was used in Chapters III and IV:

$$H_{eff} = \frac{8\pi}{3} g_e \, \mu_b \, S \, |\psi(0)|^2 . \qquad \text{V-3}$$

Here S is the spin quantum number ($+\frac{1}{2}$ or $-\frac{1}{2}$) of the single electron we have considered, and $|\psi(0)|^2$ is its probability density at the nucleus. For the reasons outlined in our discussion of the isomer shift, s electrons are the only electrons with non-vanishing $|\psi(0)|^2$. It was originally accepted that an effective hyperfine magnetic field could only arise from unpaired s electrons

whose contribution of $S = +\frac{1}{2}$ to $H_{eff}$ is not cancelled by the contribution from an identical electron with $S = -\frac{1}{2}$. However, even in the 1930's, experiments showed that free ions with closed $s$ shells also exhibited large hyperfine magnetic fields.

**D. Exchange; Core Polarization; $H_{CORE}$.**

Fermi and Segre [138,139], and later Sternheimer [140], suggested that the Pauli principle causes each of the two ($S = +\frac{1}{2}$ and $S = -\frac{1}{2}$) paired $s$ electrons to interact differently with an unpaired valence electron of the same atom. Therefore the spatial distribution of the two $s$ electrons will be perturbed differently by the electron-electron interaction with the unpaired outer electron. The $S = -\frac{1}{2}$ electron spin density will no longer be uniformly cancelled by the $S = +\frac{1}{2}$ electron, and the $s$ electron density at the nucleus will be spin-polarized. A significant hyperfine magnetic field will then arise from the Fermi contact interaction. Additionally, the spherical symmetry of the $s$ wavefunctions will be lost if the unpaired valence electron is not of $s$ character.

Closed shell distortions and their contributions to the electron spin density at the nucleus were calculated for various metal ions by Watson and Freeman [141-143] by means of an "unrestricted" Hartree-Fock method. We now discuss these calculations in order to describe their quantitative results and also to describe some important features of the "exchange energy". Recall that the Hartree-Fock method ensures an antisymmetrization under the interchange of a pair of electron coordinates for a multielectron wavefunction. This is accomplished by expressing the multielectron wavefunction as a Slater determinant of one electron wavefunctions [144-146] (See footnote section V.F.). This Hartree-Fock n-electron wavefunction is a sum of n! terms. Each term is a

product of the samenumber, n, of single electron wavefunctions, but each permutation of the electron coordinates among these n functions contributes an individual term to the sum. The sign of each term ensures the overall antisymmetry of their sum under an exchange of electron coordinates. When the atomic hamiltonian (containing individual electron operators for kinetic energy, electron-nucleus attraction, and electron-electron repulsion) operates on the Hartree-Fock wavefunction, the energy contains a positive kinetic energy term, a negative nucleus-electron Coulomb term, and a positive interelectronic Coulomb repulsion term. These same three energy terms are present in the Hartree scheme [144] where the n-electron wavefunction is approximated as only one of the n! terms in the antisymmetric sum. However, an additional term in the system energy arises when the full antisymmetric sum is used as the n-electron wavefunction. This new term is known as the exchange term (because of its form in the two electron coordinates) and is:

$$U_{Ex} = -\sum_{j<i}\sum_{i} \delta(S_i - S_j) \int_{-\infty}^{\infty}\int_{-\infty}^{\infty} \psi_i^*(\mathbf{r}_i)\, \psi_j^*(\mathbf{r}_j) \frac{e}{|\mathbf{r}_i - \mathbf{r}_j|} \psi_i(\mathbf{r}_j)\, \psi_j(\mathbf{r}_i) d^3\mathbf{r}_i\, d^3\mathbf{r}_j \quad \text{V-4}$$

where we have considered all pairs (i,j) of electrons. The delta function ensures that $U_{Ex}$ will be non-zero only for electrons of the same spin.

$U_{Ex}$ does not represent a new form of interelectronic interaction, but is a correction to the Coulomb repulsion energy which is to be expected when the Pauli principle (expressed through the antisymmetrization of the multielectron wavefunction) keeps electrons of the same spin away from each other. The Pauli principle gives rise to a correlation effect around each electron. This localized correlation is known as the Fermi hole. There is zero probability of finding a second electron of parallel spin at the precise position of a localized electron, but this probability generally rises rapidly over a distance which is small on the scale of an atomic wavefunction [143]. The Fermi hole can allow the total energy of electrons of parallel spin to be reduced when their overlap

of time-independent wavefunctions is increased; it provides a lowering of the overlap Coulomb repulsion, and this allows the electron kinetic energy to be reduced when the wavefunctions are enlarged in the region of the overlap.

The single electron wavefunctions in the Hartree-Fock wavefunction are determined by performing an iterative calculation where self-consistency is eventually achieved for the wavefunctions and their interelectronic potentials; this approach is generally necessary because the interelectronic interaction energies are awkward integral operators involving the wavefunctions. Hartree-Fock single electron wavefunctions determined in this way are equivalent to wavefunctions determined by minimizing the total electron energy (the three Hartree terms plus $U_{Ex}$) with respect to variations in the single electron wavefunctions. Some restrictions are placed on the single electron wavefunctions for computational convenience. The unrestricted, or less restricted, Hartree-Fock calculations of Watson and Freeman start with these conventional Hartree-Fock wavefunctions and then relax the restraint that paired wavefunctions of the same spin will have the same radial dependence. Even when this restriction is relaxed, wavefunctions with the same radial dependence for electrons of both spins will still minimize the system energy for an ion which has no unpaired electron spins. However, a free iron atom has the electronic configuration [Ar] $4s^2 3d^6$, and a net spin imbalance in the $3d$ shell due to four unpaired electrons. Consider the effect of the unbalanced exchange interaction on the pair of the innermost $1s$ electrons. $U_{Ex}$ will be nonzero for the interactions of the unpaired $3d\uparrow$ valence electrons with the $1s\uparrow$ electron, but no such $U_{Ex}$ will exist for the other $1s\downarrow$ electron. The exchange interaction serves to reduce the Coulomb repulsion between electrons of parallel spin, so Watson and Freeman found that their $1s\uparrow$ radial function moved outwards toward the $3d$ electron cloud with respect to the other $1s\downarrow$ electron. Although the

exchange integral of equation V-4 vanishes for electrons with antiparallel spins* , it is convenient to think of $U_{Ex}$ as providing an "exchange energy" which is negative when overlapping electrons on the same atom have parallel spins, and positive for overlapping electrons with antiparallel spins. The magnitude and sign of this exchange energy depends on the precise form of the electron wavefunctions, but it is roughly dependent on the local electron density, $\rho(\mathbf{r})$. (In particular, for free electrons the exchange energy goes as $\rho^{\frac{1}{3}}(\mathbf{r})$ [147,148].)

In a free iron atom Watson and Freeman found [141,142], as suggested by Sternheimer [140], that although exchange interactions between the unpaired $3d$ electrons and the $3s$, $2s$ and $1s$ electrons are progressively weaker because of poorer overlap, the larger $1s$ and $2s$ densities at the nucleus make these inner shell electrons important in causing hyperfine magnetic field effects. They found that the distortion of the closed $2s$ shell is the major source of the hyperfine magnetic fields in iron. Since the $2s$ (and $1s$) electrons lie "inside" the $3d$ electrons, exchange polarization will cause a negative (antiparallel to the $3d$ spin) spin density at the nucleus as the $2s\uparrow$ and $3d\uparrow$ electrons increase their overlap. On the other hand, the more distant $4s\uparrow$ electrons are drawn inwards towards the $3d\uparrow$ electrons, and they produce a small positive spin density change at the nucleus and a negative spin density in the outer parts of the atom. The $3s$ electrons lie both "inside" and "outside" the $3d$ electrons; their exchange interactions are strong, but they produce a positive spin density at the nucleus of only half the magnitude of the $2s$ contribution.

The sign of the hyperfine magnetic field in iron was determined [149] by placing an iron metal absorber in an external magnetic field. The lattice mag-

* However, Coulomb correlations as described in IV-I. do affect electrons with antiparallel spins. Watson and Freeman ignore these effects.

netization was aligned along the applied magnetic field direction and added a uniform positive (parallel to the lattice magnetization) contribution to the magnetic field everywhere, including the nucleus (recall that this is an $H_{MAG}$ contribution). The hyperfine magnetic field splitting of the sextet of iron peaks was observed to decrease upon application of the external magnetic field. The iron hyperfine magnetic field was therefore concluded to lie in the opposite direction to the lattice magnetization. Closed shell distortions were the only contribution which could be found to give large negative hyperfine magnetic fields, so they must be the dominant mechanism for producing hyperfine magnetic fields in iron. This was later verified directly in a clever semi-quantitative experiment by Song et al. [150].

In most Mössbauer experiments, including mine, the individual contributions from the $1s$, $2s$, and $3s$ closed shell distortions are not distinguished. We instead follow Van der Woude [106] and consider a combined $1s$, $2s$, and $3s$ * core polarization contribution to the hyperfine magnetic field, $H_{CORE}$. $H_{CORE}$ is proportional to the number of unpaired $3d\uparrow$ electrons, $n_{3d}\uparrow - n_{3d}\downarrow$, around the $^{57}$Fe nucleus. A proportionality has been determined from the free ion Hartree-Fock calculations of Watson and Freeman [141-143]:

$$H_{Core} = -85kG(n_{3d}\uparrow - n_{3d}\downarrow) \ . \qquad \text{V-5}$$

In iron metal the $3d$ electrons will be more spread out and the band structure calculations of Duff and Das [106,151] give:

$$H_{CORE} = -110kG(n_{3d}\uparrow - n_{3d}\downarrow) \ . \qquad \text{V-6}$$

In iron metal the $3d$ wavefunctions are mostly localized around an iron atom, and are responsible for most of the 2.2 $\mu_B$/atom magnetic moment in iron. Therefore, $H_{CORE}$ is proportional to the magnetic moment of the $^{57}$Fe atom. $H_{CORE}$ is consequently a mechanism of hyperfine magnetic field perturbations

* The exchange interaction of a $3d$ electron and a $1s$ electron is considered independently in the $H_{COND}$ contribution (see sections V. E. 3. and V. E. 4.).

which responds linearly to magnetic moments in iron alloys.

**E. Conduction Electron Polarization; $H_{CEP}$.**

Initially following Watson [143], in this section we show how the charge and spin of conduction electrons are redistributed in the vicinity of a solute atom. For 4*s* conduction electrons this redistribution will be manifested directly as a hyperfine magnetic field perturbation due to changes in the spin density of the 4*s* conduction electrons at a $^{57}$Fe nucleus. For itinerant 3*d* electrons such redistributions would be manifested indirectly through changes in $H_{CORE}$. We first describe how conduction electron states are mixed by a localized perturbation, and then show how this formalism is used in: 1) the problem of an electron charge redistribution around a charge perturbation at the solute atom site (section V.E.2.), and 2) the problem of an electron spin redistribution due to a magnetic moment perturbation at the solute atom site (section V.E.3.). (Perturbation theories of these two generic types are termed Friedel and R.K.K.Y theories, respectively.) In section V.E.4. important "cross term" interrelationships involving electron charge and spin redistributions around spin and charge perturbations , respectively, are discussed. A discussion of the importance of conduction electron Coulomb correlation effects is deferred to section V.I.

**1. First Order Perturbation Theory.**

Each electron state in a periodic potential is of the Bloch form: $\psi_{\mathbf{k}}(\mathbf{r}) = u_{\mathbf{k}}(\mathbf{r})e^{i\mathbf{kr}}$. For nearly free conduction electrons the function with the periodicity of the lattice, $u_{\mathbf{k}}(\mathbf{r})$, is only a weak modulation factor, so we assume here that it is constant and we work with free electron wavefunctions; $\psi^F_{\mathbf{k}\sigma}(\mathbf{r}) = \frac{1}{\sqrt{V}} e^{i\mathbf{kr}}\sigma$, where V is the volume of the crystal and $\sigma$ is the spin fac-

tor*. We now perturb the free electron hamiltonian with a localized potential, $\varphi(\mathbf{r})$, which we take to be a peaked function centered at the origin. To first order this perturbation mixes free electron states of differing $\mathbf{k}$ and $\sigma$ into the unperturbed $\psi^F_{\mathbf{k}\sigma}(\mathbf{r})$:

$$\psi_{\mathbf{k}\sigma}(\mathbf{r}) = \psi^F_{\mathbf{k}\sigma}(\mathbf{r}) + \sum_{\mathbf{k}',\sigma'} \frac{<\mathbf{k}',\sigma'|\varphi(\mathbf{r})|\mathbf{k},\sigma>}{|E_{\mathbf{k}\sigma} - E_{\mathbf{k}'\sigma'}|} \psi^F_{\mathbf{k}'\sigma'}(\mathbf{r}) \,. \qquad \text{V-7}$$

At all temperatures of interest we can assume that the conduction band is filled such that all one electron states with $k < k_F$ are occupied ($\mathbf{k}_F$ is a wavevector on the spherical Fermi surface). Spin orthogonality limits us to considering only matrix elements with $\sigma' = \sigma$ (we have written that $\varphi(\mathbf{r})$ is independent of $\sigma$ in setting up equation V-7 ). When mixing states of the same spin, the Pauli principle† limits us to mixing only states with $\mathbf{k}' > \mathbf{k}_F$ into our occupied $\psi^F_{\mathbf{k}\sigma}(\mathbf{r})$. With $\mathbf{k}' \equiv \mathbf{k} + \mathbf{q}$ we recognize that:

$$<\mathbf{k}+\mathbf{q}|\varphi(\mathbf{r})|\mathbf{k}> = \frac{1}{V}\int_{-\infty}^{\infty} e^{-i(\mathbf{k}+\mathbf{q})\cdot\mathbf{r}}\varphi(\mathbf{r})e^{i\mathbf{k}\cdot\mathbf{r}} = \frac{1}{V}\varphi(\mathbf{q}) \,. \qquad \text{V-8}$$

$$\Delta\rho_{\mathbf{k}}(\mathbf{r}) = \left|\frac{1}{\sqrt{V}}e^{i\mathbf{k}\cdot\mathbf{r}} + \frac{1}{V}\sum_{\mathbf{k}>\mathbf{k}_F}\frac{\varphi(\mathbf{q})}{|E_{\mathbf{k}'} - E_{\mathbf{k}}|}\frac{e^{i\mathbf{k}'\cdot\mathbf{r}}}{\sqrt{V}}\right|^2 - \left|\frac{e^{i\mathbf{k}\cdot\mathbf{r}}}{\sqrt{V}}\right|^2$$

where $\varphi(\mathbf{q})$ is the Fourier transform of $\varphi(\mathbf{r})$. The redistribution of density for the electron of wavevector $\mathbf{k}$, $\Delta\rho_{\mathbf{k}}(\mathbf{r})$,

$$\Delta\rho_{\mathbf{k}}(\mathbf{r}) \simeq \frac{1}{V^2}\sum_{\mathbf{k}>\mathbf{k}_F}\frac{\varphi(\mathbf{q})(e^{i\mathbf{q}\cdot\mathbf{r}} - e^{-i\mathbf{q}\cdot\mathbf{r}})}{\frac{\hbar^2}{2m}(\mathbf{k}^2 - |\mathbf{k}+\mathbf{q}|^2)} \qquad \text{V-9}$$

We have used the free electron result, $E_k = \frac{\hbar^2}{2m\,k^2}$, which gives the Lindhard [152-155] result when the energy denominator is averaged over all $|\mathbf{k}'|>|\mathbf{k}_F|$ and all orientations of $\mathbf{q}$ with respect to $\mathbf{k}$:

* We use the notation: $\sigma=\alpha$ means spin up (↑); $\sigma = \beta$ means spin down (↓).

† We could have accounted for the Pauli principle by working with an antisymmetric multi-electron wavefunction, $\Psi(\mathbf{r})$. We would write $\Psi(\mathbf{r})$ as a Slater determinant with each column made up of one occupied one electron wavefunction which had coordinates of a different electron at each row. The value of a determinant is unchanged when one column is added to another. We hence need to mix new, unoccupied, one electron wavefunctions into $\Psi(\mathbf{r})$ (i.e. add more columns) in order to change this multi-electron wavefunction.

$$\Delta\rho(r) = \frac{k_F}{8\pi^2 V}\sum_q \varphi(q)\cos(qr)\left\{1 + \frac{4k_F^2 - q^2}{4k_F q}\ln\left|\frac{2k_F + q}{2k_F - q}\right|\right\} \qquad \text{V-10}$$

We define the Lindhard susceptibility function, $F(q,2k_F r)$, so that:

$$\Delta\rho(r) = \frac{1}{V}\sum_q F(q,2k_F r)\,\varphi(q)\cos(q)$$

Note the zero denominator in the logarithm function when $|\mathbf{q}| = 2k_F$. This weights the $\cos(2k_F r)$ term more than any other term in equation V-10. (This singularity exists because zero energy denominators in equation V-7 may only arise if the length of $\mathbf{k}'$ is less than $2k_F$. The mixing of states with $|\mathbf{k}'|>2k_F$ therefore contributes less to $\Delta\rho(r)$ .) No matter what form $\varphi(q)$ may take, the electron redistribution, $\Delta\rho(r)$, will display this $\cos(2k_F r)$ oscillation, and in three dimensions we have the asymptotic form:

$$\lim_{r\to\infty}\Delta\rho(r) = \frac{\cos(2k_F r)}{r^3} \qquad \text{V-11}$$

Consider a $\varphi(r)$ that arises from interactions between electrons localized on the solute atom site and the conduction electrons. In the simple case of initially unpolarized conduction electrons: 1) $\Delta\rho(r)$ can be a pure charge density redistribution, $\Delta\rho^C(r)$, when the numbers of spin up and spin down electrons on the solute atom site are both changed equally with respect to their numbers for a pure iron atom, or 2) $\Delta\rho(r)$ can be a pure spin density redistribution, $\Delta\rho^S(r)$, if the change in the number of spin down electrons at the solute atom site is counterbalanced by an opposite change in the number of spin up electrons at the solute atom site. When one particular localized electron wavefunction is responsible for both a spin and a charge perturbation, $\Delta\rho^C(r)$ and $\Delta\rho^S(r)$ will have roughly similar spatial distributions and their relative intensities will be determined by the relative strengths of the charge and the spin perturbations, respectively. The situation is more complicated when the conduction electrons are initially polarized, and this is also discussed in V.E.4.

**2. Friedel Theory.**

A charge density, $n(r)$, centered about the origin sets up an electrostatic potential, $\varphi(r)$: The Fourier transform of $\varphi(r)$ is $\varphi(q)$:

$$\varphi(\mathbf{r}) = \int_0^\infty \frac{n(\mathbf{r}')}{|\mathbf{r}-\mathbf{r}'|}\, d^3r \ . \qquad \text{V-12}$$

The Fourier transfrom of $\varphi(r)$ is $\varphi(q)$:

$$\varphi(\mathbf{q}) = \frac{4\pi}{q^2}\, n(\mathbf{q}) \ ,$$

where $n(\mathbf{q})$ is the Fourier transform of $n(\mathbf{r})$. $\varphi(\mathbf{q})$ may be used in equation V-10 to calculate the conduction electron redistribution about a charge density, $n(\mathbf{r})$, at the solute atom site.

Friedel [156-158], however, did not approach the problem of electron scattering by a charge perturbation with the first order perturbation theory method of section V.E.1.. Instead, he employed scattering theory formalism as described , for example, by Schiff [159]. With a spherically symmetric potential (e.g. $\varphi(r)$ in equation V-12 for an unscreened Coulomb potential), an incident free electron wavefunction will be scattered into "partial waves" of Legendre polynomials times radial functions with each angular momentum quantum number. The radial functions* are parametrized by their "phase shifts". For a given potential these phase shifts are determined by the compatibility of the asymptotic forms of the radial functions for small and large $r$. For the case when a solute atom charge perturbation is represented by a three dimensional square well, and for the case of a screened Coulomb potential, Friedel and others [160-162] calculated the amount by which each radial function was shifted onto or off of the solute atom site by the charge perturbation. (The shift of the scattered wave at large $r$ is the physical meaning of the phase shift.) The

* The radial functions are products of a spherical Bessel function or Neumann function with a $kr$ argument times a trigonometric function of the phase shift. Only this phase shift depends on the potential.

solutions to these two charge screening problems are exact; they accounted for all phase shifts.

The screening charge density very close to the solute atom is complicated and the solute atom may be overscreened or underscreened at the solute atom site. Some charge density redistribution is expected outside the solute atom site, and the charge density at large $r$ was found by Friedel to go as $\frac{1}{r^3}\cos(2k_F r)$, in agreement with the first order perturbation theory asymptotic result (equation V-11). An important development from Friedel's work is the possibility of "virtual bound states" of the scattered electron, which occur when the centrifugal potential term in the Schroedinger equation acts to confine partial waves with nonzero angular momentum to the solute atom site. The existence of these "virtual bound states" depends sensitively on the Fermi energy, the density of states, and the relative strength of the scattering potential [163]. In all cases, the total screening charge around the solute atom was found to exactly cancel the charge of the solute atom, when integrated over all space.

### 3. R.K.K.Y. Theory.

In 1954 Ruderman and Kittel [164] calculated an interaction energy for the alignment of the spins of two nuclei separated by a few atomic distances. Their interaction occurred through the polarization of conduction electrons by a hyperfine interaction with the first nucleus. These conduction electrons are then responsible for a hyperfine interaction with the second nucleus, and this interaction energy will depend on the orientation of the spin of the second nucleus. Parallel or antiparallel alignments of the two nuclear spins can be favored depending on the spin distribution of the conduction electrons. Ruderman and Kittel considered the hyperfine interaction to occur only over the

infinitesimally small size of the nucleus itself. This use of a delta function potential in real space is mathematically convenient, However, these results only qualitatively describe the electron spin-polarization around a solute atom.

Here we show the spirit of the Ruderman and Kittel calculation of the interaction of two localized electron spins through the polarization of the conduction electrons. However, here we assume that the conduction electron polarization arises from the exchange interaction the localized electrons and conduction electrons of the same spin, and not from a hyperfine interaction involving nuclear spins. We will use the first order perturbation expression (equation V-7), so first we calculate the Coulomb exchange matrix element;

$$J(\mathbf{k}+\mathbf{q},\mathbf{k}) \equiv \langle \mathbf{k}+\mathbf{q}|\varphi|\mathbf{k}\rangle = \delta(\sigma_1,\sigma_2)\int_{-\infty}^{\infty}\int_{-\infty}^{\infty} \frac{e^{-i(\mathbf{k}+\mathbf{q})\cdot\mathbf{r}_2}}{\sqrt{V}}\psi^*_{loc}(\mathbf{r}_1) \times \frac{1}{|\mathbf{r}_1-\mathbf{r}_2|}\psi_{loc}(\mathbf{r}_2)\frac{e^{i\mathbf{k}\cdot\mathbf{r}_1}}{\sqrt{V}}\, d^3r_1 d^3r_2 \qquad \text{V-13}$$

$$J(k+q,k) = \lim_{\substack{\Delta_1\to 0\\ \Delta_2\to 0}} \lim_{V\to\infty} \frac{\delta(\sigma_1,\sigma_2)}{V}\int_0^{\Delta_1}\int_0^{\Delta_2} e^{-i(\mathbf{k}+\mathbf{q})\cdot\mathbf{r}_2}\, e^{i\mathbf{k}\cdot\mathbf{r}_1} \times \frac{1}{\Delta_1}\,\frac{1}{\Delta_2}\,\frac{1}{|\mathbf{r}_1-\mathbf{r}_2|}\, d^3r_1 d^3r_2 \,. \qquad \text{V-14}$$

Here $\delta(\sigma_1,\sigma_2)$ is a Kroneker delta to remind us that $J(k+q,k)$ is non-vanishing only for electrons with the same spin. In equation V-14 we have replaced the localized electron wavefunction, $\psi_{loc}$, with a limiting form of the Dirac delta function of height $\frac{1}{\Delta}$ and width $\Delta$ in the $r$ variable. Here we avoid mathematical considerations of the finiteness of $J(k+q,q)$ (a physical exchange energy must be finite), but merely point out that the two exponential wavefunctions for our conduction electrons will be nearly equal to 1 for any $k$ or $q$ over the range of integration in equation V-14. Therefore, with the choice of a Dirac delta function for $\psi_{loc}$ we have $J(k+q,k) = J$, which is independent of q. This

simplification leads to the Ruderman and Kittel result for the spin density around a solute atom when equation V-14 is integrated over $q$:

$$\rho^S(r) = \frac{9\pi n^2 J}{4\varepsilon_F}\left[\frac{(2k_F r)\cos(2k_F r) - \sin(2k_F r)}{(2k_F r)^4}\right] \qquad \text{V-15}$$

where n is the number of conduction electrons of each spin.

Kasuya [165], Yosida [166], and later Overhauser [167] calculated the exchange polarization of conduction electrons by a localized moment distributed over a finite volume, comparable to that of an atom. These treatments are more appropriate to our problem of the polarization of conduction electrons by exchange interactions with unpaired $3d$ electrons at a solute atom. When $\psi_{loc}$ is of atomic dimensions, the conduction electron density will not be effectively uniform in the integration of equation V-14. $J(k+q,k)$ will be significant over a reduced extent in $k$-space, and the first node of $\rho^S(r)$ is pushed to a value of $r$ larger than $r \simeq \frac{2.2}{k_F}$ of equation V-5. The singular behavior of $\rho^S(r)$ at $r = 0$, predicted by equation V-15, is also mollified. These more realistic exchange integrals are also relevant to theories of ferromagnetism. When $q = 0$ the exchange integral of equation V-14 is positive-definite because it becomes an integral involving an overlap of a charge density with itself. When $q = 0$ there are long-range consequences for the spin density, and a global repopulation of the conduction electron states is possible, as predicted in the Zener [168] theory of ferromagnetism.

Watson et al. [142,169-171] have treated the exchange polarization of $4s$ conduction electrons due to the five individual $3d$ atomic orbitals of iron. They used the O.P.W. approximation and compared these results to the polarization of free $4s$ electrons without core orthogonalization. This work showed that $J(\mathbf{k}+\mathbf{q},\mathbf{k})$ for iron metal cannot be represented by a function $J(q)$ which is isotropic in $k$-space (see also the description of the anisotropies in $H_{HYB}$).

Together with differences of $|\mathbf{k}_F|$ with direction, this work predicts that the spin density around most $3d$ atoms in an iron alloy cannot be assumed with accuracy to be merely a function of distance from the $3d$ atom. An isotropic polarization of conduction electrons in iron metal is still a popular assumption, however, for qualitative treatments of $J$.

A change in the number of paired or unpaired valence electrons at a $^{57}$Fe atom will generally cause a change in the isomer shift simultaneously with the change in the hyperfine magnetic field of the $^{57}$Fe nucleus. Consider first the effect of some perturbation which produces only an increase in the number of $4s\uparrow$ electrons at the $^{57}$Fe site. The increased number of $4s$ electrons at the $^{57}$Fe nucleus produces a negative (towards lower velocity) change in the isomer shift, $\Delta i < 0$. The increased $4s$ electron spin polarization at the nucleus will cause a positive (parallel to the lattice magnetization) contribution to the hyperfine magnetic field. Since core polarization causes the hyperfine magnetic field at a $^{57}$Fe nucleus to be negative, the $^{57}$Fe hyperfine magnetic field is reduced in magnitude. The following quantitative relationships between $4s$ electron density changes and $\Delta i$ and $\Delta H$ in iron metal are suggested [106,172]:

$\Delta i = -0.16$ mm/sec/$4s$ electron

$\Delta H = +2$ MG/unpaired $4s$ electron

With the core polarization mechanism we can also understand the $\Delta$ i and $\Delta$ H which are induced by changes in the $3d\uparrow$ electrons at our $^{57}$Fe atom.

$$\Delta\rho^{+}(r) = \frac{1}{V}\sum_{\mathbf{q}} [\varphi_{+}^{Fz}(q) + \varphi_{v}^{C}(q) + \varphi_{z}^{C}(q)] \cos(qr)\, F(q, 2k_F r) \qquad \text{V-16}$$

As an example, consider the effect of some perturbation which produces only an increase in the number of unpaired $3d$ electrons at the $^{57}$Fe atom. In this example core polarization will be enhanced, so the observed $\Delta$ H will be positive. As described in the isomer shift section, $\Delta$ i will also be positive. The following

quantitative relations for iron metal are suggested [106]:

$\Delta i$ = + 0.10 mm/sec/3$d$ electron

$\Delta H$ = -185 kG/unpaired 3$d$ electron

Again, as with 4$s$ electrons, we find that when the change in 3$d$ charge density and the change in the 3$d$ spin density at opposite $^{57}$Fe atom are in the same direction, Δ H and Δ i have the same sign. $\Delta i$ and $\Delta H$ will have the same sign when an increase in either the 3$d$ charge or spin density is accompanied by a decrease in the other. Both 3$d$ and 4$s$ electrons bring about similar relationships between simultaneous changes in $\Delta i$ and $\Delta H$. The factor of -11 difference between 4$s$ and 3$d$ hyperfine coupling constants does not in practice determine the importance of 4$s$ and 3$d$ electrons in causing $^{57}$Fe hyperfine magnetic field perturbations. It turns out that although 4$s$ and 3$d$ charge transfers are often comparable, the 3$d$ electron redistributions usually occur with much greater spin imbalances. Consequently, the mere knowledge of the relationship between $\Delta i$ and $\Delta H$ cannot discriminate between 4$s$ or 3$d$ electronic effects. Distinguishing whether hyperfine magnetic field changes arise from changes in either 4$s$ or 3$d$ electrons usually requires an independent knowledge of the net change of valence electron density at a $^{57}$Fe site, or a knowledge of the net spin density change.

**4. Cross-Terms and Other Considerations.**

Fortunately, the relationship between the signs of $\Delta i$ and $\Delta H$ can be used to check whether it is likely that $\Delta i$ and $\Delta H$ arise from the same electronic mechanism. In this sub-section we go beyond the charge and spin perturbation theories of section V.E.2 and V.E.3. which only allow for electron charge redistributions around a charge perturbation or electron spin redistributions around a spin perturbation. Both charge and spin perturbation theories can

predict similar shapes of electron redistributions around solute atoms because both are dominated by the particularly strong mixing of those unoccupied conduction electron states with $k' < 2k_F$ into the occupied conduction electron states with $0 < k < k_F$. By direct application of the versions of Friedel theory and R.K.K.Y. theory presented in sections V.E.2 and 3, we might expect to determine whether the conduction electron redistribution is due to a charge perturbation or a spin perturbation by looking for either an isomer shift or a hyperfine magnetic field perturbation at a $^{57}$Fe nucleus which neighbors the solute atom. In general, however, isomer shifts and hyperfine magnetic field perturbations are both observed for $^{57}$Fe nuclei which neighbor solute atoms.

Two straightforward suggestions are now developed which allow for simultaneous charge and spin redistributions of conduction electrons around a solute atom. 1. A solute atom is responsible for both a significant Coulomb perturbation and a significant electron spin perturbation; this leads to certain compatibility requirements for the spin and charge redistributions. 2. There are cross-terms in the susceptibility of initially spin-polarized conduction electrons which cause either spin redistributions around a pure charge perturbation, or charge redistributions around a pure spin perturbation. In this section suggestion 1 is first illustrated with convenient hypothetical examples. It is then shown how suggestion 2 depends on the electronic structure of the metal in two limiting cases. The first case is good for all $r$ (distance from solute atom), but only for small conduction electron polarizations. The second case is good for arbitrary polarizations, but large $r$. Finally, we lament the complicated puzzle which must be solved in order to properly interpret experimental data. I suggest that the important features of conduction electron redistributions around solute atoms depend mainly on the fact that the solute atom represents a localized perturbation; whether this is a charge or a spin pertur-

bation can perhaps be of secondary importance for my purposes.

Suggestion 1 is developed by considering three perturbations, which are the electronic changes when a solute atom replaces an iron atom: 1) a spin perturbation due to the change in number of unpaired valence electrons, 2) a charge perturbation due to the change in the total number of valence electrons, and 3) a charge perturbation due to the difference in ion core of the solute. These three perturbations have Fourier transforms $\varphi_{\pm}^{Ex}(q)$, $\varphi_{v}^{C}(q)$, and $\varphi_{z}^{C}(q)$, respectively, which we use in perturbation expressions like equation V-7. The redistribution of electrons with + spin and with - spin will differ because their occupied and unoccupied states are mixed differently by the spin perturbation:

$$\Delta\rho^{-}(r) = \frac{1}{V}\sum_{q}\left[\varphi_{-}^{Ex}(q) + \varphi_{v}^{C}(q) + \varphi_{z}^{C}(q)\right]\cos(qr)\,F(q,2k_{F}r) \qquad \text{V-17}$$

We next calculate the charge density redistribution in equation V-18. When we calculate the spin density redistribution, we find the uniform cancellation of the Coulomb perturbations because they affect electrons of either spin equally.

$$\Delta\rho^{C}(r) = \Delta\rho^{+}(r) + \Delta\rho^{-}(r) = \frac{1}{V}\sum_{q}\left[2\varphi_{z}^{C}(q) + 2\varphi_{v}^{C}(q) + \varphi_{+}^{Ex}(q) + \varphi_{-}^{Ex}(q)\right] \qquad \text{V-18}$$

$$\times\cos(qr)\,F(2k_{F}r,q)$$

$$\Delta\rho^{C}(r) = \frac{1}{V}\sum_{q} 2\varphi_{Zeff}^{C}\ \cos(qr)\,F(q,2k_{F}r) \qquad \text{V-18a}$$

$$\Delta\rho^{S}(r) = \Delta\rho^{+}(r) - \Delta\rho^{-}(r) = \frac{1}{V}\sum_{q}\left[\varphi_{+}^{Ex}(q) - \varphi_{-}^{Ex}(q)\right]\ \cos(qr)\,F(q,2k_{F}r) \qquad \text{V-19}$$

We have defined $\varphi_{Zeff}^{C}(q) \equiv \varphi_{z}^{C}(q) + \varphi_{v}^{C}(q)$. Since $\varphi_{z}^{C}(q)$ and $\varphi_{v}^{C}(q)$ arise from charge perturbations of opposite sign, they will tend to be mutually cancelling. The sign and magnitude of $\varphi_{Zeff}^{C}(q)$ are determined by the small number of valence electrons lost (or gained) by the solute atom when it is in the iron lattice. The charge distributions of the solute and the iron ion cores may also differ, but since we choose to define these ion cores as having the same net

positive charge, $\varphi_Z^C(q)$ should not have a significant effect on the conduction electron redistributions. We now compare the terms with the same $q$ from each of the sums of equation V-18 and V-19 , and call them $\Delta\rho_q^C(r)$ and $\Delta\rho_q^S(r)$:

$$\Delta\rho_q^C(r) = (1 + \varepsilon(q))\Delta\rho_q^s(r), \qquad \text{V-20}$$

$$\text{where} \quad \varepsilon(q) \equiv \frac{2(\varphi_{Zeff}^C(q) + \varphi_-^{Ex}(q))}{\varphi_+^{Ex}(q) - \varphi_-^{Ex}(q)}. \qquad \text{V-21}$$

If $\varphi_{Zeff}^C(q)$, $\varphi_-^{Ex}(q)$, and $\varphi_+^{Ex}(q)$ have the same functional form, then we will have a general relationship between all $\Delta\rho_q^C(r)$ and $\Delta\rho_q^S(r)$, which will consequently also hold for $\Delta\rho^C(r)$ and $\Delta\rho^S(r)$. In general, $\varphi_+^{Ex}(q)$ and $\varphi_-^{Ex}(q)$ will tend to be of the same functional form since they involve similar wavefunctions in the exchange mixing:

$$\frac{\varphi_\pm^{Ex}(\mathbf{q})}{|E_{\mathbf{k+q}} - E_{\mathbf{k}}|} = \frac{<\mathbf{k}+\mathbf{q}\,|\varphi_\pm^{Ex}\,|\mathbf{k}>}{|E_{\mathbf{k+q}} - E_{\mathbf{k}}|} = \frac{\delta(\sigma_1,\sigma_2)e^2}{|E_{\mathbf{k+q}} - E_{\mathbf{k}}|}\int_{-\infty}^{\infty}\int_{-\infty}^{\infty}\frac{e^{-i(\mathbf{k+q})\cdot\mathbf{r}_1}}{\sqrt{V}} \qquad \text{V-22}$$
$$\times\,\psi_{loc\pm}^*(\mathbf{r}_2)\,\frac{1}{|\mathbf{r}_1 - \mathbf{r}_2|}\,\psi_{loc\pm}(\mathbf{r}_1)\,\frac{e^{i\mathbf{k}\cdot\mathbf{r}_2}}{\sqrt{V}}\,d^3r_1 d^3r_2$$

The Coulomb mixing is:

$$\frac{\varphi_{Zeff}^C(\mathbf{q})}{|E_{\mathbf{k+q}} - E_{\mathbf{k}}|} = \frac{<\mathbf{k}+\mathbf{q}|\varphi_{Zeff}^C|\mathbf{k}>}{|E_{\mathbf{k+q}} - E_{\mathbf{k}}|} = \frac{+e^2}{|E_{\mathbf{k+q}} - E_{\mathbf{k}}|}\int_{-\infty}^{\infty}\int_{-\infty}^{\infty} \qquad \text{V-23}$$
$$\times\frac{e^{-i(\mathbf{k+q})\cdot\mathbf{r}_1}}{\sqrt{V}}\,\frac{(\Delta Z\delta(\mathbf{r}_2) - \psi_{loc}^*(\mathbf{r}_2)\psi_{loc}(\mathbf{r}_2))}{|\mathbf{r}_1 - \mathbf{r}_2|}\,\frac{e^{i\mathbf{k}\cdot\mathbf{r}_1}}{\sqrt{V}}\,d^3r_1 d^3r_2$$

We see that if the Coulomb mixing resulted only from the second term in the integral, $e^2\psi_{loc}^*(\mathbf{r}_2)\psi_{loc}(\mathbf{r}_2)$, it would be much larger* than the exchange mixing of equation V-22, and of opposite sign. However, since the Coulomb mixing due to the ion core perturbation (the first term of equation V-23) is quite comparable to the charge perturbation of the valence electrons, the difference of these two competing perturbations may result in conduction electron redistributions which are as small as those caused by the exchange mixing of equation V-22.

* The exchange mixing involves the overlap of the function $e^{-i(\mathbf{k+q})\cdot\mathbf{r}_1}\psi_{loc}(\mathbf{r}_1)$ with the function $e^{i\mathbf{k}\mathbf{r}_2}\psi_{loc}^*(\mathbf{r}_2)$. This overlap is large for only a few $\mathbf{r}_2$ when $\psi_{loc}(\mathbf{r}_1)$ is large. The Coulomb mixing involves the overlap of the function $\psi_{loc}^*(\mathbf{r}_2)\psi_{loc}(\mathbf{r}_2)$ with the function $e^{-i\mathbf{q}\mathbf{r}_1}$. This overlap is large for all $\mathbf{r}_2$ when $\psi(\mathbf{r}_1)$ is large.

This may be thought to be an example of how the tendency towards charge neutrality of solute atoms effectively enhances the importance of the exchange mixing.

We still have not resolved the question of validity of the desirable assumption that $\varphi^{C}_{Z_{eff}}(q)$ and $\varphi^{Ex}_{\pm}(q)$ have similar functional forms. Details of the shape of the conduction electron redistributions caused by localized pure charge or pure spin perturbations are uncertain theoretically [170]. (Some serious uncertainties are described in section V.I.) Because of the longer range of the Coulomb interaction, we generally expect that the first node of the conduction electron charge redistribution around a pure charge perturbation lies at a somewhat larger distance from the solute atom than the first node of a conduction electron spin redistribution around a similarly localized spin perturbation. However, the salient features of conduction electron redistributions around both charge and spin perturbations occur with dimensions of about $\frac{1}{k_F}$, due to the overriding importance of $F(2k_F r, q)$. Nevertheless, the differences in the functional forms of $\varphi^{Ex}_{\pm}(q)$ and $\varphi^{C}_{Z_{eff}}(q)$ may cause the shapes of the spin and charge redistributions to differ at intermediate distances (several times $\frac{1}{k_F}$) from the solute atom. So for convenience (necessity) in developing suggestion 1, we assume that the differences in functional forms of $\varphi^{C}_{Z_{eff}}(q)$ and $\varphi^{Ex}_{\pm}(q)$ are uneventful enough such that $F(2k_F r, q)$ dominates in the structure of equations V-18 and V-19. With a knowledge of the ratio of exchange mixing to the effective Coulomb mixing, we can determine $\varepsilon(q)$ (now just $\varepsilon$, since all $\varepsilon(q)$ have the same form) of equation V-21, and relate $\Delta\rho^{C}(r)$ to $\Delta\rho^{S}(r)$.

When a solute atom offers both a charge and a spin perturbation to the conduction electrons, there are four possible combinations of sign for these two perturbations. We list these four combinations below together with their

implications ( -> ) to the net spin of the screening charge density determined by equations V-18 and V-19. The redistribution of conduction electron density around a solute atom alternates in sign, and we cannot always be certain of which sign holds for a neighboring $^{57}$Fe nucleus. Therefore, through our knowledge of the sign of $\varepsilon$, we list only the expected relationship between the sign of $\Delta i$ and the sign of $\Delta H$, as described at the end of section V.D. These relationships apply only to the direct nonlocal solute contribution to the $^{57}$Fe hyperfine magnetic field; electronic changes at other Fe atoms around the solute may contribute to the $^{57}$Fe hyperfine magnetic field through $H_{INL}$, as described in Chapter VI.

Table IV

| AT SOLUTE | NET AROUND SOLUTE | AT NEIGHBORING $^{57}$Fe |
|---|---|---|
| $\Delta Z_{eff} > 0$; gain unpaired electron | --> gain +spin, $\varepsilon>0$ | --> Sgn ($\Delta i$)= -Sgn ($\Delta H$) |
| $\Delta Z_{eff} > 0$; loss unpaired electron | --> gain -spin, $\varepsilon<0$ | --> Sgn ($\Delta i$)= +Sgn ($\Delta H$) |
| $\Delta Z_{eff} < 0$; gain unpaired electron | --> loss -spin, $\varepsilon<0$ | --> Sgn ($\Delta i$)= +Sgn ($\Delta H$) |
| $\Delta Z_{eff} < 0$; loss unpaired electron | --> loss +spin, $\varepsilon>0$ | --> Sgn ($\Delta i$)= -Sgn ($\Delta H$) |

Equations V-20 and V-21 should be valid for all ratios of exchange mixing to Coulomb mixing. In the limiting case of a pure spin perturbation where $\varphi_{+}^{Ex}(q) = -\varphi_{-}^{Ex}(q)$ and $\varphi_{Zeff}^{C}(q) = 0$, we have $\varepsilon = -1$ so $\Delta\rho^{C}(r) = 0$. We are left with only the spin density redistribution, $\Delta\rho^{S}(r)$, of R.K.K.Y. theory. The other limiting case is that of a pure charge perturbation where $\varphi_{+}^{Ex}(q)=\varphi_{-}^{Ex}(q)$ , and $\varphi_{Zeff}^{C}(q)\neq 0$. Here $\varepsilon \to \infty$, so $\Delta\rho^{S}(r) \to 0$, and we are left with only the charge density redistribution, $\Delta\rho^{C}(r)$, of Friedel theory.

*We now describe suggestion* 2. In other words, we consider conduction electron redistributions around a pure charge or a pure spin perturbation at the solute atom when the conduction electrons are spin-polarized. We assume

that the unperturbed bandstructures of +spin and -spin conduction electrons have the same parabolic (free electron) shape. However, the translation to lower energy of the +spin band with respect to the -spin band results in the +spin band having occupied states with large $\mathbf{k}$ ; states that are unoccupied in the -spin band. The perturbation mixings of unoccupied conduction electron states into occupied conduction electron states will then be different for +spin and -spin electrons. We find that the electron redistributions, $\Delta\rho^{+}(r)$ and $\Delta\rho^{-}(r)$, differ in shape and magnitude because of differing $k_F^{\pm}$ and $n^{\pm}(\varepsilon_F)$, respectively*. This results in cross-terms in the conduction electron susceptibility to charge and spin perturbations. Polarized conduction electrons will show a spin redistribution around a pure charge perturbation, and a charge redistribution around a pure spin perturbation. These redistributions, $\Delta\rho^{SC}(r)$ and $\Delta\rho^{CS}(r)$, respectively, become as large as $\Delta\rho^{C}(r)$ and $\Delta\rho^{S}(r)$ predicted from Friedel and R.K.K.Y. theories when the conduction electrons are mostly spin polarized (i.e. mostly +spin).

Our first estimates of $\Delta\rho^{SC}(r)$ and $\Delta\rho^{CS}(r)$ are valid for small polarizations of the conduction electrons. We need a small polarization so that $2\Delta k_F \equiv k_F^{+} - k_F^{-}$ will be much less than $k_F^{-}$, and we can work with a Taylor series in $k_F$. For a convenient physical picture, we assume that this small polarization arises from a (Weiss) magnetic field of strength $B$. This field populates +spin states and depopulates -spin states by translating the energy of the +spin band a small amount, $2\mu_B B$, below that of the -spin band. The difference in Fermi wavevector of the two bands will be $\Delta k_F = 2\mu_B B \left.\frac{dk}{d\varepsilon}\right|_{k_F}$, which is $\Delta k_F = \frac{\mu_B B}{k_F}\frac{2m}{\hbar^2}$ for free electrons. Using the method of section V.D.1, we calculate the density redistribution of +spin and -spin electrons independently.

* For free electrons the density of states at the Fermi energy, $n(\varepsilon_F)$, goes as $k_F$.

For -spin electrons:

$$\Delta\rho^{-}(r) = \frac{1}{(2\pi)^3}\int_0^{\infty} F(2k_F^{-}r,q)\,\varphi(q)\cos(qr)dq\ . \qquad \text{V-24}$$

Recall that the Lindhard susceptibility function for free electrons, $F(k_F,q)$, comes from an integral of the form:

$$\int_{k=0}^{k_F} n(k) \int_{|\mathbf{k}'|=k_F}^{\infty} \frac{1}{|\mathbf{k}'^2 - k^2|}\, d\mathbf{k}'\, dk,$$

and it includes the density of occupied states in its dependence on $k_F$. Since $\Delta k_F$ is small, for +spin electrons we employ a Taylor series approximation for $F(2k_F^{+}r,q)$, and find:

$$\Delta\rho^{+}(r) = \frac{1}{(2\pi)^3}\int_0^{\infty}\left[F(2k_F^{-}r,q) + \Delta k_F \cdot \frac{\partial F}{\partial k_F}\Big|_{k_F^{-}}\right]\varphi(q)\cos(qr)dq\ . \qquad \text{V-25}$$

The partial derivative of $F$ with respect to $k_F$ is small, positive, and boring for large $q$ and small $q$. However, near $q = 2k_F$:

$$\frac{\partial F(2k_F r,q)}{\partial k_F} \simeq \frac{k_F}{q}\, ln\left|\frac{2k_F+q}{2k_F-q}\right|, \qquad \text{V-26}$$

which blows up to infinity very, very close to $q = 2k_F$. Our Taylor series was not expressed as an expansion in the variable $q$, so we expect that no harm is done by this singularity in $\left.\frac{\partial\, F(2k_F r,q)}{\partial\, k_F}\right|_{k_F^{-}}$. The additional term in equation V-25 which is not present in equation V-24 is:

$$Term\ \#2,\ Eqn.\ 25 = \frac{\Delta k_F}{(2\pi)^3}\int_0^{\infty}\frac{k_F}{q}\, ln\left|\frac{2k_F+q}{2k_F-q}\right|\varphi(q)\cos(qr)dq\ . \qquad \text{V-27}$$

Watson [170] finds a result similar to equation V-27 from a less direct treatment of a charge perturbation, but terminates his treatment there. However, when we consider the separation in $q$ of equal values of $\left.\frac{\partial\, F(2k_F r,q)}{\partial\, k_F}\right|_{k_F^{-}}$ which straddle $q = 2k_F$, we find that the approximation:

$$\frac{\partial F(2k_F r,q)}{\partial k_F}\Big|_{k_F^{-}} \simeq k_F\,\delta(q-2k_F) \qquad \text{V-28}$$

is excellent, at least so long as $\varphi(q)$ goes to zero as $q$ goes to infinity. Together with $\Delta k_F = \frac{2m\mu_B B}{\hbar^2 k_F}$ we find:

$$Term\ \#2,\ Eqn.\ 25 = \frac{2mg\,\mu_B B}{\hbar^2}\,\varphi(2k_F)\cos(2k_F r). \qquad \text{V-29}$$

In calculating the spin polarization induced by a pure charge perturbation, $\Delta\rho^{SC}(r)$, we note that term #1 of $\Delta\rho^{+}(r)$ (in equation V-25) exactly cancels $\Delta\rho^{-}(r)$ of equation 24 because a pure charge perturbation at the solute site, $\varphi^{C}$, redistributes +spin and -spin electrons equally, but +spin and -spin electrons make opposite contributions to the spin redistribution. Therefore:

$$\Delta\rho^{SC}(r) = \frac{2mg\,\mu_B B}{\hbar^2 r^2}\,\varphi^{C}(2k_F)\cos(2k_F r)\,. \qquad \text{V-30}$$

The $\frac{1}{r^2}$ factor is necessary when we average the flux of plane wave electrons scattered over all solid angles around the atom.

In calculating the charge polarization induced by a pure spin perturbation, $\Delta\rho^{CS}(r)$, we note that term #1 of $\Delta\rho^{+}(r)$ (in equation V-25) exactly cancels $\Delta\rho^{-}(r)$ of equation V-24 because a pure spin perturbation at the solute site, $\varphi^{Ex}$, redistributes +spin and -spin electrons oppositely, but both +spin and -spin electrons contribute equally to the net charge. Therefore:

$$\Delta\rho^{CS}(r) = \frac{2mg\,\mu_B B}{\hbar^2 r^2}\,\varphi^{Ex}(2k_F)\cos(2k_F r). \qquad \text{V-31}$$

The similarity of equations V-30 and V-31 arises because of the symmetry of the arguments which precede them. Note that $\Delta\rho^{SC}(r)$ and $\Delta\rho^{CS}(r)$ both vanish as the magnetic field, and hence $\Delta k_F$, goes to zero. In this small magnetization limit $\Delta\rho^{SC}(r)$ and $\Delta\rho^{CS}(r)$ are of smaller magnitude than $\Delta\rho^{C}(r)$ and $\Delta\rho^{S}(r)$ of Friedel and R.K.K.Y. theories, but their spatial dependence goes as $\frac{1}{r^2}$ rather than as $\frac{1}{r^3}$. The additional $\frac{1}{r}$ factor in $\Delta\rho^{C}(r)$ and $\Delta\rho^{S}(r)$ may be thought to arise from interference effects between the $\cos(qr)$ terms at large distances.

$F(k_F,q)$ is significant for all values of $q$ from 0 to $\approx k_F$, so the $\cos(qr)$ terms with these values of $q$ are all weighted significantly, and they interfere to give the additional $\frac{1}{r}$ dependence. However, since $\left.\frac{\partial F(2k_F r,q)}{\partial k_F}\right|_{k_F^-}$ is large for only one value of $q$, there are no comparable interference effects to reduce $\Delta\rho^{SC}(r)$ and $\Delta\rho^{CS}(r)$ at large $r$.

For strongly polarized conduction electrons, the ratio $\frac{\Delta k_F}{k_F^-}$ may be greater than unity, so our Taylor series approach is clearly invalid. Recalling again that $F(2k_F r,q)$ already contains our density of states information, we expect:

$$\Delta\rho^-(r) = \frac{1}{(2\pi)^3}\int_{q=0}^{\infty} F(2k_F^- r,q)\varphi(q)\cos(qr)dq\text{, and} \qquad \text{V-32}$$

$$\Delta\rho^+(r) = \frac{1}{(2\pi)^3}\int_{q=0}^{\infty} F(2k_F^+ r,q)\varphi(q)\cos(qr)dq\ . \qquad \text{V-33}$$

The structure of $\varphi(q)$ is more important here than it was in the limit of small conduction electron polarizations. However, for concreteness we assume that $\varphi(q) = \varphi$, a constant, and we find the asymptotic forms of equations V-32 and V-33 for large $r$:

$$\Delta\rho^-(r) \propto \frac{k_F^-}{r^3}\varphi\ \cos(2k_F^- r)\text{, and} \qquad \text{V-34}$$

$$\Delta\rho^+(r) \propto \frac{k_F^+}{r^3}\varphi\ \cos(2k_F^+ r). \qquad \text{V-35}$$

Now, for the spin redistribution around a pure charge perturbation, and for a charge redistribution around a pure spin perturbation we find for large $r$:

$$\Delta\rho^{SC}(r) = \Delta\rho^+(r) - \Delta\rho^-(r) \propto \frac{\varphi^C}{r^3}\left[\frac{k_F^+\cos(2k_F^+ r) - k_F^-\cos(2k_F^- r)}{k_F^+ + k_F^-}\right] \text{ and} \qquad \text{V-36}$$

$$\Delta\rho^{CS}(r) = \Delta\rho^+(r) + \Delta\rho^-(r) \propto \frac{\varphi^{Ez}}{r^3}\left[\frac{k_F^+\cos(2k_F^+ r) - k_F^-\cos(2k_F^- r)}{k_F^+ + k_F^-}\right]. \qquad \text{V-37}$$

The similarity of $\Delta\rho^{SC}(r)$ and $\Delta\rho^{CS}(r)$ again arises as described in the symmetrical arguments preceding equations V-30 and V-31. For complete polarization of the conduction electrons, the screening spin about a local charge of $1e$ will

develop a magnetic moment of $1\mu_B$. However, even for complete conduction electron polarization the net screening charge about a local magnetic moment of $1\mu_B$ will not be $1e$ unless the exchange mixing (equation V-22) and the Coulomb mixing (equation V-23) are the same. For unpolarized electrons we again find that $\Delta\rho^{SC}(r)$ and $\Delta\rho^{CS}(r)$ both vanish. However, when $\Delta k_F$ is very small, we make the two Taylor series approximations:

$$k_F^+ \cos(2k_F^+ r) \simeq (k_F^\circ + \frac{\Delta k_F}{2}) \left[ \cos(2k_F^\circ r) - \Delta k_F r \sin(2k_F^\circ r) \right]$$

$$k_F^- \cos(2k_F^- r) \simeq (k_F^\circ - \frac{\Delta k_F}{2}) \left[ \cos(2k_F^\circ r) + \Delta k_F r \sin(2k_F^\circ r) \right],$$

and find for large $r$:

$$\lim_{\Delta k_F \to 0} \Delta\rho^{SC}(r) \propto \frac{\varphi^C}{r^2} (\Delta k_F) \cos(2k_F^\circ r) \text{, and} \qquad \text{V-38}$$

$$\lim_{\Delta k_F \to 0} \Delta\rho^{CS}(r) \propto \frac{\varphi^{Ex}}{r^2} (\Delta k_F) \cos(2k_F^\circ r) . \qquad \text{V-39}$$

These limiting forms for $\Delta\rho^{SC}(r)$ and $\Delta\rho^{CS}(r)$ are the same as those from our first calculation, which gave an exact solution for all $r$ in the limit of small magnetization. (Compare equations V-30 and V-31 to equations V-38 and V-39.)

We now have four independent types of conduction electron redistributions around solute atoms: $\Delta\rho^C(r)$, $\Delta\rho^S(r)$, $\Delta\rho^{SC}(r)$, and $\Delta\rho^{CS}(r)$. For physical predictions of the importance of these four effects, we need accurate knowledge of the electronic structure of our metal and of our solute atom. We need good localized electron and conduction electron wavefunctions in order to calculate the exchange mixing and the Coulomb mixing (or phase shifts in Friedel theory). We also need to know the degree of polarization of the conduction electrons, and some details of their Fermi surface. We have so far neglected electron-electron interactions between screening electrons, but we may expect them to be important near solute atoms where large electron density changes are expected *. Sadly, I believe that the information required for quantitative

* As mentioned in section V.I., Kim and Schwartz [173-176] have performed a controversial calculation of screening effects involving interacting conduction electrons. They estimated

predictions of conduction electron redistributions around solute atoms constitutes a tall order which cannot yet be quantitatively filled. It is therefore not surprising that Chapter VI outlines a current controversy in the literature regarding the importance [208], or rather the completeness [209]. of using conduction electron redistribution mechanisms to account for the hyperfine magnetic fields in Fe-X alloys. (This controversy began in the late 1960's!)

As an experimentalist I have chosen to take an attitude oriented less towards quantitative predications and more towards a general appreciation of of how electronic interactions are important in the nature of electron redistributions around the solute atoms. The Pauli principle, in conjunction with the sharpness of the conduction electron Fermi surface, is responsible for the conduction electron sreening electron density being constructed mainly from Fourier components with $0 < q < 2k_F$. Such a square wave in $k$-space causes structure and periodic variations in the screening charge over distances on the order of $\frac{\pi}{k_F}$ around the solute atom. The range and angular dependence of the interaction between the conduction electrons and the perturbation at the solute atom will influence the structure of the conduction electron redistribution, especially in the region near the solute atom. This small $r$ region involves the largest changes in electron density, and probably includes the phenomenologically important 1n.n. and 2n.n sites around the solute atom. It is expected that $^{57}$Fe atoms at 1n.n. and 2n.n. sites experience substantial changes* in $H_{COND}$. It is unfortunate that the conduction electron redistributions in this region are the most difficult to determine with accuracy.

---

the number of electrons involved in $\Delta\rho^{SC}(r)$, and they predicted magnetic moments of much greater than $1\mu_B$ for the screening electrons surrounding a pure charge perturbation of $1e$.

* Unfortunately, $^{57}$Fe atoms at these sites may be simultaneously subjected to changes in other mechanisms such as $H_{COV}, H_{OV}, H_{HYB}$, and $H_{ORB}$.

Mechanisms of $H_{COND}$ are experimentally significant. We roughly estimate the contribution to $\Delta\rho^{SC}(r)$ from 4*s* electrons using a Fe 4*s* hyperfine coupling constant of -2 MG/(unpaired 4*s* electron) [172], and a 4*s* spin polarization of +10% [106]. Then if a 4*s* electron redistribution causes a nearby $^{57}$Fe atom to lose 0.1 4*s* electron, the hyperfine magnetic field perturbation at that $^{57}$Fe nucleus will be +20 kG. An isomer shift at a $^{57}$Fe nucleus located in a 1n.n. site, $\Delta i_1$, may be as large as a few hundredths of a mm/sec, but its magnitude and sign again depend on details of the electron redistribution around the solute atom. However, in spite of the complicated shape of the conduction electron redistributions, in two cases we can confidently relate the sign of $\Delta i_j$ to the sign of $\Delta H_j$ . In one case the solute atom offers only a pure charge perturbation and the conduction electrons are spin polarized (assume positive polarization). $\Delta i_j$ then arises from $\Delta\rho^{C}(r)$, $\Delta H_j$ arises from $\Delta\rho^{SC}(r)$. Clearly both $\Delta i_j$ and $\Delta H_j$ are consequences of the same Coulomb mixing, and therefore both must have ***exactly*** the same spatial distribution around the solute atom. If, as in the case for positively polarized free electrons, the +spin conduction electrons dominate the charge screening, then as described at the end of the section V. D.:

Sign $(\Delta i)$ = + Sign $(\Delta H)$ because $\Delta\rho^{C}(r) \propto +\Delta\rho^{SC}(r)$.

This same relationship holds true in the second simple case when the solute atom offers a pure spin perturbation, so that $\Delta H_j$ arises from $\Delta\rho^{S}(r)$ , and $\Delta_j$ arises from $\Delta\rho^{CS}(r)$. Without our assumption of parabolic free-electron bands we can no longer assume that $n^{+}(\varepsilon_F) > n^{-}(\varepsilon_F)$. For non-parabolic bands we must modify all equations V-34 to V-37 by replacing factors of $k_F^{+}$ and $k_F^{-}$ by more general factors like $n^{+}(\varepsilon_F)$ and $n^{-}(\varepsilon_F)$. If we know that $n^{-}(\varepsilon_F) > n^{+}(\varepsilon_F)$ for our metal, then -spin conduction electrons will dominate the screening so that our relationship between $\Delta H_j$ and $\Delta i_j$ becomes reversed.

When the solute atom presents both a significant charge perturbation and

a significant spin perturbation, the relation between $\Delta H_j$ and $\Delta i_j$ is not predictable without more knowledge about the nature of the perturbations. Rules similar to the four in Table IV may then be used to relate $\Delta i_j$ and $\Delta H_j$, but our confidence in these predictions must be less than the two cases of either a pure charge perturbation or a pure spin perturbation at the solute atom. (Our confidence becomes less as the Coulomb mixing and the exchange mixing develop different $k$ dependencies.) When the solute atom presents both significant charge and spin perturbations, and the conduction electrons are spin polarized, the detailed situation is hopeless without a very detailed knowledge of the electronic structure of the metal.

**F. Outer Electron Polarization:** $H_{OV}$.

In these next three sections we discuss three sources of hyperfine magnetic fields which arise from physical chemistry effects: $H_{OV}$, $H_{COV}$, and $H_{HYB}$ [143,170]. If an iron atom neighboring a $^{57}$Fe atom is replaced with a solute atom, the number and spin of the valence electrons belonging to the $^{57}$Fe atom will change. We treat these changes as changes in the electron occupancy of the atomic orbitals of each spin around the $^{57}$Fe nucleus. Changes in occupancy of these orbitals affect the $^{57}$Fe hyperfine magnetic field directly if they are $s$ orbitals, or indirectly through core polarization if they are other (i.e. $3d$) orbitals.

The origin of the overlap contribution to the hyperfine magnetic field at a $^{57}$Fe nucleus, $H_{OV}$, can be illustrated by using a three-electron wavefunction * .

* Setting up a determinant of functions ensures working with their orthogonal parts. Recall that a determinant equals zero if two columns are parallel vectors, and a determinant is unchanged if a constant times one column is added to another column. In the Hartree-Fock formalism this means that the total system wavefunction is constructed out of only the mutually orthogonal parts of each column. In our example here, the two columns involving $\psi^S\alpha$ and $\psi^S\beta$ are orthogonal for any choice of R, so the construction of the determinant serves to orthogonalize $\psi^{Fe}\alpha$ to $\psi^S\alpha$. Our new normalization factor, N, could just as well be applied to $\psi^{Fe}\alpha$ alone, and the same result of equation V-45 would be obtained.

We choose an example appropriate to a nonmagnetic Si solute atom where this three electron treatment applies to a change in the occupancy of the unpaired $3d\uparrow$ wavefunction of the $^{57}$Fe atom. We show that this $3d\uparrow$ occupancy change arises from normalization when an antisymmetric combination of this $3d\uparrow$ orbital and the overlapping $3p\uparrow$ and $3p\downarrow$ orbitals of the neighboring Si atom is constructed. In a complementary example of a magnetic Cr solute neighbor, we would have a similar three electron treatment for the polarization of the $3s\uparrow$ and $3s\downarrow$ orbitals of the iron due to the unpaired $3d$ electron at the Cr atom. In our Si example, $\psi^{Fe}(\mathbf{x}_1-\mathbf{R})\,\alpha_1$ represents the $3d$ wavefunction at the iron atom occupied by electron #1. $\psi^{S}(\mathbf{x}_1)$ is the spatial part of the Si $3p$ wavefunction occupied by electron #1, and we consider the two complete wavefunctions $\psi^{S}(\mathbf{x}_1)\alpha_1$ (spin up), and $\psi^{S}(\mathbf{x}_1)\,\beta_1$ (spin down). The Si nucleus is separated from the Fe nucleus by the distance $\mathbf{R}$. Our antisymmetric three electron wavefunction is:

$$\Psi(\mathbf{x}_1,\mathbf{x}_2,\mathbf{x}_3) = N \begin{vmatrix} \psi^{Fe}(\mathbf{x}_1-\mathbf{R})\alpha_1 & \psi^{S}(\mathbf{x}_1)\alpha_1 & \psi^{S}(\mathbf{x}_1)\beta_1 \\ \psi^{Fe}(\mathbf{x}_2-\mathbf{R})\alpha_2 & \psi^{S}(\mathbf{x}_2)\alpha_2 & \psi^{S}(\mathbf{x}_2)\beta_2 \\ \psi^{Fe}(\mathbf{x}_3-\mathbf{R})\alpha_3 & \psi^{S}(\mathbf{x}_3)\alpha_3 & \psi^{S}(\mathbf{x}_3)\beta_3 \end{vmatrix} \qquad \text{V-40}$$

We are interested in obtaining the electron density, so we calculate the probability $\Psi^*\Psi$:

$$\begin{aligned} \Psi^*(\mathbf{x}_1,\mathbf{x}_2,\mathbf{x}_3)\,\Psi\,(\mathbf{x}_1,\mathbf{x}_2,\mathbf{x}_3) = N^2[&\psi^{Fe*}(\mathbf{x}_1-\mathbf{R})\alpha_1\psi^{Fe}(\mathbf{x}_1-\mathbf{R})\alpha_1\psi^{S*}(\mathbf{x}_2)\alpha_2 \\ &\times \psi^{S}(\mathbf{x}_2)\alpha_2\psi^{S*}(\mathbf{x}_3)\beta_3\psi^{S}(\mathbf{x}_3)\beta_3 \\ &- \psi^{Fe*}(\mathbf{x}_1-\mathbf{R})\alpha_1\psi^{Fe}(\mathbf{x}_3-\mathbf{R})\alpha_3\psi^{S*}(\mathbf{x}_2)\beta_2\psi^{S}(\mathbf{x}_2)\beta_2 \\ &\times \psi^{S*}(\mathbf{x}_3)\alpha_3\psi^{S}(\mathbf{x}_1)\alpha_1 \;+\; 34\ \textit{similar terms}\,] \end{aligned} \qquad \text{V-41}$$

The first term in equation V-41 and five other terms like it arise when each electron is entirely confined to one nucleus. It is convenient to define the overlap integral, $S(\mathbf{R})$:

$$S(\mathbf{R}) \equiv \int_{-\infty}^{\infty} \psi^{Fe*}(\mathbf{x}_i-\mathbf{R})\;\psi^{S}(\mathbf{x}_i)\;d^3x_i \qquad \text{V-42}$$

When our wavefunctions are normalized, $|S(\mathbf{R})| < 1$, and we generally expect

$|S(\mathbf{R})|$ to become larger as the atomic separation, $\mathbf{R}$, decreases. When we normalize our three-electron wavefunction:

$$\frac{1}{N^2} = \int_{-\infty}^{\infty}\int_{-\infty}^{\infty}\int_{-\infty}^{\infty} \Psi^*(\mathbf{x}_1,\mathbf{x}_2,\mathbf{x}_3)\, \Psi(\mathbf{x}_1,\mathbf{x}_2,\mathbf{x}_3)\, d^3x_1 d^3x_2 d^3x_3 \prod_{i=1}^{3} \langle\sigma_i|\sigma_i\rangle\,, \qquad \text{V-43}$$

where $\sigma_i$ is the spin factor for the $i^{th}$ electron, we find by using equation V-41:

$$N = \frac{1}{\sqrt{3!(1-S^2(\mathbf{R})}} \simeq \frac{1}{\sqrt{3!}}\sqrt{1+S^2(\mathbf{R})}\,, \qquad \text{V-44}$$

when $S(\mathbf{R}) \ll 1$.

Our goal here is to evaluate the electron density changes predicted by our antisymmetric wavefunction when the Si atom is brought close to the iron atom, so that $|S(\mathbf{R})|>0$. We want to determine the total charge density associated with one electron, and we choose* to work with electron #1. We therefore integrate equation V-41 over the coordinates of electron #2 and electron #3 in order to find the new net charge density associated with electron #1. Twenty-four of the terms in equation V-41 vanish by spin orthogonality. Using the approximate equation V-44 for the normalization factor, and defining $\mathbf{x} \equiv \mathbf{x}_1 - \mathbf{R}$, we find the total single electron charge density to second order in $S$:

$$\begin{aligned}\rho(\mathbf{x}_1) = \frac{1}{3}&\left[\psi^{Fe*}(\mathbf{x})\psi^{Fe}(\mathbf{x})\,\alpha_1\alpha_1 + \psi^{S*}(\mathbf{x}_1)\psi^{S}(\mathbf{x}_1)\alpha_1\alpha_1 + \psi^{S*}(\mathbf{x}_1)\psi^{S}(\mathbf{x}_1)\beta_1\beta_1\right] \qquad \text{V-45}\\ &- \frac{S(R)}{3}\left[\psi^{Fe*}(\mathbf{x})\,\psi^{S}(\mathbf{x}_1)\,\alpha_1\alpha_1 + \psi^{S*}(\mathbf{x}_1)\,\psi^{Fe}(\mathbf{x})\,\alpha_1\alpha_1\right]\\ &+ \frac{S^2(\mathbf{R})}{3}\left[\psi^{S*}(\mathbf{x})\,\psi^{S}(\mathbf{x})\alpha_1\alpha_1 + \psi^{S*}(\mathbf{x}_1)\,\psi^{S}(\mathbf{x}_1)\alpha_1\alpha_1\right]\end{aligned}$$

We see that the first term of equation V-45 comes from the simple linear superposition of the charge densities of our three atomic orbitals. However, spin orthogonality prevents the $\psi^S\beta$ orbital** from appearing in the two correction terms in equation V-45. Consequently, a +spin density change as well as a

* Since $\Psi$ merely changes sign under the interchange of two electron coordinates, the charge density, which goes as $\Psi^*\Psi$, will be the same for any choice of electron.

** Therefore we could have deleted $\psi^S\beta$ and worked with a 2x2 determinant in equation V-40, but we carried out the 3x3 determinant calculation for comparison with the $H_{COV}$ calculation in the next section.

charge redistribution occurs when $|S(\mathbf{R})| > 0$.

The systematics of electron overlap effects on hyperfine magnetic field perturbations are given in equation V-45. We are specifically concerned with changes in the number of iron $3d$ electrons and their net spin. No change is represented by the first term of equation V-45. The change of importance is the presence of the term $\frac{+S^2(\mathbf{R})}{3}\psi^{Fe*}(\mathbf{x})\psi^{Fe}(\mathbf{x})\,\alpha_1\alpha_1$ in equation V-45, which represents a gain in the $3d\uparrow$ electron density of the iron atom. Although the second term in equation V-45 may appear to be more significant because it goes as $S^1$, when integrated over $\mathbf{x}_1$ it proves to be of order $S^2$, and provides only a small charge density close to the $^{57}$Fe nucleus. We take a risk and ignore it. We predict that the increased density of $3d\uparrow$ electrons will increase the amount of polarization at our iron atom. The isomer shift and the observed hyperfine magnetic field perturbation at a $^{57}$Fe nucleus neighboring a Si atom will both be positive. When we calculate an overlap integral, $s(\mathbf{R})$, for $\mathbf{R}$ equal to a 1n.n. separation, and using hydrogen wavefunctions we find a tiny $S \approx 10^{-2}$. Sondhi [177] has made numerical calculations of $3d$-$4s$ overlap integrals using Hartree-Fock free atom wavefunctions, and he has found them to be quite small (.05 to .08). This overlap would imply a trivial $\Delta H$ and $\Delta i$, but the use of expanded wavefunctions more appropriate to Fe and Si atoms in a Fe-Si alloy yields a $\Delta H$ and a $\Delta i$ which are experimentally significant [178].

**G. Electron Bonding Polarization:** $H_{COV}$.

We continue with the example of a nonmagnetic solute, with outer electrons in orbitals $\psi^S\alpha$ and $\psi^S\beta$, in the proximity of an iron atom with an unpaired $3d$ electron. However, now we consider the consequences for the electron density when the solute electron in the $\psi^S\beta$ (-spin) orbital spends the fraction $\frac{\gamma}{1+\gamma}$ of its time in the heretofore unoccupied $\psi^S\beta$ orbital. This is a process of

covalent bonding, and $\gamma$ is a parameterization of the bond strength. Here we make no effort to evaluate $\gamma$, but only consider how it affects the electron redistribution around the $^{57}$Fe nucleus. However, we do expect $\gamma$ to be somehow proportional to the electronegativity difference between the iron atom and the solute atom [143,179,180,181]. Instead of the $\Psi$ considered for electron overlap effects (c.f. equation V-40), our system wavefunction is now:

$$\Psi(\mathbf{x}_1,\mathbf{x}_2,\mathbf{x}_3) = \frac{1}{N}\begin{vmatrix} \psi^{Fe}(\mathbf{x}_1-\mathbf{R})\alpha_1 & \psi^{S}(\mathbf{x}_1)\alpha_1 & \psi^{S}(\mathbf{x}_1)\beta_1+\gamma\psi^{Fe}(\mathbf{x}_1-\mathbf{R})\beta_1 \\ \psi^{Fe}(\mathbf{x}_2-\mathbf{R})\alpha_2 & \psi^{S}(\mathbf{x}_2)\alpha_2 & \psi^{S}(\mathbf{x}_2)\beta_2+\gamma\psi^{Fe}(\mathbf{x}_2-\mathbf{R})\beta_2 \\ \psi^{Fe}(\mathbf{x}_3-\mathbf{R})\alpha_3 & \psi^{S}(\mathbf{x}_3)\alpha_3 & \psi^{S}(\mathbf{x}_3)\beta_3+\gamma\psi^{Fe}(\mathbf{x}_2-\mathbf{R})\beta_3 \end{vmatrix} \qquad \text{V-46}$$

We take the same approach in evaluating the system charge density that was used in section V.F. for determining overlap effects, but now we find the normalization factor for $\Psi^*\Psi$ (after extensive bookkeeping with the 144 terms):

$$N = \sqrt{6(1-S^2)(1+2S\gamma+\gamma^2)}\text{, and} \qquad \text{V-47}$$
$$\frac{1}{N^2} \simeq \frac{1}{6}(1-2S\gamma-\gamma^2+S^2)$$

to second order in small $\gamma$ and $S$. We again integrate over the space and spin coordinates of electrons nos. 2 and 3 to find the new one electron charge density for electron no. 1 (to second order in $\gamma$ and $S$):

$$\begin{aligned}\Delta\rho^{COV}(\mathbf{x}_1) = {} & \frac{1}{3}\left[|\psi^{Fe}(\mathbf{x})\alpha|^2 + |\psi^{S}(\mathbf{x}_1)\,\alpha|^2 + |\psi^{S}(\mathbf{x}_1)\beta|^2\right] \qquad \text{V-48} \\ & - \frac{S}{3}\left[\psi^{Fe*}(\mathbf{x})\,\psi^{S}(\mathbf{x}_1)\,\alpha^2 + \psi^{S*}(\mathbf{x}_1)\psi^{Fe}(\mathbf{x})\,\alpha^2\right] \\ & + \frac{S^2}{3}\left[|\psi^{Fe}(\mathbf{x})\alpha|^2 + |\psi^{S}(\mathbf{x}_1)\alpha|^2\right] \\ & - \frac{\gamma}{3}\left[2S|\psi^{Fe}(\mathbf{x})\beta|^2 - \beta^2\psi^{Fe*}(\mathbf{x})\psi^{S}(\mathbf{x}_1) - \beta^2\psi^{S*}(\mathbf{x}_1)\,\psi^{Fe}(\mathbf{x})\right] \\ & + \frac{\gamma^2}{3}\left[|\psi^{Fe}(\mathbf{x})\beta|^2 - |\psi^{S}(\mathbf{x}_1)\beta|^2\right]\end{aligned}$$

Again $\mathbf{x} \equiv \mathbf{x}_1 - R$. The first three terms of equation V-48 are the overlap induced charge redistribution of equation V-45. The last two terms arise from the covalent bonding of the -spin orbitals, $\psi^S\beta$ and $\psi^{Fe}\beta$. The important last term (times $\frac{\gamma^2}{3}$) shows the partial de-occupation of the -spin solute orbital and the

corresponding occupation of the previously unoccupied $3d\downarrow$ orbital of the iron atom. The fourth term (times $\frac{\gamma}{3}$) can be ignored if $\gamma \gg S$. The effect of the solute atom on the charge and spin redistribution of the electrons of the iron atom depends on the relative magnitudes of $\gamma$ and $S$. Using arguments similar to those at the end of section V.F. we find:

overlap dominates: $S >> \gamma \quad \Delta H < 0$

$\Delta i > 0$

V-49 $S = \gamma \quad \Delta H < 0$

$\Delta i > 0$

covalent bonding dominates: $S << \gamma \quad \Delta H > 0$

$\Delta i > 0$

for the experimentally observed effect on the isomer shift and hyperfine magnetic field perturbation at a $^{57}Fe$ nucleus which has a nonmagnetic solute atom as a nearcst neighbor. (Here a positive $\Delta H$ means a decreasc in sextet splitting.) In our simple treatment we have neglected other orbitals, such as the iron $3s$ orbitals, which may also be affected by the prescnce of the solute atom. However, unles the solute atom has unpaired valence electrons, we might expect only small hyperfine field effects to result from the influence of the solute atom on the paired iron $3s$ electrons. Sadly, the experimental situation is not as clear as our approach to $H_{OV}$ and $H_{COV}$ may suggest. This is discussed further in Chapter VI.

**H. Interband Mixing:** $H_{HYB}$.

The final mechanism by which a solute atom can effect charge and spin density changes at a nearby iron atom is interband mixing. Interband mixing is conceptually similar to the covalent bonding process described in the previous section, but now delocalized electrons are involved. In the development below

we do not evaluate the charge and spin redistributions associated with normalizing an antisymmetric multi-electron wavefunction, as we did previously. Instead, through a perturbation theory we examine the hybridization* of nearly degenerate band wavefunctions constructed from different atomic states, and find the energy of the hybridized states. This hybridization energy is expected to change near a solute atom when the solute atom is substituted for an iron atom. For illustration, we consider only two discrete states, and do not consider a realistic weighting by the density of states. Such a change will modify the spin polarization of the conduction electrons in this region through the repopulation of electron states near the Fermi energy. The electron redistributions around a solute atom turn out to be somewhat akin to R.K.K.Y. oscillations of spin density.

The general importance of interband mixing to problems of local exchange interactions in solids was pointed out recently by Anderson and Clogston [182]. Interband mixing was later used by Watson et al. [183] to explain observations of negative long-range exchange integrals, $J(\mathbf{k}=\mathbf{k}')$ in rare earth metals. ($J(\mathbf{k} = \mathbf{k}')$ of equation V-4 is positive-definite.) In iron alloys we are interested in hybridization effects starting with polarized $3d$ electrons of the solute atom and the iron atom which it replaces, and initially unpolarized $4s$ conduction electrons. Interesting effects occur when these $4s$ and $3d$ states are degenerate in energy at some particular $\mathbf{k}$. Spin polarization of the $4s$ electrons will lift this degneracy when we replace the hamiltonian H, which has unmagnetized free electron-like $4s$ and atomic-like $3d$ solutions, with H+h, where h includes interactions between $3d$ and $4s$ electrons of parallel spin.

To determine the energy of the new hybridized states we start with two nearly degenerate wavefunctions of the hamiltonian H having the same $\mathbf{k}$: 1) an

* In essence we determine how $\gamma$ of the previous section depends on $\mathbf{k}$.

occupied $\psi^{3d}(\mathbf{r})\alpha$ which is nearly independent of $\mathbf{k}$, and localized at the solute atom, and 2) an unoccupied $\psi^{4s}(\mathbf{r})\alpha$ which is strongly $k$-dependent and free electron-like. We assume the $3d\uparrow$ wavefunction has lower energy than the $4s\uparrow$ wavefunction, and as $\mathbf{k}$ decreases the energy of the $4s\uparrow$ state approaches the energy of the $3d\uparrow$ state from above. Our perturbation induced hybridization involves the construction of :

$$|hyb>\alpha = a\,|4s>\alpha + b\,|3d>\alpha, \qquad \text{V-50}$$

and the determination of $a$ and $b$ by the usual pair of homogeneous equations obtained in elementary treatments of band theory (but here H contains the unperturbed potential energy as well as the kinetic energy operator):

$$\begin{aligned}(<4s\,|H|\,4s> - \varepsilon)a + <4s\,|h|\,3d>b &= 0 \\ <3d\,|h|\,4s>a + (<3d\,|H|\,3d> - \varepsilon)b &= 0\,.\end{aligned} \qquad \text{V-51}$$

From equation V-51 comes a quadratic secular equation with the solutions:

$$\varepsilon = \frac{1}{2}(<4s\,|H|\,4s> - <3d\,|H|\,3d>) \pm \frac{1}{2}\Big[(<4s\,|H|\,4s> - <3d\,|H\,3d>)^2 + 4<3d\,|h\,|\,4s>|^2\Big]^{1/2}. \qquad \text{V-52}$$

When $\mathbf{k}$ is well-removed from its values at which the $4s$ and $3d$ wavefunctions are degenerate, the discriminant in equation V-52 is dominated by the difference in unperturbed energies of the $4s$ and $3d$ wavefunctions, and involves the mixing matrix element, $<3d\,|H|\,4s>$, only weakly. However, when $\mathbf{k}$ is varied such that the $4s$ and $3d$ states are nearly degenerate (i.e. $\mathbf{k}$ for which $<4s\,|H|\,4s> \simeq <3d\,|H|\,3d>$) the mixing term takes on a greater significance in the discriminant and serves to "repel"* the two states in energy. The lower energy of the occupied $3d\uparrow$ state is hence reduced further, and that of the $4s\uparrow$ state is increased. In iron metal we expect a complementary sort of interaction between an occupied $4s\downarrow$ state and an unoccupied higher energy $3d\downarrow$ state.

* A similar "repulsion" of states is also responsible for the energy band gap of nearly free electrons in a periodic potential. The simple $e^{ikr}$ form of the free electron wavefunctions allows the perturbation to take the very simple form of $V_G$, which is a Fourier coefficient of the periodic potential.

Here, the $4s\downarrow$ energy will be reduced and the $3d\downarrow$ energy will be increased. Additionally, because the energy bands of iron are unfilled, the Fermi level runs through both $3d\uparrow$ and $3d\downarrow$ bands, so the lowering of an occupied $4s\uparrow$ level and the raising of a $4s\downarrow$ level will be important as well. Nevertheless, since there are more occupied $3d\uparrow$ states than $3d\downarrow$ states, the net effect is a raising of the $4s\downarrow$ energies near the Fermi level with respect to the $4s\uparrow$ energies. The $4s$ band is therefore negatively polarized by hybridization in the vicinity of both the solute atom and the iron atom which it replaces. Since the iron atom usually has a larger $3d\uparrow$ moment than the solute atom, we expect that $4s$ hybridization will cause a positive $\Delta H$ (decreased sextet splitting) for $^{57}$Fe nuclei sufficiently close to the solute atom. As described below, this $\Delta H$ changes sign for more distant neighbors. Competing effects in the population of the $4s\downarrow$ states and depopulation of the $4s\uparrow$ states make $\Delta i$ more difficult to determine than $\Delta H$.

Schemes which incorporate the hybridization energy, $J'$, into the exchange energy, $J$, in equation V-22 have been suggested [170,183], but major differences exist between $J$ and $J'$. At the vector $\mathbf{k}$ where the unhybridized $3d$ and $4s$ states are degenerate, the hybridized conduction electron wavefunction becomes:

$$|hyb>\beta = |4s>\beta \pm |3d>\beta, \qquad \text{V-53}$$

but at $\mathbf{k}$ vectors removed from those producing the degeneracy, the hybridized wavefunction is approximately:

$$|hyb>\beta = |4s>\beta + \frac{<4s|h|3d>}{<4s|H|4s> - <3d|H|3d>}|3d>\beta. \qquad \text{V-54}$$

This mixing can be very anisotropic. When the plane wave used in the construction of the $(4s)$ conduction electron wavefunction is expanded:

$$e^{i\mathbf{kr}} = 4\pi \sum_{lm} i^l \, j_l\,(kr)\; Y_l^m\,(\vartheta,\varphi)\, Y_l^{-m}(\vartheta,\varphi) \qquad \text{V-55}$$

(here $\vartheta,\varphi$ are angles with respect to the $z$-direction of the $3d$ wavefunction), the matrix element $<4s|h|3d>$ which involves the $3d$ wavefunction:

$$\psi^{3d} = R_{3,l}(r)\,Y_2^{m'}(\vartheta,\varphi),$$

is expected to be largest when $l' = 2$ and $m = m'$ because of the orthogonality of spherical harmonics. Watson extracts the angular dependence of this matrix element from the radial dependence in a spin-orbit coupling scheme (more appropriate for rare earth ions). The effective exchange energy due to inter-band mixing becomes:

$$\langle 4s\,|\,\mathrm{h}\,|\,3d\rangle = J'(\mathbf{k},\mathbf{k}') \simeq P_2(\cos\vartheta)\Omega(k,k'). \qquad \text{V-56}$$

$J'(\mathbf{k},\mathbf{k}')$ shows the anisotropy of the localized $3d$ wavefunction through the Legendre polynomial. $\Omega(k,k')$ depends only on the magnitude of $\mathbf{k}$ and $\mathbf{k}'$. To illustrate such anisotropy we note that the mixing of a $3d_{z^2}\uparrow$ wavefunction with a plane wave whose $\mathbf{k}$ is in the x-y plane will be zero by symmetry, whereas if the $\mathbf{k}$ lies along the z-axis the fraction of polarized $3d\uparrow$ character of the conduction electron near the solute atom may be comparable to the amount of $4s$ character.

Watson's [169-171] Hartree-Fock estimates of $J'(\mathbf{k},\mathbf{k}')$ for iron atoms in iron metal indicate that it is of the same magnitude as $J(\mathbf{k},\mathbf{k}')$ of equation V-22. He finds that along appropriate directions, $J'(\mathbf{k},\mathbf{k}')$ contributes a negative spin polarization to the $4s$ electrons at 1n.n. distances from the solute atom. A weak oscillatory behavior is predicted at greater distances; the first node occurs at about the 3n.n. position.

**I. Coulomb Correlation Corrections.**

Exchange effects in Hartree-Fock calculations acknowledge some electron-electron interactions through the antisymmetrization of their multi-electron wavefunctions. However, there are further correlations, due to Coulomb repulsions, between the positions of electrons of both parallel and antiparallel spins. The uniform charge densities of our free electron wavefunctions:

$$\rho^C(\mathbf{r}) = e\,\psi^*(\mathbf{r},t)\psi(\mathbf{r},t) = e\,\frac{e^{-i\mathbf{kr}-i\frac{E_k}{\hbar t}}}{\sqrt{V}} \times \frac{e^{+i\mathbf{kr}+i\frac{E_k}{\hbar t}}}{\sqrt{V}} = \frac{e}{V}$$

do not allow for any such correlations. Modern formalisms for transcending a model of a single electron moving in an average potential of the other electrons make use of quantum field theory. Methods of quantum field theory calculations are largely mysterious to this author, and most such calculations have been performed for only very simple models of multi-electron systems [173-176,184-186]. Nevertheless, important insights into the possible errors associated with Hartree-Fock calculations can be gleaned by examining the results of these calculations.

In 1957 Gell-Mann and Brueckner [187] calculated an improved energy for a high density free electron gas with a spherical Fermi surface:

$$\frac{E}{N} = \frac{2.21}{\left(\frac{r_s}{a_0}\right)^2} - \frac{0.916}{\left(\frac{r_s}{a_0}\right)} + 0.0622\,ln\left(\frac{r_s}{a_0}\right) - 0.096\,, \qquad \text{V-57}$$

where $\frac{E}{N}$ is the average energy per electron in Rydbergs. $\frac{r_s}{a_0}$ is a convenient measure of electron volume (density$^{-1}$). The first term is the familiar kinetic energy term, and the second term arises from exchange effects as calculated in Hartree-Fock theory. The next two new terms are the leading terms in the correlation energy correction. For iron metal, by substitution of $\frac{r_s}{a_0} = 2$:

$$E/N = +.553 - .458 + .043 - .096.$$

The correlation corrections may appear to be small, but since $\frac{r_s}{a_0}$ is not small the expansion of equation V-57 is not quantitatively helpful. However, these terms suggest that correlation effects on conduction electron redistributions in iron metal should not be ignored. In particular, recent workers [185,188,189] have argued that although the exchange interaction alone would make a simple free electron gas ferromagnetic at electron volumes $\frac{r_s}{a_0} > 1.5$, the inclusion of

correlation effects forbids ferromagnetism at any electron density.

Very large fluctuations in free electron spin density around a localized spin were predicted in a Hartree-Fock formalism [190], but the inclusion of electron-electron Coulomb correlation effects served to drastically reduce the magnitude of these R.K.K.Y.-like oscillations [188]. Kim and Schwartz [173-176] calculated spin and charge susceptibilities for a free electron gas, and considered the spin polarization around a localized charge perturbation. They derived a remarkable result which showed that a magnetic moment of much greater than $1\mu_B$ can be developed in the electrons screening a local charge of $1e$. Gunnarson and Lundqvist [185] argued that the treatment of correlation effects by Kim and Schwartz was incomplete, and that "negative screening" (electrons of -spin avoiding a positive charge perturbation) does not occur at any magnetization of an electron gas. They further argued that in predictions of many electronic properties which depend on spin polarization, theories which include exchange effects but ignore correlation effects fare more poorly than independent electron theories which ignore both exchange and correlation effects.

Coulomb correlations will reduce the magnitude of all spin polarization effects predicted by any Hartree-Fock theory that includes exchange interactions as the only electron-electron interaction. This is because Coulomb correlations already keep the electrons of both spins separated, so exchange effects between electrons of like spin will be less effective. The magnitude of $H_{CORE}$, $H_{COND}^{R.K.K.Y.}$, $H_{OV}$, $H_{COV}$, and $H_{HYB}$ will all be reduced for this reason. No qualitative changes are expected in the spin-polarization effects described in this chapter, but quantitative results will be unreliable. In Chapter VI we sketch some theories which explain in fundamental detail the hyperfine magnetic field perturbations at $^{57}$Fe nuclei near solute atoms in Fe-X alloys. Their incomplete

treatment of electron-electron interactions makes dubious their claims to quantitative truth.

# CHAPTER VI.

## MODELS AND CALCULATIONS OF $\{\Delta H_i^X\}$ AND $\{\Delta i_i^X\}$ IN Fe-X AND Fe-Ni-X ALLOYS

First, this chapter presents an incomplete review of the many models offered to explain the perturbed $^{57}$Fe hyperfine fields which are observed when there are dilute concentrations of solutes in iron metal. Models for each class of solute atom use one or more of the mechanisms described in Chapter V together with some (occasionally speculative) features of the electronic structure of iron metal and the solute atoms. Our immediate concern is with models of hyperfine magnetic fields at $^{57}$Fe nuclei, but many tests of these models can be performed by studying the hyperfine magnetic fields at the *solute* nuclei themselves. A large body of important literature [191-200,216] has developed which is concerned with the hyperfine magnetic fields at solute nuclei in ferromagnetic alloys. However, in this chapter hyperfine fields at solute nuclei will be mentioned only occasionally.

I perceive that a consensus has been reached by experimentalists concerning the systematics of $^{57}$Fe hyperfine magnetic fields in some Fe-X alloys (including X=Cr and X=Si). These systematics were successfully explained in the 1970's by a model which invokes linear responses of hyperfine magnetic fields to the individual magnetic moments in the alloy. This consensus does not extend fully to the fundamental electronic mechanisms behind the model. The present chapter tends to avoid arguments regarding the mechanism(s) behind the model. Instead, it presents a unified picture of how the phenomenological linear hyperfine magnetic field perturbation model of Chapter IV relates to the less phenomenological model of linear response of hyperfine magnetic fields to magnetic moments. Then this linear response model is developed for our Fe-Ni-X ternary alloys in section VI.E.

The main thrust of this chapter is concerned with how the sets $\{\Delta H_j^X\}$ and $\{\Delta i_j^X\}$ for a $^{57}$Fe nucleus near an X atom are expected to change when the host metal is no longer pure Fe, but is instead a Fe-Ni alloy. The linear response model developed in this chapter requires sets of parameters, $\{g\}$, which characterize the change of magnetic moments at an atom due to its neighbors. Fortunately, the most important of these $g$ parameters are known from previous Mössbauer, NMR, and neutron diffraction work. Unfortunately, some of these $g$ parameters have not been measured, and this chapter discusses how variations in these parameters will affect $^{57}$Fe hyperfine magnetic field perturbations through the model of linear response. Actual estimates of these magnetic moment perturbations and the sets $\{g\}$ are discussed in Chapter X. The linear response model also employs a set of parameters, $\{f\}$, to quantify the response of a $^{57}$Fe hyperfine magnetic field to magnetic moments at different nearest neighbor sites. In this chapter the set $\{f\}$ is assumed constant. This assumption is discussed further in section X.A.3. in the light of the electronic mechanisms of section V.E., and is shown to be reasonable even when Ni is added to the host metal. Finally, I use the linear response model to predict that there will be no significant difference in the intensity of the "X satellites" extracted from Mössbauer spectra of Fe-X and Fe-Ni-X alloys with the same dilute X concentration when X=Cr and X=Si. However, the change in "Mn satellite" intensity when the host metal has a Ni concentration somewhere between 3% and 6% implies an important change in some of the $g$ parameters. This effect is discussed further in Chapter X.

**A. Early Models.**

In the late 1950's, Friedel [158,160] and coworkers [161,162] successfully explained the low temperature electrical resistivities of Cu and Ag alloyed with a series of $p$ elements. The scattering theory formalism of section V.E.2. was

used to predict a matrix element for the scattering of conduction electrons which is proportional to $\Delta Z$ *, and thus an electrical resistivity proportional to $(\Delta Z)^2$. The resistivity, $\rho$, is expressed in terms of differences in phase shifts of the scattered partial waves at $k_F$:

$$\rho \propto \sum_{l=0}^{\infty} (l+1) sin^2(\eta_l(k_F) - \eta_{l+1}(k_F)) \ , \qquad \text{VI-1}$$

subject to the Friedel sum rule:

$$\Delta Z = \frac{2}{\pi} \sum_{l=0}^{\infty} (2l+1)\eta_l(k_F) \ . \qquad \text{VI-2}$$

The set of phase shifts is now uniquely determined by the form of the scattering potential. However, the resistivities depend only on the total amount of scattering, and they do not differ significantly when they are calculated with different sets of phase shifts obtained from different forms of the scattering potential, such as a square well potential, or a screened Coulomb potential. Consequently, Friedel theory has much success in predicting residual resistivities, but unfortunately the shape of the conduction electron redistribution depends strongly on the choice of phase shifts, especially in the important region near the solute atom. This has proved to be a tricky problem in applying Friedel theory to problems of conduction electron redistributions around solute atoms in alloys of $3d$ transition metals [163]. Charge perturbation models employing Friedel theory have been less quantitative, and more phenomenological, than one might hope.

The first charge perturbation model is due to Daniel and Friedel [201,202]. A nonmagnetic solute atom was described as a three-dimensional square well of equal width and depth for electrons of each spin. However, beyond the edge of the solute atom the +spin potential lies below that of the -spin potential, and this produces a uniform conduction electron polarization. The difference

* Here $\Delta Z$ is the separation of the impurity element from Cu in columns of the periodic table.

between these potentials away from the square well and the potential at the bottom of the square well is different for electrons of each spin. This results in a difference in the scattering of +spin and -spin electrons by the solute atom, and a spin polarization at the solute atom.

Blandin [203] considered the complementary problem of a spin polarized transition metal solute atom with S unpaired spins in a noble metal. He offered a second sum rule:

$$\Delta S = \frac{1}{\pi}\sum_{l=0}^{\infty}(2l+1)(\eta^{+}-\eta^{-}) , \qquad \text{VI-3}$$

together with the Friedel sum rule:

$$\Delta Z = \frac{1}{\pi}\sum_{l=0}^{\infty}(2l+1)(\eta^{+}+\eta^{-}) , \qquad \text{VI-4}$$

where the +spin and -spin phase shifts, $\eta^{+}$ and $\eta^{-}$, are taken at the Fermi wavevector. However, we know from section V.E.4. that unless the conduction electron mixing by the spin perturbation is comparable to the conduction electron mixing due to the Coulomb perturbation, equation VI-3 is too strong a condition. A similar condition on the phase shifts was also offered by Caroli and Blandin [204] to explain hyperfine magnetic fields at Mn nuclei in ferromagnetic Heusler alloys. Later theories [112] avoid this problem by using square wells of depth $V^{\pm} = V_C \pm J$ for electrons of each spin. ($V_C$ is a Coulomb potential, and $J$ is an exchange potential.)

Caroli and Blandin [204], I. A. Campbell [202], and later Jena and Geldhart [205,206] offered other models which used mechanisms of $H_{HYB}$ to explain hyperfine magnetic field perturbations around solute atoms in ferromagnetic alloys. They explained nearest neighbor effects as arising from a polarization of 4*s* conduction electrons due to the presence or absence of hybridization with localized 3*d* electrons at the solute atom. This mechanism results in a negative 4*s* electron polarization, and was argued to bring charge perturbation models

in better agreement with experiment.

Blandin and Campbell [207] developed an interesting model that only accounts for hyperfine magnetic fields at solute nuclei. Their model combines a charge perturbation at the solute atom with a spin-dependent exchange interaction at a shell of nearest neighbor atoms. This model, a unique combination of R.K.K.Y. and Friedel ideas, predicts a spin density at the solute nucleus which goes as:

$$\rho^s(solute) \propto \sum_{r_n} \frac{JN_n \cos(2k_F r_n + 2\delta_o)}{r_n^3} . \qquad \text{VI-5}$$

Each term in equation VI-5 resembles the R.K.K.Y. spin density due to a shell of spin perturbations at $r_n$ ($r_n$ is the distance of each nearest neighbor shell from the solute nucleus). There are $N_n$ sites in each shell, and the sum includes all nearest neighbor distances. The phase shift, $\delta_0$, is determined with the Friedel sum rule for $l = 0$ scattering (c.f. isomer shift section; $l > 0$ scattering cannot affect the spin density at the solute nucleus). Equation VI-5 was developed for ordered Heusler alloys, but has been applied to estimates of hyperfine magnetic fields at solute nuclei in iron metal [178,207].

Grüner, Vincze, and Cser [112] considered the problem described in section V.E.1. where a spin redistribution is developed by spin-polarized conduction electrons when they screen a pure charge perturbation. Although they approached this problem with Friedel's scattering formalism, their result for small conduction electron polarizations, $p$, is:

$$\rho^s(r) \propto \frac{p \sin(2k_F r + \delta)}{r^2} , \qquad \text{VI-6}$$

which is very similar to equations V-30 and V-38 which were obtained by a straightforward perturbation theory approach.

The conduction electron redistributions predicted by all of the charge perturbation models sketched so far are capable of predicting large hyperfine

magnetic fields at solute nuclei, and significant hyperfine magnetic field perturbations at $^{57}Fe$ nuclei near solute atoms. Therefore, they cannot be ignored. Stearns [207-209] and others [210] have criticized these models as being unrealistic and incapable of predicting experimental trends with quantitative and often even qualitative accuracy. This should come as no surprise because a square well potential is clearly an unrealistic way to depict a solute atom, and the phase shifts which result from it will produce an unrealistic electron redistribution near the solute atom.

Experimentally it is observed [211] that the hyperfine magnetic field at a solute nucleus in a series of *sp* solute atoms of increasing valence in iron will change sign, usually when $\Delta Z = 2$ or 3. The preceding models that were sketched are all capable of explaining this observation. Consider iron metal* alloyed with solutes that lie increasingly to the left of iron on the periodic table. We start with $\Delta Z = 0$ (for iron in iron). As $\Delta Z$ becomes more negative, the solute provides a weaker nuclear attraction, and this causes an increase in energy of a local $3d$ bound state at the solute atom. Interesting effects occur when one of these local† levels rises above the Fermi energy at some $\Delta Z'$, and then loses its electrons. The conduction electron redistribution around the solute atom comes from the mixing of unoccupied conduction electron states with this occupied local level, so the conduction electron redistribution will be affected very strongly at this $\Delta Z'$. All conduction electron redistribution effects involving the local solute level will disappear as $\Delta Z$ becomes negative enough so that significant energy separates the local level from the Fermi energy. This pushing of a local level through the Fermi energy is how the various charge perturbation models predict a sign reversal for the hyperfine magnetic field at solute nuclei. Prediction of the $\Delta Z$ at which the sign reversal occurs seems an

* A Ni host may give more convincing results because of its filled +spin band.
† However, the level is hybridized to some extent with the iron $3d$ and $4s$ bands.

appropriate goal for a simple model.

Campbell suggests [202,286] that the temperature dependence of hyperfine magnetic fields in Fe-Mn alloys is explained by a bound $3d\uparrow$ state at the Mn atom that rises through the Fermi level. Campbell assumes that the $3d\uparrow$ level at the Mn atom has a well-defined energy so that it has a large density of states just below the Fermi level. The Mn $3d\downarrow$ level is assumed to lie above the Fermi energy so that it is unoccupied and the Mn atom has a positive magnetic moment. In this situation a small decrease in the Fermi energy can have a big effect on the magnetic moment at the Mn atom. This big effect is supplied by thermal smearing of the Fermi energy, which causes Mn atoms to lose $3d\uparrow$ electrons. The magnetic moment at the Mn atom therefore drops rapidly with temperature. This magnetic moment change could be reflected in the hyperfine magnetic field at a neighboring $^{57}$Fe nucleus through an electronic mechanism which is sensitive to the change in Mn magnetic moment, or is sensitive to the reduction of $3d$ charge at the Mn atom. We expect that a similar sort of Mn magnetic moment change could be caused by alloying the Fe host with Ni. This is discussed further in section X.A.1.

Stearns [207] offers another criticism of charge perturbation models in pointing out that hyperfine magnetic fields at $^{57}$Fe nuclei, and at solute nuclei, do not depend strongly on $\Delta Z$ for some series of solute atoms -- most early charge perturbation models predict a strong $\Delta Z$ dependence. Stearns' explanation of this discrepancy involves the concept of $\varphi_{Z_{eff}}$ in section V.E.4. Solute atoms tend to retain some of their valence electrons when dissolved in iron metal. Consequently, $Z_{eff}$ will not necessarily be either equal to $\Delta Z$, or even proportional to $\Delta Z$. Instead, $Z_{eff}$ will depend on charge transfer effects involving the solute atom valence electrons and the $3d$ or $4s$ electrons of iron metal.

Even the relatively simple $^{57}$Fe hyperfine magnetic field perturbations

around Si atoms require a more detailed treatment than can be provided by a simple charge screening model involving only one type of conduction electron mechanism. Vincze and Aldred [107] and others [109,112,212] offer a charge perturbation model for *sp* series solutes in iron metal which originated with Mott [213] and Marshall. I first summarize how their picture of electronic effects explains the neutron diffraction observations [214] that Si atoms develop no magnetic moment in iron metal, and cause no perturbation of the magnetic moments at nearby Fe atoms. Vincze and Aldred propose that the 3*s* states of Si are free atom-like, and lie well below the Fermi energy of iron metal. These Si 3*s* electron states are localized, occupied, and therefore have no effect on the iron 3*d* or 4*s* electrons. The 3*p* levels of Si, however, become part of the iron 4*s* band (in the same hybridizing way that the iron 4*s* atomic states become a 4*s* band). If some Si 3*p* electrons are donated to the 4*s* band, a charge perturbation would remain at the Si site, but the iron 4*s* electrons would be able to efficiently screen this charge perturbation. In the simplest model there is no such screening effect involving the 3*d* band, but it is necessary to consider how the 4*s* band may shift in energy relative to the 3*d* band. Such a shift may result in electrons transferring between the 4*s* and 3*d* bands, thus complicating the problem by causing a change in occupancy of the 3*d* electron states. However, a theorem proved by Friedel [215] shows that the 3*p* electrons added to the 4*s* band will increase the Fermi level with respect to the bottom of the band, but the negative energy of screening the charge perturbation will serve to translate the entire 4*s* band to lower energy. The result is that the Fermi energy of the 4*s* band does not shift with respect to the Fermi energy of the 3*d* band, and 3*d* occupation is unaffected.

The major result of this model is that the screening of the Si excess charge causes no changes in the iron 3*d* electrons. Therefore there is no change of

the iron magnetic moments, and no change in the core polarization contribution to hyperfine magnetic fields at $^{57}$Fe nuclei which neighbor Si atoms. Furthermore, the $^{57}$Fe hyperfine magnetic field cannot be affected through electronic changes that might otherwise occur at neighboring Fe atoms which are themselves near Si atoms. The electronic mechanisms responsible for $\Delta H_i^{Si}$ can, however, involve electronic changes that are associated with the 4*s* electron redistribution near the Si atom when the Si atom replaces a Fe atom.

Vincze and Aldred [107] have obtained experimental evidence for the importance of charge screening in intra-series effects for *sp*-series solutes in iron metal. As $\Delta Z$ increases, for instance in going from Al ($s^2p^1$) to Si ($s^2p^2$) in iron, the charge perturbation at the solute atom becomes larger. Local isomer shifts indicate that the iron 4*s* electrons are screening a $\Delta Z_{eff}$ which is about twice as positive for Si than for Al. Vincze and Aldred observe that other series of *sp* solutes cause localized $^{57}$Fe isomer shifts that are linear in $\Delta Z$. It therefore seems possible that the screening charge density around these solute atoms is linear in $\Delta Z$. However, $\Delta H_1^{Si}$ is only about 15% larger than $\Delta H_1^{Al}$, and for other *sp* solutes only a small $\Delta H^{sp_1}$ contribution is linear in $\Delta Z$. It seems unlikely that charge screening of a $\Delta Z$ is directly responsible for most of the contribution to $\Delta H^{Si_1}$.

Instead, $\Delta\rho^S(r)$, which is caused by the change in spin density around a nearest neighbor site when the unpaired Fe $3d\uparrow$ electrons are replaced with paired electrons of a Si ion, is primarily responsible for $\Delta H^{Si_1}$. This contribution, arising from a "magnetic hole" at the solute site, is the same for all *sp* series solutes in iron. Stearns [216,221] argues that changes in hyperfine magnetic field perturbation mechanisms involving hybridization of conduction electrons will also affect the 4*s* conduction electron distribution around the solute atom, in addition to the changes in mechanisms involving the larger exchange

mixing. She argues that the first node of the conduction electron redistribution around the solute atom occurs within the 1n.n. distance, and this explains why $\Delta H_1^{Si}$ is positive. Systematics of hyperfine magnetic field perturbations for 3*d* solutes in iron metal (as described in section VI.B) also indicate that $\Delta\rho^S(r)$ is the major cause of $\Delta H_j^X$ ; these systematics show good correlation between magnetic moments and hyperfine magnetic field perturbations. Vincze and Aldred further argue [107] that in the case of unpolarized Ge or Sn solutes, their atomic $4s^2$ and $5s^2$ levels may lie at higher energy than the Si $3s^2$ levels, and therefore may hybridize with the 3*d* levels of iron. A change in the magnetic moments of iron atoms neighboring Ge or Sn atoms is thus expected, resulting in an observed positive contribution to $\Delta H_1^{Ge}$ and $\Delta H_1^{Sn}$ because of decreased core polarization. Such inter-series effects are observed. However, they amount to only about 15% of $\Delta H_1$, and this again implies that the predominant contribution to $\Delta H_1$ comes from the spin redistributions, $\Delta\rho^S(R)$, around a magnetic hole.

When are other mechanisms of hyperfine magnetic field perturbations, $H_{OV}$ and $H_{COV}$, important? $H_{OV}$ (and $H_{COV}$) depends on the overlap of the solute atom and its 1n.n. iron atoms. Shirley [192], and later Stearns [198,209,216] have phenomenologically treated these mechanisms in a "volume misfit" model. They pointed out similarities in periodic trends of hyperfine magnetic fields at *solute nuclei* and the atomic volume difference between the solute atom and an iron atom. A protracted (~ 10 years) controversy [208,209,172] indicates that it is still unclear whether hyperfine magnetic fields at solute nuclei can be explained by conduction electron effects alone, as suggested by the Vincze and Aldred evidence [107] of a $\Delta Z$ dependence of $\Delta H_1^{sp}$, or whether a "volume misfit" model explains the experimental data better.

There is a good counter-example to a volume misfit model for hyperfine

magnetic field perturbations at $^{57}$Fe nuclei neighboring solute atoms. In the case of Sb and Sn in iron metal, $\Delta H_1^{Sb}$ equals $\Delta H_1^{Sn}$ (+22 kG) and $\Delta i_1^{Sb}$ equals $\Delta i_1^{Sn}$ (+0.06 mm/sec), to the limits of experimental accuracy [107]. However, the atomic volume misfit of Sb in an Fe lattice is 25% larger than that of Sn. This insensitivity of $\Delta H_1$ and $\Delta i_1$ to volume misfit either implies that volume misfit is only of minor importance, or it implies that volume misfit is too crude a parameterization for $H_{COV}$ or $H_{OV}$.

Fortunately, the controversy regarding a "volume misfit" term need not concern us. For the solute atoms Ni, Cr, Mn, and Si, the volume misfit contribution to the neighboring $^{57}$Fe hyperfine magnetic fields is negligible because: 1) these four solute atoms have nearly the same atomic volume as iron, and 2) the overlap due to each solute atom is shared by its eight iron neighbors; therefore, the "volume misfit" contribution is about a factor of 8 less significant than it would be for the hyperfine magnetic field at the solute nucleus itself. Furthermore, our interest in the origin of hyperfine magnetic fields arises from the need to understand possible changes in $\{\Delta H_i^X\}$ and $\{\Delta i_i^X\}$ for Fe-Ni hosts. We therefore can ignore changes in any volume misfit contribution because: 3) the volume misfit contribution involves only the solute atom and its neighboring $^{57}$Fe atom, and is not expected to be significantly affected by the presence Ni.

**B. Linear Response of Hyperfine Magnetic Fields to Magnetic Moments.**

From many workers starting with Shirley et al. [191], there has evolved [217,218,41,113,127,219,220] a particularly successful model of hyperfine magnetic field perturbations at a $^{57}$Fe nucleus neighboring a 3*d* transition metal solute atom. Although different authors may justify the model with different electronic mechanisms, I find it most useful merely as a semi-phenomenological model. In this semi-phenomenological model, the hyperfine magnetic field at a $^{57}$Fe nucleus is a sum of contributions, where each contribution is linearly

related to the magnetic moment of each atom in an Fe-X alloy. For convenience, we express the hyperfine magnetic field at a $^{57}$Fe nucleus as a sum of two lumped terms, one arising from the magnetic moment of the atomic electrons at the $^{57}$Fe site itself, and a second term due to the conduction electron response to the magnetic moment at each neighboring site. This second term depends strongly on the concentration of the X element, $c_X$. We expect that the hyperfine magnetic field at a $^{57}$Fe nucleus situated at $\mathbf{r}$ is coupled to its own magnetic electrons by core polarization (through $\alpha_{CP}$), and is coupled to the magnetic moments around it by the conduction electrons (through $\alpha_{CEP}$) [41]:

$$H_{Fe}(\mathbf{r}) = \alpha_{CP}\mu_{Fe}(\mathbf{r}) + \alpha_{CEP}\sum_{\mathbf{r}'} \mu(\mathbf{r}')f(\mathbf{r}' - \mathbf{r}) . \qquad \text{VI-7}$$

Unquenched orbital angular momentum will detract somewhat from the core polarization contribution in the first term of equation V-7. Conduction electron polarization is responsible for the second term through $H_{COND}$ and $H_{HYB}$. As suggested in section VI.A., the mechanisms of $H_{OV}$ and $H_{COV}$ may make only small contributions to hyperfine magnetic field perturbations at 1n.n. sites (and thereby may only slightly modify $f(r_{1.n.n.})$. Equation V-7 is useful so long as the $3d$ electrons responsible for core polarization are localized enough* to predominately affect the core polarization at only their own atom.

Perhaps the function $f(\mathbf{r}' - \mathbf{r})$ looks something like:

$$f(0) \text{ is a finite constant}$$

$$f(r' - r) \propto \frac{\sin(2k_f|r' - r| + \delta)}{|r' - r|^3} \quad \text{for} \quad r \neq r'.$$

Stearns [219,220] has developed a detailed model for dilute Fe-X alloys which explicitly considers changes in the magnetic moments of all iron atoms (all

* In fact, Stearns [221] parameterized the degree of itinerancy of the $3d$ electrons in an equation similar to equation V.7. Her analysis of the concentration dependence of hyperfine magnetic fields in Fe-Si alloys led her to conclude that the $3d$ electrons are $\approx$5% itinerant. However, she retracted this conclusion later [220] after developing new ideas for the spin polarization distributions of itinerant $3d$ wavefunctions.

$\mu_{Fe}(\mathbf{r}')$) due to the solute atom at $\mathbf{r}_s$. In her model (where we designate $|\mathbf{r}'|$ by $r_{jn.n.}$, and will later sum over sites in each jn.n. shell):

$$\mu_{Fe}(0)f(0) \equiv \frac{H'_S}{\alpha'_{CEP}} \quad \text{is a finite constant}$$

As explained in section X.A.1., Stearns used $\Delta H_i^{Si}$ to calibrate the set $\{ f(\mathbf{r}-\mathbf{r}')\}$ because a Si atom causes no magnetic moment perturbations at surrounding $^{57}$Fe atoms.

$$\alpha'_{CEP}\mu_X(\mathbf{r}_S)f(r_s) = \frac{\mu_X}{\mu_{Fe}^0}\Delta H_i^{Si}, \qquad \text{VI-8b}$$

where the solute is in the $i$n.n. shell. Specifically, Stearns used:

$$\alpha'_{CEP}\mu_{Fe}(r_{jn.n.})f(r_{jn.n.}) = -\left[1 + M\left(\frac{r_{1n.n.}}{|\mathbf{r}_S - \mathbf{r}_{jn.n.}|}\right)^m\right]\Delta H_j^{Si} \qquad \text{VI-8c}$$

The $^{57}$Fe nucleus is now at the origin ($\mathbf{r}$=0). The constants $m$ and $M$, which parameterize the magnetic moment perturbations, were determined by fitting NMR data to computed spectra; best fits were obtained for $m$=3, and $M$ depending on the specific solute atom [219].

We treat non-dilute alloys by assuming an additivity of magnetic moment perturbations; the total magnetic moment perturbation at a site due to several nearby solute atoms equals the sum of the magnetic moment perturbations that would arise from each individual solute atom. For notational convenience and generality we rewrite the perturbed magnetic moment of equation VI-8c:

$$\mu_{Fe}(r_{jn.n.}) = \mu_{Fe}^0 + yg_X^{Fe}(r_1) + zg_X^{Fe}(r_2) + \cdots \qquad \text{VI-9}$$

Here there are y solute atoms of type X in the 1n.n. shell of an Fe atom located in the jn.n. shell of the $^{57}$Fe nucleus. This Fe atom also experiences magnetic moment perturbations (of strength $g_X^{Fe}(r_2)$) from z solute atoms in its 2n.n. shell. An expression similar to equation VI-9 is also necessary for specifying the magnetic moment at the solute atom situated in the jn.n. shell of the $^{57}$Fe nucleus; we use a set of parameters $\{g_X^X(r_i)\}$ for the solute atom.

Vincze and Campbell [41,113] find a simple expression for a lattice averaged hyperfine magnetic field which includes the hyperfine magnetic field at the solute nucleus. The concentration dependence of this average is [41]:

$$\frac{d}{dc}\langle H_{Fe+X}\rangle = \frac{150kG}{\mu_B}\left(\frac{d}{dc}\langle\mu\rangle + \mu_{Fe} - \mu_X\right) + \frac{80kG}{\mu_B}(\mu_X - \mu_{Fe}) , \qquad \text{VI-10}$$

where $\langle\mu\rangle$ is the average magnetic moment of the alloy, and the constants were determined from measured hyperfine fields in dilute Fe-Cu solutions. Using equation VI-10, Vincze and Campbell have had excellent success in predicting $\frac{d}{dc}\langle H_{Fe+X}\rangle$ for different $3d$ solutes in iron, given only a knowledge of magnetic moments. They even suggest that this linear response model works so well that data of hyperfine magnetic fields and average magnetizations can be used to determine magnetic moments of solute atoms.

Vincze and Campbell [41] observed that $\langle\mu_{Fe}\rangle$ and $\langle i_{Fe}\rangle$ both increase in the positive direction as the solutes go from left to right across the $3d$ series. They suggest that charge screening effects involving $3d\uparrow$ electrons will explain this trend. In their suggestion, solutes such as Cr and Mn offer repulsive $3d\uparrow$ potentials, so that there is a depletion of $3d\uparrow$ electrons at the Cr and Mn sites, as well as at Fe sites near these solute atoms. Likewise, they suggest that Ni atoms attract $3d\uparrow$ electrons around themselves. The $3d\downarrow$ electrons are assumed to be unimportant because they have a lower density of states at the Fermi surface, and Vincze and Campbell suggest that their Fermi wavevectors are too large. These simple ideas cannot provide a detailed picture of magnetic moments at solute atoms and their Fe neighbors. However, they can account for a lattice averaged sign of $\{g(r_j)\}$. Vincze and Campbell do not describe a detailed mechanism for the origin of the parameters $\{f(r_j)\}$, but suggest that it involves conduction electron redistributions.

In a series of papers [209,216,219-223], Stearns presents a detailed model

of hyperfine magnetic field perturbations at $^{57}Fe$ nuclei near solute atoms. Neglecting small overlap effects, this model is phenomenologically similar to the model of Vincze and Campbell in its linear response of the $^{57}Fe$ hyperfine magnetic field to the magnetic moments in the alloy (c.f. discussion of equation VI-8). In both models, the function $f(\mathbf{r}-\mathbf{r}')$ of equation VI-7 is primarily due to the response of the $4s$ conduction electrons to the magnetic hole (or partial magnetic hole) at the solute atom site. These mostly unpolarized $4s$ electrons are spin-polarized by exchange and hybridization interactions with unpaired, localized $3d$ electrons, and the substitution of a solute atom for an iron atom usually reduces these interactions. The Stearns, and Vincze and Campbell, models differ in their explanations of the detailed electronic mechanisms responsible for these magnetic moment perturbations, and the resulting hyperfine interactions.

In Stearns' model [220] the magnetic moment perturbations around the solute atom are due to redistributions of $3d_i$ (itinerant $3d$) electrons. The strongly polarized $3d_i$ electrons are affected by the solute atom, resulting in a spin redistribution which perturbs the magnetic moments at nearby atoms. The solute atom affects the $3d_i$ states in its vicinity by raising or lowering their energies, and hence their occupancies and Fermi wavevectors. Stearns argues that the occupancies of the $3d_i$ states in the vicinity of the solute is decreased for solutes increasingly to the right across the $3d$ series; a parabolic $3d_i$ band is assumed to rise in energy. As the Fermi wavevector of the $3d_i$ electrons is decreased, the first node of their spin redistribution around a solute atom increases beyond the $3d$ electrons 1n.n. radius, and the $3d_i$ electrons provide a coupling between the local magnetic moments that changes from antiferromagnetic to ferromagnetic somewhere near Mn in the $3d$ series. In this model, solutes without $d$ electrons will not perturb the magnetic moments in their

vicinity by this mechanism. Some features of these $3d_i$ electrons are unclear. For example, this author is confused by the difference in exchange interactions involving local $3d$ electrons and the $3d_i$ electrons, and the intra-atomic exchange interactions between $3d$ electrons. More importantly, there are very few ($\approx$0.2) $3d_i$ electrons in iron metal, and the number of $3d_i$ electrons around a Ni solute atom in iron is even fewer. If the magnetic moment at neighboring iron atoms is to increase, the redistribution of $3d_i$ electrons around the Ni atom must be large enough to offset the decreased number of $3d_i$ electrons -- a ponderous assumption if several nearest neighbor shells around the Ni atom are involved, and if the $3d_i$ electrons have parabolic bandstructures, as assumed by Stearns.

**C. Linear Response in Binary Alloys.**

The following development of the "model of linear response of hyperfine magnetic fields to magnetic moments" separates the electronic mechanisms of $^{57}$Fe hyperfine magnetic field perturbations as shown in Chart 1*. The goal of this separation is a convenient parameterization of the hyperfine magnetic field perturbations expressed in equation VI-7 in terms of the magnetic moments in the alloy. The local contribution to the $^{57}$Fe hyperfine magnetic field perturbation, $\Delta H_L$, is a consequence of the perturbation of the magnetic moment at the $^{57}$Fe atom itself, $g_X^{Fe}(0)$, caused by a nearby solute stom. This change in the pairing of $3d$ electrons at the $^{57}$Fe atom will affect the spin density at the $^{57}$Fe nucleus by core polarization of the $1s$, $2s$, and $3s$ electrons, as well as by the spin-polarization of the $4s$ wavefunction at the origin.

Especially for dilute alloys, the nonlocal contribution to the $^{57}$Fe hyperfine magnetic field (the $\alpha_{CEP} \sum_{\mathbf{r}' \neq \mathbf{r}} \mu(\mathbf{r}')\, f(\mathbf{r}' - \mathbf{r})$ term of equation VI-7) is conveniently

* Therefore the model should be properly, but awkwardly termed "the model of linear responseS of hyperfine magnetic fields to magnetic moments".

separated into two parts. The first partial nonlocal contribution to the $^{57}$Fe hyperfine magnetic field perturbation, $\Delta H_{DNL}$, comes from the changed magnetic moment at the solute site when a Fe atom is replaced by the solute atom. Note that the magnetic moment of the replaced Fe atom is perturbed by the other solute atoms, but the true magnetic moment change responsible for $\Delta H_{DNL}$ involves replacing an unperturbed Fe magnetic moment with the solute moment. However, our choice of $\Delta H_{DNL}$ permits us to subtract the perturbed Fe magnetic moment in second partial nonlocal contribution, $\Delta H_{INL}$ ($\Delta H_{INL}$ will be most conveniently evaluated by including the perturbed Fe magnetic moment at the solute site). $\Delta H_{INL}$ is the $^{57}$Fe hyperfine magnetic field perturbation which comes from changes in the conduction electron polarization due to the perturbed magnetic moments at all *host atoms* in the alloy except the $^{57}$Fe atom itself.

Chart 1

| | |
|---|---|
| $g_X^{Fe}(r_j) \longrightarrow \mu_{Fe}(r_i) \longrightarrow 4s \longrightarrow \alpha_{CEP} f(r_i) g_X^{Fe}(r_j)$ <br> + *terms for Fe atoms at other* $r_j$ | $\equiv \Delta H_{INL}$ |
| $g_X^X(r_i) \longrightarrow$ <br> $\mu_X(r_i) - \mu_{Fe}(r_i) \rightarrow 4s \rightarrow \alpha_{CEP} f(r_i)[(\mu_X^0 - \mu_{Fe}^0) + (g_X^X(r_j) - g_X^{Fe}(r_j))]$ <br> $g_X^{Fe}(r_i) \longrightarrow$ <br> + *terms for X atoms at other* $r_j$ | $\equiv \Delta H_{DNL}$ |
| $g_X^{Fe}(0) \longrightarrow \mu_{Fe}(0) \longrightarrow 3d \rightarrow \{1s, 2s, 3s\} \rightarrow (\alpha_{CP} + \alpha_{CEP} f(0))\, g_X^{Fe}(r_j)$ <br> $3d \rightarrow 4s \longrightarrow (\alpha_{CP} + \alpha_{CEP} f(0))\, g_X^{Fe}(r_j)$ | $\equiv \Delta H_L$ |

*Assumptions which maintain distinct terms* $H_L$, $H_{DNL}$, and $H_{INL}$ :

1.) $1s$ , $2s$ , $3s$ electrons at the $^{57}$Fe atom (at origin) are spin-polarized by unpaired $3d$ electrons at the $^{57}$Fe atom only.

2.) $3d$ electrons at the $^{57}$Fe atom are well-localized.

3.) The number of unpaired $4s$ electrons is much less than the number of unpaired $3d$ electrons.

For both $\Delta H_{INL}$ and $\Delta H_{DNL}$, the same factors, the $\alpha_{CEP}\, f(r_j)$, are used to parameterize the conduction electron spin-polarization at a jn.n. distance from the magnetic moment. Treating the $\alpha_{CEP}\, f(r_j)$ factors as constants of the host material is perhaps best justified by the phenomenological success of the model of linear response, but the R.K.K.Y. mechanism of $1s$ electron polarization by local $3d$ electrons (see section V.E.2) also suggests that this is reasonable. The set $\{g_j^Z(r_j)\}$ are, of course, specific parameters for Y and Z atoms. The following approach which assumes additivity of these magnetic moment perturbations (as in equation VI-9) is probably risky for many concentrated alloys. Fortunately, in most of this work we are interested in finding the changes in hyperfine magnetic fields due to 1.) slightly non-dilute solute additions, and 2.) small solute concentration changes in non-dilute solutions. Nevertheless, we try to use the assumption of additivity for the $\{g\}$ parameters with caution, as discussed in section X.A.

The present development of the model of linear response approximately includes effects of nonlocal character of $3d$ electrons. Since such electrons will have zero probability density at the $^{57}$Fe nucleus, they can only affect the $^{57}$Fe hyperfine magnetic field through a polarization of the $1s$,$2s$,$3s$ core electrons, or through a polarization of the $4s$ electrons. Since the local $3d$ electrons and nonlocal $3d_i$ electrons have similar wavefunctions near the $^{57}$Fe nucleus, these polarizations are assumed (with some approximation for $3s$ and $4s$ electrons)

to be proportional to the number of unpaired $3d_{\downarrow}$ electrons in the same way as for the local $3d$ electrons. (This simplification is a further reason for working with only the magnetic moments in the alloy, and not the individual electronic wavefunctions themselves.)

We continue with an example which offers some insight into the relationship between $^{57}$Fe hyperfine magnetic field perturbations on the one hand, and solute magnetic moments and host magnetic moment perturbations near the solute atom on the other hand. In a bcc Fe lattice, Mn and Ni magnetic moments are similar, $\sim 1\mu_B$ , and less than the $2.2\mu_B$ Fe moment for which they are substituted. However, the average $^{57}$Fe hyperfine magnetic field perturbation caused by Ni solutes is positive, whereas the average $^{57}$Fe hyperfine magnetic field perturbation caused by Mn is negative. This difference is caused by the large magnetic moment perturbations at Fe atoms near Ni atoms that result in a significant $\Delta H^{M}_{NL}$.

Using neutron diffraction data for magnetic moments [224-229], and Stearns' NMR [220] data for magnetic moment perturbations at the first five Fe neighbors of the solute atom, the two contributions to $\overline{\Delta H^{X}_{NL}}$ for the solutes of interest are listed in Table V, and are now described. Unlike the case for Ni, the substitution of a smaller solute magnetic moment for an Fe magnetic moment results in a $\overline{H_{DNL}}$ that is the dominant hyperfine field effect for Cr and Mn solutes, and especially for a Si solute (since Si causes no magnetic moment perturbations at neighboring Fe atoms).

TABLE V

Some Important Magnetic Moment Combinations for Fe-X Alloys ($\mu_B$)

| Solute | $\mu_X^0 - \mu_{Fe}^0$ | $M(\{g_X^{Fe}(r_j)\})$ |
|---|---|---|
| Ni | -1.1 | +1.8 |
| Cr | -2.9 | +0.52 |
| Mn | -1.2 | -0.44 |
| Si | -2.2 | 0 |

In pure Fe the *local* contribution is:

$$H_L^0 = \left[\alpha_{CP} + \alpha_{CEP} f(0)\right]\mu_{Fe}^0$$

The local contribution at a $^{57}$Fe nucleus in an Fe-X alloy, averaged over all $^{57}$Fe atoms, is:

$$\overline{H_L^X}(c_X) = \left[\alpha_{CP} + \alpha_{CEP} f(0)\right]\overline{\mu_{Fe}}(c_X) \qquad \text{VI-11}$$

Using the result of equation VI-27 for the average Fe magnetic moment:

$$\overline{H_L^X}(c_X) = \left[\alpha_{CP} + \alpha_{CEP} f(0)\right]\left[\mu_{Fe}^0 + c_X M(\{g_X^{Fe}(r_j)\})\right]$$

The change in the average local hyperfine magnetic field contribution when the X concentration is increased from zero to $c_X$ is:

$$\overline{\Delta H_L^X}(c_X) \equiv \overline{H_L^X}(c_X) - H_L^0 = c_X[\alpha_{CP} + \alpha_{CEP} f(0)]\, M(\{g(r_j)\}) \qquad \text{VI-12}$$

Our $^{57}$Fe nucleus at the origin in pure Fe experiences a nonlocal contribution to its hyperfine magnetic field of:

$$H_{NL}^0 = \overline{H_{NL}^0} = \mu_{Fe}^0 \sum_{r>0} f(r)\,. \qquad \text{VI-13}$$

When the Ni concentration is increased from zero to $c_{Ni}$, we expect an average nonlocal contribution to the $^{57}$Fe hyperfine magnetic field of:

$$\overline{H_{NL}^{Ni}}(c_{Ni}) = (1 - c_{Ni})\,\overline{\mu_{Fe}} \sum_{r>0} f(r) + c_{Ni}\overline{\mu_{Ni}} \sum_{r>0} f(r) \qquad \text{VI-14}$$

Conveniently, from neutron diffraction data [224,229] and Table V we know that the Ni magnetic moments are essentially unchanged with Ni concentration (i.e.

$\{g_M^{Ni}(r_j)\} \simeq 0$), so $\overline{\mu_{Ni}} = \mu_{Ni}^{o}$. We substitute $\overline{\mu_{Fe}}$ from equation VI-27 into the first term of equation VI-14, and we take the difference of equation VI-14 and equation VI-13. This difference is the average nonlocal hyperfine magnetic field perturbation caused by increasing the Ni concentration from zero to $c_{Ni}$:

$$\overline{\Delta H_{NL}^{Ni}} = \overline{H_{NL}^{Ni}} - H_{NL}^{\bullet} = c_{Ni}[M(\{g(r_j)\}) + (\mu_{Ni}^{\bullet} - \mu_{Fe}^{\bullet})] \sum_{r>0} f(r) \qquad \text{VI-15}$$

The two terms in the square brackets of equation VI-15 are the average contributions to the nonlocal hyperfine magnetic field perturbation from the Ni enhancement of Fe magnetic moments (indirect nonlocal contribution), and from the substitution of a Ni magnetic moment for an Fe magnetic moment (direct nonlocal contribution). The sum of these two terms should tell us the sign and magnitude of the average nonlocal contribution to the $^{57}$Fe hyperfine magnetic field.

Taking the average local hyperfine magnetic field contribution of equation VI-15 and the average nonlocal contribution of equation VI-15, we can find the average total hyperfine magnetic field change which accompanies the increase of X concentration from zero to $c_X$:

$$\overline{\Delta H^X}(c_X) \equiv \overline{\Delta H_{NL}^X}(c_X) + \overline{\Delta H_L^X}(c_X) \qquad \text{VI-16a}$$

$$\overline{\Delta H^X}(c_X) = c_{Ni}\Big\{[\alpha_{CP} + \alpha_{CEP} f(0) + \alpha_{CEP} \sum_{r>0} f(r)]\, M(\{g_X^{Fe}(r_j)\}) + (\mu_{Ni}^{o} - \mu_{Fe}^{o})\, \alpha_{CEP} \sum_{r>0} f(r)\Big\}$$

As discussed in sections VI.B. and X.A.1., Fe-Si Mössbauer spectra can be analyzed to find:

$$\alpha_{CP} + \alpha_{CEP} f(0) \simeq \frac{-86kG}{\mu_B} \quad \text{and} \quad \sum_r f(r) = \frac{-70kG}{\mu_B}. \qquad \text{VI-16b}$$

Equation VI-16 predicts that the average hyperfine magnetic field perturbation should be proportional to the solute concentration. This is consistent with the additivity assumption of Chapter IV. However, we must beware of the dangers of an implicit approximation we made in equation VI-15 and again when adding

equations VI-15 and VI-15. The assumption that the average indirect nonlocal contribution from the perturbed Fe magnetic moments is proportional to the average perturbed Fe and Ni magnetic moments is exact by itself, but the independence of this average indirect nonlocal contribution from the direct nonlocal contribution and the local contribution is not generally valid for non-dilute alloys.

We now discuss this important, but subtle point. Except for very dilute solutions when the additivity assumption for hyperfine magnetic field perturbations is unnecessary, the phenomenological hyperfine magnetic field perturbation model of Chapter IV is generally inconsistent with strong magnetic moment perturbations around solute atoms. The phenomenological model of Chapter IV is adequate for a hypothetical type of solute atom, and for such a solute atom we now show the formal connection between the phenomenological model of Chapter IV and the less phenomenological model of linear response of hyperfine magnetic fields to magnetic moments. Our hypothetical type of solute atom (of element Hy) is characterized by causing the same magnetic moment perturbations at neighboring solute atoms as it causes at its neighboring Fe atoms:

$$g_{Hy}^{Fe}(r_j) = g_{Hy}^{Hy}(r_j) \text{ for all } j. \qquad \text{VI-17}$$

Consider the effect of one 1n.n. X atom on the hyperfine magnetic field at a $^{57}$Fe nucleus -- at a $^{57}$Fe nucleus we want the difference between the hyperfine magnetic field at a $^{57}$Fe nucleus with only 1n.n. X atom, $H^X(1,0,0...)$, and the hyperfine magnetic field at a $^{57}$Fe nucleus in pure* Fe, $H^X(0,0,0...)$. We use equation VI-7, and explicitly consider the local magnetic moment perturbations around the 1n.n. X atom in the bcc structure, in contrast to our average derivation of equation VI-16. The contribution to the $^{57}$Fe hyperfine magnetic field perturbation from all atoms through its 2n.n. shell is:

* Or, equivalently, at a $^{57}$Fe nucleus with no X neighbors in a dilute Fe-X alloy.

$$\Delta H^X(1,0,0) = H^X(1,0,0) - H^X(0,0,0) = (\alpha_{CP} + \alpha_{CEP} f(0))\,(\mu^0_{Fe} + g^{Fe}_X(1)) \qquad \text{VI-18}$$
$$+ \alpha_{CEP} f(r_1)\Big[\mu^0_X + 3(\mu^0_{Fe} + g^{Fe}_X(2)) + 3(\mu^0_{Fe} + g^{Fe}_X(3)) + \mu^0_{Fe} + g^{Fe}_X(5))\Big]$$
$$+ \alpha_{CEP} f(r_2)\Big[3(\mu^0_{Fe} + g^{Fe}_X(1)) + 3(\mu^0_{Fe} + g^{Fe}_X(4))\Big]$$
$$- \Big[(\alpha_{CP} + \alpha_{CEP} f(0))\mu^0_{Fe} + \alpha_{CEP}(f(r_1)8\mu^0_{Fe} + f(r_2)6\mu^0_{Fe})\Big]$$

$$\Delta H^X(1,0,0) = (\alpha_{CP} + \alpha_{CEP} f(0)) g^{Fe}_X(1) \qquad \text{VI-19}$$
$$+ \alpha_{CEP} f(r_1)\Big[(\mu^0_X - \mu^0_{Fe}) + 3g^{Fe}_X(2) + 3g^{Fe}_X(3) + g^{Fe}_X(5)\Big]$$
$$+ \alpha_{CEP} f(r_2)\Big[3g^{Fe}_X(l) + 3g^{Fe}_X(4)\Big]$$

For comparison, now consider the difference in the hyperfine magnetic field at a $^{57}$Fe nucleus with only two 1n.n. X atoms, $H^X(2,0,0)$, and the hyperfine magnetic field at a $^{57}$Fe nucleus with no neighboring X atoms. We must choose a specific configuration, and we pick a configuration where the two solute atoms are themselves separated by the $r_{2n.n.}$ distance. We find that the contribution to the $^{57}$Fe hyperfine magnetic field perturbation from all atoms through its 2n.n. shell is:

$$\Delta H^X(2,0,0) = 2\Delta H^X(1,0,0) + 2\alpha_{CEP} f(r_1)(g^X_X(2) - g^{Fe}_X(2)) \qquad \text{VI-20}$$

From a comparison of equations VI-19 and -20, we see that the additivity assumption is valid (i.e. $\Delta H^X(2,0,0) = 2\Delta H^X(1,0,0)$) if and only if $g^X_X(r_2) = g^{Fe}_X(r_2)$. In other words, two solute atoms in the jn.n. shell of a $^{57}$Fe nucleus will produce twice the hyperfine magnetic field perturbation as one solute atom in the jn.n. shell if and only if the two solute atoms produce the same magnetic moment perturbation on each other as they would on the Fe atoms which they replace.

We now compare equations VI-16 and VI-19,20. Both approaches relate $^{57}$Fe hyperfine magnetic field changes to changes in the solute concentration. Equation VI-16, which was derived for Ni solutes for which $g^{Ni}_{Ni}(r_j) \simeq 0$, neglects magnetic moment perturbations at solute atoms caused by other solute atoms. Together with an Fe magnetic moment perturbation neglected in equation VI-16, this can be included for solutes other than Ni by a term going as $c^2_X$:

$$\overline{\Delta H^X}(c_X) = c_X \times \left\{ \left[ \alpha_{CP} + \alpha_{CEP} f(0) + \alpha_{CEP} \sum_{r>0} f(r) \right] M(\{g_X^{Fe}(r_j)\}) \right. \qquad \text{VI-21a}$$

$$\left. + (\mu_X^2 - \mu_{Fe}^2)\, \alpha_{CEP} \sum_{r>0} f(r) \right\}$$

$$+ c_X^2 \times \left\{ \left[ M(\{g_X^X(r_j)\}) - M(\{g_X^{Fe}(r_j)\}) \right] \alpha_{CEP} \sum_{r>0} f(r) \right\}$$

$$\alpha_{CP} + \alpha_{CEP} f(0) \simeq \frac{-86\text{kG}}{\mu_B} \quad \text{and} \quad \alpha_{CEP} \sum_{r>0} f(r) \simeq \frac{-70\text{kG}}{\mu_B} \qquad \text{VI-21b}$$

Now the additivity assumption is violated in a similar way by both the average approach of equation VI-21 and the explicit nearest neighbor approach of equation VI-20. The additivity assumption cannot account for the last term in these equations because it is nonlinear in $c_X$.

What is physically wrong with the additivity assumption? The problem is that the additivity assumption necessarily neglects the local environment of the solute atom. This is fine so long as all of the solute atoms have the same local environment, such is the case when all solute atoms see only Fe atoms around them in very dilute Fe-X alloys. Of course, for dilute alloys the additivity assumption is unnecessary anyway; only when two or more solute atoms are near the same $^{57}$Fe atom are we forced to use the additivity assumption. When two or more solutes are in $^{57}$Fe nearest neighbor shells where they can cause significant hyperfine magnetic field perturbations, these solutes are generally close enough to each other to perturb each other's magnetic moment. For instance, we see in equation VI-19 that the addition of a solute atom to the $^{57}$Fe 1n.n. shell affects the magnetic moment at a Fe atom in the 1n.n. shell that is located at a 2n.n. separation from the solute atom. This perturbed Fe magnetic moment affects the $^{57}$Fe hyperfine magnetic field with an indirect nonlocal contribution. However, when this Fe atom in the $^{57}$Fe 1n.n. shell is replaced with a solute atom (see eqn VI-20), this indirect nonlocal contribution will change unless the new solute atom magnetic moment is perturbed by the same amount

as was the replaced Fe magnetic moment. Accounting for these indirect nonlocal contributions is necessarily beyond the additivity assumption because it treats only the total number of solute atoms in each $^{57}$Fe nearest neighbor shell, and not how they are positioned with respect to one another.

For dilute solutions the indirect and direct nonlocal contributions to the $^{57}$Fe hyperfine magnetic field are best treated by the approach taken for equation VI-19, where the magnetic moment at each neighboring site around the $^{57}$Fe nucleus is considered explicitly. Unfortunately, this requires specific knowledge of the type of atom at each site and its distance from each solute atom. Equation VI-20 starts to indicate the difficulty of dealing with multiple solute atoms. Just knowing the number of solute atoms in each nearest neighbor shell is not sufficient information, since one must distinguish between the relative of solute atoms in the same shell, and even between the relative positions positions of solute atoms located in different shells. Nevertheless, for dilute solutions the explicit consideration of each magnetic moment around the $^{57}$Fe nucleus is a reasonable approach since we need consider only one solute atom at a time. This was done by Stearns in 1976 [220]. Using NMR data from which the $\{\Delta H_i^X\}$ were identified, the magnetic moments of the solute atoms and the magnetic moments of Fe atoms around the solute atoms were determined by using equations VI-7 and VI-8. The reasonable agreement between the solute moments and the Fe magnetic moment perturbations determined in this way, and the same magnetic moments determined by neutron diffraction methods [220.5], is strong evidence for the validity of the model of linear response of hyperfine magnetic fields to magnetic moments. Alternatively, if we already know the Fe and X magnetic moments in an Fe-X alloy, we can then predict the set $\{\Delta H_j^X\}$.

From equation VI-20 we found that the $^{57}$Fe hyperfine magnetic field per-

turbation from two solute atoms in its 1n.n. shell will be twice as large as that from one solute atom in its 1n.n. shell if and only if:

$$\mu_{Fe}^{o}\, g_{X}^{Fe}(r_2) = \mu_{X}^{o}\, g_{X}^{X}(r_2).$$

By thinking about other arrangements of solute atoms beyond the 2n.n. shell, and also by considering solute atoms in several shells simultaneously, we find that the general additivity assumption:

$$\Delta H^{X}(ni,nj,nk) = n\Delta H^{X}(i,j,k)\ , \qquad \text{VI-22a}$$

is true if and only if:

$$g_{X}^{Fe}(r_j) = g_{X}^{X}(r_j) \text{ for all } j. \qquad \text{VI-22b}$$

This is equation VI-17 which characterizes our hypothetical solute atom. For this Hy solute atom, the additivity assumption is consistent with the model of linear response of hyperfine magnetic fields to magnetic moments. Therefore, the phenomenological model of Chapter IV can be conveniently employed to predict shapes of Mössbauer peaks from concentrated Fe-Hy alloys.

Si is a fine example of our hypothetical solute atom because:

$$g_{Si}^{Fe}(r_j) = g_{Si}^{Si}(r_j) = 0 \text{ for all } j\ .$$

With no magnetic moment perturbations around a Si atom it is easy to use equation VI-25 to determine:

$$\Delta H^{Si}(2,0,0) = 2\Delta H^{Si}(1,0,0) = 2\alpha_{CEP} f(r_1)(\mu_{Si}^{o} - \mu_{Fe}^{o}) \qquad \text{VI-23}$$

$$\Delta H^{Si}(2,0,0) = -2\alpha_{CEP} f(r_1)\mu_{Fe}^{o} \qquad \text{VI-24}$$

The phenomenological model of Chapter IV should work well for non-dilute Fe-Si alloys.

On the other hand, Ni is a particularly poor example of our hypothetical solute atom. Ni causes only small magnetic moment perturbations at other Ni atoms, but large magnetic moment perturbations at neighboring Fe atoms; $g_{Ni}^{Ni}(r_j) \simeq 0$, while from Table X we see that $M(\{g_{Ni}^{Fe}(r)\}) > \mu_{Fe}^{o} - \mu_{Ni}^{o}$. It turns out that a Ni concentration of 9% is large enough so that the structure of

Mössbauer peaks from a Fe-9Ni alloy will depart significantly from predictions of the phenomenological model of Chapter IV with its additive assumption. In Fe-9Ni there is a significant probability of finding two Ni atoms in the 1n.n. shell of a $^{57}$Fe nucleus, so we first try to use equations VI-19 and 20 to roughly estimate the error in using the additivity assumption to predict Fe-9Ni lineshapes. We should really perform an average over nearest neighbor configurations, but we make our rough estimate by using equations VI-19 and VI-20 directly with experimental data of Stearns [220] and Collins [224,225]. In this way, we find a positive $\simeq$ 10% error associated with the additivity assumption.

A similar, but less rough, estimate of the error caused by assuming additive $\Delta H_i^{\mathcal{M}}$ parameters can be made with the average treatment of equation VI-21. Using data from Table X and equation VI-21, we find that for Ni the average changes in the local, the direct nonlocal, and the indirect nonlocal contributions to the $^{57}$Fe hyperfine magnetic fields are of relative magnitudes +155, -77, and +126, respectively. Therefore, when $c_{\mathcal{M}} \simeq 0.1$ , the second term of equation VI-21 (times $c_{\mathcal{M}}^2$), which represents the deviation from the additivity assumption, is ~ 6+% as large as the first term (which is the prediction with the $c_{\mathcal{M}}$-dependent additivity assumption). This is only the error in the average hyperfine magnetic field; the error on the high Doppler shift energy side of the Fe-Ni Mössbauer peaks will be several times larger. Consequently, the high Doppler shift energy side of the peaks, which comes from $^{57}$Fe nuclei with a greater than average number of Ni neighbors, will not move to higher energy with Ni concentration as rapidly as predicted by the phenomenological model of Chapter IV. The low Doppler shift energy side, however, will be better approximated by this model. This asymmetric effect, which gets larger with increasing Ni concentration, can account for much of the observed skewness* of Fe-Ni

* Recall that the skewness, which parameterizes the asymmetry of a function, goes as $\langle X^3\rangle - 3\langle X^2\rangle\langle X\rangle + \langle X\rangle^3$.

Mössbauer peaks, which is inconsistent with the skewness predicted with the phenomenological model of additive $\Delta H_i^M$ parameters. This is discussed in detail in X.A.2.

From the data of Table X we expect that the additivity assumption should be more consistent with the model of linear response of hyperfine magnetic fields to magnetic moments in the case of Cr and Mn solutes. In the case of Cr and Mn solutes, the direct nonlocal contribution to the $^{57}$Fe hyperfine magnetic field is larger, and the indirect nonlocal contribution is smaller, than in the case of Ni. Nevertheless, caution should be used when the phenomenological model of Chapter IV is used for predicting shapes of Mössbauer peaks from concentrated Fe-Cr and Fe-Mn alloys.

**D. A Compromise Treatment of Linear Response in Non-Dilute Binary Alloys.**

So far we have used two approaches to find solute-induced hyperfine magnetic field perturbations in binary alloys. Both approaches are of limited usefulness for our purposes. The average approach of equation VI-16 is mathematically tractable for non-dilute alloys, but cannot predict the detailed structure we need in order to determine the intensity, shape, and position of the satellite peaks in binary alloys. On the other hand, the detailed local environment approach, of which equations VI-19 and VI-20 are specific examples, treats the satellite peaks explicitly. Although this detailed nearest neighbor approach is mathematically tractable for dilute alloys, it is rendered mathematically intractable by the large number of probable local environments in Fe-9Ni-1X alloys. In the remainder of this section we develop a compromise approach for binary alloys. This approach, which combines elements of the average approach and the detailed local environment approach, is first developed for non-dilute binary alloys so that we can later modify it for non-dilute ternary alloys in section VI.E.

The compromise approach now developed is, in some respects, just a long-winded way of reproducing equation VI-16. However, when performing lattice averages of terms to obtain equation VI-30, we are able to suggest a reasonable approximation for the $\{\Delta H_j^X\}$ used in the phenomenological model of Chapter IV. This approximation, equation VI-31, suffers from defects associated with a neglect of specific local environment effects. However, for small solute concentration changes it is an appropriate means of determining the effective $\{\Delta H_j^X\}$, given knowledge of the appropriate $\{f\}$ and $\{g\}$ parameters. Equation VI-31 is, in fact, our best effort to reconcile the phenomenological model of Chapter IV with the model of linear response of hyperfine magnetic fields to magnetic moments.

With the compromise approach, we neglect some average changes with increasing X concentration like:

$$c_X M(\overset{Fe}{X}) \equiv c_X\,[8g_X^{Fe}(1) + 6g_X^{Fe}(2) + 12g_X^{Fe}(3)] \;\rightarrow\; c_X M'(\overset{Fe}{X}) \equiv c_X\,(1-\delta)M(\overset{Fe}{X})$$

Such changes are expected as the number of X atoms increases because the number of Fe atoms around each X atom decreases. The factor $\delta$ is approximately $c_X^2$. Consequently, the average magnetic moment perturbation that we predict with the compromise approach will be in error by a small fractional amount. To minimize this defect in our compromise approach, we treat only small X concentration changes (i.e. small $\Delta c_X$) in an alloy with an initial X concentration of $c_X$. This is consistent with the experimental approach of finding the change in the "X satellite" peaks revealed when the X concentration is changed from $c_X$ to $c_X + \Delta c_X$. Over a small range of $\Delta c_X$ we can be assured that the new $\Delta H_j^X(c_X)$ is mostly constant; we will be able to use the additivity assumption to accurately predict the difference spectrum because we largely cancel out the errors from non-additivity when we take a difference like:

$$(c_X + \Delta c_X)^2 - c_X^2 = 2c_X\Delta c_X + \Delta c_X^2\,,$$

which is negligible when $\Delta c_X \ll c_X$.

For simplicity we first consider the perturbation of the $^{57}$Fe hyperfine magnetic field, $\Delta H_j^X(c_X)$, due to adding one X solute atom to the jn.n. shell of the $^{57}$Fe nucleus in a Fe-X alloy. We know that the fraction of Fe atoms in the alloy is $1 - c_X$, and the fraction of X atoms is $c_X$. We temporarily leave the Fe and X magnetic moments unspecified as $\mu_{Fe}(\mathbf{r})$ and $\mu_X(\mathbf{r})$, respectively. Using equation VI-21 with the $^{57}$Fe nucleus at the origin we have:

$$\Delta H_j^X(i,j,k,l) \equiv H^X(i,j+1,k,l) - H^X(i,j,k,l)\ ,$$

or treating all atoms except our new solute atom in an average way:

$$\begin{aligned}\Delta H_j^X(c_X) = \Bigg\{&[\alpha_{CP} + \alpha_{CEP} f(0)]\mu'_{Fe}(0) + \alpha_{CEP}(1-c_X)\sum_{0<\mathbf{r}\neq\mathbf{r}_j} f(\mathbf{r})\mu'_{Fe}(\mathbf{r}) \\ &+ \alpha_{CEP} c_X \sum_{0<\mathbf{r}\neq\mathbf{r}_j} f(\mathbf{r})\mu'_X(\mathbf{r}) + \alpha_{CEP} f(\mathbf{r}_j)\mu'_X(\mathbf{r}_j)\Bigg\} \\ -\Bigg\{&[\alpha_{CP} + \alpha_{CEP} f(0)]\mu_{Fe}(0) + \alpha_{CEP}(1-c_X)\sum_{0<\mathbf{r}\neq\mathbf{r}_j} f(\mathbf{r})\mu_{Fe}(\mathbf{r}) \\ &+ \alpha_{CEP} c_X \sum_{0<\mathbf{r}\neq\mathbf{r}_j} f(\mathbf{r})\mu_X(\mathbf{r}) + \alpha_{CEP} f(\mathbf{r}_j)\mu_{Fe}(\mathbf{r}_j)\Bigg\}\end{aligned} \qquad \text{VI-25}$$

We cannot yet perform the subtraction of the terms in the curly brackets of equation VI-25 because the magnetic moments of $\mu_{Fe}(\mathbf{r})$ and $\mu_X(\mathbf{r})$ are affected by the substitution of the new X atom for the Fe atom at $\mathbf{r}_j$. We now include these magnetic moment perturbations at Fe and X atoms with our sets $\{g_X^{Fe}(r_j)\}$ and $\{g_X^X(r_j)\}$, respectively. In the compromise treatment we account explicitly for the effect of the single solute atom configuration change on the magnetic moment of the $^{57}$Fe atom, but all other magnetic moment perturbations are treated in an average way. This approximate treatment ends up giving us an additivity relationship for the $c_X$-dependent $\Delta H_j^X(c_X)$.

Of course we do not expect that all Fe moments are perturbed by the same amount; they will depend on the specific configuration of X atoms around them. Each such specific X atom configuration is also responsible for a specific $^{57}$Fe

hyperfine magnetic field perturbation as well. Unfortunately, since the hyperfine magnetic field perturbation is evaluated at the central $^{57}$Fe nucleus, and the magnetic moment perturbation is evaluated at each nearest neighbor site around the $^{57}$Fe nucleus, there is no simple and general relationship between specific hyperfine magnetic field perturbations and specific magnetic moment perturbations. Our approximate treatment is therefore a practical necessity for avoiding the extensive bookkeeping inherent to a detailed nearest neighbor approach. We first evaluate the Fe magnetic moment perturbation averaged over the probability of each local environment in a random bcc Fe-X alloy:

$$\overline{\mu_{Fe}}_{Fe-X}(c_X) = \sum_i^8 \sum_j^6 \sum_k^{12} \cdots P(8,i,c_X)\, P(6,j,c_X)\, P(12,k,c_X) \cdots \times (\mu_{Fe}^0 + i g_X^{Fe}(r_1) + j g_X^{Fe}(r_2) + k g_x^{Fe}(r_3)) \qquad \text{VI-26}$$

where we have expressed the binomial probability as:

$$P(N,i,c) \equiv \frac{N!}{(N-i)!\,i!} c^i (1-c)^{N-i}.$$

In equation VI-26 we recognize the first moments <i>,<j>, and <k> of the binomial distributions, so equation VI-26 becomes:

$$\overline{\mu_{Fe}}_{Fe-X}(c_X) = \mu_{Fe}^0 + c_X M(\{g_X^{Fe}(r_j)\}) \qquad \text{VI-27}$$

where:

$$M(\{g_X^{Fe}(r_j)\}) \equiv 8 g_X^{Fe}(r_1) + 6 g_X^{Fe}(r_2) + 12 g_X^{Fe}(r_3) + \cdots$$

Similarly:

$$\overline{\mu_X}_{Fe-X}(c_X) = \mu_X^0 + c_X M(\{g_X^X(r_j)\}) \qquad \text{VI-28}$$

The constants $\mu_{Fe}^0$ and $\mu_X^0$ are the magnetic moments of Fe and X atoms in pure Fe and very dilute Fe-X alloys, respectively.

Using these average magnetic moment perturbations, we continue with the treatment of $\Delta H_j^X(c_X)$. We start with an Fe-X alloy with an X concentration of $c_X$ and we end up increasing the X concentration by the small amount $\Delta c_X$ when

adding jn.n. X atoms. Using equations VI-27, VI-28, and VI-25, we find (using the notation $M(\overset{Fe}{X}) \equiv M(\{g_X^{Fe}(r_j)\})$ and $g_X^{Fe}(2) \equiv g_X^{Fe}(r_2)$:

$$\begin{aligned}
\Delta H^X_{j\,Fe-X}(c_X) = \Big[&(\mu^0_{Fe} + c_X M(\overset{Fe}{X}) + g_X^{Fe}(j))(\alpha_{CP} + \alpha_{CEP} f(0)) \\
&+ \alpha_{CEP}(1-c_X) \sum_{0<r\neq r_j} f(r)(\mu^0_{Fe} + (c_X + \Delta c_X) M(\overset{Fe}{X})) \\
&+ \alpha_{CEP} c_X \sum_{0<r\neq r_j} f(r)(\mu^0_X + (c_X + \Delta c_X) M(\overset{X}{X})) \\
&+ \alpha_{CEP} f(r_j)(\mu^0_X + c_X M(\overset{X}{X}))\Big] \\
-\Big[&(\mu^0_{Fe} + c_X M(\overset{Fe}{X}))(\alpha_{CP} + \alpha_{CEP} f(0)) \\
&+ \alpha_{CEP}(1-c_X) \sum_{0<r\neq r_j} f(r)(\mu^0_{Fe} + c_X M(\overset{Fe}{X})) \\
&+ \alpha_{CEP} \sum_{0<r\neq r_j} f(r)(\mu^0_X + c_X M(\overset{X}{X})) \\
&+ \alpha_{CEP} f(r_j)(\mu^0_{Fe} + c_X M(\overset{Fe}{X}))\Big]
\end{aligned} \qquad \text{VI-29}$$

After rearranging and performing lattice sums we find:

$$\begin{aligned}
\Delta H^X_{j\,Fe-X}(c_X) = {}& 1 g_X^{Fe}(j)(\alpha_{CP} + \alpha_{CEP} f(0)) \\
&+ \alpha_{CEP}\Big[f(r_1) + 6f(r_2) + 12f(r_3) + \cdots\Big](\Delta c_X)\Big[(1-c_X)M(\overset{Fe}{X}) + c_X M(\overset{X}{X})\Big] \\
&+ \alpha_{CEP} f(r_j)\Big[\Big[\mu^0_X + c_X M(\overset{X}{X})\Big] - \Big[\mu^0_{Fe} + c_X M(\overset{Fe}{X})\Big]\Big]
\end{aligned} \qquad \text{VI-30}$$

The new jn.n. X atom perturbs the magnetic moment at the $^{57}$Fe atom by an amount equal to the first factor of the first term in equation VI-30. This first term is the local contribution to $\Delta H_j^X$. The second term is unaffected by the particular nearest neighbor site occupied by the new solute atom; this is an artifact of our approximation of independent hyperfine magnetic field and magnetic moment perturbations; we have not considered local environments explicitly. This second term is the change in the nonlocal indirect contribution to $\Delta H_j^X$. Here $\Delta H_{INL}$ is determined by how the average magnetic moment perturbations at Fe and X atoms depend on the small average change in X concentration, $\Delta c_X$. The third term is the direct nonlocal response of the conduction electrons at the $^{57}$Fe nucleus (through the $f(r_j)$ parameter) caused by the substitution

of an X atom for an Fe atom at a jn.n. site. If we were to double the number of solute atoms we had placed in each $^{57}$Fe shell, we would also double our $\Delta c_X$, and we would also have twice the direct nonlocal contribution to $\Delta H_j^X(c_X)$. Clearly then, our compromise treatment for $\Delta H_j^X(c_X)$, with its substantial independence of hyperfine magnetic field perturbations and magnetic moment perturbations, is consistent with an additivity assumption.

Our notation, $\underset{Fe-X}{\Delta H_j^X}(c_X)$, in equations VI-29 and VI-30 is perhaps misleading because these parameters cannot be used with the phenomenological model of Chapter IV unless we relate $\Delta c_X$ to the change in number of solute neighbors around the $^{57}$Fe nucleus. Nevertheless, equation VI-30 is useful for the prediction of the average $^{57}$Fe hyperfine magnetic field perturbation associated with changing the X concentration from $c_X$ to $c_X + \Delta c_X$. Additionally, equation VI-30 is valuable for inspiring the following relation for use as $\Delta H^X(i,j,k)$ of equation IV-1. Including the first three nearest neighbor shells:

$$\begin{aligned}\Delta H^X(i,j,k,c_X) \simeq & \left[i g_X^{Fe}(1) + j g_x^{Fe}(2) + k g_x^{Fe}(3)\right]\left[\alpha_{CP} + \alpha_{CEP} f(0)\right] \\ & + \alpha_{CEP}\left[8f(r_1) + 6f(r_2) + 12f(r_3)\right]\left[\frac{i+j+k}{8+6+12}\right]\left[(1-c_X)M(\overset{Fe}{X}) + c_X M(\overset{X}{X})\right] \\ & + \alpha_{CEP}\left[i f(r_1) + j f(r_2) + k f(r_3)\right]\left[\left[\mu_X^0 + c_X M(\overset{X}{X})\right] - \left[\mu_{Fe}^0 + c_X M(\overset{Fe}{X})\right]\right]\end{aligned} \qquad \text{VI-31}$$

Equation VI-31 is reasonable but nonrigorous. One of its main virtues is that it predicts the same average $\Delta\overline{H}^X(c_X)$ as does equation VI-30. (I have verified this by setting up an analog to equation VI-32 which uses equation VI-31 instead of VI-30.) However, equation VI-31 predicts the same indirect nonlocal contribution to the $^{57}$Fe hyperfine magnetic field if one X atom is added to any of its first three nearest neighbor shells. This deficiency will be reflected in the shape of the "X satellite" predicted with the set $\{\Delta H_j^X\}$ from equation VI-31. For dilute Fe-X solutions equation VI-31 does only a fair job of reconstructing $\{\Delta H_j^X\}$ when we use Stearns' data [220] for $\{g_X^{Fe}(r_j)\}$ and $\mu_X$. Curiously, most of the

error arises from the local contribution to $\Delta H_j^X$ ($\Delta H_2^{Cr}$ is especially inaccurate for this reason), but the local contribution should be accurate and independent of our approximations for the nonlocal contributions anyhow. This is a bit confusing, and casts some doubt on the accuracy of Stearns' method of determining $\{g_X^{Fe}(r_j)\}$.

Equation VI-31 could perhaps be improved with a correction term going as $\Delta c_X^2$ or $\left[\frac{i+j+k}{8+6+12}\right]^2$ (c.f. equation VI-21), but since the X concentration changes are very small this should not be important. An additional improvement could possibly be effected by replacing the factor $\left[\frac{i+j+k}{8+6+12}\right]$ in equation VI-31 with the new factor $\left[\frac{(1+\Delta_1)i + (1+\Delta_2)j + (1+\Delta_3)k}{8+6+12}\right]$, subject to the condition: $8\Delta_1 + 6\Delta_2 + 12\Delta_3 = 0$. The parameters $\Delta_1 = +.2$, $\Delta_2 = 0$, $\Delta_3 = -.133$ are reasonable, but are not used for any predictions in this thesis.

Using equation VI-30 (with its generalization of the local contribution to include several solute atoms around the $^{57}Fe$ nucleus), we now find* the lattice averaged hyperfine magnetic field perturbation associated with an increase in solute concentration from $c_X$ to $\Delta c_X$ in a random, non-dilute bcc alloy:

$$\overline{\Delta H_X^X}_{Fe-X}(c_X) = \sum_i^8 \sum_j^6 \sum_k^{12} \cdots P(8,i,\Delta c_X)\, P(6,j,\Delta c_X)\, P(12,k,\Delta c_X) \qquad \text{VI-32}$$

$$\times \Big\{ + \Big[ i g_X^{Fe}(1) + j g_X^{Fe}(2) + k g_X^{Fe}(3) \Big] \Big( \alpha_{CP} + \alpha_{CEP} f(0) \Big)$$

$$+ \alpha_{CEP} \Big[ i f(r_1) + j f(r_2) + k f(r_3) \Big] \Big[ \Big[ \mu_X^0 + c_X M(X^X) \Big] - \Big[ \mu_{Fe}^0 + c_X M(X^{Fe}) \Big] \Big] \Big\}$$

$$+ \alpha_{CEP} \Big[ 8 f(r_1) + 6 f(r_2) + 12 f(r_3) \Big] (\Delta c_X) \Big[ (1 - c_X) M(X^{Fe}) + c_X M(X^X) \Big]$$

We identify independent first moments of the binomial distribution and find:

$$\overline{\Delta H_X}_{Fe-X}(c_X) = \Delta c_X \Big[ \alpha_{CP} + \alpha_{CEP} f(0) \Big] M(X^{Fe}) \qquad \text{VI-33}$$

* Equation VI-33 was also found by by starting with a more explicit indirect nonlocal term of Eqn. V-31.

$$+ \Delta c_X \alpha_{CEP} \left[8f(r_1) + 6f(r_2) + 12f(r_3)\right]$$
$$\times\left[(\mu_X - \mu_{Fe}) + 2c_X\left[M(\overset{X}{\phi}) - M(\overset{Fe}{\phi})\right] + M(\overset{Fe}{\phi})\right]$$

Equation VI-33 can be obtained directly from equation VI-21 by taking the difference:

$$\Delta H^X(c_X + \Delta c_X) - \Delta H^X(c_X),$$

and then ignoring the small term in $\Delta c_X^2$. However, equation VI-33, which is consistent with an additivity assumption, cannot be obtained from equation VI-16a because the additivity assumption of equation VI-33 has been extended to include the effect of $c_X$ on the indirect nonlocal contribution in an average way. This is why I refer to equations VI-30-33 as a compromise treatment of the model of linear response of hyperfine magnetic fields to magnetic moments.

**E. A Compromise Treatment of Linear Response in Non-Dilute Ternary Alloys.**

With faith kindled by its success with binary alloys, we take the semi-phenomenological model of linear response of hyperfine magnetic fields to magnetic moments and see what sort of Mössbauer peaks are predicted for Fe-9Ni-1X ternary alloys. The motivation for doing this arises from the need to understand possible changes in the shape and intensity of "X satellite peaks" seen in difference spectra when the Fe host is alloyed with Ni (See Figs. 27 and 28). We treat non-dilute ternary alloys with an extension of the compromise treatment used for non-dilute binary alloys, in which the complicated local environment changes around the new solute atoms affect nonlocal contributions to the $^{57}$Fe hyperfine magnetic field in only an approximate way. Again an additivity assumption will be consistent with this treatment of the "X satellite peak", so the $\Delta c_X^2$ correction terms (c.f. equation VI-21) will be ignored. (This should be no problem for the small $\Delta c_X$ in our experiments.) However, interactions betwen Ni and X atoms give terms which go as $c_{Ni}\Delta c_X$, and these terms are included in the following treatment.

The average Fe magnetic moment is now perturbed by both Ni and X atoms. Instead of equation VI-27 we have:

$$\overline{\mu_{Fe}}_{Fe-Ni-X}(c_{Ni},c_X) = \sum_{i_1}^{8}\sum_{j_1}^{6}\sum_{k_1}^{12}\cdots\sum_{i_2}^{8}\sum_{j_2}^{6}\sum_{k_2}^{12}\cdots P(8,i_1,c_{Ni})\,P(6,j_1,c_{Ni}) \times P(12,k_1,c_{Ni})\,P(8,i_2,c_X)\,P(6,j_2,c_X) \times P(12,k_2,s_X)\times\Big\{\mu^0_{Fe} + i_1 g^{Fe}_{Ni}(1) + j_1 g^{Fe}_{Ni}(2) + k_1 g^{Fe}_{Ni}(3) + i_2 g^{Fe}_{X}(1) + j_2 g^{Fe}_{X}(2) + k_2 g^{Fe}_{X}(3)\Big\} \qquad \text{VI-34}$$

Note that this treatment involves independence of magnetic moment perturbations around Ni and X atoms, and does not even prevent both Ni and X atoms from simultaneously occupying the same lattice site. This could be a big problem in more concentrated alloys, but we expect no seriously misleading results for Fe-9Ni-1X alloys. The virtue of our independent treatment is that it allows us to get answers when we identify first moments of the binomial distribution:

$$\overline{\mu_{Fe}}_{Fe-Ni-X}(c_{Ni},c_X) = \mu^0_{Fe} + c_{Ni}M(\{g^{Fe}_{Ni}(r_j)\}) + c_X M(\{g^{Fe}_{X}(r_j)\}) \qquad \text{VI-35a}$$

$$\overline{\mu_{Ni}}_{Fe-Ni-X}(c_{Ni},c_X) = \mu^0_{Ni} + c_{Ni}M(\{g^{Ni}_{Ni}(r_j)\}) + c_X M(\{g^{Ni}_{X}(r_j)\}) \qquad \text{VI-35b}$$

$$\overline{\mu_{X}}_{Fe-Ni-X}(c_{Ni},c_X) = \mu^0_{X} + c_{Ni}M(\{g^{X}_{Ni}(r_j)\}) + c_X M(\{g^{X}_{X}(r_j)\}) \qquad \text{VI-35c}$$

We now write, in analogy to equation VI-29, the hyperfine magnetic field difference which is related to the separation of the jn.n. satellite peak from the main absorption peak of a Fe-Ni-X alloy, whose Ni concentration is $c_{Ni}$, and whose X concentration is $c_X$. As was the case for the binary treatment, adding these jn.n. solute atoms increases the X concentration by an amount $\Delta c_X$. Although we could conceivably substitute the new X atoms for Ni atoms as for well as Fe atoms, this would confuse the effect of Ni on $\Delta H_j^X(c_X)$ by altering the Ni concentration of the lattice, so we only substitute one new X atom for the Fe atom at $r_j$:

$$\Delta H_j^X(c_{Ni},c_X) = \Big[\Big(\alpha_{CP} + \alpha_{CEP} f(0)\Big)\Big(\mu^0_{Fe} + c_{Ni}M(^{Fe}_{Ni}) + c_X M(^{Fe}_{X}) + 1 g^{Fe}_{X}(\mathbf{r}_j)\Big) + \alpha_{CEP}(1 - c_{Ni} - c_X)\sum_{0<r\neq r_j} f(\mathbf{r})\Big(\mu^0_{Fe} + c_{Ni}M(^{Fe}_{Ni}) + (c_X + \Delta c_X)M(^{Fe}_{X})\Big)\Big] \qquad \text{VI-36}$$

$$+ \alpha_{CEP} c_{Ni} \sum_{0<\mathbf{r}\neq\mathbf{r}_j} f(\mathbf{r}) \left[ \mu^0_{Ni} + c_{Ni} M(\overset{Ni}{Ni}) + (c_X + \Delta c_X) M(\overset{Ni}{X}) \right]$$

$$+ \alpha_{CEP} c_X \sum_{0<\mathbf{r}\neq\mathbf{r}_j} f(\mathbf{r}) \left[ \mu^0_X + c_{Ni} M(\overset{X}{Ni}) + (c_X + \Delta c_X) M(\overset{X}{X}) \right]$$

$$+ \alpha_{CEP} f(\mathbf{r}_j) \left[ \mu^0_X + c_{Ni} M(\overset{X}{Ni}) + c_X M(\overset{X}{X}) \right] \Big]$$

$$- \Big[ \left[ \alpha_{CP} + \alpha_{CEP} f(0) \right] \left[ \mu^0_{Fe} + c_{Ni} M(\overset{Fe}{Ni}) + c_X M(\overset{Fe}{X}) \right]$$

$$+ \alpha_{CEP} (1 - c_{Ni} - c_X) \sum_{0<\mathbf{r}\neq\mathbf{r}_j} f(\mathbf{r}) \left[ \mu^0_{Fe} + c_{Ni} M(\overset{Fe}{Ni}) + c_X M(\overset{Fe}{X}) \right]$$

$$+ \alpha_{CEP} c_{Ni} \sum_{0<\mathbf{r}\neq\mathbf{r}_j} f(\mathbf{r}) \left[ \mu^0_{Ni} + c_{Ni} M(\overset{Ni}{Ni}) + c_X M(\overset{Ni}{X}) \right]$$

$$+ \alpha_{CEP} c_X \sum_{0<\mathbf{r}\neq\mathbf{r}_j} f(\mathbf{r}) \left[ \mu^0_X + c_{Ni} M(\overset{X}{Ni}) + c_X M(\overset{X}{X}) \right]$$

$$+ \alpha_{CEP} f(\mathbf{r}_j) \left[ \mu^0_{Fe} + c_{Ni} M(\overset{Fe}{Ni}) + c_X M(\overset{Fe}{X}) \right] \Big]$$

After rearranging and performing lattice sums:

$$\Delta H_j^X_{Fe-Ni-X}(c_{Ni}, c_X) = 1 g_X^{Fe}(\mathbf{r}_j) \left[ \alpha_{CP} + \alpha_{CEP} f(0) \right] \qquad \text{VI-37}$$

$$+ \alpha_{CEP} \left[ 8 f(r_1) + 6 f(r_2) + 12 f(r_3) + \cdots \right] (\Delta c_X)$$

$$\times \left[ (1 - c_{Ni} - c_X) M(\overset{Fe}{X}) + c_{Ni} M(\overset{Ni}{X}) + c_X M(\overset{X}{X}) \right]$$

$$+ \alpha_{CEP} f(\mathbf{r}_j) \left[ \left[ \mu^0_X + c_{Ni} M(\overset{X}{Ni}) + c_X M(\overset{X}{X}) \right] - \left[ \mu^0_{Fe} + c_{Ni} M(\overset{Fe}{Ni}) + c_X M(\overset{Fe}{X}) \right] \right]$$

The first term of equation VI-37 is the same as the first term of equation VI-30. The second term is the indirect nonlocal term which arises from the magnetic moment perturbations at all Fe, X, and Ni atoms. It comes about with the increase in X concentration by an amount $\Delta c_X$. The third term is the direct nonlocal response of the conduction electrons at the $^{57}$Fe nucleus (through the $\{f(r_j)\}$ parameters) caused by the substitution of an X atom for an Fe atom at a jn.n. site. Much of the discussion following equation VI-30 is relevant here.

In analogy to equation VI-31 we now offer an approximate expression for $\{\Delta H_j^X\}$, appropriate for Fe-Ni-X alloys, which can be used with the phenomenological model of Chapter IV:

$$\Delta H^X(i,j,k,c_{Ni},c_X) = \left[ig_X^{Fe}(1) + jg_X^{Fe}(2) + kg_X^{Fe}(3)\right]\left[\alpha_{CP} + \alpha_{CEP}f(0)\right] \qquad \text{VI-38}$$
$$+ \alpha_{CEP}\left[8f(r_1) + 6f(r_2) + 12f(r_3)\right]\left[\frac{i+j+k}{8+6+12}\right]$$
$$\times\left[(1 - c_{Ni} - c_X)M(\overset{Fe}{X}) + c_{Ni}M(\overset{Ni}{X}) + c_X M(\overset{X}{X})\right]$$
$$+ \alpha_{CEP}\left[if(r_1) + jf(r_2) + kf(r_3)\right]$$
$$\times\left[\left[\mu_X^g + c_{Ni}M(\overset{X}{Ni}) + c_X M(\overset{X}{X})\right] - \left[\mu_{Fe}^g + c_{Ni}M(\overset{Fe}{Ni}) + c_X M(\overset{Fe}{X})\right]\right]$$

The same deficiencies of equation VI-31 are present in equation VI-38. However, equation VI-38 has the same main virtue of equation VI-31; the average of $\Delta H^X(i,j,k,c_{Ni},c_X)$ over all probable solute configurations yields the same result as the lattice average of equation VI-37 in its generalized form for several solute atoms around a $^{57}$Fe nucleus. Using this generalized form for equation VI-37 we now find the bcc lattice averaged hyperfine magnetic field perturbation associated with an increase in solute concentration by the amount $\Delta c_X$:

$$\overline{\Delta H^X}_{Fe-Ni-X}(c_{Ni},c_X) = \sum_i^8 \sum_j^6 \sum_k^{12} \cdots P(8,i,\Delta c_X)\, P(6,j,\Delta c_X)\, P(12,k,\Delta c_X) \qquad \text{VI-39}$$
$$\times\Bigg[ + \left[ig_X^{Fe}(l) + jg_X^{Fe}(2) + kg_X^{Fe}(3) + \cdots\right]\left[\alpha_{CP} + \alpha_{CEP}f(0)\right]$$
$$+ \alpha_{CEP}\left[if(r_1) + jf(r_2) + kf(r_3) + \cdots\right]$$
$$\times\left[\left[\mu_X^g + c_{Ni}M(\overset{X}{Ni}) + c_X M(\overset{X}{X})\right] - \left[\mu_{Fe}^g + c_{Ni}M(\overset{Fe}{Ni}) + c_X M(\overset{Fe}{X})\right]\right]$$
$$+ \alpha_{CEP}\left[8f(r_1) + 6f(r_2) + 12f(r_3) + \cdots\right]$$
$$\times(\Delta c_X)\left[(1 - c_{Ni} - c_X)M(\overset{Fe}{X}) + c_{Ni}M(\overset{Ni}{X}) + c_X M(\overset{X}{X})\right]$$

Identifying independent first moments of the binomial distributions, we find:

$$\overline{\Delta H^X}_{Fe\ Ni\ X}(c_{Ni},c_X) = \Delta c_X\left[\alpha_{CP} + \alpha_{CEP}f(0)\right]M(\overset{Fe}{X}) \qquad \text{VI-40}$$
$$+ \Delta c_X\alpha_{CEP}\left(8f(r_1) + 6f(r_2) + 12f(r_2)\right)$$
$$\times\left[\left[\mu_X^g - \mu_{Fe}^g\right] + 2c_X\left[M(\overset{X}{X}) - M(\overset{Fe}{X})\right]\right.$$
$$\left. + M(\overset{Fe}{X}) + c_{Ni}\left[M(\overset{Ni}{X}) + M(\overset{X}{Ni}) - M(\overset{Fe}{X}) - M(\overset{Fe}{Ni})\right]\right]$$

With a knowledge of the constants $\alpha_{CP}$, $\alpha_{CEP}$, $\{f(r_j)\}$, and the necessary sets $\{g\}$, we can now determine the effects of Ni on the "X satellite" peak found in difference of spectra from Fe-9Ni-100·$c_X$X and Fe-9Ni-100 ·($c_X$+$\Delta c_X$)X alloys. This understanding clears the way for using our difference spectrum procedure for quantitatively measuring small X concentration changes in Fe-9Ni~1X alloys. We determine the average effect of Ni on the position of the X satellite peaks with respect to the main absorption peaks by comparing equations VI-33 and VI-40. Their difference is:

$$\overline{\Delta H}^{X}_{Fe-Ni-X}(c_{Ni},c_X) - \overline{\Delta H}^{X}_{Fe-X}(c_X) = c_{Ni}\Delta c_X\,\alpha_{CEP}\Big[8f\ (r_1) + 6f\ (r_2) + 12f\ (r_3)\Big] \times\Big[M(\overset{Ni}{X}) + M(\overset{X}{Ni}) - M(\overset{Fe}{X}) - M(\overset{Fe}{Ni})\Big] \quad \text{VI-41}$$

Note that this average difference of equation VI-41 goes as $c_{Ni}\Delta c_X$. There are no terms going as $c_{Ni}$ or $\Delta c_X$ because they were cancelled out in taking the differences in equations VI-29, VI-36, and VI-41. Terms going as $c_{Ni}^2$ and $\Delta c_X^2$ are beyond the additivity assumption, but they, too, would have been largely cancelled out after taking the difference. Nevertheless, the predicted shape of the "X satellite" difference peak from Fe-9Ni-1X and Fe-9Ni spectra will suffer from the same defect as the Fe-9Ni peak shape predicted with an additivity assumption; the peak will have the wrong skewness (c.f. section X.A.).

On the average, from equation VI-39 we see that the substitution of an X atom for an Fe atom causes a different $^{57}$Fe hyperfine magnetic field change in an Fe-9Ni-1X alloy than in an Fe-1X alloy because:

1) in Fe-Ni-X there is a perturbation of Ni moments by X atoms,

2) in Fe-Ni-X there is a perturbation of X moments by Ni atoms,

3) in Fe-Ni-X the increase of Ni concentration is at the expense of Fe atoms; consequently, there are fewer Fe magnetic moments to be perturbed by X atoms, and

4) in Fe-Ni-X the X atom replaces an Fe atom whose magnetic moment was enhanced by Ni.

All four of these effects increase in proportion to $c_{Ni}$ , and all four also become more important in proportion to $\Delta c_X$. Depending on the relative magnitude of the magnetic moment perturbation, these four effects can be roughly of equal importance for all $c_{Ni}$ and $\Delta c_X$. The position of the "X satellite" with respect to the main absorption peak will be unchanged when the Fe host is alloyed with Ni only if the X atoms perturb Fe and Ni magnetic moments equally, and if the Ni atoms perturb Fe and X magnetic moments equally, that is if:

$$M(\overset{Ni}{X}) = M(\overset{Fe}{X}) \quad \text{and} \quad M(\overset{X}{Ni}) = M(\overset{Fe}{Ni})$$

If, as we generally expect, these conditions are not met, a greater or lesser satellite peak separation is expected in Fe-9Ni-1X than in Fe-1X alloys.

We can now determine the effect of Ni on the parameters $\{\Delta H_j^X\}$ by examining the difference between equations VI-38 and VI-31:

$$\begin{aligned}\Delta H^X(i,j,k,c_{Ni}) - \Delta H^X(i,j,k) = {} & \alpha_{CEP}\left[8f\ (r_1) + 6f\ (r_2) + 12f\ (r_3)\right] \\ & \times \left(\frac{i+j+k}{8+6+12}\right)\left[c_{Ni}\,M(\overset{Ni}{X}) - c_{Ni}\,M(\overset{Fe}{X})\right] \\ & + \alpha_{CEP}\left[if\ (r_1) + jf\ (r_2) + kf\ (r_3)\right]\left[c_{Ni} - - M(\overset{X}{Ni})c_{Ni}M(\overset{Fe}{Ni})\right].\end{aligned} \qquad \text{VI-42}$$

We find, as we must, the same four effects of Ni that were enumerated after equation VI-41. However, equation VI-42 is different for each nearest neighbor shell perturbation parameter. For a specific example, consider the effect that alloying the Fe host with Ni has on the hyperfine magnetic field perturbation parameter $\Delta H_1^{Cr}$. Unfortunately, there are two terms in equation VI-42 for which there is no known experimental data, $M(\overset{Ni}{Cr})$ and $M(\overset{Cr}{Ni})$. However, we can use equation VI-42 and Table X to qualitatively predict that there will still be a significant hyperfine magnetic field perturbation associated with $\Delta H_1^{Cr}$ so long as $M(\overset{Ni}{Cr})$ and $M(\overset{Cr}{Ni})$ are less than $\sim +30\mu_B$. From a naïve glance at Table V this would seem a safe assumption. For a second example, $\Delta H_3^{Cr}$ is very small; it is

experimentally insignificant in Fe-X alloys [41] and our equation VI-31 predicts $\Delta H_3^{Cr} < +4$ kG. With equation VI-42 we predict that $\Delta H_3^{Cr}$ will still be experimentally insignificant, or at most will contribute only a slight broadening to the main absorption peak in a Fe-9Ni-1Cr alloy, provided that as $|\mu_{Ni} M(^{Ni}_{Cr})|$ is less than $\sim 10\mu_B$. Cr solutes situated at a greater distance than the 3n.n. shell have experimentally insignificant effects on the $^{57}$Fe hyperfine magnetic field in dilute Fe-Cr alloys. Equation VI-42 predicts that there will be no change of this insignificant effect when the Fe host is alloyed with Ni.

In the case of Mn, we will argue in section X.A.1. that $g_{Ni}^{Mn}(1)$ and $g_{Ni}^{Mn}(2)$ are very large. If, for the sake of these arguments, we assume that $g_{Ni}^{Mn}(1) = g_{Ni}^{Mn}(2) = \frac{1}{2}\mu_B$, then equation VI-42 predicts a change in $\Delta H_2^{Mn}$ of 4.2 kG. This is large enough to be a prediction that Ni atoms could have a qualitative effect on the "Mn satellite" by transforming the insignificant $\Delta H_2^{Mn}$ of a Fe-1Mn alloy into a significant $\Delta H_2^{Mn}$ in a Fe-9Ni-1Mn alloy. However, unless we have such very large magnetic moment perturbations, equation VI-42 predicts that the nearest neighbor sites at which a solute atom produces a significant (insignificant) $^{57}$Fe hyperfine magnetic field perturbation in an Fe host will still produce a significant (insignificant) $^{57}$Fe hyperfine magnetic field perturbation in a Fe-9Ni host.

Since a Si atom has no magnetic moment and causes no magnetic moment perturbations at Fe and Ni atoms around it, *there are no unknowns* preventing us from making concrete predictions with equation VI-42.

$$\Delta H^{Si}(i,j,k,.09) - \Delta H^{Si}(i,j,k,0) = \alpha_{CEP}\, f(r_j)\, M(^{Fe}_{Ni})\,(.09) \qquad \text{VI-43}$$

is predicted when the Ni concentration of the host changes from 0 to .09. This gives changes of -1.8 kG, -1 kG, and +0.3 kG for $\Delta H_1^{Si}$, $\Delta H_2^{Si}$ and $\Delta H_3^{Si}$, respectively. Adding Ni to the alloy will therefore have an insignificant effect on the "Si satellite", and our value of $N_s^{Si}$ (in equation IVI-5) for Fe-Si alloys should be

unchanged for Fe-9Ni-Si alloys, at least so long as the response parameters $\{f(r_j)\}$ are unchanged with Ni concentration.

In experimental data, the effects of solutes in distant nearest neighbor shells are seen as only a small $c_X$-dependent shift (and sometimes a broadening) of the "unperturbed" main absorption peak. In my experimental calibration work which determined "X satellite" peak intensities from difference spectra of Fe-9Ni-1X and Fe-9Ni alloys, I assumed that this shift of the main peak was the same as the main peak shift in an Fe-1X alloy. However, the effect of not shifting the main peak before differencing, which effectively assumes the elimination of all distant nearest neighbor effects, resulted in only a slight (~ 10%) error in the experimentally determined "X satellite" intensity. This was comparable to the errors from experimental difficulties. I therefore believe that even relatively large Ni-induced changes in the magnetic moments of distant solute atoms will have a negligible effect on the observed spectra.

Although our Fe-9Ni-1Si alloy is a fortunate exception, for Fe-9Ni-1X alloys when X=Cr or Mn, I know of no data for the parameters $\{g_{\mathrm{Ni}}^{X}(r_j)\}$ and $\{g_{X}^{\mathrm{Ni}}(r_j)\}$. Furthermore, the set $\{g_{X}^{\mathrm{Ni}}(r_j)\}$ may depend on the Ni concentration. We must also consider the possibility that the response parameters $\{f(r_j)\}$ may depend on the Ni concentration. These effects are discussed in Chapter X.A.

# CHAPTER VII

# EXPERIMENTAL

## A. Materials and Specimen Preparation.

Commercial 9Ni steel plate of 35 mm thickness was kindly supplied by the Nippon Kokan Company in the QT heat-treated condition. The N.K.K. mill sheet gave the chemical composition listed in Table I in Chapter II. This composition was verified with atomic absorption spectroscopy by Anamet Laboratory. My interest was in studying how the tempering heat treatment (the "T" step) altered microstructural features of the austenitized ("Q" treated) material, so the as-received material was reprocessed in one of two ways. In early transmission geometry experiments a piece of the commercial plate was cold rolled to a thickness of 5 mils, and given a solution treatment at 1100°C in a quartz ampule, as described below for the high purity materials. The "Q" treatment of these specimens also followed the procedure for the high purity materials. Unfortunately, the formation of austenite in these rolled foils was significantly slower than expected from previous work with 9Ni steel [58]; reasons for this are discussed in Section X.B.5.

For later transmission geometry experiments, in backscatter 14.41 keV $\gamma$-ray experiments, and in x-ray diffractometry experiments, the commercial 9Ni material was heat treated as bars with a minimum dimension of 1.2 to 1.8 cm. The bars were enclosed within two sealed stainless steel bags containing pieces of tantalum metal to getter oxygen. A solution treatment was performed at 1050°C for three hours, followed by an iced brine quench. The stainless steel bags were violently ripped open with a sharpened steel rod during the quench. The brine stopped boiling after 1-1/2 to 2 minutes. A similar procedure was followed for the 800°C Q treatment of the bars.

Sections were carefully cut from the center of the Q treated bars with an abrasive wheel saw under flood cooling. For x-ray diffraction measurements, one cut surface was ground on 120 to 600 grit silicon carbide papers with water cooling, and then polished at room temperature for 1 to 2 minutes in a fresh solution of 3 ml HF in 100 ml of 30% $H_2O_2$. Specimens cut for backscatter and transmission Mössbauer experiments were polished directly to thicknesses of 15 mils and 0.5 to 2.0 mils, respectively. All polished surfaces exposed to the atmosphere for more than a minute were given a thin coating of silicone vacuum grease to retard oxidation. (The vacuum grease was removed prior to any further heat treatments.) Only the specimens prepared for transmission geometry experiments were re-used for tempering studies after their Q spectra were obtained. Tempering of these transmission geometry specimens was performed in quartz ampules, as described below for the high purity specimens. Thin specimens for backscatter and x-ray experiments were tempered as thick bars that were cut from the Q treated plate and enclosed in stainless steel bags during tempering. The initial heating rate of these specimens was about 20°C/minute. Water quenching of the tempered bars for backscatter and x-ray measurements was similar to the quench after the Q treatment, as was the further preparation of surfaces for experimental study.

The early Mössbauer spectrometry studies indicated that the difference spectrum technique would be sensitive to some impurity concentrations of 0.1% or less. This necessitated the use of high purity alloys for the chemical composition calibration work. Unfortunately, the expense of the starting materials prevented the use of large bars for heat treatments like those of the commercial 9Ni steel. Consequently the $\alpha' \rightarrow \gamma$ reaction kinetics of the high purity and the commercial materials may not be strictly comparable because their Q microstructures were not prepared in the same way. The high purity alloys

started with Materials Research Corp. MARZ grade Fe of approximately 99.995% purity. Inco Ni shot of 99.95% purity was adequate since the total amount of Ni was relatively small. The X element (Si,Mn,Cr, and C) starting materials for the high purity alloys were at least 99.9% pure. The surfaces of the metal pellets of each element were cleaned, polished and stored in ethanol prior to melting. To minimize surface area, only one pellet of each element was used. Control of the Ni and X element concentrations was obtained by filing the Ni and X pellets until their masses were within 2 mg of the desired amount. Control of the Ni content was especially important because the "X satellite" was revealed by differencing Mössbauer spectra from Fe-Ni-X and Fe-Ni alloys with, hopefully, identical Ni contents. The 20 g high purity ingots were melted in new alumina crucibles in a high vacuum furnace with electrical resistance heating. This furnace was baked out at about 2000°C under vacuum prior to each melt. The ingots were melted at 1650°C for 2 hours under a helium pressure of 2-3 psi over atmospheric pressure. This helium gas helped to increase the specimen cooling rate, which was up to 50°C/minute. After cooling, the surfaces of the ingots and the crucibles showed no contamination. Weight losses of the ingots were only 2 or 3 mg, except for the Mn-containing ingots which showed approximately 10 mg weight losses. The chemical compositions of these ingots were therefore accurately know by calculation from the weights of the starting materials.

For their solution treatment, the high purity ingots were sealed in quartz tubes under a helium pressure of about ¼ atmosphere. A small piece of tantalum metal was also included in the quartz ampule in order to getter residual oxygen. These quartz ampules were placed in a furnace at 1150°C for 3 hours. The ingots were cooled by breaking the hot quartz ampules under water. After polishing, the ingots were then cold rolled into 5 mil foils, with the rolling direction perpendicular to the direction of gravity during melting. Specimens

intended for chemical composition calibration work were further rolled to 1-1/2 mils.

After cleaning the rolled foil and cutting it to size, it was again sealed in a quartz ampule with helium and tantalum and placed in a furnace for its Q treatment. Commercial 9Ni steel foils used in early transmission geometry experiments were also Q treated in this way. Initial heating rates of 100°C/minute were estimated. The austenitizing Q treatment temperature* was 800°C for all alloys with a Ni content of 6% or greater. Fe-3Ni alloys were give a Q treatment at 900°C, and Fe-X binary alloys were Q treated at 950°C. The Q treatments were one hour at 800°C, but were shorter for the higher temperatures. The specimens were cooled from the Q treatment temperature by breaking the quartz ampule under water, or by air cooling in the ampule, depending on whether the specimens were intended for chemical composition calibrations, or for austenite precipitation studies, respectively.

The Q-treated foils were chemically polished at room temperature in fresh solutions of 3 ml HF in 100 ml of 30% $H_2O_2$. With careful polishing technique, specimens intended for X or Ni difference spectrum chemical calibration work were polished to 0.2-0.3 mil thicknesses, so that thickness distortion of their spectra would be small. Specimens intended for succeeding tempering studies were polished to various thicknesses between 0.5 and 2.0 mils. Transmission geometry Mössbauer spectra of these polished Q-treated specimens were taken at room temperature with the specimen mounted in one of three ways: 1.) taped to a simple aluminum holder, 2.) between the pole pieces of a 2.5 kG permanent magnet, and 3.) sandwiched between beryllium discs in a vacuum furnace filled with helium gas. The tempering of the 0.5 to 2.0 mil foils mounted in the

* Mössbauer spectra of the specimens were not affected by the precise choice of the Q treatment temperature. In one test, three Fe-3Ni foils were Q-treated at 800°C, 900°C, and 1000°C, and their Mössbauer spectra showed no discernible differences.

vacuum furnace (mounting no. 3) is described in detail in Section G. and in Fig. 1c.

For experimental mountings nos. 1 and 2, after the spectrum for the Q-treated material was obtained, the spectrometer was used for collecting a pure Fe calibration spectrum while the specimen was being tempered. For tempering, the specimen was again sealed in a quartz ampule. The ampule was loosely inserted in a copper tube in the furnace to help maintain temperature stability and homogeneity. A thermocouple inserted between the copper tube and the quartz ampule suggested an initial heating rate of 50-70°C/minute. The stated tempering temperature was maintained within 5°C. After tempering, the quartz ampule and the copper tube were removed from the furnace and air cooled together. Initial cooling rates of 200°C/minute were estimated. Surface oxidation of the specimens was at worst only apparent as a slight tint, but usually was not apparent at all. Subsequent temperings followed similar procedures, and the collection of pure Fe calibration spectra alternated with the collection of Mössbauer spectra from the specimens themselves.

**B. X-ray Diffractometry and Analytical Scanning Transmission Electron Microscopy.**

The author would be naïve to suppose that even the most reasonable results obtained by Mössbauer spectrometry would be accepted without suspicions by the metallurgical community if they were later found to be in disagreement with measurements by more well-known techniques. Consequently, ancillary measurements were made of the volume fraction of austenite and its chemical composition for comparison with corresponding measurements by Mössbauer spectrometry. Austenite chemical composition information was provided by the scanning transmission electron microscopy (STEM) technique of analyzing characteristic x-ray emissions excited by an electron beam

convergent on an austenite particle. The volume fraction of austenite was quantitatively determined by x-ray diffractometry as described below. X-ray peak shifts and therefore the mean microstrains in the austenite and martensite crystals, were also determined. X-ray data were further processed numerically to deconvolve the instrumental broadening through Rachinger [230] and Stokes [231] corrections, and the deconvolved x-ray peaks were fit to convolutions of Gaussian and Lorentzian functions to determine the mean squared strain and the mean particle size of the austenite and martensite crystals.

This more sophisticated x-ray and STEM work is worthy of a more detailed discussion than can be supplied here [232] , but the results of the STEM measurements of the chemical composition of the austenite formed in commercial 9Ni steel after temperings at 600°C are now described. The Ni content of the austenite determined by STEM appeared to increase from 14% to 18% as the tempering time increased from 1 hour to 21 hours, and remained at 18% for longer tempering times. These measurements had good precision. However, the absolute Ni composition of the austenite found for short tempering times may be artificially low because of x-ray excitations in the adjacent martensite matrix (after a 1 hour tempering the austenite particles have dimensions as small as a few hundred angstroms). STEM measurements determined a Mn composition of the austenite of 2-3%. The segregation of Cr and Si to the austenite was indicated by STEM. Unfortunately, difficulties with a background of Cr $K_\alpha$ x-rays and a poor signal-to-noise ratio impaired the quantitative determinations of Cr and Si concentrations of the austenite, respectively. Analysis of C concentration in the austenite by electron energy loss spectrometry was not attempted.

X-ray diffractometry measurements of the austenite volume fraction were performed with a diffractometer of the Bragg-Brentano configuration, model

3488K manufactured by Picker X-ray, Inc. The Fe $K_\alpha$ x-ray tube was always operated at 40 kV with a tube current of 7 ma. A parafocusing LiF monochrometer in the diffracted beam was used to enhance the effective energy resolution of the Th-activated NaI scintillation counter. Output pulses from the counter preamplifier were sent to a Bay Engineering Company x-ray diffractometer controller unit model PAD-8 for shaping, energy window discrimination, and counting. Counting at each $2\vartheta$ angle proceeded for times from 5 sec to 300 sec, depending on the peak intensity. After the pre-selected counting time, the $2\vartheta$ angle and corresponding number of counts were punched out on paper tape, and the PAD-8 controller incremented a stepper motor to advance the $2\vartheta$ angle by 0.05°. Although the x-ray peaks typically had a width in $2\vartheta$ angle of less than 1°, the diffractometer was scanned over a range of 5° to 15° in $2\vartheta$ angle to accurately measure the tails and background associated with each peak. The completed paper tapes were read into the Z-80 computer system of the Mössbauer spectrometer, and stored on floppy disc for later processing.

Determinations of the volume fraction of austenite were inspired by the method of Miller [233,234], which averages the 311 and 220 austenite peak intensities* , I(311) and I(220), and compares them to the 211 martensite peak intensity, I(211):

$$vol\%\,\gamma = \frac{M\frac{1}{2}[I(311) + I(220)]}{M\frac{1}{2}[I(311) + I(220)] + I(211)} \qquad \text{VII-1}$$

The peak intensities, I(311), I(220), and I(211), were determined by numerical integration of the number of counts in the peak minus a sloping linear background. The background was usually defined by the average intensity of the first and last ten data points in the $2\vartheta$ range. For Mo $K_\alpha$ x-ray diffractometry,

* The $311\gamma$ and $220\gamma$ x-ray peaks generally had an intensity ratio of 2:1, but this ratio varied by + 15% from specimen to specimen, possibly indicating some textural variations in the orientations of austenite crystals.

Miller's diffraction work gave $M$ = 1.4 for equation VII.1. When our Mössbauer spectrometry data were converted into volume fraction of austenite as described in Section VIII.C, correlation to x-ray diffractometry data suggested that M=1.25 for our Fe $K_\alpha$ x-ray work with 9Ni steel. Using M=1.25, the agreement between the volume fraction of austenite determined by Mössbauer spectrometry and x-ray diffractometry methods was within the expected experimental error (usually less than 1-2%). This excellent agreement between Mössbauer spectrometry and x-ray diffractometry measurements of austenite volume fractions has previously been noted by other investigators [23-25,27] for different alloys and calibration standards.

A hot stage was to have been installed on the Picker diffractometer so that the amount of austenite formed at 600°C could be measured directly. Unfortunately, the x-ray hot stage is still not available, and Mössbauer spectra taken at 500°C were the only way to determine the amount of austenite which transformed martensitically upon cooling to room temperature.

**C. Radiation Source.**

The radiation source used in these experiments was fabricated by the Radiochemical Center at Amersham, England. The $^{57}$Co of the source was diffused into a Pd disc of 6$\mu$m thickness by 7 mm diameter. The Radiochemical Center measured a source linewidth, $\Gamma_s$ (of Section III.B. and Eqn. VIII-4), which was 0.11 mm/sec. Over the duration of the experiments, the source intensity decayed from 105 mCi to 40 mCi. When the source intensity was 70 mCi, I measured $\Gamma$s by collecting a Mössbauer spectrum of absorption peaks nos. 3 and 4 of a pure Fe absorber. After assuming an absorber linewidth of 0.0937 mm/sec, and after correcting for a thickness distortion of 0.006 mm/sec from the 5$\mu$m absorber, $\Gamma_s$ was found to be 0.12 mm/sec. The source was epoxied to an aluminum rod that threaded onto the Doppler drive transducer, and was

covered with a mylar window for protection. The source was at room temperature, 18 ± 1/2°C, for all experiments.

An effect known as "cosine broadening" of Mössbauer peaks occurs when the radiation source is too close to the specimen. Those $\gamma$-rays which travel from source to specimen at the small angle $\Theta$ with respect to the direction of the radiation source velocity will receive only the fraction 1-cos$\Theta$ of the Doppler shift expected from the radiation source velocity. The source-specimen separation was nearly 4 in., and the specimens were usually less than 3/4 in. wide. Using the calculated results of reference [27], Fig. 6, one finds an approximate cosine broadening of peaks nos. 1 and 6 of about 0.005 mm/sec. For my experimental data this amounts to an increase in width of peaks nos. 1 and 6 of about 0.2 data channels. This is not a large effect, and by maintaining the same source-specimen geometry from run to run, the cosine broadening was kept constant. Cosine broadening therefore had a minimal effect on my difference spectra.

**D. Detectors.**

Three different detectors were used for the Mössbauer spectrometry experiments. Backscatter 14.41 keV Mössbauer spectra were collected with a unique detector of my own design. Patent considerations forbid disclosure of details of its construction and operation to readers who are not employed by the United States Department of Energy.

Early transmission geometry experiments were performed with a conventional Kr + 10% $CO_2$ gas filled proportional counter manufactured by LND, Inc. This detector showed a saturation behavior which was responsible for a peculiar asymmetric distortion of Mössbauer absorption peaks. This distortion was especially prominent when the count rate at the detector was large (14.41 keV $\gamma$-ray count rates of 30 kHz) and the absorption peaks gave large dips in count rate (a

ratio of peak depth to background count rate of ≥ 10%). The magnitude of this asymmetry was enough to cause the observed count rate on the right hand side of a strong absorption peak to be up to 0.5% larger than on the left hand side. I believe that this peak distortion was due to a detector "recovery" effect. At low count rates the anode of a gas-filled proportional counter collects an effective charge which is the same for each detected photon of monochromatic radiation. However, when the average count rate of these monochromatic photons becomes large enough such that a second pulse frequently arrives before the detector has recovered from the previous pulse, the collected charge from this second pulse will be less than that of the first pulse. Consequently the second pulse may not result in a voltage pulse from the main amplifier that is large enough to fall within the window of the single channel analyzer, and may not be counted. Missed pulses are a well-known consequence of detector recovery phenomena.

Unfortunately, the usual recovery effects associated with pulse pair pileup cannot explain the observed asymmetry of my absorption peaks because the time spent scanning a Mössbauer peak was 4 msec, and the recovery time usually associated* with pulse pair pileup is less than 0.1 msec. The number of missed counts would therefore expected to be equal on both sides of the absorption peak. I suspect that my Kr + $CO_2$ gas filled proportional counter had a recovery after high count rates that persisted longer than is normally expected of well-quenched proportional counters, possibly because of complicated ion neutralization processes at the wall of the detector. If this recovery persisted, even only weakly, for about a millisecond, the detector output pulse

* The mobile electrons are collected quickly at the anode. The detector recovery time is determined by the time required for the less mobile positive ions to drift to the cathode and become neutralized. If a second ionizing event (detected photon) occurs before the positive ions have drifted to the detector wall (cathode), the remaining positive ions from the first pulse will neutralize some of the electrons created in the second event. The net number of electrons collected by the anode will be thereby reduced for the second event.

intensity will have recovered slightly from the high background count rate after the spectrometer scanned through a large dip in count rate. The output pulse height would therefore increase as the absorption peak is scanned, and the counting efficiency at each of the two sides of a strong absorption peak would consequently be different.

Specimen to specimen variation in the absorption peak intensity caused variations in this asymmetric peak distortion. Such variations caused substantial intensities to appear in the difference of spectra from different specimens. Unfortunately, these artificial difference spectrum intensities overlapped the intensities due to Ni and X composition differences. Fortunately, the magnitude of this asymmetric peak distortion could be accurately determined experimentally, even for peaks that were asymmetric anyway. The cyclic motion of the Doppler drive enables the collection of twin pairs of Mössbauer spectra that are associated with opposite accelerations of the drive. The peaks of each spectrum should be mirror images of each other, after they are corrected for the parabolic intensity distortion described in Section VIII.A.. The asymmetric peak distortion will break this mirror symmetry because the count rate distortions will occur on opposite Doppler shift energy sides of the peaks in each spectrum. By inverting one of the twin spectra and overlaying it on the other spectrum, one could thereby identify and quantify any asymmetric peak distortions. This operation was performed for all experimental data.

I was able to reduce this asymmetric peak distortion by using a detector filled with an Ar+10%$CH_4$ gas mixture. Ar does not have the advantageous 14.3 keV K absorption edge characteristic of Kr gas, so its specific ionization efficiency for 14.41 keV $\gamma$-rays is much lower. For efficient $\gamma$-ray detection with Ar gas it is therefore necessary to permit the $\gamma$-rays to transverse a longer length of gas. Widening the detector tube has the undesirable effect of increas-

ing the drift time of the Ar ions to the detector wall, and slowing the detector response time. Consequently the unconventional end-window detector design of Fig. 5 was employed instead of a conventional side window design. The aluminium cathode tube was 9 in. long by 2-1/2 in. diameter, and was machined to a narrow wall thickness so that the Compton scattering background would be reduced. The 0.002 in. tungsten anode wire was epoxied into the center of the front entrance window. The 0.03 in. thick acrylic plastic window had good transmission of 14.41 keV $\gamma$-rays while reducing the count rate for Fe $K_\alpha$ x-rays and other lower energy radiations. Acrylic plastic insulators around the ends of the anode wire help to prevent the counting of ions formed in the region near the ends of the cylindrical cathode*. The radiation shield (made of sundry metals) at the front of the detector helps to keep the incident $\gamma$-ray beam away from the walls of the detector, and reduces the count rate from $\gamma$-rays that miss the specimen. A steady flow of an Ar + 10% $CH_4$ gas mixture through the detector at a rate of about 200 ml/minute was maintained, and the vented gas bubbled through ethyl alcohol to eliminate back diffusion of atmospheric oxygen. The anode was biased through the preamplifier at + 2000V by a Power Designs HV-1556 regulated high voltage power supply.

In my experimental configuration the count rate with our end-window Ar + $CH_4$ detector was over twice that of the conventional Kr + $CO_2$ detector. The output pulses from the main pulse amplifier are recorded in the oscilloscope photograph of Fig. 5. Time exposures (20 sec) of oscilloscope traces are shown which were triggered by the pulses themselves (on the left), and triggered by the output from the adjusted single channel analyzer (on the right). In spite of the fact that the $\gamma$-ray beam had traversed a specimen foil mounted in the

* In these end regions the electric field is distorted. In the end region the ionization cascade process, and therefore the output pulse height, differs from that in the rest of the active volume of the detector.

vacuum furnace, the energy resolution is seen to be excellent; the 6.3 keV Fe $K_\alpha$ x-rays, the 14.41 keV $\gamma$-rays, and the 21 keV Pd $K_\alpha$ x-rays are all well-resolved. Most importantly, with the new Ar + $CH_4$ detector the asymmetric peak distortion due to the long recovery time effect was reduced by a factor of 5 below that of the Kr + $CO_2$ detector (see Fig. 8). Nevertheless, the following steps were taken to further reduce this distortion and its effects: 1.) the specimens for calibration work were very thin (their $\approx 5\mu m$ thickness also minimized their thickness distortion). 2.) the single channel analyzer window was set as wide as possible without counting too many 6.3 or 21 keV x-rays, 3.) the gas flow and electronics for the detector were never turned off, and 4.) the radiation source was substantially weaker by the time this new detector was operational. In addition, when calibrating the intensities of the "X element satellites" (i.e. finding $N_S^X$ of equation IV-5) their difference spectrum intensities around both peaks nos. 1 and 6 were compared; the small observed difference in the two satellite peak intensities (10% or less) reflects the smallness of this asymmetric peak distortion.

All three detectors were used with the charge sensitive preamplifier model CSP-400A manufactured by Austin Science Associates. A conventional capacitor input to a gate of a field effect transistor served to integrate the negative charge deposited on the anode wire. The preamplifier output was sent to the ND510 main amplifier, whose shaping circuit was modified to be compatible with the output from the preamplifier. The slow decay of the charge on the capacitor input to the preamplifier was cancelled by a differentiator stage in the main amplifier. This cancellation enabled the main amplifier to reach a flat baseline voltage shortly ($\sim 5\mu sec$) after the peak of its output pulse. Further baseline restoration and D.C. offset correction was provided by a baseline restorer/linear gate model ND505. The single channel analyzer, model ND602,

was operated in window mode with independent upper and lower level thresholds. The pulse pair resolution of this single channel analyzer unit was specified as 600 nsec by Nuclear Data Inc., which also manufactured the ND505 and ND510 units. These three units were mounted in a nuclear instrument module (NIM) bin / power supply designed at the Lawrence Livermore National Laboratory in conformance to AEC TID-20893.

**E. The Doppler Drive and Mechanical Vibrations.**

The radiation source was connected to the reciprocating drive shaft of an electromagnetic transducer model K-3 manufactured by Austin Science Associates. The transducer contains two coils, each moving in its own steady magnetic field. The coils are both mechanically connected to the drive shaft, but are electrically independent. A long, precisely wound coil moves in a small magnetic gap to serve as the sensor of the drive shaft velocity. The voltage induced across this coil is accurately proportional to the rate at which its turns enter and leave the magnetic gap. End effects are avoided with a long coil, so if the turns of the coil are accurately spaced, the coil voltage will be accurately proportional to the velocity of the drive shaft. This "velocity signal" is carefully shielded and sent to an Austin Science Associates model S-600 Mössbauer spectrometer controller.

The most desirable periodic motion for the radiation source is a cycle in which its velocity increases linearly with time to a maximum positive velocity, and then decreases linearly with time to a maximum negative velocity; the radiation source should alternately move with a constant positive acceleration towards the absorber, followed by a constant negative acceleration. The velocity signal is referenced to a triangular waveform derived from the 4 MHz clock of the Z-80 computer. After a long chain of frequency dividers, a 6.2500 Hz square wave is derived and sent to the S-600 where it is integrated to produce

the desired 6.25 Hz triangular reference waveform. Synchronization of the valley and the peak of this triangular waveform to data channels 0 and 512 is assured by using the frequency divider chain as a binary data channel counter that is read by the Z-80 microprocessor during data service routines (See Section VII.C.).

The difference between this desired triangular reference waveform and the actual velocity signal is computed by a difference amplifier in the S-600, and a power amplifier sends the inverse of this error signal to the second coil, the drive coil, in the transducer. When the velocity signal and the triangular reference waveform are not properly balanced at the input of the difference amplifier, the voltage applied to the drive coil will accelerate the drive shaft to rapidly correct for this difference. The velocity signal and the reference waveform at the inputs of the difference amplifier will never be precisely balanced because the drive coil must supply the force required for the constant acceleration of the drive shaft. It is expected that this force should be provided by a constant drive voltage from the power amplifier during half-cycles of constant acceleration, and a large spike at the two points per cycle when the acceleration is discontinuous. In the absence of other forces, over most of the drive cycle the square wave drive voltage should not require a high gain error amplifier to rapidly correct the transducer velocity. This is fortunate because the drive shaft itself is subject to a high frequency oscillation at about 8 kHz in which the velocity sensor coil and the power coil move out of phase. This oscillation is mechanically damped by the phenolic plastic in the moving components, but still serves as the effective limit to the error amplifier gain. (An 8 kHz whine is clearly audible from the transducer at excessive gains.) Unfortunately, there are other time-varying forces on the drive shaft due to vibrations of its stiff centering springs, and due to vibrations from the laboratory

floor. These forces require rapid correction of the transducer velocity, and the accuracy of their correction is proportional to the gain of the error amplifier.

Vibrations of the centering springs were damped with moderate effectiveness by fresh pieces of foam rubber squeezed between the springs and the transducer housing. Vibrations of the laboratory floor were damped by the mechanical suspension shown in Fig. 4. The table of the Mössbauer spectrometer was centered on a partially inflated truck inner tube that rested on a box of sand and foam rubber. The table weighed several hundred pounds because of its lead shielding, and since the inner tube was so compliant, the table and suspension displayed no vibrational modes at frequencies higher than 2 Hz. This was much slower than most of the vibration spectrum of the laboratory floor. In spite of these attempts to reduce erratic vibrations, I believe that mechanical vibrations of the centering springs and the laboratory floor were the major source of artificial Mössbauer peak broadening. Consequently, to help prevent specimen to specimen variations of this peak broadening, the Doppler drive was never turned off, and the author guarded the spectrometer against unwarranted laboratory vibrations. Doppler drive linearity also required good electrical practice in isolating the S-600 from low and high frequency fluctuations of the mains supply, and in careful shielding and grounding of the velocity sensor signal.

**F. The Computer System.**

The computer system of the Mössbauer spectrometer served to control the collection of data. store the data, and process the data. Numerical data processing is the subject of Chapter VIII, here the data collection and storage is discussed. The computer system was built around a Mostek Z-80 microprocessor, which in 1977 seemed a good choice from hardware and software standpoints. I chose a Northstar Computers, Inc. floppy disc system which included a

5 in. floppy disc drive and interface hardware for the computer mainframe. The software in this system included a monitor, a disc operating system, and a BASIC interpreter. The I.M.S. Associates, Inc. mainframe was modified to actively terminate the S-100 bus and permit a 4 MHz clock cycle. The system memory is currently 56 kilobytes. A standard keyboard and a homemade paper tape reader are parallel interfaced to the computer through a Processor Technology model 3P+S interface card and appropriate input software.

Graphics hardcopy is provided by a Diablo Hytype I daisy wheel printer. A homemade interface card for the S-100 bus, and home-written software codes permit the positioning of characters on the printout in increments of 1/60 in. horizontally and 1/48 in vertically. This resolution is adequate for plotting spectra, and the negligible mechanical drift of the printer permits a precise comparison of different spectra by overlaying them. The importance of precise graphics hardcopy to the experimental work can hardly be overstated.

The major adaptation of the microcomputer for Mössbauer spectrometry was the construction of specialized hardware and software to count pulses from the single channel analyzer, and to synchronize the timing of the data collection [235] (See Fig. 6). This adaptation permits the microcomputer to serve multichannel scaler. An electronic gate served to switch the detected pulses to one of the two data counters for each data cycle. While one of the data counters was actively counting pulses, the other data counter was being serviced by the central processor. In this way there is no lost counting time while the central processor is servicing one of the counters. In the data service routine the central processor reads the contents of the inactive counter, and stores the contents in consecutive locations in the computer memory that serve as the $n^{th}$ data channel. This inactive counter is then filled with the contents of the $n + 2^{nd}$ data channel, and the central processor waits* for its next

* Data analysis programs in the language BASIC were occasionally run during these waiting periods.

interrupt signal. At the time of the interrupt, the gate switches the detected pulses to the formerly inactive counter, and the central processor jumps to the service routine for the other counter. The data from this currently inactive counter is stored as the $n + 1^{st}$ data channel, and this counter is filled with the contents of the $n + 3^{rd}$ data channel. This alternation of active and inactive counters occurs 1024 times for each 1/6.25 Hz cycle of the Doppler drive. The data service routines were written in Z-80 machine language code, and made efficient use of the register exchange and data transfer instructions.

All timing signals for data collection are derived from the 4 MHz computer clock through a synchronous counter that serves as a frequency divider. This counter is read by the central processor during the data service routine so that it will know the memory location where the data belongs. The timing of the interrupts is derived from this synchronous counter. The most significant bit of this counter, which changes 12.5 times per second, is also used as the synchronization signal for the S-600 Doppler drive controller. All custom hardware for the S-100 backplane was implemented on three 5 in. by 10 in. cards that employed 65 integrated circuits and about 1500 wire-wrapped connections.

**G. Tempering Experiments in the Vacuum Furnace.**

The vacuum furnace for high temperature Mössbauer spectrometry experiments was originally a model VF-1000 manufactured by Austin Science Associates. However, the VF-1000 was substantially redesigned so that eventually only the original vacuum chamber remained (See Fig. 7). A reliable heating element with good temperature homogeneity was constructed. A copper bore tube with a 1/8 in. wall thickness was first coated with a ceramic cement* on its outer wall. One layer of 22 gauge Kanthal A-1 resistive wire was wound around the

* I used Ceramacote ®
made by Aramco, Inc.

coated bore tube in a bifilar (non-inductive) helix. The density of turns was greater at the ends of the bore tube where the heat losses are larger. The lead-in wires had poor heat dissipation in the furnace vacuum, so reliable lead-in wires were made of thicker (18 gauge), less resistive, Kanthal A-1 wires that were attached to the heating coil by numerous spot welds over a 1 in. length. A final layer of ceramic cement was used to cover the heating element windings, and the completed heating element was wrapped with tantalum sheet for thermal radiation shielding. Tantalum annuli were used for radiation shielding at the ends of the heating element and inside the copper bore tube. The heating element assembly was wrapped with fiberous high temperature insulation and was mounted in a transite frame that centered it accurately in the vacuum chamber. Foil specimens for transmission geometry Mössbauer spectra were mounted in the center of the heating element bore tube. For temperature homogeneity, the specimen was sandwiched between six beryllium discs with a total thickness of 0.13 in. I found it necessary to clamp the discs together with about 16 molybdenum circumferential edge clips (See Fig. 7). This specimen package was centered in the furnace with two copper rings that fit accurately inside the copper bore tube. The $\gamma$-ray windows of the vacuum chamber were beryllium discs of 0.006 in. thickness that were epoxied over 3/4 in. holes in the stainless steel end flanges. These epoxy vacuum seals required water cooling to ensure their integrity when the furnace was hot. A small Mössbauer peak near zero Doppler shift energy was present in all Mössbauer spectra taken with this furnace. It is unclear whether this background peak was due to the stainless steel end flanges or iron impurities in the beryllium. Fortunately, this background spectrum was largely cancelled out when differences of spectra were taken.

The vacuum furnace was pumped continuously during the collection of a

Mössbauer spectrum. Vibrations in the pumping line from the Welch model 1402 mechanical pump were damped by holding the pumping line rigidly at several locations. A liquid nitrogen cold trap was installed in the pumping line. The pressure near the vacuum pump was about 5 mTorr, but the pressure in the furnace itself was not measured. Oxidation of the specimen after 10 days at 500°C and 600°C was generally slight; the beryllium metal in the specimen package was an efficient oxygen getter. However, the temperature of the specimen was affected by oxidation of the beryllium discs. Calcium metal, which oxidizes more readily than beryllium, was used as an oxygen getter in the vacuum furnace, and the calcium was effective in keeping the beryllium clean for several days of operation. Nevertheless, it was frequently necessary to remove the oxide from these beryllium discs when the specimen was changed. The extreme toxicity of beryllium dust necessitated a cleaning procedure in which the discs were sanded under a bath of ethyl alcohol. After rinsing, the discs were polished in a solution of 70% $H_2PO_4$, 25% $H_2SO_4$ and 5% $HNO_3$. All solutions contaminated with beryllium were disposed by the environmental health and safety group at the Lawrence Berkeley Laboratory.

The furnace temperature was controlled by an A.C. phase angle fired proportional controller model 919, and a 10 ampere thyristor unit model 931, manufactured by Eurotherm International. The output from a chromel-alumel thermocouple mounted between a copper ring and the specimen package was referenced to the controller set point to maintain the specimen temperature with closed-loop temperature control. In analogy to the problem caused by the phase lag between the velocity coil and drive coil in the Doppler drive, the response time of the reference thermocouple to the heat input resulted in characteristic thermal oscillations of about 0.002 Hz. The model 919 controller unit was designed for electronic damping of this oscillation through indirect

adjustments of error amplifier gain and response time characteristics. The controller and furnace were operated as a slightly overdamped system for temperature control at 500°C. Heating and cooling cycles were performed with manual control of furnace power so that temperature changes of 20°C/minute were achieved without overshooting or undershooting the final temperature by more than 5°C. A second chromel-alumel thermocouple for monitoring the furnace temperature was located near the end of the copper bore tube. The two thermocouples generally agreed within 2°C.

The Curie temperature of iron is about 770°C, so at 500°C small temperature drifts or temperature inhomogeneities of the specimen resulted in artificial broadenings of the absorption peaks. Such peak distortions from temperature variations provided a much greater need for precise temperature control than that required for reproducible metallurgical reactions during tempering. Mössbauer spectra of pure Fe taken at 470°C, 500°C, and 530°C showed that at 500°C the peaks nos. 1 and 6 moved by +0.0027 mm/sec/°C and -0.0045 mm/sec/°C, respectively. The temperature dependence of the mean positions of peaks nos. 1 and 6 arises from both: 1.) the second order Doppler shift (See Section III.B.), which shifts both peaks towards more negative velocities with increasing temperature, and 2.) the temperature dependence of the $^{57}$Fe hyperfine magnetic field, which shifts both peaks to lower magnitudes of velocity with increasing temperature. From the above data we find that near 500°C the temperature dependence of the second order Doppler shift is 1/2(-0.0045 + 0.0027) mm/sec/°C = - 0.0009 mm/sec/°C, and the temperature dependence of the $^{57}$Fe hyperfine magnetic field is found to be: $\frac{1}{2}(-0.0045 - 0.0027)\text{mm/sec/}^\circ C(\frac{-330\text{kG}}{5.6\text{mm/sec}}) = +0.21\text{kG/}^\circ C$. In 470°C 500°C and 530°C spectra, it was found that peaks nos. 1 and 6 of NKK 9Ni steel showed almost the same temperature dependence as did the pure Fe peaks; the 9Ni

peaks were about 10 - 20 % less temperature-dependent, but this is not experimentally significant.

Mössbauer spectra of pure Fe foils gave an excellent indication of the performance of the vacuum furnace. After the furnace was debugged, Mössbauer spectra of an 0.0008 in. Fe foil actually had sharper peaks at 500°C than at room temperature. This is expected on the basis of different thickness distortions at the two temperatures. From equation III-8 we know that the absorption efficiency will be significantly less at 500°C than at room temperature, so at 500°C the thickness broadening of the absorption peaks will also be less. After correcting for these differences in thickness broadening, (see Eq. VIII-6) it was found that the widths of pure Fe Mössbauer peaks at 500°C and at room temperature were almost identical; their difference indicated that at 500°C the specimen temperature was constant within ± 1/2°C.

Except near the end of very long temperings when the amount of austenite would not change significantly during the collection of a Mössbauer spectrum, few Mössbauer spectra were obtained at the tempering temperature itself. Conveniently, the amount of austenite present after tempering at 600°C is expected to remain unchanged if the specimen temperature is reduced and maintained at 500°C. Consequently, after each 600°C tempering the specimen was brought to 500°C for the collection of a Mössbauer spectrum, as indicated in Fig. 1c.

Although the amount of austenite present at 500°C could be accurately determined, calibration work showed that the significant $\Delta H_i^{Ni}$ and $\Delta H_i^{X}$ parameters were both positive at 500°C, so changes in Ni and X concentrations of the martensite could not be independently determined. (This is discussed in Chapter IX). The tempering of Fe-Ni binary alloys involved no segregation of X solutes, so in their 500°C Mössbauer spectra there was no ambiguity about the segregation of Ni. In fact, the austenite in Fe-Ni binary alloys mostly

transformed to martensite upon cooling to room temperature, so their 500°C Mössbauer spectra were essential for determining both austenite content and changes in the Ni content of the martensite after tempering. In later experiments with Fe-Ni binary alloys, the specimen was not cooled to room temperature after spectra were obtained at 500°C, but was instead tempered at 600°C again.

In Fe-9Ni-1Mn and commercial 9Ni alloys, the austenite was more stable; after moderate tempering times there was no observable transformation of austenite to martensite upon cooling to room temperature. The heating cycle of Fig. 1c was useful for these alloys because the spectra taken at room temperature were able to give independent information on Ni and X composition changes. Unfortunately, I did not have the capability of applying a saturating magnetic field to specimens in the vacuum furnace at room temperature, so the anisotropic hyperfine magnetic field perturbations in these spectra were uncontrolled . Therefore the later chemical segregation experiments with commercial 9Ni steel, without the vacuum furnace but with the magnetic field, gave more accurate chemical segregation information. It was, of course, important to have previously verified that the amount of austenite present in Fe-9Ni-1Mn and commercial 9Ni specimens was unchanged after cooling to room temperature. Sadly, independent measurements of Ni and Cr or Ni and Si chemical segregations in Fe-Ni-Cr and Fe-Ni-Si alloys were not very quantitative because substantial amounts of the austenite in these alloys transformed to martensite upon cooling to room temperature.

**H. Magnet.**

For later transmission geometry Mössbauer experiments, and some backscatter geometry Mössbauer experiments, a saturating magnetic field was applied to the specimen so that anisotropic hyperfine magnetic field

perturbations would be reproducible for each spectrum obtained with the same specimen (See Sections III.C. and X.A.5.). Our magnet used two $Co_5Sm$ permanent magnets for pole pieces with a vertical dimension of 1.4 in. (the specimen itself was 0.7 in. high by 0.75 in. wide). The return paths for the magnetic flux were along 1 in. square stock of 1018 steel. The flux path was essentially shaped as a theta ($\vartheta$) with the magnetic gap in the center of the cross line of the $\vartheta$. Symmetric flux return paths above and below the gap help ensure a homogeneous magnetic field in the gap [236]. The magnetic field in the the gap was 1.9 to 2.7 kG, as measured with a Hall probe. By symmetry we expect that the magnetic field always lay in the plane of the specimen. Variations in field direction within the specimen plane are expected to cause only minor effects in difference spectra involving different temperings of the same specimen because the specimen was always carefully oriented in the same way in the magnetic field. There was no observable background spectrum due to iron in the $Co_5Sm$ or the 1018 steel yoke.

**I. Spectrometer Performance and Operation.**

It was crucial in experimental practice to maintain the geometry of the radiation source, specimen, and detector as similar as possible from run to run. All other experimental parameters were kept as constant as possible. (The Doppler drive, detector, and all electronics except the printer and floppy disc drive, were not turned off for months at a time.) Thickness distortions, baseline distortions, instrumental broadenings, and counting efficiencies were thereby maintained as similar as possible for all spectra. Meticulous attention to these details ensured that the experimental errors in all spectra were very similar, so upon differencing these errors will cancel. This cancellation of systematic experimental errors was the major reason for my preference of difference spectrum procedures over other methods of data analysis.

The performance of a Mössbauer spectrometer can conveniently be judged on the basis of how well the spectrum it gives for a very thin foil of pure Fe corresponds to six Lorentzian curves of appropriate positions, heights, and width. When the Doppler drive scanned a velocity range of about ± 2.5 mm/sec, peaks nos. 3 and 4 were found to have a full-width-at-half-maximum (FWHM) of 0.21+ mm/sec, which compares very favorably with the theoretical FWHM of 0.187 mm/sec. Most of this excess broadening of the experimental peak was presumed to arise from the non-monochromatic nature of the radiation source. When larger velocity ranges were scanned by the Doppler drive, small relative errors in the velocity of the Doppler drive become more important. When the scanned velocity range was ± 7 mm/sec, linewidths of 0.24, 0.23, and 0.22 mm/sec were found for the average FWHM of peak pairs 1 and 6, 2 and 5, and 3 and 4, respectively. The reproducibility of pure Fe absorption peak positions and widths was often excellent; in Fig. 8b a nearly flat baseline is seen for the difference of two pure Fe spectra obtained at different times (the differenced peaks were larger than the Fe-Ni-Si peaks of Fig. 8a). I also computed the difference between peaks in a spectrum from a thin specimen and computer-generated Lorentzian functions of appropriate widths, positions, and heights. At peaks nos. 1 and 6 this difference intensity was not exactly a flat line, but the difference amplitudes were only about as large as the data scatter of Fig. 8b.

Without any electric quadrupole effect the separations between peaks nos. 1 and 2, 2 and 3, 4 and 5, and 5 and 6 should all be exactly the same. Since the electric quadrupole splitting in pure Fe is barely measurable [98,99], the Doppler drive linearity was adjusted so that these separations were the same. In early experiments [128] we looked for the electric quadrupole splitting in spectra from Fe-12Ni alloys, and possibly found it to be three times as large as

that of iron metal.

The major shortcoming of the Mössbauer spectrometer was in the long term stability of its velocity scanning range. Whenever possible, pure Fe spectra were collected every day or so to check for drifts in positions of peaks. These positions frequently changed by less than 0.1 data channels for periods of one week or longer. Unfortunately, sudden increases or decreases in the velocity scanning range, which occurred symmetrically about the zero Doppler shift energy, caused shifts of peaks nos. 1 and 6 of up to 0.5 data channels. The source of these shifts was never identified, but must have involved a change either in the amplitude of the triangular reference waveform, or in the sensitivity of the velocity sensing signal in the Doppler drive system. It was possible to correct spectra taken before and after such a shift so that they could be differenced without large difference peaks due to the shift itself (See Section VIII.A.). Unfortunately, there was occasionally some uncertainty about the appropriate magnitude of such a correction, and a Doppler drive with greater long term stability would have been superior for the difference spectrum work. It is the opinion of this author that the most valuable experimental development for furthering the difference spectrum methods that were used for chemical analysis, would be the development of a Doppler drive system with improved long-term stability. A closed-loop drive system that uses an optical interferometer for generating a velocity sensing signal could provide such an improvement.

Counting statistics limit the quality of Mössbauer spectra by providing an uncertainty for each data channel that is dependent on the number of counts in that channel. For most transmission geometry experiments the peaks have a maximum dip in the number of counts below the background count, D, that is much less than the background count itself, B. Therefore the data scatter is

effectively determined by the background count. In my work I needed to accurately measure the *areas* of peaks, so the signal-to-signal-uncertainty ratio (S/U) was effectively:

$$S/U = D\sqrt{\frac{W}{B}}$$

where $W$ is the width of the peak in data channels.

The S/U ratio can be improved with a longer data collection time, but a practical limit of a few days was imposed by the long term instability of the Doppler drive. For the spectrometer, $W$ was fixed by the choice of velocity scanning range, and the effects of incident $\gamma$-ray intensity and detector performance were the same for all specimens. The most effective remaining way of increasing the S/U ratio was to increase the specimen thickness. For thin specimens the maximum dip, D, is approximately proportional to the specimen thickness, while B actually decreases a little with specimen thickness. Unfortunately, the thickness distortion will also increase. In essence, the choice of specimen thickness for transmission geometry experiments amounts to balancing the S/U ratio against the thickness distortion. For calibration work with Fe-9Ni alloys, I used thin (0.0002 in.) specimens. After several days of counting, I collected a spectrum from them with $B \simeq 6\times10^6$, $D \simeq 2\times10^5$, so with $W \simeq 15$ , the S/U ratio will be over 200 for a spectrum requiring little thickness distortion correction. In tempering studies, thicker (0.001 in) specimens were used so that a set of clean spectra were obtained before the Doppler drive changed its velocity scanning range. The thickness distortion corrections were consequently larger (and less certain) for the tempering experiments.

I point out that the scatter in a difference spectrum is always greater than the scatter in the two spectra that are differenced. With regard to peak intensities, if two spectra have peaks with uncertainties of $\sqrt{WB_1}$ and $\sqrt{WB_2}$ in area, the corresponding area uncertainty in their difference spectrum will be

$\sqrt{W(B_1+B_2)}$. If normalized differences are computed by multiplying $B_2$ by $N$, the uncertainty in the corresponding difference spectrum area will be $\sqrt{W(B_1 + N^2B_2)}$. A better S/U ratio in the difference spectrum will be obtained for a fixed counting time by dividing the counting time equally between the two spectra to be differenced. However, since the Q spectrum served as the reference for many other spectra in tempering experiments, the S/U ratio of the Q spectrum was usually 1.5 to 1.8 times better than spectra from the tempered specimen.

The advantages of backscatter 14.41 keV $\gamma$-ray Mössbauer spectrometry in specimen preparation and in its consistency of thickness distortions from specimen to specimen [237,238] motivated me to try to develop the backscatter technique for chemical analysis. I now enumerate the differences in S/U ratio of backscatter and transmission geometry Mössbauer spectrometry experiments. After resonant absorptions by $^{57}$Fe nuclei in the specimen, the backscatter experiment detects only re-emitted 14.41 keV $\gamma$-rays. Because of competition from internal conversion processes, these 14.41 keV $\gamma$-rays represent only about 1/9 of the total number of $\gamma$-ray absorptions. On the other hand, in transmission geometry Mössbauer experiments the type of re-emitted radiation is not relevant, since the absorption itself causes the observed loss of intensity from the detected $\gamma$-ray beam. For $\gamma$-rays traveling the same distance into and out of the specimen material, the peak in the backscatter spectrum will have only about* 1/10 of the number of counts in the dip of the transmission geometry peak.

However, although the signal intensity is 9 times lower for backscatter

* There are also geometrical differences in the number of $\gamma$-rays which can contribute to the detected Mössbauer spectrum (e.g. for a backscatter $\gamma$-ray to be detected, it must travel out of the specimen), and differences in the amount of material traversed by the $\gamma$-rays in the transmission and backscatter Mössbauer experiments. I believe that these two effects largely cancel out, however.

geometry Mössbauer experiments, the data scatter can be much less. A strong transmission geometry Mössbauer experiment may have a nonresonant background of 14.41 keV $\gamma$-rays that is 4 times greater than the maximum dip associated with the peaks. However, for backscatter geometry Mössbauer experiments the background of nonresonant detected radiation could be made zero with effective radiation shielding. So although the signal intensities for backscatter and transmission geometry Mössbauer experiments differ by a factor of 10, the ratio of S/U ratios for these two experiments can be about $\frac{10}{\sqrt{4 \cdot 10}} \simeq 1.7$ or less. The transmission geometry technique has the better S/U ratio at the tip of a strong absorption peak, but the backscatter geometry technique can actually have the better S/U ratio for the satellite peaks themselves. Equal S/U ratios could be expected for peaks in backscatter and transmission geometry experiments when the transmission peak dips 10% below its background count.

Unfortunately, all attempts to use the backscatter geometry technique for these satellite intensity measurements were hampered by a background count that resulted from 129 keV $\gamma$-rays from the $^{57}$Co radiation source that caused x-ray flourescense in the radiation shielding. We estimated that the peak to background ratio would have had to have been at least 3 for the backscatter technique to be preferred for the present work. Sadly, the best peak to background ratio achieved for my materials in backscatter geometry experiments was about 1. Nevertheless, given longer counting times, the backscatter geometry technique was capable of giving results that were quite comparable to results of the transmission geometry Mössbauer technique (See Fig. 9).

# CHAPTER VIII

# DATA PROCESSING

This chapter describes numerical manipulations that were used in extracting quantitative phase and chemical analysis information from experimental Mössbauer spectra. Data processing operations were basically of two types: 1.) corrections of known distortions caused by characteristics of the experimental technique (sections VIII. A. and C.), and 2.) operations that actually extracted the quantitative information from Mössbauer spectra (section VIII.B.).

## A. Corrections for Doppler Drive Performance.

Since radiation intensity decreases with the inverse square of distance, the incident $\gamma$-ray flux on the specimen is dependent on the cyclical separation of the radiation source and the specimen. A parabolic variation of incident $\gamma$-ray intensity is expected in a Mössbauer spectrum taken with a constant acceleration mode of operation. In the present operation with a velocity scan ranging between $+V_m$ and $-V_m$, with a mean source-specimen separation, $R$, of 100 mm, and with a 6.25 Hz Doppler drive cycle, we expect a time-dependent separation between source and specimen which goes as:

$$S\text{–}S\ separation = R - V_m t + 12.5 V_m t^2 \text{ for first acceleration}$$

$$S\text{–}S\ separation = R + V_m t - 12.5 V_m t^2 \text{ for second acceleration}$$

Our aperture for the $\gamma$-ray beam did not intercept any $\gamma$-rays that would otherwise have reached the specimen in a straight line. Therefore, for 1024 channels* of data collection, and with a constant counting time per channel, the radiation intensity reaching the specimen is proportional to:

* We designate the number of each data channel by $i$, and the number of counts in it as $N(i)$.

$$I(i) = \left[\frac{R}{R - \frac{V_m}{12.5}\left(\frac{i}{512}\right) + \frac{V_m}{12.5}\left(\frac{i}{512}\right)^2}\right]^2 \text{ for } 0 \le i < 512 \qquad \text{VIII-1}$$

$$I(i) = \left[\frac{R}{R + \frac{V_m}{12.5}\left(\frac{1024-i}{512}\right) - \frac{V_m}{12.5}\left(\frac{1024-i}{512}\right)^2}\right]^2 \text{ for } 512 \le i < 1024$$

It was easy to correct Mössbauer spectra for this parabolic intensity distortion by multiplying the number of counts in the $i^{th}$ data channel by $\frac{1}{I(i)}$. This correction was frequently performed for spectra in the calibration work. However, for comparisons of spectra in a series of temperings with the same specimen, this parabolic intensity distortion correction is unnecessary. In such comparisons, the difference of two normalized spectra taken under nearly identical conditions will cause the parabolic intensity distortion to be largely cancelled out. The parabolic intensity distortion was much smaller than the >10% absorption peak dip found for the thick specimens used in tempering studies. For $\pm V_m$ = 7 mm/sec, $I(i)$ only varies from 0.997 to 1.003, and varies much less than this over the width of a peak. The smooth variation of $I(i)$ across the Mössbauer peaks caused only a minimum of interference with the sharp features of interest in the difference spectra.

In section VII.E. it was described how an unidentified long term instability in the Doppler drive caused spontaneous changes in the velocity scanning range. An ongoing record of the positions of pure Fe peaks nos. 1 and 6 versus date and time was kept for the spectrometer. It was found that the shifts of peaks nos. 1 and 6 always occurred with equal magnitudes, but in opposite directions. The shifts of peaks nos. 3 and 4 were negligible. The shifts of peaks nos. 2 and 5 followed the pattern of peaks nos. 1 and 6, but were of a smaller magnitude. Consequently, a procedure to correct for the small shifts of $V_m$ was developed, in which an entire spectrum was expanded symmetrically about the zero Doppler shift energy. This correction was performed by adding data chan-

nels together in pairs. For example, if it was necessary to expand a 512 channel experimental spectrum by +0.5 data channels at $\pm V_m$, the contents of data channels 1 and 511 were replaced by $\frac{1}{2}N(1) + \frac{1}{2}N(2)$ and $\frac{1}{2}N(511) + \frac{1}{2}N(510)$, respectively. No such change would be performed for data channels $N(255)$ and $N(256)$, which straddled the expected zero Doppler shift energy. The amount of expansion was linear between channels 1 and 255; in our example of a +0.5 channel expansion at $\pm V_m$, the number of counts in data channel 128 would be replaced by $\frac{2}{3}N(128) + \frac{1}{3}N(129)$.

Adding data channels together in pairs has the undesirable effect of slightly broadening spectral features. For instance, if a hypothetical spectrum consisted of a flat baseline and one deviant point at channel 128, the above correction procedure would spread the intensity of channel 128 over both channels 128 and 129. The difference between a spectrum corrected for a shift of the Doppler drive and an uncorrected spectrum would therefore show artificial features due to the broadening from the shift correction procedure. To minimize this problem, the shift correction procedure was simultaneously performed on both spectra that were differenced. For example, consider a correction in which spectrum no. 1 is in need of an expansion of +0.5 channels at $V_m$ before its velocity scale corresponds to that of spectrum no. 2. The correction procedure that was used entailed an expansion of spectrum no. 1 by +0.25 channels at $V_m$, and a simultaneous contraction of spectrum no. 2 by -0.25 channels at $V_m$. Such a symmetric procedure may have a small effect on the shapes of peaks in difference spectra, but will have only a negligible effect on their intensities. By far the biggest problem with this correction procedure was in accurately knowing the shifts of the velocity scanning range. The record of pure Fe calibration spectra was not always reliable for supplying this information; it was sometimes unclear when the shift occurred, and more than one

such shift may have occurred between the collection of two Fe calibration spectra.

## B. PROCEDURES FOR STRIPPING PEAKS AND DIFFERENCING SPECTRA.

### 1. Austenite Analysis.

The fraction of austenite in the specimens was determined in a natural way by examining areas of peaks in Mössbauer spectra. In this method the integrated areas of the six martensite peaks and the one austenite peak are corrected for parabolic intensity variations and thickness distortion. The fraction of $^{57}$Fe in the austenite is then simply determined by the ratio of the austenite peak area to the total area of all seven peaks. A similar procedure was used by Marcus et al. [20], and then by others [12]. The volume fraction of austenite can be determined with knowledge of the differences in iron concentrations* and molar volumes of the austenite and martensite phases.

A numerical peak stripping procedure was frequently used for determining the amount of austenite present in a specimen. First, two Lorentzian functions were subtracted from the Mössbauer spectrum to remove peaks nos. 3 and 4 of the martensite sextet. The heights, widths, and centers of these two Lorentzians were adjusted until the stripping procedure gave a smooth baseline at the former positions of these two peaks. A successful example of this procedure is seen in Fig. 10 for a backscatter spectrum. Since peaks nos. 3 and 4 are not exactly Lorentzian functions, after stripping there may remain some residual intensity at their former positions. This residual intensity was added to the area of the stripped Lorentzian function to determine the area of the marten-

* The average mass difference of $^{57}$Fe atoms will result in a small ($\sqrt{\frac{55.8}{57}} \simeq 0.99$) isotopic depletion of $^{57}$Fe in the austenite due to the well-known isotope effect in diffusion. We ignore this effect.

site peak more accurately. (Otherwise the area of the martensite peak is the area of the Lorentzian function, which is simply $\frac{\pi}{2} \times FWHM \times Height$.) After stripping peaks nos. 3 and 4 of the martensite sextet, the area of the remaining austenite peak could be determined directly by numerical integration, or by a similar stripping procedure that used an approximately 20-30% fatter* Lorentzian function that was characteristic of the austenite peak. The areas of martensite peaks nos. 3 and 4, and the area of the austenite peak were then corrected for thickness distortion with equation VIII-6, and the procedure following it.

The areas of the other four martensite peaks (nos. 1,2,5, and 6) are conveniently known when a saturating magnetic field is applied to the specimen perpendicularly to the incident $\gamma$-ray direction; we have already determined the areas of martensite peaks nos. 3 and 4**, and we know the sextet of martensite peaks must have corrected areas in the ratio 3:4:1:1:4:3. However, when the saturating magnetic field is not present, the relative intensities of peaks nos. 2 and 5 were usually between 2.2 and 3.0. In this case we need to determine the areas of peaks nos. 2 and 5 precisely, and this determination should include independent thickness distortion corrections for these peaks. However, for convenience the relative areas of these peaks nos. 2 and 5 were determined by an uncorrected integration of the peaks nos. 1, 2, 5, and 6. The relative intensity of peak no. 2 was then determined to be: $3.0 \times \frac{Area(2)}{Area(1)}$. This approach is not unreasonable for thin absorbers because peaks nos. 1, 2, 5, and 6 usually had approximately the same maximum dip, and therefore approximately the

* The austenite peak width was sensitive to alloy composition. In N.K.K. 9Ni steel, the austenite peak width at 18°C was 30% greater than the width of martensite peaks nos. 3 and 4. In a Fe-9Ni-1Mn alloy the austenite peak width at 18°C was 22% wider than martensite peaks nos. 3 and 4, and in a binary Fe-9Ni alloy at 500°C this excess width was 15%.

** The areas of peaks nos. 3 and 4 were checked to be consistently the same within experimental error.

same thickness distortion corrections.

To summarize the approach outlined above, I first accurately determined the areas of the austenite peak and martensite peaks* nos. 3 and 4. There is a precise 3:1 relation between the true areas of the martensite peaks nos. 1 and 6 and martensite peaks nos. 3 and 4, and we also know that with the saturating magnetic field the true areas of martensite peaks nos. 2 and 5 and martensite peaks nos. 1 and 6 will be in the ratio 4:3; without the magnetic field we know this ratio approximately. With a saturating magnetic field applied to the specimen, the percentage of $^{57}$Fe atoms in the austenite is:

$$at.\%\,\gamma = \frac{\dfrac{A_\gamma}{A_{M3}}}{\dfrac{A_\gamma}{A_{M3}} + 2\times(3 + 4 + 1)} 100\% . \qquad \text{VIII-2}$$

Without the saturating magnetic field the percentage of $^{57}$Fe atoms in the austenite is:

$$at.\%\,\gamma = \frac{\dfrac{A_\gamma}{A_{M3}}}{\dfrac{A_\gamma}{A_{M3}} + 2\times(3 + 3\times\dfrac{A_{M2}}{A_{M3}} + 1)} 100\% . \qquad \text{VIII-3}$$

Note that a change in $3\times\dfrac{A_{M2}}{A_{M1}}$ from 2.6 to 2.7 will result in a change in $at.\%\,\gamma$ by at most only 0.1%. The percentage of $^{57}$Fe atoms in the austenite was converted into volume percent of austenite, for comparison with x-ray data, by multiplying by the factor**:

$$\frac{c_{Fe}^{\alpha'}}{c_{Fe}^{\gamma}}\,\frac{v_\gamma}{v_{\alpha'}} ,$$

where $c_{Fe}^{\alpha'}$ and $c_{Fe}^{\gamma}$ are the concentrations of iron in the martensite and austenite, respectively, and $v_\gamma$ and $v_{\alpha'}$ are the molar volumes of the austenite and

* I sometimes used, with success, variations in this procedure which carefully measured the areas of other martensite peaks, or sometimes the areas of all martensite peaks.
** This factor is about 1.18 for commercial N.K.K. 9Ni steel.

martensite, respectively. The difference in austenite content between two different specimens could readily be determined from the difference of their two spectra when the spectra were normalized to have the same area in their martensite peaks. In this case, the difference in austenite peak areas could be determined by direct integration of the difference spectrum intensity of the austenite peak. Then the difference in thickness distortion area corrections for the starting austenite peaks must be added to the area determined in the difference spectrum.

I have neglected the difference in recoil-free fractions of the austenite and martensite phases because I believe that they are essentially the same. Reasonable estimates of the recoil-free fraction can be made with the Debye model [239] using equation III-8. With specific heat Debye temperatures of 420°K for martensite and 450°K for austenite [240,241], equation III-8 predicts that the recoil-free fractions of austenite and martensite will differ by 1% or less at both room temperature and 500°C. However, in a study of Fe-N alloys having relatively stable austenite, De Christofaro and Kaplow [242] (see also [243]) reported that above $M_s$ (the temperature at which martensite first starts to form upon cooling) the recoil-free fractions of martensite and austenite were probably the same, but below $M_s$ the recoil-free fraction of the metastable austenite was about 16% smaller than that of the martensite. This observation was attributed to the development of large amplitude phonon modes which precede the martensite transformation, and reduce the recoil-free fraction according to equation III-7. With Mössbauer spectra obtained at 500°C and at room temperature, I was able to look for such relative changes in the recoil-free fractions of the austenite and the martensite. Such changes should be apparent as a change in the ratio of austenite peak area to martensite peak area between room temperature and 500°C. The corrected ratios of austenite

peak area to martensite peak area at room temperature and at 500°C were found to be the same within 5% (the limit of my measurement) for specimens with austenite that did not thermally transform upon cooling to room temperature. Therefore the ratio of recoil-free fractions of the austenite and martensite changes by less than 5% between room temperature and 500°C. Intensity measurements indicated that the recoil-free fractions of both phases were reduced by about 30% when the specimens were heated from room temperature to 500°C. This is in fine agreement with predictions of the Debye model. For specimens with thermally unstable austenite, it was assumed* that the reduction in austenite peak intensity at room temperature was entirely due to the $\gamma \rightarrow \alpha'$ transformation, and was not due to a changing recoil-free fraction of the austenite. Consequently, I made no correction for recoil-free fraction differences between the austenite and the martensite in any of the materials.

**2. Difference Spectrum Procedures.**

When Mössbauer spectra were obtained from the same specimen before and after a tempering treatment, the difference of these two spectra was used for determining the change in austenite content as well as the change in the Ni and X element concentrations of the martensite. Since there were only two phases present, the chemical composition of the austenite which formed during tempering was deduced from this single difference spectrum. The details of preparing the Mössbauer spectra for differencing are described in this section.

In order to employ Mössbauer spectrometry for measuring chemical and phase changes during two-phase tempering, Mössbauer spectra from materials with different heat treatments were obtained under experimental conditions as similar as possible. I undertook an approach to data processing which

* I did not check this assumption by cycling these specimens between room temperature and 500°C, as did De Christofaro and Kaplow.

concentrated on identifying changes in Mössbauer spectra due to small chemical and phase *changes* in the material, instead of quantifying the chemistry and phase information with respect to their levels of zero concentration. In this approach, intensity differences between the two starting Mössbauer spectra were revealed by digitally subtracting the data points of the second spectrum from the data points the first spectrum. The difference spectrum method was a direct approach to extracting the useful experimental information from Mössbauer spectra; it involved a minimum of data manipulations. Systematic experimental errors common to both starting spectra were largely cancelled out in this way. The difference spectrum method, used with repeatable conditions of data collection, provides a most direct and sensitive approach to quantifying small changes in Mössbauer spectra.

In the differencing procedure it was often necessary to adjust the shift of the starting spectra along the Doppler velocity axis. Such shifts were necessary in order to compensate for the experimental problems described in section VIII.A., but these shifts were also used to compensate for the very small changes in the hyperfine magnetic field of the "unperturbed" main peak ($H_o$ of equation IV-1) caused by differences in the X element concentration of the two spectra. Such a $c_X$ dependence of $H_o$ is known to be small for Fe-X alloys [41,105]. Approximate measurements of the $c_X$ dependences of $H_o$ were performed in calibration work when correlating satellite peak intensities to known X element concentration differences of about 1%. An appropriate Fe-Ni peak was used as the unperturbed main peak for subtraction from the Fe-Ni-X peak in order to reveal X satellite intensities through the high energy tail matching procedure described below. The shift of the Fe-Ni spectrum with respect to the shift of the Fe-Ni-X spectrum was compared with reported $\frac{d\ H_o}{d\ c_X}$ measurements for Fe-X alloys [41]. Good agreement was found for Cr. Probably good agreement was

found for Mn and Si, but with their smaller characteristic shifts these effects were hard to measure. Even for Cr such shifts amounted to less than 0.2 data channels when 10% austenite had formed, so such corrections were generally unnecessary. Corrections for the $c_X$ dependence of $H_0$ were not performed when taking the differences of spectra in a tempering series. However, the lack of such corrections was probably an important source of error in chemical composition analyses of the few specimens which formed large amounts (>20%) of austenite.

The most important parameter in the differencing procedure is the normalization factor. The normalization factor is necessary to ensure that before differencing the two starting martensite sextets will have comparable intensities. In this work four different normalization criteria were used. With my experimental data, the choice of a particular normalization criterion is to some extent a matter of taste*; at least semi-quantitative success in chemical composition analysis could be obtained with all four methods, once suitable calibrations were established. However, there are characteristic differences between these four criteria that led me to use only one of them for most of the chemical analysis data reported in the next chapter.

Normalizing Mössbauer peaks by the criterion of equal areas is probably the most widely used procedure for finding small differences between Mössbauer spectra. When the starting martensite peaks have equal areas, it is clear that the intensities of their difference will be both positive and negative, and the difference spectrum will have zero net area. Unfortunately, although the magnitude of this difference spectrum intensity on the low Doppler shift side of the main peak can be proportional to the X element composition

* When higher quality experimental data are available, it is hoped that the most suitable normalization criterion will become self-evident.

difference, the intensity of the "X satellite" is not revealed directly. A formula like equation IV-5 can still be used for relating difference spectrum intensities to chemical composition changes, but the constant $N_S^X$ will not have any fundamental relation to the number of $^{57}Fe$ nuclei whose hyperfine magnetic fields are significantly perturbed by the X atoms. Furthermore, a formula like equation IV-5 used with the area normalization criterion assumes that the basic shape of the difference spectrum is unchanged with changes in the solute concentrations. (For my data this assumption seems to be largely true, however). On the other hand, the criterion of area normalization is good for determining changes in the austenite content; after the austenite peak in the difference spectrum is integrated, its area can be compared with the total area of either starting spectrum to find the change in austenite content with respect to that specimen.

In my early "X satellite" calibration work [128], the starting martensite peaks were normalized by a criterion based on the best overlap of their tails on the high Doppler shift energy side. This criterion involved both normalizing the heights and shifting the positions of the starting peaks, so that the data points of their high energy tails were nearly coincident. The tail region was defined as that part of the peak extending from the background count to 40% of the peak dip. This region is chosen for overlap because it was rather insensitive to changes in the X element concentration. The best tail overlap was determined in an iterative process in which the root mean squared difference spectrum intensity from the high energy tail region was minimized by varying both the peak heights and the peak shifts. It was later found that the "Cr satellite" intensities produced by this tail matching procedure were typically 20% larger than those produced by the height normalization procedure, although the "Mn and Si satellite" intensities were about the same. This artificial enhancement of

the "Cr satellite" intensities results from a Cr-induced broadening of the "unperturbed" main absorption peak (due to Cr neighbors beyond the 2n.n. shell of the $^{57}$Fe atom). Since additional Cr induces additional broadening of the main absorption peak, when high energy tails are matched an excess difference spectrum intensity appears on the "Cr satellite". This is seen as a protuberance towards the high Doppler shift energy side of the "Cr satellite", and it led me to overestimate $N_S^{Cr}$ for Fe-Ni-Cr alloys [128]. The second shortcoming of the high energy tail matching procedure is that it cannot be used for revealing changes in the "X satellite" intensity after tempering of Fe-Ni-X alloys; after tempering we expect changes in the high energy tail region due to changes in the Ni content.

The normalization criterion preferred by the author was a peak height normalization. In its implementation the starting peaks were first shifted to compensate for errors in the Doppler drive (and to compensate for $\frac{dH_o}{dc_X}$ in the calibration work). After shifting, the peaks were normalized so that their dips below the background count were equal, and they were then differenced. A major advantage of this procedure is that it required a minimum amount of data manipulation, and could be performed quickly. This height (or dip) normalization procedure will accurately discriminate between Ni and X concentration differences if their effects are confined to the high and low Doppler shift energy sides of the main peak, respectively. Fortunately, the "X satellites" seem to be confined to the low energy side of the main peak, as seen in Figures 26-28 . However, the difference spectrum intensity seen in Figure 13 for peak no. 1 height normalized spectra from specimens with different Ni concentrations does extend somewhat across the tip of the main peak. Furthermore, it appears to the author that the overlap of difference spectrum intensities due to Ni and X concentration changes becomes worse as these concentration changes

become larger. I therefore expect that that the height normalization procedure will underestimate the Ni and X concentration changes when they are large.

I attempted to avoid these difficulties encountered when quantifying large Ni and X concentration changes with the height normalization criterion by employing an alternative "3:4:1 criterion". The 3:4:1 normalization procedure was only used for spectra taken from specimens that were exposed to a saturating magnetic field perpendicular to the incident $\gamma$-ray direction. For such spectra the thickness distortion corrected peak intensities of the martensite sextet are known to be in the ratio 3:4:1:1:4:3. Therefore, if the main unperturbed peaks are normalized to have the same area, the intensities in the difference spectrum around each peak of the sextet must also be in the ratio of 3:4:1:1:4:3. However, actual measurements of difference spectrum intensities usually did not give a 3:4:1:1:4:3 ratio. Part of the reason for this comes from the deceptively large fraction of area of a Lorentzian-like peak which is contained within its tails. Finding the area in the tails requires an accurate knowledge of the baseline of the peak, but the slow decrease of the peak tails caused underestimates of the baseline, and hence the area of the peak. With the 3:4:1 criterion the baseline-induced errors in difference spectra were compensated by changing the normalization factor until a 3:4:1:1:4:3 ratio was nearly obtained for the difference spectrum intensities from the six martensite peaks. The author does not fully understand the "3:4:1 criterion", and can justify it only phenomenologically. The basic parameters in this procedure depend on the detailed shape of the difference spectrum peaks. Understanding this procedure also requires accounting for small deviations from the 3:4:1 ratio for different spectra. Nevertheless, I suggest that a normalization factor that imposes this ratio on difference peak intensities will overestimate the difference

spectrum intensity by about the ratio that the difference intensity around peak nos. 3 or 4 was increased over its intensity when height normalization for peak no. 1 was employed. As a rule of thumb, when 10% austenite had formed, the 3:4:1 normalization procedure gave about a 20% overestimate of $\Delta c_M$ and $\Delta c_X$, but this error was smaller when more austenite had formed and the baseline error was less significant.

There are a few features of Mössbauer spectra from Fe-Ni-X alloys that can assist the implementation of difference spectrum procedures. Although the difference spectrum intensities around either peak no. 1 or no. 6 should be adequate for determining $\Delta c_M$ and $\Delta c_X$, the difference spectrum intensity around peak no. 1 is less sensitive to experimental problems with the Doppler drive. This is because the localized isomer shifts of Ni cause peak no. 6 to be sharper than peak no. 1, and a larger artificial difference spectrum intensity will appear around peak no. 6 than around peak no. 1 for the same shift of both peaks in the starting spectra*. Estimates of the shifts in the Doppler drive could be obtained in this way; when the difference spectrum intensity around peak no. 6 was much greater than that around peak no. 1, it was clear that the shift of the Doppler drive was not adequately corrected. A second feature of assistance is the fact that good quality difference spectra should show features around peaks nos. 2 and 5 which are qualitatively similar to the intensities around peaks nos. 1 and 6, provided that the relative intensities of the six peaks in the two starting spectra are the same. These intensities around peaks nos. 2 and 5 were particularly useful for looking for experimental problems in spectra obtained with the specimen in the saturating magnetic field.

* If a function, $f(x)$, is given a small shift, $\Delta x$, the difference $f(x + \Delta x) - f(x)$ is approximately $\frac{df}{dx}\Delta x$. Hence differences of *sharp* peaks (large $\frac{df}{dx}$) are more sensitive to a given instrumental drift ($\Delta x$) than are more rounded peaks.

I am dissatisfied with the normalization part of the difference spectrum procedure; it was always a major source of error in chemical composition analysis when changes in both Ni and X concentrations were present. The height normalization procedure is impaired when there is overlap of the difference spectrum intensities due to changing Ni and X concentration changes. The 3:4:1 normalization procedure is based primarily on the phenomenology of experimental errors, and depends on one's ability to reproducibly underestimate a baseline for peaks in the difference spectra. That the 3:4:1 normalization and height normalization procedures mostly agree is perhaps best regarded as a characteristic of the shapes of the present Fe-Ni-X peaks. I believe that until a more quantitative procedure for normalizing starting peaks in the presence of overlapping difference peak intensities is found (and better quality data is obtained), the analyses of chemical composition changes of Ni and of X elements are at best a bit better than semiquantitative and marginally quantitative, respectively. Fortunately, such data is still valuable for a metallurgical understanding of 9Ni steel. On a brighter note, when only the X element concentration or only the Ni concentration was changed, the normalization procedure was much less ambiguous. The calibration work has shown that quantitative measurements can be made of either X element concentration changes or (probably) Ni concentration changes in an Fe-Ni-X alloy, provided that the concentration of the other solute is unchanged.

**3. Other Data Processing Procedures.**

Some manipulations of pairs of data channels were useful. A "compressing" operation was developed in which the content of channel 1, $N(1)$, was replaced with the sum $N(1) + N(2)$, the original $N(2)$ was replaced with the sum $N(3) + N(4)$, the original $N(3)$ was replaced with the sum $N(5) + N(6)$, etc. This compressing operation doubles the number of counts per channel at the

expense of halving the number of independent data channels. The S/U ratio for the intensity of a compressed peak is the same as the peak intensity before compressing. However, the compressing operation may be thought to have improved the ratio of peak height to scatter at the expense of having fewer data points over the width of the peak. The compressing operation serves to broaden the peaks slightly because it effectively reduces the resolution of the spectrometer. This slight broadening was not a problem in difference spectra because the compressing operation was applied to both starting spectra. The compressing operation had very little effect on peak *intensities*, which were the important quantities from the experimental work.

Manipulating pairs of data channels in a "folding" operation is also useful for spectra collected in a constant acceleration mode of operation. In a folding operation the data channels corresponding to the same velocity interval, but with opposite accelerations of the Doppler drive, are added together. The folding operation will increase the S/U ratio by the factor $\sqrt{2}$ over its value for one spectrum with one acceleration. "Folding" may broaden Mössbauer peaks if the change in transducer acceleration does not exactly correspond to the center of folding; this is a likely consequence of any nonlinearity in the $V(t)$ of the Doppler drive. However, this broadening is slight in a 1024 channel spectrum, and has no significant effect on difference spectrum intensities when both starting spectra were folded before being compressed.

Numerical integration of peak areas was performed by first adding together the contents of the data channels that defined the peak. The average background count times the number of channels defining the peak was subtracted from this sum to get the total counts within the peak. The background count was determined from the counts near the ends of the velocity scanning range plus some correction for the tail intensities of peaks nos. 1 and 6 in this

region. The background count in difference spectra was determined by averaging the data channels in the flat regions adjacent to the difference peaks. Analog integration procedures were inspired by the good quality of the graphics hardcopy. I used procedures such as weighing peaks cut out from paper of even thickness, counting squares on graph paper, and measuring heights and widths of peaks with a pair of calipers. These methods were checked against the digital integration technique, and were found to be surprisingly accurate. Errors in integrated areas were caused more by the scatter in the data and the differencing procedure, than by the integration technique.

**C. Thickness Distortion Corrections.**

Thickness distortion is caused by a saturation effect in which a thicker absorber is unable to produce proportionately more resonant absorptions. Maximum thickness distortion occurs at Doppler shift energies at which the specimen exhibits its strongest resonant absorptions. At these energies, the incident $\gamma$-ray intensity will be substantially weakened after it has traversed much of the specimen thickness, so further increases in specimen thickness will not produce proportionately more resonant absorptions. For a transmission geometry experiment with a monochromatic radiation source, the normalized $\gamma$-ray intensity leaving the specimen at each Doppler velocity, $V$, is [244]:

$$I(V) = (1 - f_s) + \frac{f_s \Gamma}{2\pi} \int_{-\infty}^{\infty} \frac{e^{-f_A n_A \sigma_A(E) t}}{\left(E - V \frac{14keV}{c}\right)^2 + \left(\frac{\Gamma}{2}\right)^2} dE \qquad \text{VIII-4}$$

The observed dip in count rate will be largest when the source $\gamma$-ray energy is shifted to a velocity, $V$, where $\sigma_A(E)$ is large, and the integral in equation VIII-4 is small. For a specimen with a single Lorentzian absorption peak, the area, $A$, under the *observed* peak can be evaluated analytically [245] and is found to be:

$$A = f_S \frac{1}{2} \Gamma \pi e^{-\frac{\tau}{2}} \left[ I_0\left(\frac{\tau}{2}\right) + I_1\left(\frac{\tau}{2}\right) \right] \qquad \text{VIII-5}$$

where $\tau$ is approximately the specimen thickness normalized by the mean resonant scattering length in the specimen at the center of the peak. By expanding the exponential function and the zero and first order modified Bessel functions of the first kind suggests* an excellent approximation for our moderately thick absorbers. The following expression offers excellent agreement with the published [245-247] evaluations of Eqn. VIII-5 :

$$A \simeq \frac{\pi f s}{4} \tau \left(1 + e^{-\frac{\tau}{2}}\right) . \qquad \text{VIII-6}$$

The most difficult and least accurate part of correcting the areas of the absorption peaks for thickness distortion was the determination of the actual specimen thickness. A micrometer was used to measure the thickness of the foil at several locations, but since the specimen thickness was typically 0.0005 in. and the micrometer accuracy was not better than ± 0.0001 in., this procedure was of very limited accuracy. Since the mean resonant scattering length of the material was mostly the same for all specimens, the peak no. 1 depth to background count ratio should be an indicator of the specimen thickness. The peak depth to background count ratio will also depend on changes in the spectrometer performance from run to run, but I tried to keep the experimental technique as similar as possible for all specimens. Martensite peak no. 1 depth to background count ratios were compared for numerous specimens** and were correlated to their thicknesses as determined with a micrometer. For Fe-9Ni alloys without the furnace and without the magnet, a 0.0007 in. thickness corresponded to a dip of peak no. 1 that was 10% of the background count. For Fe-9Ni specimens in the vacuum furnace at room temperature, a 10% dip of peak no. 1 below the background count corresponded to a thickness of 0.0011 in. and, for specimens mounted in the magnet, this 10% ratio corresponded to a

* Convergence of this expansion has not been shown in detail.
** These specimens had low austenite contents, but values of $\tau$ determined from this reference work should be good even when the amount of austenite was relatively large.

thickness of 0.0018 in.

For determining specimen thickness, I also attempted to utilize the fact that the integrated resonant scattering cross-section for peak no. 1 is exactly 3 times that for peak no. 3. Any reduction of this ratio below 3 in an observed spectrum is caused by a greater thickness distortion of peak no. 1 than peak no. 3. The ratio of the dip of peak no. 1 to the dip of peak no. 3 was used to determine the relative peak area correction for different thicknesses by using equation VIII-6. The thickness of the specimen was inferred to be that for which the area correction resulted in a 3:1 peak intensity ratio. Unfortunately, these evaluations of $\tau$ gave only rough agreement with micrometer measurements and determinations of $\tau$ based on the ratio of the dip of peak no. 1 to background count. I presume that this poor agreement involved 1.) the non-Lorentzian shape of peaks nos. 1 and 3 (equation VIII-2 is strictly valid for Lorentzian peaks only), and 2.) inadequate consideration of peak tails when determining the areas of peaks nos. 1 and 3. These matters were not pursued further because the other methods of thickness determination were considered adequate.

Thickness distortion corrections for the volume fraction of austenite were straightforward. First, the areas of peaks nos. 3 and 4 of the martensite spectrum were corrected for thickness distortion through the relation $\tau_{M3} = \frac{t_{M3}}{0.0024in.}$ and equation VIII-6. The thickness of the martensite, $t_{M3}$, was determined from the dip of peak no. 1 below the background count, or by a micrometer measurement approximately corrected for the amount of austenite that was present. The maximum dip of the austenite peak, $D_\gamma$, was related to the dip at peak no. 3 or no. 4 of the martensite spectrum, $D_{M3}$. The austenite peak area was corrected for thickness distortion with the relationship: $\tau_\gamma = \frac{t_{M3}}{0.0024in.} \frac{D_\gamma}{D_{M3}}$, and with equation VIII-6. When the dip at the austenite

peak is the same as the dip at peak no. 3 or 4 of the martensite spectrum, the thickness distortion corrections for these two peaks will be the same. When the saturating magnetic field was applied perpendicularly to the incident $\gamma$-ray direction, the determination of the austenite volume fraction was especially straightforward because it was not necessary to correct the intensities of martensite peaks nos. 1, 2, 5, and 6 for thickness distortion; we know that the six martensite peaks are in the ratio 3:4:1:1:4:3. In the special case when $D_\gamma = D_{M3}$, and with the saturating magnetic field, the austenite volume fraction is nearly:

$$vol.\,\%\,\gamma = \frac{c_{Fe}^{\alpha}}{c_{Fe}^{\gamma}} \frac{1}{1 + 2\times(3 + 4 + 1)} \frac{A_\gamma}{A_\alpha} 100\,\% \simeq 9.5\,\% . \qquad \text{VIII-7}$$

We have used $\frac{c_{Fe}^{\alpha}}{c_{Fe}^{\gamma}} = 1.19$, $\frac{A_\gamma}{A_\alpha} = 1.4$, $\frac{v_\gamma}{v_\alpha} = 0.99$, and have approximately included the small effects of the peak tails (assumed to be Lorentzian functions) on the intensities of martensite and austenite peaks.

When determining chemical composition differences, it is possible to individually correct each spectrum for thickness distortion before the two spectra are differenced. However, I found it far easier and more direct to perform the differencing first. Quantitative information obtained from the difference spectrum was then multiplied by a thickness distortion correction factor. It was especially straightforward to perform the correction of the ratio of X satellite peak area to the total absorption peak area (the ratio $\frac{I_X}{I_T}$ of equation IV-5) when the peaks in the starting spectra required similar thickness distortion corrections. The dip in count rate at the energies of the satellite peaks was much less than the dip of the main absorption peak itself. Therefore thickness distortion corrections were only performed on $I_T$, so the ratio $\frac{I_S}{I_T}$ was simply divided by the thickness distortion correction factor for $I_T$. After determining the specimen thickness, the relationship $\tau = \frac{t}{0.0012in.}$ was used for peaks nos.

1 and 6 of Fe-9Ni alloys, and equation VIII-3 was then used to correct $I_T$ of these peaks for thickness distortion. At most, these corrections amounted to an increase of 20% for $I_T$ for the thicker specimens that were used in the tempering studies. Thinner specimens for the calibration of satellite peak intensities required thickness distortion corrections that were only about 5% of $I_T$.

Correcting the ratio of difference spectrum height due to Ni concentration changes, $\Delta h_{Ni}$, to total absorption peak area, $I_T$, was less accurate. This correction required some consideration of the effect of thickness distortion on $\Delta h_{Ni}$ itself because there was substantial absorption intensity on the side of the main peak where $\Delta h_{Ni}$ originated. Somewhat arbitrarily, this correction was taken to be 30% as large as the correction required for $I_T$. The ratio $\frac{\Delta h_{Ni}}{I_T}$ was thereby reduced by about $\frac{2}{3}$ of the amount that the ratio $\frac{I_S}{I_T}$ was reduced.

In contrast to the simplicity of corrections of integrated areas of peaks for thickness distortion, a thickness distortion correction for the actual shapes of Mössbauer peaks requires equation VIII-4 and a non-trivial computer code. A number of such methods have been proposed for thickness distortion corrections (for a review see [12]), but I chose a deconvolution procedure similar to that of Dibar-Ure and Flinn [248], which is based on the convolution theorem for Fourier transforms. Using a fast Fourier transform algorithm [249] written in the language BASIC, the sine and cosine transforms of a 256 point Mössbauer spectrum were calculated. These Fourier coefficients were divided by the coefficients of the Fourier cosine transform of a symmetric Lorentzian function characteristic of the source lineshape. This denominator goes exponentially to zero for higher order coefficients, but the Fourier coefficients of Lorentzian-like peaks of the Mössbauer spectra also go to zero approximately exponentially. Unfortunately, the Fourier transform of the scatter in the spectrum due to

counting statistics has a constant amplitude distribution in Fourier space. Consequently, the scatter in the data becomes strongly emphasized by the vanishing denominators of the highest order Fourier coefficients, and the inverse Fourier transform procedure yields a wild and scattered spectrum. I circumvented this problem by multiplying the higher order Fourier coefficients with a function like $e^{-\alpha(k-k_0)^2}$, which goes to zero with increasing $k$ faster than the exponential denominator. With suitable parameters $\alpha$ and $k_0$ for this filtering, the inverse Fourier transform procedure produced a result with controlled scatter. Unfortunately, the resulting deconvolved peaks were not as narrow as theoretically predicted; with good counting statistics the Gaussian filtering caused the deconvolution procedure to reduce the width of a pure Lorentzian peak by only 80-85% of the predicted amount.

Thickness distortion corrections are performed after the source lineshape is deconvolved from the spectrum, so that only the exponential kernel of equation VIII-4 remains. The thickness distortion correction is performed by taking the natural logarithm of the deconvolved and normalized data. This logarithm is proportional to the absorber resonant scattering cross-section, $\sigma_A(E)$. The data for Figures 20 and 25 were processed in this way. It may be desirable to convolve the radiation source lineshape back into $\sigma_A(E)$ to yield the experimentally expected shape of Mössbauer peaks for a zero thickness absorber. This was done in Figure 20. However, it is obvious that there is no change of any significance between the zero thickness peaks of Figure 20 and the peaks from thin absorbers in Figure 17.

A few difference spectra were calculated after both starting spectra were given thickness distortion corrections with the deconvolution procedure. These corrections are more elegant and precise than the thickness distortion corrections that were made for the ratios $\frac{I_s}{I_T}$ and $\frac{\Delta h_{Ni}}{I_T}$ obtained directly from the

difference of unprocessed spectra. Sadly, the time and effort required by the deconvolution procedure with the present computer system were at least an order of magnitude greater. Furthermore, the additional accuracy of the deconvolution procedure is of no value, given the expected uncertainty of the specimen thickness. In addition, the distribution of thicknesses within the specimen (i.e., the specimens did not have uniform thicknesses) has been shown to be an important source of error in thickness distortion corrections [39]. Including these uncertainties in the specimen thickness, it is estimated that a typical 10% correction of the ratio $\frac{I_S}{I_T}$ was accurate within ± 2%. Relatively more uncertainty was involved in the thickness distortion for $\frac{\Delta h_{Ni}}{I_T}$; a typical 6% correction was probably accurate within ± 2%.

# CHAPTER IX

# EXPERIMENTAL RESULTS

## A. Chemical Analysis Development.

The size of relevant chemical effects in Mössbauer spectra can be qualitatively appreciated from Figs. 11 and 12. Figure 11 shows that Ni solutes cause the sextet of martensite peaks to display a more negative average hyperfine magnetic field than pure Fe at room temperature. Some broadening of the peaks from Fe-9Ni is also apparent, so when comparing peak no. 1 height normalized spectra, the specimen with more Ni display increased absorption intensity primarily on the high Doppler shift energy side of peaks nos. 1 and 6 at 18°C. Intensity changes caused by the other alloy additions to commercial 9Ni steel can be seen in Fig. 12 for spectra taken at 18°C and 500°C. At both temperatures, the other (X) alloy elements cause some $^{57}$Fe nuclei in the martensite to absorb $\gamma$-rays at lower magnitudes of Doppler shift energy. For height-normalized spectra, the specimens with more X will display increased absorption intensity on the low Doppler shift energy side of peaks nos. 1 and 6, as seen in Fig. 26. At the concentrations of interest it is apparent that neither Ni nor X solutes cause especially large effects in Mössbauer spectra. Nevertheless, it is found that these effects correlate well with average changes of Ni and X concentrations in the martensite. The present methods of comparing changes in absorption intensities to determine changes in Ni and X concentrations are primarily limited by the quality of experimental data which can be obtained.

### 1. Ni Analysis.

The temperature-dependent effects of Ni concentration on the shapes of martensite peaks are seen in Figs. 13 through 20. At 18°C the difference of height-normalized spectra from martensites with different Ni concentrations is

mostly seen as a difference in intensity on the *high* Doppler shift energy side of the absorption peaks (see Fig. 13). However, at 500°C the difference spectrum intensity due to a difference in Ni concentrations appears almost entirely on the *low* Doppler shift energy side of the absorption peaks (see Fig. 14). This trend of Ni-induced hyperfine magnetic field perturbations becoming more positive with increasing temperature is shown in Fig. 19, where the two absorption peaks nos. 1 and 6 from a binary Fe-8.9Ni alloy are shown at 18°C, 500°C, and 600°C, along with corresponding peaks from pure Fe obtained at these temperatures for reference.

However, although the significant $\Delta H_j^{Ni}$ parameters became positive at 500°C, the $\Delta H_j^{X}$ parameters for X solutes were positive at both 18°C and 500°C. Consequently, when both Ni and X concentrations were different in the starting spectra of Fe-Ni-X alloys, the difference spectrum intensities due to the differences in Ni and X concentrations overlapped on the low Doppler shift energy sides of the absorption peaks obtained at 500°C. Therefore, at 500°C the changes in the Ni and X concentrations could not be measured independently. The contributions of Ni and X concentration changes to the net difference spectrum intensity were, however, approximately additive at 500°C. Unfortunately, a combined Ni + X solute depletion of the martensite could not be determined from 500°C spectra because changes in the Ni and X solute concentrations did not have an equal weight in producing the difference spectrum intensity changes. Nevertheless, spectra taken at 500°C for a series of temperings of Fe-9Ni-Cr and Fe-9Ni-Mn alloys show larger difference spectrum intensities than does a Fe-9Ni alloy with the same amount of austenite (compare Figs. 31 and 33 to Fig. 29). It might be reasonable to attribute this extra difference spectrum intensity entirely to the depletion of Mn and Cr from the martensite, but I made no quantitative efforts to do this.

Unfortunately, the austenite formed at 600°C in some of the high purity ternary alloys had insufficient thermal stability to avoid the $\gamma \rightarrow \alpha'$ transformation upon cooling to 18°C, and the Ni and X concentration changes of the martensite could not be accurately determined when a large amount of solute-rich fresh martensite was present. (The resulting inhomogeneous martensite chemistry caused its average Ni and X concentrations to be underestimated, and therefore the austenite Ni and X concentrations were overestimated. See section IV.D.) Sadly, this meant that no good quality Ni or X chemical segregation information was obtained from Fe-9Ni-1Cr, Fe-9Ni-1Si, or Fe-9Ni-0.3C alloys, since much of the austenite formed in these materials during tempering had transformed to martensite before their 18°C spectra could be obtained, and separating the combined effects of Ni and X solutes in their 500°C spectra was not attempted.

Peaks nos. 1 and 6 of pure Fe and binary Fe-Ni alloys were analyzed to provide the data of Fig. 21a. The first moments of these peaks were calculated numerically, and were used to determine the difference in the average isomer shift, and the average hyperfine magnetic field, between the Fe-Ni alloys and pure Fe. The full-width-at-half-maximum (FWHM) of each peak was also measured, and Fig. 21b shows the difference in FWHM between the Fe-Ni peaks and the pure Fe peaks. The average isomer shift for $^{57}$Fe nuclei in Fe-Ni alloys is positive with respect to pure Fe at 18°C. However, Fig. 19 shows that this average isomer shift is apparently reduced with increased temperature. Much of this apparent reduction in the average isomer shift may be due to differences in the second-order Doppler shift between the Fe-Ni alloys and pure Fe (see section III.B). Consequently, the apparent reduction in the average isomer shift with temperature actually may be evidence that the temperature dependence of $\langle V_{vibr}^2 \rangle$ for $^{57}$Fe nuclei in Fe-Ni alloys is greater than the temperature depen-

dence of $<V^2_{vibr}>$ for pure Fe.

Figure 19 also shows that the $\Delta i_j^{Ni}$ parameters change with temperature. Again note that in Fig. 19, peaks no. 1 from the Fe and the Fe-9Ni are normalized to have the same dips. We know that peaks nos. 1 and 6 in the same spectrum must have equal intensities, but at 18°C Fig. 19 shows that for Fe-9Ni the dip of peak no. 6 is greater than the dip of peak no. 1. This is because the significant $\Delta i_j^{Ni}$ parameters are negative at 18°C, as described in section IV.G. However, at 500°C peaks nos. 1 and 6 of Fe-9Ni have the same dip, and even good mirror symmetry. This is also evident for other Fe-Ni alloys at 500°C (see Figs. 17 and 18). From the symmetry of peaks nos. 1 and 6 of Fe-Ni alloys at 500°C, I conclude that the significant $\Delta i_j^{Ni}$ parameters are nearly zero at 500°C. However, at 600°C the dip of peak no. 6 is again greater than the dip of peak no. 1 for Fe-9Ni (see Fig. 19). At 600°C the peaks from Fe-9Ni lie on the low Doppler shift energy side of the pure Fe peaks, so the significant $\Delta i_j^{Ni}$ parameters have apparently changed sign, and are positive at 600°C.

It is possible that local differences in $<V^2_{vibr}>$ for $^{57}$Fe atoms surrounded by different numbers of Ni neighbors may account for some of the apparent reduction in magnitude of the $\Delta i_j^{Ni}$ parameters with temperature. However, I do not believe this is the major effect for three reasons:

1.) The temperature dependences of the $\Delta H_j^{Ni}$ and the apparent $\Delta i_j^{Ni}$ parameters are very similar, as would be expected if they both arise from the same electronic changes caused by the Ni atoms.

2.) The change in the significant $\Delta i_j^{Ni}$ parameters over the small temperature range 500°C-600°C is approximately as large as their change over the larger temperature range 18°-500°C. Changes in $<V^2_{vibr}>$ are expected to be more proportional to temperature over the range 18°C to 600°C because the Debye tem-

perature of Fe is around 150°C.

3.) The observed mirror symmetry between peaks nos. 1 and 6 of Fe-Ni alloys at 500°C would be a remarkable coincidence due to local changes in $<V^2_{vibr}>$ accurately cancelling the $\Delta i_j^{Ni}$ parameters.

The moments* from peak no. 1 of Fe-Ni spectra taken at 18°C were numerically calculated from the data used for Fig. 15. With Fig. 22 the relationship**

$$c_{Ni} = k_{Ni}^{M1} \times \frac{\Delta h^{Ni}(M1)}{D(M1)} \qquad \text{IX-1}$$

was justified in section IV.E. when $\Delta c_{Ni}^{\sigma}$ is on the order of 0.01 and $c_{Ni}^{\sigma} = 0.09$. Quantitative determinations of $k_{Ni}^{M1}$ were made with the data of Figs. 13 and 14 for 18°C and 500°C spectra. At 18°C, the constant $k_{Ni}^{M1} = 20\%Ni$ ; at 500°C $k_{Ni}^{M1} = 23\%Ni$. For the difference spectrum intensity around peak no. 6 due to Ni concentration changes, at 18°C the constant $k_{Ni}^{M6} = 17\%Ni$, and at 500°C $k_{Ni}^{M6} = 22.5\%Ni$. The relation:

$$c_{Ni} = k_{Ni}^{M6} \times \frac{\Delta h^{Ni}(M6)}{D(M6)} \qquad \text{IX-2}$$

was not verified with the approach of section IV.E. using data like that of Fig. 22, nor was the use of equation IX-1 justified rigorously for 500°C spectra. Examinations of Figs. 15 through 18 make equations IX-1 and IX-2 seem reasonable for both 18°C and 500°C spectral peaks, however. The constants $k_{Ni}^{M1}$ and $k_{Ni}^{M6}$ were mostly unaffected by the presence of about 1% X solute, at least at 18°C. This is consistent with the success of subtracting binary Fe-Ni peaks from Fe-Ni-1X peaks to reveal the "X satellite"; clearly the absorption intensity on the high Doppler shift energy side of the peaks is not seriously affected by the presence of the X solute if a binary Fe-Ni spectrum can be successfully used as a

* The moments were computed in terms of data channel number; the velocity ordinate of Fig. 22 has meaning only for the first moment.
** Here $\Delta h^{Ni}(M1)$ is the difference spectrum height associated with the Ni concentration change, and $D(M1)$ is the maximum dip in absorption intensity associated with peak no. 1. ($D(M1)$ is the same for both starting spectra when they are height normalized.)

starting spectrum for the difference spectrum.

In determining $k_M^{M1}$ and $k_M^{M6}$, some effort was invested in performing thickness distortion corrections of the Fe-Ni peaks before performing the differencing. However, the specimens that were used in the present calibration work were quite thin (0.0002 to 0.0003 in.), and other experimental difficulties were more important than thickness distortion corrections. For instance, it is seen upon comparing Figs. 17 and 20 that the differences in peak shapes and widths caused by the lengthy thickness distortion correction procedure were unimportant. It was more important to correct the data for shifts in the velocity scanning range of the Doppler drive.

**2. X analysis in Fe-Ni-X**

The hyperfine magnetic field perturbations due to carbon in Fe-Ni-C alloys were difficult to quantify for two reasons. First, the amount of C in these alloys was small — at most 0.3 at.%. An ingot with a Fe-9Ni-1C composition was prepared, but even after much effort it could not be rolled into a specimen foil. Tempering studies of this material would surely be confused by the formation of carbides before the formation of austenite [250]. Nevertheless, some backscatter geometry experiments were performed with the Fe-9Ni-1C alloy, and a fuzzy "C satellite" was identified. It indicated that $N_s^C \simeq 4$, and this points out the second problem with C analysis; the same amount of C produces only about one-third the satellite intensity produced by Mn, Cr, and Si. Consequently, for experimental spectra of comparable quality, if a ± 15% error is found for the "Mn satellite" intensity in a Fe-9Ni-1Mn alloy, in a Fe-9Ni-0.3C alloy the "C satellite" would be in error by ± 150%, and would therefore be experimentally insignificant.

At their concentrations in commercial 9Ni steel, it is Mn and Si that are primarily responsible for the "C satellite" identified by Kim and Schwartz [26].

At its low concentration in 9Ni steel, C contributes only an insignificant intensity to the "X satellite". This is seen in Fig. 23, which is taken from early backscatter 14.41 keV $\gamma$-ray spectra of $Fe-9Ni-X_1-X_2$... alloys*. The top difference spectrum in Fig. 23 shows that carbon has at most a weak effect on the shape of martensite peaks, but the bottom difference spectrum shows that an "X satellite" is found when the two starting spectra differ in their net Mn + Si concentration. With $N_s^{Mn+Si} = 14$, the "X satellite" intensity in Fig. 23 is consistent with a difference in net Mn + Si concentration of 0.0009.

The weakness of the "C satellite" made it impossible to subtract Fe-8.9Ni peaks from Fe-8.8Ni-0.3C peaks in order to determine $N_s^C$. However, a small effect attributable to a loss of carbon by the martensite was observed in a transmission experiment in which a Fe-8.8Ni-0.3C alloy was tempered for 3 hours at 600°C. (See Fig. 24 and its caption.) If the formation of austenite and carbides is arbitrarily assumed responsible for a 50% depletion of the C content of the martensite, then Fig. 24 suggests that $N_s^C = 4$. In the present work I have been unable to measure $N_s^C$ with accuracy. I believe that $N_s^C = 6$ for Fe-9Ni-C alloys because this is consistent with what is found for binary Fe-C alloys [251-253] (see also [9-11]). The $N_s^C = 6$ in Table VI is listed for this reason.

The intensities of "X satellites" were determined by the difference spectrum procedures of section VIII.B. for Fe-Ni alloys with known X concentrations. I verified that the number of sites at which a X solute atom produces a significant hyperfine magnetic field perturbation $N_s^X$, did not depend on whether or not the specimen was exposed to a saturating magnetic field. Values of $N_s^X$ are listed in Table VI. Values with standard deviations were measured in this work. All data in Table VI are for 18°C spectra.

* This work served to check the additivity of "X satellite" intensities when different solutes were added to Fe-9Ni at their commercial concentrations. Although additivity was confirmed when good data were obtained, technical problems with operating the Doppler drive in "offset mode" or "partial mode" distorted most of these spectra.

| TABLE VI | | | | | |
|---|---|---|---|---|---|
| $N_s^X$ for Fe-Ni-X Alloys | | | | | |
| | Fe | Fe-3Ni | Fe-6Ni | Fe-9Ni | Fe-12Ni |
| Mn | 7 ± 2 | 13 ± 3? | 13 ± 3 | 13 ± 2 | - |
| Cr | 13 ± 2 | 14 ± 3 | 15 ± 3 | 14 ± 2 | 15 ± 4 |
| Si | 13 ± 3 | - | - | 13 ± 3 | - |
| C | 6 | -> | -> | 6 (5 ± 3) | - |

For a Fe-Ni host at 500°C, I have found: $N_s^{Mn}$ = 12 ±4, and $N_s^{Cr}$ = 16 ±4.

The specimens used for determining $N_s^X$, like those used for determining $k_M^{X1}$, were very thin (0.0002 to 0.0003 in.). Thickness distortion corrections were performed on a few spectra before extracting the "X satellite". However, this was considered to be a waste of effort because the values of $N_s^X$ were more dependent on proper corrections for the changes in the Doppler drive, and small shifts of the main unperturbed peak due to $\frac{dH_0}{dc_X}$. Some thickness distortion corrected data is shown in Fig. 25, which shows processed experimental data from Fe-0.75Mn and Fe-0.73Cr alloys that are placed above computer calculated sums of Lorentzian curves. A Lorentzian function with the source linewidth was first deconvolved from the experimental data and then small thickness distortion corrections were performed; the result is the resonant scattering cross-section of the absorber, $\sigma_A(E)$. The calculated curves are sums of Lorentzian functions with a width characteristic of identically processed peaks of pure Fe. The positions of all Lorentzian functions were determined from the data of Vincze and Campbell [41]. The intensities of these Lorentzians were determined by the binomial probability distributions $P(8,i,c_{Mn})$ and $P(14,i,c_{Cr})$ for the Fe-Mn alloy and the Fe-Cr alloy, respectively. Good agreement between observed and calculated "satellite peak" intensities is apparent.

In the processed experimental Fe-0.73Cr spectrum the main "unperturbed part" of peak no. 1 is broader than that of the Fe-0.75Mn spectrum by about 1.5 data channels, an effect due to 3n.n. and more distant Cr atoms. The main "unperturbed part" of peak no. 1 of the Fe-0.73Mn alloy is within 0.2 data channels of that of a pure Fe spectrum that was processed in an identical way.

I have strong confidence in the important $N_s^{Mn}$ and $N_s^{Cr}$ for a Fe-9Ni host. For each datum, specimens were prepared with ternary solute concentrations of 0.75 at.% and 1.25 at.%, and spectra were taken from two specimens of each solute concentration. This was repeated with the 1.25 at.% specimens in the magnetic field. The "Mn and Cr satellites", revealed in the difference spectra of Figs. 27 and 28, were mostly obtained with the high energy tail normalization method. However, the heights of the starting spectra for this procedure were the same within 2%. Figure 28e shows two examples of difference spectra that were obtained by height normalized starting spectra that were given inappropriate shifts. Notice that the difference intensity on the high Doppler shift energy side (left side) of the main peak is positive for too much shift, but becomes negative for a shift of the opposite sign. For "Mn satellites" an approximately flat baseline is expected in the difference spectrum on the high Doppler shift energy side of the main peak because Mn solutes cause little broadening of the main "unperturbed" absorption peak of binary Fe-Mn.

However, in the case of binary Fe-Cr alloys, the main "unperturbed" peak is broadened by the presence of distant Cr neighbors, so there must be some positive intensity on the high Doppler shift energy side of the main peak when a correctly shifted pure Fe peak is subtracted from a Fe-Cr peak. It is true that a large shift of the Fe and Fe-Cr starting spectra can nearly eliminate this difference intensity on the high Doppler shift energy side of the main peak, but this occurs at the expense of developing an artificial large protuberance* on

* I have found that the size of this protuberance in difference spectrum intensity, and whether it lies on the high or low Doppler shift energy side of the main absorption peak, is a

the high Doppler shift energy side of the "Cr satellite". (This is seen on the left side of the top difference spectrum in Fig. 27a.) There seems to be less intensity on the high Doppler shift energy side of the main peak in the difference spectra which reveal "Cr satellites" in Fe-Ni-Cr alloys (see Fig. 27c-e). This effect is barely experimentally significant, but it may indicate that Ni has an effect on the long-range electron redistributions around a Cr atom. Perhaps this is indicative of a Ni-induced damping of R.K.K.Y. oscillations around a Cr atom, such as could be caused by a Ni scattering of the perturbed electron density around a Cr atom [254].

I am less confident in the value of $N_s^{Mn}$ obtained for a Fe-3Ni host. Two experiments with a Fe-3Ni-0.75Mn ingot gave values for $N_s^{Mn}$ of 12 and 14, but an experiment with an Fe-4Ni-1.3Mn ingot gave a $N_s^{Mn}$ of 9 or 10. Nevertheless, I am confident that $N_s^{Mn}$ changes from about 8 to 14 as Ni is added to the host, although the precise composition at which this occurs is somewhat uncertain, and may depend on the Mn concentration in the alloy.

**B. Tempering Experiments.**

Sequences of difference spectra from specimens with different isothermal temperings are shown in Figs. 29-33 and 36-39. The Mössbauer spectrum obtained from the specimen in its "Q"-treated condition is shown at the top of each figure. Each spectrum obtained from the specimen after further temperings was subtracted from this Q spectrum, and the succession of difference spectra appears directly below the Q spectrum in each figure. Scales for abscissa and ordinate of the difference spectra are the same as for their corresponding Q spectrum. Before differencing, all starting spectra were corrected as well as possible for any shifts of the Doppler drive. The

handy guide for determining the correct shift for the starting peaks. Fortunately, the area of the "X satellite" is relatively insensitive to this protuberance; changes in $I_S$ of only +20% were found when the protuberance was clearly too large in the author's judgment.

normalization used for all the starting spectra was the criterion of equal height for martensite peaks no. 1 (except in Fig. 36 where the starting peaks no. 1 were normalized to have equal areas).

**1. Kinetics of Austenite Formation.**

Since the austenite formed during tempering will not transform to martensite upon cooling to 500°C, the entire amount of austenite formed during tempering was determined by measuring austenite peak intensities in spectra taken at 500°C immediately after tempering. These data were used for Fig. 42, which shows the kinetics of austenite formation. Figure 42 shows that in the cases of Fe-9Ni-1Mn and N.K.K. 9Ni alloys, austenite content data taken at 18°C can also be used for determining the entire amount of austenite that was formed. After short to medium temperings, these materials retained virtually all of their austenite at room temperature. However, in most other high purity alloys, Fe-9Ni, Fe-9Ni-1Cr, Fe-9Ni-0.4Si, and Fe-9Ni-0.3C, much of the austenite had transformed to martensite upon cooling to room temperature.

The overall effects of the X elements in Fe-9Ni-X alloys on the kinetics of austenite formation, with respect to the kinetics of a binary Fe-9Ni alloy, are seen in Fig. 42. The addition of Cr reduces the kinetics of austenite formation, but the addition of Mn enhances the kinetics. From 18°C spectra it appears that Si also reduces the kinetics of austenite formation, but the amount of austenite present in the tempered Fe-9Ni-0.4Si alloy was not measured at 500°C. A Fe-9Ni-0.3C alloy prepared by a less-controlled arc melting method also showed only small amounts of retained austenite at 18°C. The alloy chemistry of the commercial N.K.K. 9Ni steel appears to be well-chosen for the rapid formation of stable austenite.

Figure 42 also shows that the alloy additions which enhance austenite formation kinetics also increase the stability of the austenite against the $\gamma \rightarrow \alpha'$

transformation upon cooling to room temperature. The thermal stability of the austenite formed in N.K.K. 9Ni steel, and that formed in the Fe-9Ni-1Mn alloy, is quite good, and these austenites form quickly. On the other hand, the addition of Cr (and probably Si) makes the austenite even less stable than the austenite in the binary Fe-9Ni alloy, and this austenite forms slowly.

Upon comparison of Figs. 42 and 43, we see that the overall kinetics of austenite formation are slower in the specimens that were rolled into foils between their solution treatment and their Q treatment. The specimens that received the most reduction in area were the ones with the slowest austenite formation.

**2. Kinetics of Solute Segregation.**

The austenite that formed after different isothermal tempering times appears to have a constant chemical composition. This was first evidenced by the constant FWHM of the austenite peak. This austenite FWHM is greater than the pure Fe FWHM because of localized isomer shifts and electric quadrupole effects caused by the many solute atoms in the paramagnetic austenite. Unfortunately, a systematic study of how the FWHM of the austenite peak depended on the austenite solute concentrations was not possible because of uncertainties in forming austenites of known compositions.

My most quantitative results for the austenite solute concentration were obtained from: 1.) 18°C spectra of the Fe-9Ni-1.25Mn alloy and the N.K.K. 9Ni alloy, and 2.) 500°C spectra of the binary Fe-9Ni alloy. The data of Figs. 44 and 45 were obtained from measurements of the changes in martensite solute concentrations, together with the assumption that all the Ni and X solutes lost by the martensite were incorporated into new austenite. It may occasionally appear from these data that the solute concentration of the austenite

decreases with tempering time, but claims of such a trend are not justified because of the experimental error. Notice that the error bars are largest for the shorter tempering times when the amount of austenite that had formed was small, and only small solute depletions of the martensite had occurred. After more austenite had formed (see Fig. 45), the precision of the austenite solute concentration data obtained by Mössbauer spectrometry was comparable to that obtained by STEM methods.

From the data of Fig. 44, the austenite in the binary Fe-9Ni alloy formed at 600°C has a Ni content of about 23 at.%. This is somewhat more than the 20 at.% indicated by the equilibrium Fe-Ni phase diagram of Fig. 1a, but this discrepancy may be explained by systematic experimental errors of 500°C spectra. However, the Ni content of the austenite in both Fe-9Ni-1.25Mn and N.K.K. 9Ni alloys is only about 15 at.%, and I am confident that these 18°C data indicate an austenite Ni concentration that is lower than predicted by the Fe-Ni phase diagram. Although it was leaner in Ni, the austenite in the Fe-9Ni-1.25Mn alloy had a Mn concentration of about 8 at.%, and the austenite in the N.K.K. 9Ni alloy had an X solute concentration of about 4 at.%. Apparently Mn and other alloy elements can substitute for Ni to allow the austenite to form with a lower Ni content. In the Fe-9Ni-1.25Mn alloy this substitution of Mn for Ni was on an approximately 1:1 basis, and in N.K.K. 9Ni steel the substitution of X for Ni was on approximately a 1:2 basis. The segregation of C to the austenite in N.K.K. 9Ni steel may be the reason why only a small change in the "X satellite" occurs when the austenite is 8% leaner in Ni than the austenite in the binary Fe-9Ni alloy. Although the carbon content of the austenite cannot be accurately determined, I suggest that in N.K.K. 9Ni steel the small change in "X satellite" intensity indicates that C substitutes for Ni on a 1:10 basis. Although the thermal instability of the austenite in Fe-9Ni-1Cr and Fe-9Ni-0.4Si alloys precluded

quantitative measurements, it appears that Cr and Si segregation to the austenite is similar to that of Mn at 600°C.

The equilibrium Fe-Ni binary phase diagram predicts an increased Ni concentration for austenite as it is formed at lower temperatures. In fact, this trend is observed for the austenite formed in N.K.K. 9Ni steel at 630°C. This 630°C austenite has 2% less Ni than the 600°C austenite; the equilibrium Fe-Ni binary phase diagram indicated that the Ni content should be 3% less for the 630°C austenite. The equilibrium Fe-Ni binary phase diagram further states that the Ni concentration of the 550°C austenite should be 6% greater than that of 600°C austenite. However, we see in Fig. 44 that for N.K.K. 9Ni steel it is actually more than 2% *less*, and this 8+% discrepancy cannot be attributed to experimental error. Figure 45 shows that the 550°C austenite has a 3% larger X element concentration than the 600°C austenite. The change of this balance of Ni and X solutes in austenite with temperature again indicates that in N.K.K. 9Ni steel the X elements substitute for Ni on a 1:2 basis. These effects can be seen in Fig. 40 by examining the structures in the differences of martensite peaks (nearly the same amount of austenite had formed at the three temperatures). Figure 40 also shows the large difference in the time required to form nearly the same amount of austenite at these three temperatures.

I have data from a small experiment which I find particularly satisfying as a demonstration of the success and limitation of difference spectrum procedures for chemical and phase analysis of N.K.K. 9Ni steel. At the bottom of Fig. 41 is the difference between the Mössbauer spectrum obtained from a Q-treated specimen, and the spectrum from the same material after tempering for 29 hours at 600°C. (This same difference spectrum also appears at the bottom of Fig. 38.) This "Q - QT29" difference spectrum clearly shows the formation of a large amount of austenite and shows a large loss of Ni and X solutes from the

martensite. This QT29 austenite is thermo-mechanically unstable; hammering the specimen at 77°K served to transform most of the austenite to martensite. This transformation is seen in the top difference spectrum of Fig. 41, which is the difference between spectra of the QT29 specimen before and after cold-hammering. In addition to the loss of austenite, this top difference spectrum also shows a greater average concentration of Ni and X solutes in the martensite after cold-hammering. That the difference spectrum intensities corresponding to Ni and X concentration changes in the martensite are not exactly the reverse of the difference spectrum intensities at the bottom of Fig. 41 is expected for two reasons: 1.)some austenite still remains in the cold-hammered specimen, and 2.) the chemical composition of the martensite in the cold-hammered material is not homogeneous. After accounting for reason no.1, Fig. 41 suggests that each atom in the solute-rich fresh martensite causes only about $\frac{2}{3}$ of the difference spectrum intensity produced by the solutes in the tempered martensite. This is a consequence of reason no. 2, which is described in section IV.D.

**C. Anisotropic Hyperfine Magnetic Field Perturbations Around Ni Atoms at 18°C.**

I first describe early tempering sequences of Fe-9Ni-1.25Cr and Fe-9Ni-1.25Mn alloys. The difference spectra shown in Figs. 32 and 30 were obtained at 18°C with no magnetic field applied to the specimen. In Fig. 30 the difference spectrum intensities associated with an apparent Ni and Mn loss by the martensite increase as more austenite forms. However, these difference intensities are already large after very short temperings when very little austenite had formed. Notice also in Fig. 30 that the difference spectrum intensities around peaks nos. 2 and 5 are also disproportionately large after very short temperings. In Fig. 32 the same sort of correlation is evident; the Q - QT$\frac{1}{3}$ and Q - QT27 difference

spectra show a disproportionately large difference intensity around peaks nos. 2 and 5 simultaneously with larger difference spectrum intensities around peaks nos. 1 and 6. On the other hand, in Fig. 32 the Q - QT3 difference spectrum shows nearly zero difference spectrum intensity around peaks nos 2 and 5, and uncharacteristically small difference spectrum intensities around peaks nos. 1 and 6. This same correlation between the difference spectrum intensities around peaks nos. 1 and 5, and the apparent Ni- and X-induced difference spectrum intensities around peaks nos. 1 and 6 was also observed in several tempering sequences of N.K.K. 9Ni steel which are not included in the figures.

Figure 34 shows difference spectra obtained from a binary Fe-9Ni specimen in a sequence of low-temperature isochronal temperings, which formed no austenite in the specimen. Again we see the simultaneous change in the ratio of intensity of peak no. 1 to the intensity of peak no. 2, and a change in the difference spectrum intensities around peaks nos. 1 and 6. The quantitative correlation between these two effects in the difference spectrum is close to that described in the previous paragraph for Fe-9Ni-1.25X alloys. This same correlation was also found in a sequence of low temperature isochronal temperings of a Fe-9Ni-1.25Mn alloy which is not included in the figures.

Difference spectra of an Fe-8.9Ni specimen with different states of magnetization are shown in Fig. 35. Again we see the same correlation between the changed ratio of intensity of peak no. 1 to the intensity of peak no. 2, and the difference spectrum intensities around peaks nos. 1 and 6. As described in section IV.F., there is no basic geometrical relationship between the angles $\vartheta$ and $\varphi$. Nevertheless, I believe that the observed correlation results from changes in the anisotropic hyperfine magnetic field perturbations at $^{57}$Fe nuclei near Ni atoms when the lattice magnetization directions are changed. The small magnitude of these effects implies that the significant $\Delta D_j^M$ parameters are roughly

5% as large as the significant $\Delta H_j^{Ni}$ parameters. In experimental practice with height-normalized difference spectra, I found that when the ratio of intensity of peak no. 2 to the intensity of peak no. 1 changed by 10%, the difference spectrum heights around peaks nos. 1 and 6 were about 3% as large as the dip of peak no. 1. All martensite solute concentration differences obtained from spectra of specimens that were not exposed to an external magnetic field were corrected in proportion to this amount. Even when the specimens were in the magnet there was not complete control over the angles $\vartheta$ and $\varphi$, and some such corrections were still necessary. These corrections were, however, much smaller than those required by data from unmagnetized specimens.

I found a feature of 500°C difference spectra that may qualify as an interesting observation about the temperature dependence of the anisotropic hyperfine magnetic field perturbations. Notice in Fig. 29 that although there is a substantial change in the ratio of intensity of peak no. 2 to the intensity of peak no. 1, this does not correlate to any change in the difference spectrum intensity around peaks nos. 1 and 6. This lack of correlation also appears to be true for the 500°C difference spectra in Fig. 31. (However, Fig. 33 seems to show a correlation comparable to that of the 18°C spectra.) One explanation of this lack of correlation may be that the effective relation between angles $\vartheta$ and $\varphi$ at 500°C is different from the relation at 18°C, but this explanation requires a lucky cancellation of changes in anisotropic hyperfine magnetic field perturbations at 500°C. Instead, I believe that this lack of correlation indicates that the anisotropic hyperfine magnetic field perturbations do not exist at 500°C. More careful experiments with single crystals of Fe-Ni are clearly needed to test this hypothesis.

# CHAPTER X

# DISCUSSION

## A. ELECTRONIC EFFECTS.

### 1. Electron Transfer and Magnetic Moment Perturbations.

*How Electron Transfer is Important.*

In order to treat the Mössbauer spectra from Fe-Ni-X alloys with the model of linear response, we need to estimate the otherwise unknown sets $\{g_{Ni}^{X}(r_j)\}$ and $\{g_{X}^{Ni}(r_j)\}$*. To make such predictions, we must first discuss the electronic origin of magnetic moment perturbations around solute atoms. The goal of this section X.A.1. is to use estimates of the parameters $\{g\}$ to predict how the intensity of the "X satellite" at 18°C may change with the Ni content of the host. Our understanding of the magnetic moment perturbations must be fairly detailed since there are so many varieties of $\{g\}$.

When X is a 3*d* transition metal atom, the parameter $g_{Y}^{X}(r_j)$ is the result of an unbalanced change in the number of 3d↑ and 3d↓ electrons at the X atom when it is separated from a Y atom by the distance $r_j$. The parameters $g_{Y}^{X}(r_1)$ and $g_{Y}^{X}(r_2)$ may be thought to arise from localized electron transfer between the X and Y atoms, modified by the surrounding atoms of the iron-based matrix. Local details of this modification may be important. For instance, if a 1n.n. (with respect to the X atom) Y atom itself neighbors a 2n.n. Z atom with which it strongly covalently bonds, the change in numbers of 3d↑ and 3d↓ electrons at the X atom caused by the Y atom may no longer be parameterized by the same $g_{Y}^{X}(r_1)$ appropriate for the configuration without the 2n.n. Z atom. Such effects are expected when the covalent mixing of the local electron states at the Y and

* Recall that these sets parameterize the perturbation of the X magnetic moments by neighboring Ni atoms, and the perturbation of the Ni magnetic moments by neighboring X atoms, respectively.

Z atoms substantially alters their occupancies. With an altered Y atom electron density, $g_Y^Y$ will be modified. An analogous effect will occur for the parameter $g_Z^Y(r_2)$. In essence, these local bonding considerations amount to considerations of how well the effects at the X atom due to the three-atom interaction between the X, Y, and Z atoms can be approximated by two pairs of interactions involving the X, Y and the X, Z pairs of atoms. The concentration dependence of each pairwise interaction is assumed irrelevant because we are only concerned with very *small* composition *changes*. The diversity of local environments in a Fe-9Ni-1X ternary alloy makes the complete consideration of all configuration-dependent magnetic moment perturbation nearly hopeless, without computerized bookkeeping. Consequently the goal of the following discussion is the schematic illustration of some likely magnetic effects of Ni-X valence and conduction electron interactions. This development relies on simple pairwise interactions for all alloys except Fe-Ni-Mn, in which large density of state changes are proposed for the Mn atom due to its Ni neighbors.

Currently there are published measurements for the important parameters $\{g_X^{Fe}\}$, $\{g_M^{Fe}\}$, $\{g_M^{Ni}\}$(which ~0), $\{g_X^Y\}$, and the magnetic moments $\mu_{Fe}$, $\mu_M$, and $\mu_X$. To complete the picture of solute-induced hyperfine magnetic field perturbations at $^{57}$Fe nuclei, as presented in the model of linear response in Chapter VI, we are in the position where we must develop at least a qualitative understanding of two unmeasured effects: 1.) the magnitudes of $\{g_X^{Ni}(r_j)\}$ and $\{g_M^X(r_j)\}$, and 2.) how the parameters $\{g_X^{Fe}(r_j)\}$ (and also possibly $\{g_M^{Fe}(r_j)\}$, $\{g_X^{Ni}(r_j)\}$, and $\{g_M^X(r_j)\}$) change with the Ni content of the host matrix.

A qualitative understanding of these unmeasured effects 1 and 2 above will supply the missing pieces needed for the extension of the model of linear response to our ternary alloys, as formally developed in Chapter VI. Fortunately, the goal of this discussion is not the evaluation of quantitative

changes in $\{\Delta H_i^X\}$ with Ni content of the host matrix, but is rather the identification of potentially large qualitative changes, in which an experimentally insignificant $\Delta H_i^X$ may become experimentally significant, or vice-versa. Although even a small change in an already significant $\Delta H_i^X$ may affect the shape of the "X satellite", only such a large qualitative change of a $\Delta H_i^X$ will affect the intensity of the "X satellite" peak by changing the value of $N_s^X$ in equation IV-5. Knowing such changes clearly has quantitative importance for the present method of determining the X solute concentration of martensite. Finally, we note that although Ni-induced changes in the sets $\{g\}$ can affect the $H_L$, $H_{DNL}$, and $H_{INL}$ contributions to $\Delta H_i^X$, it is also conceivable that $H_{DNL}$ and $H_{INL}$ can be affected by Ni-induced changes in the linear response parameters $\{f(r_j)\}$. This is considered later in Section X.A.3.

*Previous Estimates of Electron Transfer.*

The amount of covalent electron transfer between an occupied (electron) state and an unoccupied (hole) state is proportional to the square of two factors: 1.) the matrix element of the perturbing potential (a nonzero electron-electron exchange and Coulomb potential) in the region where the two wavefunctions have significant overlap, times, 2.) the inverse of the energy difference between the two states. The density of states is included as a weight for factor (2) for determining the net electron transfer when one of the states is in a continuum. Often factor (1) is considered constant, and only factor (2) is integrated against the density of states when calculating electron transfer. However, factor (1) is closely related to the energy width of the band [255], and its smooth variation across the $3d$ series can often be approximately included [181].

In their treatment of alloy phase formation, Watson and Bennett [180,181,256-258] offer a model of charge transfer effects in $3d$ transition metal

alloys. On the basis of the large Mössbauer isomer shifts at $^{57}$Fe impurities in various host metals, and on the basis of a little photo-emission data, they argue that the 3*d* charge transfer between Wigner-Seitz cells of two transition metal atoms is in the opposite direction to the larger 4*s* charge transfer. In their model, which started with Friedel [163,259], the occupied (unoccupied) 3*d* levels of a solute hybridize with the unoccupied (occupied) 3*d* band states of the metal, and this accounts for most of the bonding energy. The 4*s* electrons then screen the lost (gained) 3*d* charge at the solute site, and then these 4*s* electrons hybridize with the 3*d* electrons, further reducing the system energy. In this model there is an overscreening by the 4*s* electrons in the Wigner-Seitz cell of the solute atom, so the net charge transfer is in the same direction as the 4*s* charge transfer. (Such overscreening is not inconsistent with the Friedel theory sketched in Section V.E.2.) With some 4*s* overscreening, an examination of equation V-15 tells us that isomer shifts from both 4*s* and 3*d* electrons will be of the same sign, but the 4*s* contribution will be about twice as large.

Much of the current theoretical work on 3*d* charge transfer problems with transition metal alloys is oriented towards calculating the heats of formation of alloy phases [257-271]. The overall 3*d* charge transfer effects used in these models are valuable for estimating isomer shifts, but our immediate concern is with how electron transfer causes magnetic moment perturbations -- our goal is an understanding of changes in electron spin density. The simplest way to include spin dependence in the iron band states is to translate the +spin band to lower energy with respect to the -spin band, so that when both bands are filled to the Fermi level there is a spin imbalance of 2.2 electrons per atom. Hasegawa and Kanamori [273,274] set up spin-dependent coherent potential approximation (CPA) calculations* for Fe-X alloys in just this way, using

* These CPA calculations [272] are a type of tight-binding calculation useful for Fe-X alloys which starts with Fe and X atomic energy levels. With an initial density of states for pure Fe metal, one knows how the Fe atomic levels are modified by its nearest neighbors. The addi-

triangular density of states curves for Fe $3d$ electrons. They did not include $4s-3d$ hybridization, and their calculatations treat nearest neighbor effects on local densities of states in only an average way. For instance, if a solute magnetic moment were to drop precipitously when the number of its solute neighbors increased from 5 to 6, such a change would appear in a much less dramatic way in their CPA calculation, and would occur only at high solute concentrations. Our model of linear response of hyperfine magnetic fields to magnetic moments is oriented towards specific effects of local solute environments rather than towards average effects of solute concentrations. Nevertheless, average magnetic moment perturbations determined by Hasegawa and Kanamori [274] were boldly used for depicting the electronic effects in Fe-Ni, Fe-Mn and Fe-Cr binary alloys shown in Figs. 47, 49, and 50, and discussed below. These figures are reasonable adaptions of average electronic effects to specific nearest neighbor configurations, but their reliance on average CPA calculations may be risky. To varying extents, analogous electronic effects in Fe-Ni-X alloys were assumed to be modified by the presence of a Ni atom near the X atom; local magnetic effects in Ni-X alloys were considered when making such modifications [275-280].

More recently, other workers [262-265,280-285] have explicitly incorporated nearest neighbor configurations into the CPA method. Not surprisingly, averaged covalent bonding effects such as heats of formation have little sensitivity to details of electron transfers associated with each nearest neighbor configuration [262-265]. However, it has been found that the dependence of the magnetic moment of an atom on the specific number of its solute neighbors

tion of X atoms to the nearest neighbor shell of a central Fe atom changes the local density of states as determined by a self-consistent average Green function for the alloy. This results in nearest neighbor-induced occupancy changes of the Fe atomic levels which cause electron transfers to or from the Fe sites. Similar local densities of states are obtained for the X atoms.

can be as large as its dependence on the average solute concentration. Miwa and Hamada [285] have performed cluster CPA calculations for 3d↑ and 3d↓ electron states in Fe-V and Fe-Co alloys. These calculations determined the local density of states for an Fe atom surrounded by a specific number of V first nearest neighbors for different average V concentrations. They found that at an average V concentration of 80%, Fe atoms surrounded by 3 and 4 first nearest neighbor V atoms have magnetic moments of $1.2\mu_B$ and $0\mu_B$, respectively. This effect is due to a high density of Fe 3d↑ states moving through the Fermi surface, and is closely analogous to the electronic model proposed by Campbell [202,286] to explain the temperature dependence of Fe-Mn Mössbauer spectra (see section VI.A). Unfortunately, I am not aware of such detailed calculations for the iron alloys of immediate interest.

*Spin Polarizations Around X Atoms*

The conventions used in Figs. 47-50 are described in Fig. 46. All other atoms in the lattice, which are not drawn, are assumed to be Fe atoms in the case of Fe-X alloys, or Fe and Ni atoms in the case of Fe-Ni-X alloys. The energy of electron states increases in the vertical direction, and the Fermi level is represented by the flat line at the top of each stylized atom. The gain or loss in the number of 3d↑ and 3d↓ electrons with respect to their numbers at the same atom in their reference metal is shown by an arrow of appropriate size and direction above each density of states curve. The reference metal is pure iron for Fe atoms; the Fe 3d↑ and 3d↓ density of states in pure Fe are drawn in Fig. 46. The reference metal for X atoms is effectively pure iron -- a dilute Fe-X alloy. However, the reference metal for Ni atoms in Fe-Ni-X alloys is a binary Fe-Ni alloy of the same Ni concentration. In comparing hyperfine magnetic field perturbations in Fe-Ni-X alloys to hyperfine magnetic field perturbations in Fe-X alloys, I ignore any changes in the atomic volumes associated with the charge

transfers. (I thereby ignore any volume effects [177-179,192,198,208,209,216] in the overlap contributions to the $^{57}$Fe hyperfine magnetic field involving $H_{OV}$.) The difference in atomic volume between any of the atoms Fe,Ni,Mn,Cr, and Si is small, and the effective atomic volume changes upon alloying the Fe host with Ni will presumably be even smaller.

For use in the formal model of linear response for ternary alloys developed in section VI.E., Figs. 48-50 include representatives of the three contributions to $\Delta H_2^X$. The direct nonlocal contribution ($H_{DNL}$ from the 2n.n. solute atom through $f(r_2)$), and the local contribution ($H_L$ arising from the magnetic moment perturbation at the $^{57}$Fe atom itself), are indicated explicitly. I have depicted the indirect nonlocal contribution from only one atom (the 1n.n. Fe atom), so the $H_{INL}$ contribution to $\Delta H_2^X$ is indicated in only an average way. The dominant contribution to $\Delta H_2^X$, if reasonably known, is underlined in the figures. The change in the $^{57}$Fe isomer shift is also indicated, and is consistent with the change in the 4$s$ screening charge. Parts B of Figs. 48-50 illustrate the effect of Ni on $\Delta H_2^X$. For each part B, the changes in occupancies of electronic levels, the changes in magnetic moments ($\delta\mu$), and the changes in contributions to the $^{57}$Fe hyperfine magnetic field ($\delta H$), are all referenced to their changes in part A of the figures.

Figures 47-50 could be naively misinterpreted in several ways. In Fig. 49B the large gain of 3$d$ electrons by the Mn atom is supplied by all of its neighboring Fe and Ni atoms, and not by just the Fe atom drawn in the figure. I have tried to indicate this by drawing 3$d$ arrows leaving the Fe atom which are smaller than the 3$d$ arrows entering the Mn atom. Another cautionary note concerns the conservation of electrons but nonconservation of spins. For example, even if we neglect electron transfer between the 4$s$ and 3$d$ states, the net number of the 3$d\uparrow$ electrons gained by all the Fe atoms in a Fe-Ni alloy will

not generally equal the number of $3d\uparrow$ electrons lost by all the Ni atoms. Any energy shift of the $3d\uparrow$ states and/or the $3d\downarrow$ states of an atom will usually cause a net nonconservation of spin because the number of occupied $3d\uparrow$ and $3d\downarrow$ states will change independently at this atom -- this spin imbalance need not be compensated by magnetic moment perturbations at surrounding atoms. Again I have tried to indicate such effects with the size of the electron transfer arrows.

*Fe−Si*. The electron transfers caused by a Si atom, and the consequent hyperfine magnetic field perturbations at neighboring $^{57}$Fe nuclei, were described in section VI.B. with the Marshall-Mott model [213]. In the simple case of a dilute Fe-Si alloy, the Si atom has no effect on the magnetic moments of Fe atoms, so $g_{Si}^{Fe}(r_j) = 0$ for all $r_j$. Since the Si atom cannot sustain an imbalance of its own $3p\uparrow$ and $3p\downarrow$ electrons, $\mu_{Si} = 0$. The hyperfine magnetic field at the $^{57}$Fe nucleus in Figure 48A arises exclusively from the absence of a magnetic moment at the 1n.n. Si site -- $\Delta H_{DNL}$ is the only contribution to $\Delta H_2^{Si}$. Therefore the measured $\Delta H_2^{Si}$ can be used* to evaluate the linear response parameter $\alpha_{CEP} f(r_2)$:

$$\alpha_{CEP} f(r_2) = \frac{\Delta H_2^{Si}}{\mu_{Si} - \mu_{Fe}} = -5\ \frac{kG}{\mu_B}\ ; \quad \text{similarly,} \quad \alpha_{CEP} f(r_1) = -11\ \frac{kG}{\mu_B}$$

No localized isomer shift perturbation is expected due to changes in the $^{57}$Fe $3d$ occupancies, but since the 2n.n. separation is probably beyond the first node† of the $4s$ conduction electron redistribution, a positive $\Delta i_2^{Si}$ is expected and observed [107,109,112].

*Fe−Ni*. The magnetic moment perturbations in Fe-Ni alloys are depicted in Figure 47. Following calculations by Hasegawa and Kanamori [274], and with

* Other "magnetic hole" impurities give very similar estimates of $\alpha_{CEP} f(r_2)$ [109,212,216].
† If the 2n.n. separation lies within the first node, then a negative $4s$ polarization would be consistent with a positive $\Delta i_2^{Si}$.

neutron diffraction evidence [226,227,229], the iron magnetic moments near a Ni atom are shown to be enhanced by favorable energy shifts of both the Fe $3d\uparrow$ and the Fe $3d\downarrow$ states. (However, the depletion of electrons from the Fe $3d\downarrow$ states is probably not as substantial as the gain in Fe $3d\uparrow$ electrons.) The increase in energy of the Fe $3d\downarrow$ states arises because the Fe $3d\downarrow$ states are at higher energies than the Ni $3d\downarrow$ states, and with hybridization these two sets of states repel (see section V-C.). Such repulsion* (Eqn. V-52) causes most of the Fe $3d\downarrow$ states to lie at even higher energies. The shape of the Fe $3d\downarrow$ density of states curve is therefore significantly modified, but we are mainly concerned with the net loss of Fe $3d\downarrow$ electrons (so the distortion of the density of Fe $3d\downarrow$ states is not indicated in Fig. 47). In the case of $3d\uparrow$ electrons, the Fe and Ni states lie closer in energy. By spreading its wavefunction over Fe atoms, a Ni $3d\uparrow$ electron can lower its kinetic energy. The net transfer of $3d$ electrons from the Ni atoms to the Fe atoms** causes $4s$ electrons to pile up around Ni atoms. The average loss of $4s$ electrons and gain of $3d$ electrons by the $^{57}$Fe atom ensures a positive average isomer shift, and this is observed [41,113] (also see Fig. 47).

Unlike Fe-Si alloys, in Fe-Ni alloys $\Delta H_L$, $\Delta H_{INL}$, and $\Delta H_{DNL}$ are all important contributors to the $^{57}$Fe hyperfine magnetic field The magnetic moment of the Ni atom is less than that of the Fe atom which it replaces, so $\Delta\mu < 0$ and a positive $\Delta H_{DNL}$ is developed through $f(r_2)$. The neighboring 1n.n. Fe atom, however, has a larger magnetic moment than it would have in pure Fe ($g_M^{Fe} > 0$), so it offers a negative $\Delta H_{INL}$ through $f(r_1)$. $\Delta H_{INL}$ is probably the largest contributor to the $^{57}$Fe hyperfine magnetic field perturbation, although the negative $\Delta H_L$

* This is more clearly reflected in electronic heat capacities and other effects sensitive to details of the Fermi surface.
** Ni atoms apparently retain most of their additional two $3d$ electrons in Fe-Ni alloys, as evidenced by the large x-ray scattering factors for superlattice diffractions from ordered Fe-Ni alloys [287].

due to the enhanced magnetic moment at the $^{57}$Fe atom is comparably large. Section IV-G discussed how the significant localized isomer shifts are observed to be negative for Fe-Ni alloys at 18°C. Figure 47 suggests that $\Delta i_2^{Ni}$ is dominated by its indirect nonlocal contribution due to the $3d$ electron density changes at Fe atoms near Ni atoms.

*Fe−Ni−Si*. Figure 48B synthesizes the electronic effects in Fe-Si and Fe-Ni alloys to illustrate the changes of $\Delta H_2^{Si}$ in a Fe-9Ni-1Si alloy. Again we assume the impotence of Si in causing magnetic moment perturbations at surrounding Fe as well as Ni atoms. The only significant contribution to the $^{57}$Fe hyperfine magnetic field due to a Si atom is $\Delta H_{DNL}$, as it was for a Fe-Si alloy.

The change, $\delta H_{DNL} > 0$ in our model. $\Delta H_2^{Ni}$ is somewhat larger for Fe-Ni-Si alloys than it is for Fe-Si alloys because the average Fe moment which the Si atom replaces is larger in Fe-Ni-Si alloys due to the surrounding Ni atoms. This also is reflected in the shift of the main unperturbed (e.g. unperturbed by Si) peak, which is not indicated in Fig. 48B. However, using Table V this difference in $\Delta\mu$ for $c_{Ni} = 0.09$ is only:

$$\Delta\mu = c_{Ni}\ M(g_{Ni}^{Fe}) \simeq 0.016\mu_B\ ,$$

so it is negligibly small in comparison to the difference in Fe and Si magnetic moments (for which $\Delta\mu = -2.2\mu_B$). Although the parameters in the set $\{\Delta H_i^{Si}\}$ will all be enhanced by $\frac{0.016}{2.2} \simeq 7\%$, the number of nearest neighbor sites that offer significant contributions to the "Si satellite" intensity will still be the same in Fe-Ni-Si alloys as in Fe-Si alloys. Therefore no change in the "Si satellite" intensity will occur when the Fe host is alloyed with 9% Ni.

*Fe−Mn* and *Fe−Ni−Mn*. Section VI.A. described Campbell's model of a vital electronic effect in Fe-Mn alloys. In order to explain the temperature dependence of the hyperfine magnetic field at a $^{55}$Mn nucleus in an Fe host, he suggested [286] that the Fermi level runs through a large peak in the density of Mn

$3d\uparrow$ states, but runs through a lower density of Mn $3d\downarrow$ states. Changes in the energy of Mn $3d$ states with respect to the Fermi level will rapidly cause uncompensated changes in the number of Mn $3d\uparrow$ electrons, and therefore a rapid change in the Mn magnetic moment. The local density of states situation in a dilute Fe-Mn alloy and its corresponding $\Delta H_2^{Mn}$ is indicated in Figure 49A, but this situation is more controversial than for Fe-Si and Fe-Ni alloys. Stearns [117,120], and Vincze and Campbell [41] disagree on whether or not $\Delta H_2^{Mn}$ is experimentally significant in Fe-Mn Mössbauer spectra. I believe that Stearns has misinterpreted her experimental data (see footnote in Section IV-B), especially since my own experimental data indicates that $\Delta H_2^{Mn}$ is experimentally insignificant (See Table VIII and compare satellite intensities in Fig. 25).

Curiously, if $\Delta H_2^{Mn}$ is experimentally insignificant, and because the linear response parameter $f(r_2)$ is assumed to be a characteristic of the Fe host metal, it is essential that $\Delta H_{INL}$ and $\Delta H_L$ serve to accurately cancel the positive $\Delta H_{DNL}$. ($\Delta H_{DNL}$ must necessarily be positive and large because the Mn magnetic moment is significantly less than that of an Fe atom, and $\alpha_{CEP} f(r_2) \simeq \frac{-6kG}{\mu_B}$.) Of course, this precise cancellation of the $\Delta H_L$, $\Delta H_{INL}$ and $\Delta H_{DNL}$ contributions may be destroyed in Fe-Ni-Mn alloys, if Ni atoms affect the Mn magnetic moment or the Mn-induced magnetic moment perturbations of the Fe or Ni host stoms. We expect that if this cancellation of competing contributions were destroyed, the parameter $\Delta H_2^{Mn}$ would become experimentally significant.

In calibration work with "Mn satellite" intensities in Fe-Ni-Mn alloys, I found that for Ni compositions of greater than about 3 or 4%, the parameter $\Delta H_2^{Mn}$ became experimentally significant and positive. This effect may result in part from changes in $\Delta H_L$ and $\Delta H_{INL}$ which result from Ni-Mn electronic interactions. The sets $\{g_{Mn}^{Fe}\}$ and $\{g_{Mn}^{Ni}\}$, which are important in determining $\Delta H_L$ and $\Delta H_{INL}$, may be substantially modified by Ni-Mn interactions; if the number of $3d\uparrow$ and

$3d\downarrow$ electrons at a Mn atom are altered by the presence of a neighboring Ni atom, the electron transfers between this Mn atom and its other neighbors will be affected. It is unlikely that the changes in $\Delta H_2^{Mn}$ result from changes in $\{g_{Mn}^{Fe}\}$ and $\{g_{Mn}^{Ni}\}$ because the Mn concentration is so low. I confine my speculation to changes in $\Delta H_{DNL}$, which arises from Ni-induced perturbations of the Mn magnetic moment (i.e. from the set $\{g_M^{Mn}(r_j)\}$). If the Fermi surface does intersect a peak in the density of Mn $3d\uparrow$ states, dramatic changes in the Mn magnetic moment and $\Delta H_{DNL}$ seem especially likely as the Fe host is alloyed with Ni, and such changes can themselves be large enough to account for the Ni dependence of $\Delta H_2^{Mn}$.

To explain the observed Ni dependence of $\Delta H_2^{Mn}$ by changes in $\Delta H_{DNL}$, it is necessary to propose that the Mn magnetic moment becomes less positive when the Mn atom is surrounded by Ni neighbors. A reduction of $\mu_{Mn}$ of 1-2$\mu_B$ appears reasonable upon comparison of the shapes of "Mn" and "Cr satellites" in Figs 27 and 28. Perhaps, since Mn $3d\uparrow$ and Mn $3d\downarrow$ states lie at higher energies than most Fe $3d\uparrow$ and Fe $3d\downarrow$ states, hybridization of the Mn $3d$ states with the Ni $3d$ states causes a repulsion of both Mn $3d\uparrow$ and Mn $3d\downarrow$ states, unlike the situation for Fe, whose $3d\downarrow$ states only are pushed to higher energies by hybridization. Although this hybridization with Ni $3d$ states may offer comparable energy shifts to Mn $3d$ states of either spin, the Mn magnetic moment will decrease because of the more rapid reduction in the number of Mn $3d\uparrow$ electrons. A problem with this mechanism is that it is not consistent with Watson and Bennett's model of $3d$ charge transfers. Electronegativity increases as the $3d$ series is traversed from left to right [256] , and we expect a net $3d$ electron transfer from the Ni to the Mn. Then Campbell's proposed peak in the density of Mn $3d\uparrow$ states at the Fermi surface implies that the Mn magnetic moment would become more positive with more Ni neighbors, but this is a change in the

wrong direction for predicting a significant, positive $\Delta H_2^{Mn}$.

It is also possible that an increasing number of Ni neighbors around a Mn atom could cause a sudden reversal of the magnetic moment at that Mn atom. Such an effect has been predicted for Mn-Ni fcc alloys [278,279] and experimentally verified with NMR and neutron diffraction experiments [276,277,280] With a reversed Mn moment, the change in the direct nonlocal contribution, $\delta H_{DNL}$, will be strongly positive. This is the effect illustrated in Figure 49B. In this model involving a Mn magnetic moment reversal at a critical local Ni concentration, and also in the milder effects calculated with the cluster CPA method by Miwa and Hamada [285], pairwise treatments of electron transfers between atoms may be inadequate for concentrated alloys. The model of linear response relies on summing pairwise interactions, and the model will have trouble when there is a diversity of local environments in which Mn atoms are surrounded by both a greater and a lesser number than the critical number of Ni neighbors. In this case equation VI-42 will clearly require more detailed information than one additive set of constant $\{g_M^{Mn}(r_j)\}$ parameters. Fortunately, in Fe-9Ni-1Mn alloys virtually all of the Mn atoms will have more Ni neighbors than the critical number; the Mn satellite intensity does not change for Fe-Ni-Mn alloys when the Ni concentration increases from 6 to 12%. A nearest neighbor shell analysis with a set of additive $\{g_M^{Mn}(r_j)\}$ parameters could again be appropriate for Fe-9Ni-1Mn alloys, although this new set would be different from the set appropriate for a Fe-1Ni-1Mn alloy.

The intent of Fig. 49 is merely to illustrate a plausible effect at a Mn atom which occurs at a critical number of nearest neighbors (~ 1 or 2 in the first two bcc nearest neighbor shells), or maybe at a critical Ni concentration, (≈ 4%), or maybe both. There may be other detailed interpretations which are consistent with both my data and with the model of linear response. It is important to

note that Fe-Mn alloys have a history of controversy. Early neutron diffraction experiments indicated that the Mn magnetic moment was zero [225], but later work [193,220,229,288] indicated a positive Mn magnetic moment of anywhere from 0.8 to over $2\mu_B$. ($1.2\mu_B$ seems to be a reasonable compromise.) The reported magnetic moment perturbations of Fe atoms around Mn atoms [220] also require further verification, in my opinion. In Figure 49A I have indicated that $g_{Mn}^{Fe}(r_1)$ and $g_{Mn}^{Fe}(r_2)$ are positive in order to predict a $\Delta H_L$ and a $\Delta H_{INL}$ which cancel the positive $\Delta H_{DNL}$ that is expected when $\mu_{Mn} - \mu_{Fe}$ is less than zero.

*Fe−Cr* and *Fe−Ni−Cr*. I know of no experimental data which might indicate a change in the Cr magnetic moment with the Ni content of the host, that is as dramatic as the proposed change in the Mn magnetic moment. Unfortunately, I know of no theoretical data for the local Cr density of states in Fe-Cr alloys, either. In the case of Cr, it might seem reasonable that the peak in the density of $3d\uparrow$ states, which was proposed to be intersected by the Fermi level in the case of Mn, would now lie above the Fermi level but still below its corresponding peak in the density of Cr $3d\downarrow$ states. However, the real situation is not so simple. Unlike the case for Mn, neutron diffraction has shown [225] that the Cr magnetic moment is negative.

Instead, for Cr I propose that the Fermi level intersects neither the Cr $3d\uparrow$ nor the Cr $3d\downarrow$ density of states curves at a peak, nor at any position where there is a large net difference in the densities of Cr $3d\uparrow$ and Cr $3d\downarrow$ states. (This uneventful situation is depicted in Fig. 50.) Consequently, the Cr magnetic moment should not change rapidly with Ni concentration. This means that the set $\{g_{Ni}^{Cr}\}$ (and possibly $\{g_{Cr}^{Ni}\}$) will be neither large, nor significantly changed, by an increased Ni content of the alloy, even if there is some covalent bonding between Ni and Cr atoms. Without large Ni-induced changes in the numbers of Cr $3d\uparrow$ and Cr $3d\downarrow$ electrons, the Cr and Fe $3d$ states may still undergo compar-

able mixing with or without neighboring Ni atoms. The set $\{g_{Cr}^{Fe}\}$ will then remain largely unchanged with the Ni content of the alloy. This set $\{g_{Cr}^{Fe}\}$, and hence $\Delta H_{DNL}$, was small in binary Fe-Cr alloys anyhow [220].

With a Cr magnetic moment of $-0.7\mu_B$ [193,225], and with equation VI-31, I predict that in binary Fe-Cr alloys $\Delta H_L$ and $\Delta H_{DNL}$ are much smaller than $\Delta H_{DNL}$. The electronically uneventful situation I have suggested for Fe-Ni-Cr alloys implies that the addition of Ni to the Fe host will result in no change in the relative importance of these three contributions to the $^{57}$Fe hyperfine magnetic field perturbations. There is then no reason to expect that the number of significant $\Delta H_j^{Cr}$ parameters will be different in Fe-Cr binary and Fe-Ni-Cr ternary alloys. This is consistent with the experimental observations that the intensity of the "Cr satellite" remained unchanged with the Ni content of the host (see Fig. 27 and Table VI).

**2. The Shape of Mössbauer Peaks from Fe-10Ni.**

At the higher Ni concentrations used in this study, the Mössbauer peaks of Fe-Ni alloys at 18°C have qualitatively different shapes than predicted by the phenomenological model of Chapter IV. Specifically, since the $\Delta H_1^{Ni}$ and $\Delta H_2^{Ni}$ parameters are negative, the phenomenological model of Chapter IV requires that the magnitude of the slope on the high Doppler shift energy side of a Fe-Ni peak is less than the magnitude of the slope on the low Doppler shift energy side. In other words, it will be shown that with the additivity assumption, the Fe-Ni peak is predicted to have a negative skewness. The observed skewness is positive. It will then be shown that an approximate adaptation of the model of linear response accounts for most of this skewness discrepancy for Fe-10Ni Mössbauer peaks.

With the additivity assumption, the skewness of the $^{57}$Fe hyperfine magnetic field distribution will be the skewness of the binomial distribution

appropriate to the nearest neighbor shell causing the perturbations. If several shells are involved, and their additive $\Delta H$ parameters have the same sign, then the hyperfine magnetic field distribution will have a skewness which is approximately the skewness of a combined nearest neighbor shell with an average $\Delta H$ parameter. The Fe-Ni Mössbauer peaks would have this same skewness if there were no further broadening by the Lorentzian energy distribution for each source and absorber nucleus. Nevertheless, the convolution of a symmetric Lorentzian function with the asymmetric binomial distribution may change the magnitude of the skewness, but not its sign*. (The skeptical reader may compare the asymmetry of the peaks in Figures 17 and 20 for a verification of this assumption.) The skewness of the binomial distribution for 14 trials, $M_3^{14}(x)$, was calculated from the first three moments of Table VII:

$$M_3^{14}(x) \equiv \langle x^3 \rangle - 3\langle x^2 \rangle \langle x \rangle + 2\langle x \rangle^3 \qquad \text{X-1}$$
$$M_3^{14}(x) = 28c^3 - 42c^2 + 14c$$

The skewness, $M_3^{14}(x)$, equals zero when $c = \frac{1}{2}$ and the binomial distribution is symmetric. When c=0.1, $M_3^{14}(x) = +1.008$. With the constant given below in equation X-4, the $^{57}$Fe hyperfine magnetic field distribution of an Fe-10Ni alloy will have a skewness of $-1.008 \cdot (8kG)^3$.

However, a positive skewness of Mössbauer peaks from non-dilute Fe-Ni alloys at 18°C is apparent** from Figs. 13, 15, and 16. It is now shown that a major source of this non-negative skewness is associated with the incompatibility of the additivity assumption with a proper treatment of the model of linear response of hyperfine magnetic fields to magnetic moments. A general discussion of this incompatibility and its effect on shape of the hyperfine magnetic field distributions was given in sections VI.B and C. There it was shown for

* However, I have not explicitly calculated how the skewness of a function is modified by convolution with a Lorentzian function.
** Count the number of data points from the tip of the peak to the same height on each side.

dilute alloys that the error in using a simple additivity assumption arises from its inability to properly account for $\Delta H_{INL}$ ($\Delta H_L$ and $\Delta H_{DNL}$ are additive in the model of linear response). To estimate this error for non-dilute Fe-Ni alloys we compare the skewness of the binomial distribution of additive perturbations (the $-1.008\cdot(8kC)^3$ found above) to the skewness of a binomial distribution of perturbations which have the non-additive form of $i + bi^2$ where $i$ is the number of nearest neighbor solute atoms. It will be shown how the constant, $b$, is chosen to approximately account for the inequality:

$$0 < g_M^{Fe}(r_j) \neq g_M^{Ni}(r_j) = 0.$$

Since this effect modifies $\Delta H_{INL}$ more and more as the Ni concentration becomes large, for brevity we shall loosely term this an effect of "Ni-Ni interactions". As the Ni concentration increases, $H_{INL}$ involves perturbed magnetic moments at more and more solute atoms in addition to the host atoms, so $H_{INL}$ becomes a complicated term to consider exactly. We therefore treat the nonlocal contribution to the $^{57}$Fe hyperfine magnetic field in an average way for this rest of the section. For Fe-10Ni alloys the hyperfine magnetic field perturbations contributed by magnetic moment changes at all nearest neighbor sites are conveniently treated as one nonlocal term, $\Delta H_{NL}$, which is the $\alpha_{CEP}\sum_{r'>0} f(r'-r)\mu(r')$ term in Eqn.VI-7.

To aproximately include the effect of Ni-Ni interactions on $\Delta H_{NL}$, we assume that the local Ni concentration is homogeneous in an idealized way; if a $^{57}$Fe nucleus is surrounded by 3 Ni atoms in one of its first two nearest neighbor shells, then each of these 3 Ni atoms is unable to enhance a Fe magnetic moment at 3 of these 14 nearest neighbor sites around the $^{57}$Fe nucleus. With this assumption, the number of lattice sites at which a Ni atom can perturb magnetic moments is the same as the number of lattice sites which significantly perturb the $^{57}$Fe hyperfine magnetic field. This idealization necessarily ignores

the specific nearest neighbor configurations of the bcc structure. However, the Ni magnetic moment perturbations and the $^{57}$Fe hyperfine magnetic field perturbations both involve about two significant nearest neighbor shells, so this assumption seems reasonable in the same average way as equations VI-31 and 38. The 14 neighbors of the $^{57}$Fe nucleus would all have their magnetic moments enhanced the amount $3g_M^{Fe}(1+2)$ by the 3 Ni atoms if we ignored Ni-Ni interactions. However, $\frac{3}{14}$ of the potent sites around the $^{57}$Fe nucleus are occupied by Ni atoms, and their magnetic moments will be enhanced by $3g_M^{Ni}(1+2)$ rather than by $3g_M^{Fe}(1+2)$. With $i$ Ni nearest neighbors in the 1n.n. and 2n.n. shells, the contribution to the $^{57}$Fe hyperfine magnetic field perturbation from the magnetic moment changes at all nearest neighbor sites is:

$$\Delta H_{NL} = H_{NL}^{Fe-Ni} - H_{NL}^{Fe} \qquad \text{X-2}$$

$$\Delta H_{NL} = \alpha_{CEP}\{(14-i)(\mu_{Fe}^{\bullet} + ig_M^{Fe}(1+2)) + i(\mu_{Ni}^{\bullet} + ig_M^{Ni}(1+2))f(1+2)\} - \alpha_{CEP}14\mu_{Fe}^{\bullet}f(1+2) \qquad \text{X-3}$$

For convenience we have assumed that the linear response parameter, $f(1+2)$, and the magnetic moment perturbation parameter, $g_M^{Fe}(1+2)$, are the same for the first two nearest neighbor shells. They were constructed from an average of $f(1)$ and $f(2)$ [41,107,220], and an average of $g_M^{Fe}(1)$ and $g_M^{Fe}(2)$ [220,229]. With $g_M^{Ni}(1+2) = 0$, and with $\mu_{Fe}^{0} - \mu_{Ni}^{0} \sim 14g_M^{Fe}(1+2) = +1.1\mu_B$ we have:

$$\Delta H_{NL} \simeq + i^2(0.8kG) \qquad \text{X-3}$$

Clearly the nonlocal contributions to the $^{57}$Fe hyperfine magnetic field perturbations in Fe-Ni alloys are not additive. On the other hand, the additivity of the *local* contributions to the $^{57}$Fe hyperfine magnetic field perturbations is not affected by Ni-Ni interactions:

$$\Delta H_L \simeq (\alpha_{CP} + \alpha_{CEP}f(0))\, i\, g_M^{Fe}(1+2) \simeq -i\ 8kG \qquad \text{X-4}$$

Nevertheless, the non-additivity of the $\Delta H_{NL}$ contributions will cause the shape of $^{57}$Fe hyperfine magnetic field distribution to differ from the shape of the binomial distribution. To find the skewness of this new approximate shape, we

compute the moments of the $^{57}$Fe hyperfine magnetic field distribution:

$$<\Delta H^n> = \sum_{i=0}^{14}(\Delta H_L + \Delta H_{NL})^n \cdot P(14,i,c) \qquad \text{X-5}$$

$$<\Delta H^1> = (-8kG)\times\left[<i>_B - \frac{1}{10}<i^2>_B\right]$$

$$<\Delta H^2> = (-8kG)^2\times\left[<i^2>_B - \frac{1}{5}<i^3>_B + \frac{1}{100}<i^4>_B\right]$$

$$<\Delta H^3> = (-8kG)^3\times\left[<i^3>_B - \frac{3}{10}<i^4>_B + \frac{3}{100}<i^5>_B - \frac{1}{1000}<i^6>_B\right]$$

The notation $<i^n>_B$ designates the $n^{th}$ moment of the binomial distribution for 14 trials. I have evaluated the first six moments of this binomial distribution by a simple ruse*, and they are listed in Table VII. With care and patience all the higher moments of the binomial distribution can be evaluated with repeated applications of similar procedures. For small $c_{Ni}$, the Ni concentration dependence of the first moment of equation X-5 is -101 kG. This is in fair agreement with the -160 kG determined by Vincze and Campbell [41] for dilute Fe-Ni alloys, but is in good agreement with the initial slope of Fig. 21. When we use the results of Table VII in equation X-5, we find an improved skewness for the $^{57}$Fe hyperfine magnetic field distribution for $c_{Ni} = 0.1$:

$$M_3'(x) = <\Delta H^3> - 3<\Delta H^2><\Delta H^1> + 2<\Delta H^1>^3 \simeq 0\ . \qquad \text{X-6}$$

This approximate treatment of Ni-Ni interactions in the model of linear response has eliminated the negative skewness predicted for the $^{57}$Fe hyperfine magnetic field distribution when additive perturbations were assumed. The additivity assumption in the phenomenological model of Chapter IV is inadequate for treating the nonlocal contribution to the $^{57}$Fe hyperfine magnetic field in non-dilute alloys when $g_{Ni}^{Fe}(r_j) \neq g_{Ni}^{Ni}(r_j)$. These Ni-Ni interactions can account for most of the difference between the small positive skewness

* As an example, we develop the relation for the third moment of the binomial distribution for 14 trials in terms of lower moments of the binomial distribution for 13 trials in Appendix A.

| TABLE VII | |
|---|---|
| Moments of the Binomial Distribution for 14 Trials | |
| $\langle X^n \rangle$ | $\equiv \sum_{i=0}^{14} i^n \frac{14!}{i!(14-i)!} c^i (1-c)^{14-i}$ |
| $\langle X^0 \rangle$ | $= 1$ |
| $\langle X^1 \rangle$ | $= 14c$ |
| $\langle X^2 \rangle$ | $= 182c^2 + 14c$ |
| $\langle X^3 \rangle$ | $= 2{,}184c^3 + 546c^2 + 14c$ |
| $\langle X^4 \rangle$ | $= 24{,}024c^4 + 13{,}104c^3 + 1{,}274c^2 + 14c$ |
| $\langle X^5 \rangle$ | $= 240{,}240c^5 + 240{,}240c^4$ $+ 54{,}600c^3 + 2{,}730c^2 + 14c$ |
| $\langle X^6 \rangle$ | $= 2{,}162{,}160c^6 + 3{,}603{,}600c^5$ $+ 1{,}561{,}560c^4 + 196{,}560c^3 + 5{,}642c^2 + 14c$ |

observed for Fe-9Ni Mössbauer peaks, and the negative skewness predicted with the simple additivity assumption. Whether these considerations can account for all of the skewness discrepancy, or whether other effects are necessary to account for the exact shape of Fe-9Ni Mössbauer peaks, cannot be answered here because of the approximate nature of the preceding treatment and the uncertainties in the parameters that were used.

A second effect which could be important in determining the shape of Fe-9Ni Mössbauer peaks is a possible Ni dependence of the parameters $g_M^{Fe}(r_j)$. For example, if the Fe magnetic moments exhibited a saturation behavior where each additional Ni neighbor produced a smaller and smaller change in each Fe magnetic moment, then the indirect nonlocal contribution to the $^{57}$Fe hyperfine magnetic field from each Fe neighbor will not be proportional to the number of surrounding Ni atoms. This would more strongly reduce the negative hyperfine magnetic field perturbation for Ni-rich configurations, and therefore increase the positive skewness of the $^{57}$Fe hyperfine magnetic field distribution. It is hard to ascertain the importance of this Ni dependence of the set $\{ g_M^{Fe}(r_j) \}$ -- after roughly accounting for the effect of Ni-Ni interactions it is unclear how much skewness remains to be explained by this second effect. Nevertheless, after accounting for the effect of Ni-Ni interactions on the shape of the Mössbauer peaks, I believe that the remaining skewness discrepancy does indicate that the $\{ g_M^{Fe}(r_j) \}$ are reduced with increasing Ni content. This reduction is in agreement with neutron diffraction data [229].

### 3. Changes in $\{f(r_j)\}$ with Ni Concentration.

When applying the model of linear response to Fe-Ni-X alloys, we should consider the possibility that the linear response parameters, $\{f(r_j)\}$, may change with the Ni concentration of the host metal. Again, as in section X.A.1., we need only be concerned with a qualitative change in a $f(r_j)$ parameter

which results in a changed $N_s^X$ of equation IV-5. For $r_j \neq 0$ the parameters $\{f(r_j)\}$ describe the nonlocal response of 4s spin density at the $^{57}$Fe nucleus to all magnetic moments other than that of the $^{57}$Fe atom. (As described in section VI.C., nonlocal effects involving itinerant 3d electrons are naturally included in the magnetic moments.) Recall that mechanisms of $H_{COND}$ rely on the mixing of electron states above and below the Fermi surface (see section V.E.1.). If a section of the Fermi surface is eliminated by filling all states above it or depleting all states below it, this mixing will no longer be possible. A mechanism of conduction electron response to solute atoms is thereby eliminated and the $\{f(r_j)\}$ will be modified. We now take a rigid band approach* and examine the Fe Fermi surface as Ni donates electrons to the bands. We also try to determine whether any new Fermi surface features are expected when Ni is added to the alloy.

The Fermi surface of ferromagnetic bcc Fe has a number of independent sections, or features. We refer to a paper by Tawil and Callaway [289] (see also [290]) for notation and their clear illustration of these features. At the center of the Brillouin zone around Γ is a large electron spheroid for conduction electrons of both spins (features I and VI). The wavevector at this spheroid is larger for +spin electrons than -spin electrons, but both imply conduction electron redistributions with a periodicity of about $2a_0$. The -spin electrons are beginning to fill hole pockets around N and H (features IV and VIII). The -spin Fermi surface also includes electron pockets along Δ, and a large hole surface around H (features VII and V). A +spin hole pocket surrounds H (feature III), and a +spin hole surface including H and N (feature II) provides a substantial density of states near the Fermi level. The largest density of states near the Fermi level seems to be associated with the electron spheroid around Γ, however.

* A manageable, but at best qualitative, approach for Fe-Ni alloys.

Section V.E.1. did not treat the mixing of states near the Fermi surface of a hole pocket, but the formalism of that section is easily extended to include this problem. The perturbation treatment of equation V-7 will still involve strong mixing of unoccupied states with occupied states separated by small wavevectors, but now the zero denominator occurs for **q** vectors of magnitude small enough to be enclosed by the hole pocket. The electronic susceptibility associated with mixing occupied electron states with states in the hole pocket goes as $F(2k'r)$ when free electron states are assumed (c.f. equation V-10). Here $k'$ is not the large $k_F$ associated with electron states at the hole pocket, but is instead the small $k$ that is the radius of the hole pocket. Of course, the hole density redistribution around the solute atom is the complement of the electron density redistribution around the solute atom.

In the unlikely event that each Ni atom were to donate one electron exclusively into states in the +spin hole pockets (features II and III), these hole pockets will become filled at a Ni concentration of about 10 at.%. The filling of the hole states associated with features II and III is one of two qualitative Fermi surface changes which we might expect with the addition of 0.1 electron/atom to a rigid Fe bandstructure. The other possible qualitative Fermi surface change is an appearance of small isolated hole pockets around N and maybe Γ for the -spin Fermi surface. What is the experimental significance to $N_s^X$ of the disappearance or appearance of these hole pockets with small k'?

These small hole pockets found for +spin electrons in iron, and perhaps for -spin electrons in Fe-Ni alloys, are associated with long-range electron redistributions around solute atoms (on the order of 5-10 $a_o$). The first node of this shielding redistribution may envelope about 200 nearest neighbor sites. However, the first node of the electron screening density associated with the larger spheroids around Γ probably does not even envelope the 2n.n. shell. The

number of states at these two features (spheroids and hole pockets) is comparable. Since the central electron spheroids distribute the screening charge over fewer nearest neighbor sites than the small hole pockets, they are therefore responsible for larger electron density changes at each site. Some observable shifts of the main NMR absorption peaks from dilute alloys [23,107] may arise from these long-range charge redistributions around hole pockets, however. In summary, except for the insignificant appearance of -spin hole pockets, or the insignificant disappearance of +spin hole pockets, no other qualitative changes of the Fe Fermi surface are expected with a rigid band shift of -1 eV. This seems comfortably larger than bonding energy changes, and gives us faith that the important features of the Fe-Ni Fermi surface will be similar to those of the pure Fe Fermi surface.

I believe (as in [216,220]) that the relatively large $f(r_1)$ and $f(r_2)$ linear response parameters mostly originate with the mixing of occupied and unoccupied states above and below the central electron spheroids of the Fe Fermi surface (features I and VI). These central electron spheroids are associated mostly with $d$-like electron states, but these states must have some hybrid $4s$ character. Changes in the amount of $4s-3d$ hybridization at sites that neighbor solute atoms should be considered in addition to a pure R.K.K.Y.-like response to the solute moment. I do not try to predict the relative amounts of hybridization-induced and R.K.K.Y.-induced $4s$ spin density redistributions around solute atoms, and refer to work by others [118,291]. However, to some extent the local changes in both the $4s-3d$ hybridization, and the $\Delta\rho^S(r)$ will exhibit a similar dependence on features of the Fermi surface. At least the appearance or disappearance of a section of the Fermi surface will have a qualitative effect on both of these mechanisms of $H_{NL}$. Unfortunately, I have not considered this problem in detail, and I can only hope that these hybridization

changes cause no capricious effects.

If the 1n.n. and 2n.n. shells are between the first and second nodes of the 4s conduction electron redistributions [118], there exists the possibility that as Ni is added to the alloy, a growing electron spheroid may cause the second node to contract to within the 2n.n. shell. This would cause $f(r_2)$ and the $H_{DNL}$ contribution to change sign. However, the observed similarity in shape and intensity of "Si satellites" and "Cr satellites" from both Fe and Fe-9Ni hosts provides the strongest evidence that we need not be concerned with a Ni dependence of the $\{f(r_j)\}$ parameters. I suggest that the set $\{f(r_j)\}$ is largely unchanged with Ni concentration.

**4. The Temperature Dependence of $\{\Delta H_i^{Ni}\}$.**

I cannot offer a fully satisfying discussion of the temperature dependence of the satellite peak positions because this topic is so controversial. Two extensive Mössbauer research programs have studied the temperature dependence of $^{57}$Fe hyperfine magnetic fields in Fe-X alloys from 77°K to their Curie temperatures. Unfortunately, the two groups, [108-110,112,292] (the Vincze group), and [106,120,121,293] (the Van der Woude group), report mutually inconsistent experimental data and interpretations (see also [294]). Both groups agree that the temperature dependence of $H_o$ (and therefore the average position of the main unperturbed peak) is accurately proportional to the lattice magnetization for all solutes. Their disagreement begins with the nearest neighbor configuration that they assign to each satellite peak. For this reason and other less clear reasons, the two groups report very different results from their processed experimental data. In particular, the two groups report qualitatively different measurements of the difference between the temperature dependence of $|H_o + \Delta H_1^X|$ (which marks the center of the 1n.n. satellite peak), and the temperature dependence of $|H_o|$ (which marks the center of

the main unperturbed peak). The Vincze group claims that the ratio:

$$h(T) \equiv \frac{|H_o(T)| - |H_o(T) + \Delta H_1^X(T)|}{|H_o(O)|} \simeq \frac{|H_o(T)|}{|H_o(O)|} - \frac{|H_o(T) + \Delta H_1^X(T)|}{|H_o(O) + \Delta H_1^X(O)|}$$

is not temperature dependent for most solutes such as V, Ti, Cr, and Co, but is temperature dependent only for a few "anomalous" solutes such as Mn and Ni. On the other hand, the Van der Woude group finds $h(T)$ to be markedly temperature dependent for most solutes including V, Ti, Cr, and Co. However, the two groups report functions $h(T)$ for Fe-Mn alloys which are in good agreement, and agreement is fair for Fe-Ni alloys. Nevertheless, for most alloys the disagreement is qualitative, so the two groups give completely different interpretations of their results.

The Vincze group and the Van der Woude group both agree that the temperature dependence of h can be parameterized:

$$h(T) = A\mu_{Fe}(T) + B(\mu_X(T) - \mu_{Fe}(T)), \quad \text{or} \quad h(T) = A\mu_{Fe}(T) + B\bar{\mu}_x(T) .$$

In the second expression (used by Van der Woude), $\mu_{Fe}(T)$ refers to the magnetic moment at an Fe atom with one solute neighbor, and $\bar{\mu}_X(T)$ is averaged over different local environments of the solute. Although these two expressions are not strictly equivalent to begin with, the two interpretations become irreconcilable when the Vincze group assumes A=0 and the Van der Woude group assumes B=0. The model of linear response was developed after these temperature dependent studies of Fe-X alloys were published, but we now see that the Vincze group essentially attributed all the temperature dependence of $h(T)$ to a temperature dependence of $\Delta H_{DNL}$, and the Van der Woude group attributed the temperature dependence to $H_L$ and $H_{INL}$.

Some of the Fe-Ni-X and Fe-Ni materials used for calibration of the "X satellite" intensity at room temperature were also used for similar calibration work at 500°C. As well as could be determined, for Fe-9Ni-1Mn and Fe-9Ni-1Cr

alloys the "X satellite" intensity at 500°C still gave $N_s^{Cr} = 14$ and $N_s^{Mn} = 14$ ($N_s^X$ is defined in equation IV-5), but the error was perhaps ±4. Although this indicates no temperature dependence of the "Cr or Mn satellites", the $\Delta H_i^X$ parameters may be somewhat temperature-dependent. A constant "X satellite" intensity merely means that no $\Delta H_j^X$ is changed from being experimentally insignificant to experimentally significant with temperature. Shape changes of the "X satellite" are perhaps observable, however, (compare Figures 26-28) and could be due to the ratios $\frac{\Delta H_1^{Mn}}{\Delta H_2^{Mn}}$ and $\frac{\Delta H_1^{Cr}}{\Delta H_2^{Cr}}$ increasing with temperature.

The temperature dependence of the significant $\Delta H_i^{Ni}$ parameters observed by me is poignant. Unfortunately, neither the Vincze group nor the Van der Woude group reported the change in sign of the significant $\Delta H_i^{Ni}$ parameters between 18°C and 600°C (see Fig. 19). (In fact, both groups report that the significant $\Delta H_i^{Ni}$ parameters obtained at room temperature are positive, a claim that is clearly wrong in the light of my work and that of numerous later workers including Vincze himself [41,113].) The model of linear response of hyperfine magnetic fields to magnetic moments can explain the temperature dependence of $\Delta H_i^{Ni}$ in one of three ways:

1.) The Fe magnetic moments may decrease, causing $H_L$ and $H_{DNL}$ to become more positive. The main unperturbed peak, with its average hyperfine magnetic field of $H_0$, is used as a reference for determining the temperature dependence of the satellite peak, so the rapidly decreasing Fe magnetic moments must be near the Ni atoms. The temperature dependence of $h(T)$ results from the temperature dependence of the set $\{g_{Ni}^{Fe}(r_j, T)\}$. This is essentially the interpretation of the Van der Woude group.

2.) The Ni magnetic moments may decrease rapidly with temperature, forcing the average $H_{DNL}$ to become more positive. This is the sort of model used by

the Vincze group. All Ni magnetic moments may decrease uniformly, or their temperature dependence may be determined by the number of their own Ni neighbors. (In other words, $\mu_{Ni}$ may decrease with no dependence on the local Ni environments, or the temperature dependence of $\mu_{Ni}$ may be associated with a temperature dependence of the $g_M^{Ni}(r_j)$ parameters.) Since all Mössbauer peaks from Fe-Ni alloys with from 3 to 12% Ni showed similar temperature dependences (compare Figs. 15-17) and since $\{g_M^{Ni}(r_j)\} \simeq 0$ at room temperature, a temperature dependence of $\{g_M^{Ni}(r_j)\}$ is an unlikely explanation of the temperature dependence of $h(T)$ for Fe-Ni alloys. No temperature dependence of $\mu_{Ni}$ was found in neutron diffraction work by Child and Cable [229]. This second explanation therefore seems untenable.

3.) The linear response parameters $\{f(r_j)\}$ may be temperature-dependent. This could be caused by a temperature-dependence of the occupancies of the $4s\uparrow$ and $4s\downarrow$ states, for example. However, the "X satellites" in Fe-Ni-X alloys are not significantly different at 18°C and 500°C, so we presume that the significant $f(r_j)$ parameters are not temperature-dependent. Since the set $\{f(r_j)\}$ and its lack of temperature dependence are considered properties of the Fe-Ni host, this explanation is inconsistent with the model of linear response.

Since the results of the work by the Vincze group, the work by the Van der Woude group, and the work by myself are all in serious disagreement, it may seem that more experimental work is needed before any firm conclusions can be reached regarding the temperature dependence of the significant $\Delta H_j^{Ni}$ parameters. However, presuming that my own data and explanation no. 1 above is correct, the temperature dependence of $\Delta H_j^{Ni}$ results from a temperature dependence of the set $\{g_M^{Fe}(r_j)\}$. This explanation is mostly consistent with the observed temperature dependence of the significant localized isomer shift

parameters, $\Delta i_j^{Ni}$. At 18°C the significant $g_{Ni}^{Fe}(r_j)$ are large and positive, and are associated with a net $3d$ electron transfer from Ni to Fe atoms. As drawn in Figure 47, the positive localized isomer shift is caused by these $3d$ electron transfers through the $\Delta i_{NL}$ contribution. As the temperature increases, the net electron transfers associated with the decreasing $g_{Ni}^{Fe}(r_j)$ parameters also decrease, so the significant $\Delta i_j^{Ni}$ parameters can be reduced in magnitude as well. The significant $\Delta i_j^{Ni}$ parameters have become nearly zero at 500(deC, and have become positive at 600°C. It may be also true that the significant $g_{Ni}^{Fe}(r_j)$ parameters have become negative above 500°C; this is consistent with my data and with the temperature dependence of neutron diffraction data for a Fe-3Ni alloy obtained by Child and Cable [229] (see also end of Section X.A.2.).. Although a more complicated electronic mechanisms(s) is possible, the temperature dependences of the $\Delta H_i^{Ni}$ and $\Delta i_i^{Ni}$ parameters are consistent with a less locally-dependent transfer of less-polarized $3d$ electrons from Ni to Fe atoms with increasing temperature.

## 5. Anisotropy of Hyperfine Magnetic Fields: Martensite Magnetic Anisotropy and Temperature Dependence

This section discusses observations involving the mysterious anisotropy of hyperfine magnetic field perturbations, which were phenomenologically parameterized by the set $\{\Delta D_i^{Ni}\}$ in section IV.F. Recall that the anisotropy of hyperfine magnetic field perturbations depends on the angle , $\varphi$, formed between the vector connecting the $^{57}$Fe nucleus and its solute neighbor ($\mathbf{r}_{n.n.}$), and the direction of the lattice magnetization. We first pause to discuss some previous ideas [114,295] about the origin of anisotropic hyperfine magnetic field perturbations, or "pseudo-dipole interactions".

A classical magnetic mechanism of $H_{DIP}$ (see section IV.B.) predicts that a $\Delta D_1^X$ of ~1 kG at the $^{57}$Fe nucleus will be caused by a typical localized magnetic

moment at a 1n.n. solute atom. This direct $H_{DIP}$ contribution has the correct sign, order of magnitude, and average $\varphi$-dependence to account for the difference of our polycrystalline Fe Mössbauer spectra taken with differing specimen magnetizations (this interpretation of difference spectra is described below). However, even for pure Fe metal we expect some part of the observed anisotropy of hyperfine magnetic field perturbations to arise from the $\varphi$-dependence of the unquenched spin-orbit coupling of localized Fe $3d$ electrons. Nevertheless, the simple mechanism of $H_{DIP}$ seems consistent with the observation that anisotropic effects in Fe-Si alloys [115] behave mostly as if substituting a Si atom for an Fe atom has caused the Si site to lose its potency for generating a positive $\Delta D_1^{Si}$ perturbation. However, previous workers have found this $H_{DIP}$ mechanism incapable of accounting for the anisotropic hyperfine magnetic field perturbations in other Fe-X alloys*. Especially noteworthy is the $\approx 20\mu_B$ magnetic dipole moment that this mechanism suggests for Mo solutes in Fe-Mo alloys [39], which is an order of magnitude larger than the Mo moment as measured by neutron diffraction.

The mechanism responsible for the anisotropy of hyperfine magnetic field perturbations could involve an isotropic electron redistribution around the solute atom; as seen by the $^{57}$Fe nucleus this electron redistribution would have symmetry only around ($\mathbf{r}_{n.n.}$). However, the direction of the ($3d$) electron spin at the $^{57}$Fe atom is necessarily also involved in such a mechanism. With a simple band model, it has been argued [295] that when an electric field gradient is due to a rearrangement of $3d$ electrons, a solute atom will also cause a $\varphi$-dependent

* Unfortunately, these workers did not consider the contribution of perturbed magnetic moments at host atoms near the solute atom (i.e. $\{g_X^{Fe}\}$) to the anisotropic perturbations. This effect may help make the $H_{DIP}$ mechanism more consistent with observations with Fe-Cr alloys. We further note that when the host dipole moment perturbations are considered, an assumed additivity of anisotropic perturbations from solute neighbors will be incorrect for Fe-9Ni alloys. The failure of the additivity assumption for the anisotropy of hyperfine magnetic field perturbations will occur for the same general reasons that the additivity assumption fails for the isotropic part of the hyperfine magnetic field perturbation.

magnetic moment perturbation at the $^{57}$Fe atom in proportion to this solute-induced electric field gradient. Both a change in the orbital and spin dipole fields of the 3*d* electrons at the $^{57}$Fe atom are thereby affected, and an anisotropic change in $H_{CORE}$ may also be possible. With the simple band model it was suggested that the $\varphi$-dependence of the electric quadrupole effect and the anisotropic hyperfine magnetic field perturbations are the same [295], however, in real Fe metal the 3*d* spin rearrangement and the concurrent electric field gradient change need not be directly related. Perhaps we should merely think of the electronic part of the anisotropy of hyperfine magnetic field perturbations as involving some unspecified but $\varphi$-dependent distortion of 3*d* wavefunctions at the $^{57}$Fe atom [106]. Cranshaw [114] also suggests that elastic lattice distortions around solute atoms could be responsible for the anisotropy of hyperfine magnetic field perturbations. Except for work by Asano and Schwartz [12,39], which explicitly verified the $\varphi$-dependence of anisotropic hyperfine magnetic field perturbations for Fe-Mo single crystals, the experimental situation seems to have changed little since 1972 when Cranshaw warned [114], "Further speculation on these questions should be more profitable when the measurements have been made on a wider range of solute atoms".

My primary concern with the anisotropy of hyperfine magnetic field perturbations was with the nuisance it caused; the hyperfine magnetic field perturbations changed as the lattice magnetization changed direction. The relevant lattice magnetization is the magnetization of each martensite crystal. A detailed specification of all these lattice magnetization is, of course, a hopeless task, so I am content to discuss an average "martensite magnetization", parameterized only by the average angle between the martensite crystal magnetization and the easy [100] axes of magnetization. In the absence of external fields and magnetic return flux, all martensite crystals will be magnetized along [100]

directions at low temperatures. However, the demagnetization factor for the martensite crystal and the magnetic fields of neighboring crystals may favor a magnetization direction other than [100]. The resulting magnetization direction chosen by our martensite crystal will be a compromise between the <100> direction favored by the magnetic anisotropy*, and the direction favored by the shape-dependent demagnetization factor and the microstructure-dependent external fields from neighboring crystals.

The problem of finding the magnetization direction of a martensite crystal amounts to a minimization of the free energy with respect to the magnetization direction when the internal energy term includes a magnetic anisotropy energy term and demagnetization and external field energy terms. The magnetic anisotropy provides a restoring torque (to <100>) to counteract the average tendency of the external fields to rotate** the martensite magnetization into the plane of the foil specimen. The shape of the martensite crystal and its surrounding microstructure was not changed by tempering. However, the average martensite magnetization rotated out of the plane of the specimen foil after tempering. This is clearly seen*** in the difference spectra such as Fig. 30 as dips at the positions of peaks nos. 2 and 5. This average reorientation of the martensite magnetization is consistent with an increased magnetic anisotropy energy after tempering, which would force the average martensite magnetization into [100] directions. No attempt to measure a change in bulk magnetostriction of tempered Fe-9Ni steel was made, but it should have been simultaneously increased. The intensities of the martensite Mössbauer peaks never

* The magnetic anisotropy energy is defined as that part of the free energy of a crystal which depends on the crystallographic orientation of the lattice magnetization.
** If the martensite crystal cannot rotate in response to this torque, it will undergo a small shear deformation. This is the origin of forced magnetostriction.
*** The two no. 1 peaks were height normalized before differencing, so a dip at the position of peak no. 2 indicates a reduction of the intensity ratio of peak no. 2 to peak no. 1. From section III-C.3 we know this indicates an average rotation of magnetization out of the plane of our foil specimen.

reached the 3:2:1:1:2:3 ratio after tempering, which indicates that the magnetization direction never became random with respect to the plane of the foil.

If the average martensite crystal became magnetized more along a [100] direction after tempering, we expect that the distribution of the strengths of the anisotropic parts of the hyperfine magnetic field perturbations would be changed. I believe that the magnitudes of the anisotropic perturbations and their diversity should be reduced after tempering, because when the magnetization is along a [100] direction, the large anisotropic components of hyperfine magnetic field perturbations at 1 n.n. sites are all zero ($3\cos^2(54.7) - 1 = 0$). With a [100] magnetization the 2n.n. sites experience inequivalent anisotropic hyperfine interactions, but they are expected to be smaller than the interactions involving 1n.n. sites. A reduction in the magnitude and distribution of anisotropic contributions to hyperfine magnetic field perturbations is expected to make the martensite Mössbauer peaks sharper after tempering. This is observed as a dip in the difference spectrum intensity on the high and low Doppler shift energy sides of peaks nos. 1 and 6 in Figs. 34 and 35.

At first I naively believed that the dips in difference spectrum intensity on the high and low Doppler shift energy side of peaks nos. 1 and 6 resulted entirely from Ni and X solute depletion of the martensite. (Such observations were, after all, the goal of this work.) However, it was found that unexpectedly large dips occurred when very little austenite had formed (see section IX.C.) and this first led to the suspicion that Ni-Ni or Ni-X clustering was occurring in the martensite (so that the average $^{57}$Fe nucleus had fewer Ni and X neighbors). Isochronal temperings of Fe-9Ni and Fe-9Ni-1Mn foils at intervals from 300°C to 530°C showed that these dips increased gradually after tempering at temperatures above 360°C (see Fig 34 ). This is a plausible temperature range for Ni-Ni clustering, but Ni-Ni clustering should cause the dips to appear only on the

high Doppler shift energy side of the martensite peaks in the binary Fe-9Ni alloy. Furthermore, these dips always appeared simultaneously with a change in the lattice magnetization of the martensite, it was found that the dip in the difference spectrum at the position of peaks 2 and 5 also increased with tempering temperature. From the preceding discussion, it is suggested that this dip indicates a rotation of the martensite magnetization into [100] directions so that the anisotropic part of the $^{57}Fe$ hyperfine magnetic field perturbation is reduced. The dips in difference spectrum intensity on the high and low Doppler shift energy side of peaks nos. 1 and 6 were therefore a result of the narrowing of these peaks as the anisotropic perturbations were changed. Further examinations of difference spectra for 600°C temperings (described in section I.C.) showed a similar effect for other Fe-9Ni alloys; discontinuous changes in the apparent Ni and X concentration of the austenite were correlated to rotations of the average martensite magnetization direction out of the plane of the foil. This correlation was impressively consistent.

In order to circumvent the nuisance of the changing anisotropic hyperfine magnetic field perturbations, some control of martensite crystal magnetizations was achieved by applying a saturating magnetic field to the specimen in the spectrometer. The experimental geometry (especially the specimen orientation) was kept constant for all spectra of the particular specimen foil. This novel technique for polycrystalline materials ensured that the change in the martensite magnetic anisotropy after tempering was no longer able to affect the directions of magnetization of the martensite crystals. The anisotropic hyperfine magnetic field perturbations were thereby maintained constant for spectra that would be compared by the difference procedure. The intensity ratio of peaks nos. 1 and 2 was consistently 3:4 (within 2-3%) when the magnetic field was used: this is the expected ratio when the magnetization direction is in

the plane of the foil. The best evidence of the success of the technique, however, was the substantial elimination of the sudden dips in the difference spectrum which were originally attributed to sudden austenite composition changes.

The origin of the magnetic anisotropy of tempered martensite is almost as mysterious as the origin of the anisotropy of hyperfine magnetic field perturbations themselves. Review articles [296,297] suggest a number of microstructural features which may affect the magnetic anisotropy. Barton et al. [298] have observed a similar magnetic anisotropy change in cold rolled Fe-Mn Mössbauer specimens, and have dubiously speculated that it indicated the "formation of Fe-Mn pairs (short-range order)". I have observed that the changes in magnetic anisotropy depended on tempering temperatures in the range of 360-500°C, and this corresponds to the temperature range used for stress-relief treatments of steels [300]. There are significant recovery effects in this temperature range [300]. The martensite magnetic anisotropy could be affected by changes in microstrains through carbon atom redistributions between the different interstitial sites (associated with tetrahedral distortions along the x-, y-, or z-axes). Large magnetic anisotropy effects in Fe-0.015C alloys are attributed to this mechanism [297]. This carbon distribution between the three types of interstitial sites is also affected by the local microstress, so this distribution will be changed after heat treating. Perhaps after a stress-relief treatment the carbon would be more uniformly distributed among the three sites, and the intrinsic magnetic anisotropy of the material would be free to cause [100] magnetizations.

As described in section IX.C., the $\Delta D_i^{Ni}$ parameters may be zero at 500°C. Explanations of such a temperature dependence are imprudent until the temperature dependence of the $\{\Delta H_i^{Ni}\}$ parameters themselves is better understood. Nevertheless, if the temperature dependence of $\{\Delta H_i^{Ni}\}$ is due to a decrease of

$g_M^{Fe}(r_j)$ parameters with temperature (see section X.A.4.), then it is suggested that the electron transfer mechanisms responsible for the $g_M^{Fe}(r_j)$ could also be responsible for the origin of the anisotropy of the Fe-Ni hyperfine magnetic field perturbations.

## B. FERROUS METALLURGY

### 1. Time-Temperature-Transformation Characteristics of the $\alpha' \rightarrow \gamma$ Reaction.

H. I. Aaronson et al. [301] assert that phase transformations producing a simultaneous change in chemistry and crystal structure can only proceed by a nucleation and growth mechanism. I can think of no counter-example which seems consistent with my data on austenite content and changes in martensite chemistry during isothermal temperings. The data show that the Ni and X solute concentrations in the austenite remain constant during isothermal tempering; This observation largely rules out the possibility that the austenite formed by a diffusionless transformation followed by a diffusional enrichment [302]. In such a shear and enrichment mechanism the changes in martensite chemistry cannot be strictly proportional to the amount of austenite which has formed. Only if the shear process occurred continuously during, the entire isothermal tempering could there be any possibility of a close proportionality between changes in martensite chemistry and changes in the austenite content. Continuous nucleation, however, is not an expected characteristic of a shear transformation. If the shear transformation were to occur suddenly upon heating above $A_s$,* then allowing for experimental uncertainty , the data show that the net volume fraction of austenite formed by this reverse shear mechanism can be at most 1%.

This section develops a general treatment of nucleation and growth kinetics so that we can interpret the experimental data of $\gamma$-phase precipitation kinetics. The TTT diagram for the $\gamma \rightarrow \alpha'$ transformation in Fe-9Ni steel was determined long ago* by Marschall et al. [58]. However, any TTT diagram which

* $A_s$ and $A_f$ are empirically determined upon heating as the temperature at which austenite is first observed, and at which the material becomes 100% austenite, respectively.
* A $\alpha' \rightarrow \gamma$ TTT diagram is more difficult to determine experimentally because there exists the question of whether the high temperature $\gamma$-phase is all present at room temperature where the phase analysis is most conveniently done.

describes the decomposition of the $\gamma$-phase upon cooling will differ qualitatively from a TTT diagram which describes the formation of the $\gamma$-phase upon heating. For the heating TTT behavior the diffusion kinetics and the nucleation kinetics can no longer compete, as they do for the cooling TTT behavior, to give the maximum rate of transformation at some moderate undercooling below $T_o$. ($T_o$ is the temperature at which the Gibbs free energies of the $\alpha$ and $\gamma$ phases are equal; $\Delta T$ is the difference between the actual reaction temperature and $T_o$.) For precipitation reactions occurring above $T_o$, both the driving force for nucleation and the diffusive mobility of solute species increase with temperature, so the reaction rate monotonically increases with $\Delta T$.

It is necessary to estimate the temperature dependence of the diffusion process which serves to limit growth of the austenite particles. We assume that this diffusion is an average solute diffusion in the martensite lattice which has the temperature dependence:

$$D_X^g(T) = D_o\, e^{\frac{-Q^a}{RT}}$$

Although the diffusion equation has been solved in detail for both spherical and ellipsoidal sinks [303-305], these detailed solutions require detailed data for diffusivities and geometries to be useful. Here we merely calculate a general time-dependent growth in which the volume of each active nucleus, $V_\gamma(t,T)$, goes as:

$$V_\gamma(t,T) \simeq (\sqrt{2D_X^g t}\,)^3 \simeq t^{\frac{3}{2}}\, e^{\frac{-3Q^a}{2RT}} \qquad \text{X-7}$$

We also need some estimate of how the number of active nuclei depends on temperature. Unfortunately, the number of nucleation sites, or the initial nucleation rate, is sensitive to uncharacterized microstructural details of our material. For instance, we know that the austenite nucleates on martensite lath boundaries and prior austenite grain boundaries [28,51,52,56], but this

knowledge substantially complicates the problem because it suggests that the energy barriers to nucleation will nucleation will depend on microstructural details of grain boundaries. The kinetics of a grain boundary precipitation process may be qualitatively affected by the fact that grain boundary diffusion is generally much faster than lattice diffusion. This feature has been incorporated into a "collector plate model" by Aaronson et al. [301,306,307], which requires knowledge of $\alpha' - \alpha'$ surface diffusion, $\gamma - \alpha'$ surface diffusion, bulk $\alpha'$ diffusion, and two surface energies. In addition, nucleation details such as the size distribution of nuclei, nonequivalency of nucleation sites, precipitate shape effects, and incubation effects should all be considered in developing a realistic model of $\alpha' \rightarrow \gamma$ precipitation reaction. There may be other insidious effects due to recovery of microstrains and defect structures during the $\gamma$-phase precipitation [232]. In other words, there are presently too many unknown details to justify the use of any quantitative model of the $\alpha' \rightarrow \gamma$ precipitation reaction.

In spite of this complexity, we proceed to determine the fraction of austenite as a function of time by considering the simplest model for austenite nucleation. The nucleation process is assumed to be thermally activated, and the activation energy for the formation of a critical nucleus, $\Delta G^*$, is assumed to be dependent on $\Delta T$. We first use the well-known classical model, which parameterizes the nucleus by its number of atoms, $n$, so that its free energy of formation will have a surface contribution of $\sigma \cdot n^{\frac{2}{3}}$ opposing its formation, and a volume free energy of $n \cdot g_n(T)$ favoring its formation. Assuming that the volume free energy can be written as $n \cdot \Delta T \cdot g_V$, where $g_V$ is a constant, it is easy to show that the number of critical (i.e. growing) nuclei, $N(T)$, is:

$$N(T) = N_o \, e^{-\frac{\Delta G^*}{RT}} , \qquad \text{X-8}$$

where:

$$\Delta G^* = \frac{\sigma^2}{g_V^2(\Delta T)^2}\left(\frac{4}{9} - \frac{8}{27}\right) \text{ for } \Delta T \geq 0$$

$$\Delta G^* = \infty \text{ for } \Delta T < 0.$$

I know of no appropriate data for the surface energy. Furthermore, there is no reason to disregard other contributions such as strain energy when determining the nucleation barrier. It therefore seems likely that the $\Delta T$ dependence of the nucleation process may not have the form of equation X-8. We generalize equation X-8:

$$N(T) = N_o\, e^{-\frac{\Delta G^*}{RT}} \qquad \text{X-9}$$

$$\Delta G^* = \sum_{m=-\infty}^{\infty} g_m(\Delta T)^m \text{ for } T \geq 0$$

$$\Delta G^* = \infty \text{ for } \Delta < 0$$

For the small $\Delta T$ of interest to us, it is physically unreasonable that a positive $\Delta G^*$ can be dominated by terms with positive values of $m$. If this were true, the maximum number of critical nuclei would occur at the smallest $\Delta T$. With a constant nucleation barrier, this means that the maximum free energy difference between the $\alpha'$ and $\gamma$ phases must occur at infinitesimally small values of $\Delta T$. This is absurd. Domination by the $m=0$ term is also physically unreasonable, especially for cooling TTT diagram where $N(T)$ is not a maximum at the smallest $\Delta T$. Therefore, for generality we rewrite:

$$\Delta G^* = \sum_{m<0} g_m(\Delta T)^m \text{ for } T \geq 0 \;\; ; \;\; \Delta G^* = \infty \text{ for } T < 0 \qquad \text{X-10}$$

Finally, for simplicity we assume that all nuclei start to grow at the time $t=0$, so the volume fraction of the austenite, $f_\gamma(t,T)$, will be:

$$f_\gamma(t,T) = N(T)\; V(t,T) \qquad \text{X-11}$$

Substituting equations X-7, X-9, and X-10 in equation X-11 we find:

$$f_\gamma(t,T) \propto t^{\frac{3}{2}}\left[\frac{-\sum_{m<0} g_m(\Delta T)^m - \frac{3}{2}Q^a}{R(T_o + \Delta T)}\right] \qquad \text{X-12}$$

A TTT diagram tells the time required for a specific fraction of new phase to

form at a given temperature. We therefore fix $f_\gamma$ in equation X-12, and find the temperature-dependence of the time required to form this $f_\gamma$:

$$t \propto \exp\left[\frac{+\frac{2}{3}\sum_{m<0} g_m(\Delta T)^m + Q^\alpha}{R(T_o + \Delta T)}\right] \quad \text{for } \alpha' \rightarrow \gamma \qquad \text{X-13}$$

Parallel reasoning allows us to compare the time required for the $\gamma \rightarrow \alpha$ transformation after cooling below $T_o$:

$$t \propto \exp\left[\frac{+\frac{2}{3}\sum_{m<0} g_m|\Delta T|^m + Q^\gamma}{R(T_o + \Delta T)}\right] \quad \text{for } \gamma \rightarrow \alpha \qquad \text{X-14}$$

For comparison, we have assumed the same nucleation barrier and a free energy difference of the two phases that is symmetric in $|\Delta T|$.

Figure 51 compares characteristic $\alpha' \rightarrow \gamma$ and $\gamma \rightarrow \alpha$ TTT diagrams. Observe that the time required for the $\alpha' \rightarrow \gamma$ nucleation and growth reaction is extremely temperature dependent at small $\Delta T$. This temperature dependence decreases as $\Delta T$ becomes larger, and eventually at large $\Delta T$ the temperature dependence of the reaction time is determined only by the activation energy for solute diffusion in the $\alpha'$-phase. Likewise in the TTT diagram for the $\gamma \rightarrow \alpha$ reaction, the temperature dependence of the reaction time becomes dominated by the activation energy for solute diffusion in the $\gamma$-phase when $\Delta T$ is very negative. The knee and nose of the two TTT diagrams are at a $(\Delta T)_k$ and $|\Delta T|_n$, respectively, such that:

$$\frac{2}{3}\sum_{m<0} g_m\,(\Delta T)_k^m = Q^\alpha \text{ and } \frac{2}{3}\sum_{m<0} g_m\,|\Delta T|_n^m = Q^\gamma$$

I suggest that $Q^\alpha$ and $Q^\gamma$ are similar enough so that they will not cause any significant difference $(\Delta T)_k$ and $|\Delta T|_n$. It seems more likely that differences in the $g_m$, associated with differences in the two nucleation processes, may cause a difference in $(\Delta T)_k$ and $|\Delta T|_n$.

Figure 51b is consistent with my experimental observations of austenite

precipitation kinetics in N.K.K. 9Ni steel at 550°C, 600°C, and 630°C. From the precipitation kinetics data of Fig. 43, we can determine the total activation energy for the reaction appropriate to each pair of temperatures. For the pair 550°C and 600°C, we find a net activation energy of 160 kcal/mole, and for the pair 600°C, and 630°C we find an activation energy of 95 kcal/mole. This reduction in activation energy is consistent with 600°C being in the knee of Fig. 51b. $Q^{\alpha}$ is expected to be 50-60 kcal/mole, so at 630°C there is probably still some change in the number of nucleation sites with temperature. The temperature $T_0$ is perhaps around 500°C, and we expect the net activation energy for austenite precipitation to become even larger than 160 kcal/mole as this temperature is approached. The nose of the $\gamma \rightarrow \alpha$ TTT curve determined by Marschall et al. [58] occurs at a smaller $|\Delta T|$ than does the knee of our $\alpha' \rightarrow \gamma$ TTT curve. This may indicate that the nucleation barrier for the precipitation of austenite from martensite is larger than the nucleation barrier for the precipitation of ferrite from austenite.

This evidence for a more prevalent nucleation of austenite particles at higher temperatures also helps to explain the importance of the 670°C "L treatment" in 6Ni "QLT" steel. It has been shown that the L treatment serves to form partially solute-enriched austenite particles that transform to martensite upon cooling [49,68]. These enriched martensite particles serve as effective nucleation sites for austenite formation during the subsequent 600°C tempering. It was suggested that the slow Ni diffusivity at 600°C permitted only a slow austenite precipitation unless there was some help from a previous solute segregation at 670°C [49,68]. This suggestion is completely consistent with the present work, but the present work further shows that there will be a much denser distribution of sites at which austenite may form at 670°C than at 600°C. The L treatment should therefore serve to increase the number of sites at which the

austenite may form during tempering, in addition to providing a pre-enrichment of solute elements.

**2. Equilibrium Austenite Precipitation in Ternary Alloys.**

In this section I suggest that it is possible to account for my major experimental observations of the $\alpha' \rightarrow \gamma$ reaction by considering only the equilibrium thermodynamics of $\alpha' - \gamma$ coexistence. It is shown that in contrast to binary Fe-Ni alloys, in ternary Fe-Ni-X alloys the kinetics diffusion have a degree of freedom in determining the ratio of $c_X^\gamma$ to $c_{Ni}^\gamma$ (the X and Ni solute concentrations of the austenite, respectively). The Gibbs phase rule is:

$$p + f = c + 2 \qquad \text{X-13}$$

where $p$ is the number of phases, $f$ is the number of degrees of freedom, and $c$ is the number of components of the system. When the temperature and pressure are specified, a two-phase tempering of a binary Fe-Ni alloy allows for no degree of freedom in the equilibrium austenite composition. In a series of 600°C temperings of binary Fe-Ni alloys, a $c_{Ni}^\gamma$ of 23 ±3 at.% was determined from 500°C Mössbauer spectra, in good agreement with the equilibrium Fe-Ni phase diagram [308]. A recent scanning transmission electron microscopy study of Fe-Ni alloys by Romig and Goldstein also showed that austenite precipitates with its equilibrium composition [70-72,250].

Now consider two-phase tempering of an Fe-Ni-X ternary alloy at constant temperature and pressure. There are still two phases to share the alloying elements, but now there are three components in the system. By the Gibbs phase rule, the equilibrium precipitation of the austenite will proceed with one degree of freedom in the austenite composition. The material may therefore select its tie-line across the two-phase field in response to diffusion kinetics. For example, if the X solutes were immobile, the tie-line would be determined by the condition that $c_X^\gamma = c_X^{\alpha'}$. The segregation of X elements into or out of the austenite

will move this tie-line, and in general this will change $c_{Ni}^{\gamma}$. For the rest of this section, I express the interdependence of the equilibrium $c_{Ni}^{\gamma}$ and $c_{X}^{\gamma}$, for small $c_X$, as:

$$\Delta c_{Ni}^{\gamma} \equiv c_{Ni}^{\gamma} - c_{Ni}^{0} = -k_X \, c_X^{\gamma} \, . \qquad \text{X-14}$$

Here the variable $\Delta c_{Ni}^{\gamma}$ denotes the difference in Ni concentration between the equilibrium austenite in the ternary Fe-Ni-X alloy and the binary Fe-Ni alloy. Given an equilibrium precipitation reaction, experimental determinaions of the concentrations of Ni and X in the austenite of an Fe-Ni-X ternary alloy should allow an estimate of the constant $k^X$, and hence the shape of the ternary austenite phase boundary. Independent determinations of both $\Delta c_{Ni}^{\gamma}$ and $c_X^{\gamma}$ were only quantitatively possible for Fe-Ni-1Mn alloys and commercial 9Ni steel because only these two materials retained sufficient austenite at room temperature to permit a martensite chemical analysis of adequate accuracy. For Fe-9Ni-1Mn alloys, the constant $k^{Mn}$ was about +1 for 600°C temperings. In other words, Mn atoms replace Ni atoms at the growing austenite crystal on approximately a 1:1 basis. For N.K.K. 9Ni steel tempered at 600°C, $k^X$ was about +2. However, the observed changes in "X satellite" intensity reveal Cr, Ni, and Si concentration changes with equal sensitivity, but are rather insensitive to C concentration changes. Therefore the measured $k^X$ for 9Ni steel may be larger than $k^{Mn}$ for the Fe-9Ni-1Mn alloy because of a very large $k^C$. Much of the precipitated austenite in Fe-9Ni-Cr and Fe-9Ni-Si alloys had undergone a martensite transformation upon cooling to room temperature. Nevertheless, the similarity of their Q - QT difference spectra to those of Fe-9Ni~1Mn alloys seems to indicate that that the ternary $\gamma$-phase field is moved to lower $c_{Ni}^{\gamma}$, as $c_{Cr}^{\gamma}$ and $c_{Si}^{\gamma}$ are increased.

With a degree of freedom in $c_{Ni}^{\gamma}$ and $c_X^{\gamma}$ for a Fe-9Ni-1X ternary alloy, the actual balance of $c_{Ni}^{\gamma}$ and $c_X^{\gamma}$ is determined by the constant $k^X$ describing the

shape of the $\gamma$ phase boundary in conjunction with the relative diffusive mobilities of Ni and X solutes in the $\alpha'$ phase. For instance, since we know that Mn can substitute for Ni at the austenite crystal surface, the higher Mn diffusive mobility ensures that $\Delta c_{Mn}^{\gamma}$ of equation X-14 will be significant. Furthermore, the higher activation energy for Ni diffusion [309,310] should also result in $\Delta c_{Mn}^{\gamma}$ becoming even more negative as the tempering temperature is decreased. This is observed in commercial N.K.K. 9Ni steel for which $\Delta c_{Mn}^{\gamma}$ = −3%,−5%,and−13% for temperings at 630°C, 600°C, and 550°C, respectively. The experimental error in $\Delta c_{Mn}^{\gamma}$ is nearly as large as $\Delta c_{Mn}^{\gamma}$ itself for 600°C and 630°C temperings. However, at 550°C the Fe-Ni binary phase diagram predicts very large martensite Ni depletions per percent austenite formed. This is not consistent with my data for 9Ni steel, even with generous allowances for experimental error. Additionally, changes in the "X satellite peak" indicated an X solute depletion of the martensite at 550°C which was over twice as large per percent austenite as the depletion at 630°C. This is also consistent with the suggestion that the more rapidly diffusing X solutes increasingly replace Ni at the austenite surface at lower temperatures.

We can estimate the relative Ni and X diffusive mobilities from the measured austenite enrichments in Ni and X. We assume that the arrival of the Ni and X solutes at the austenite is limited by a 1-dimensional diffusion process with no overlapping diffusion fields; perhaps the martensite lath boundary serves as an efficient, flat, and fast collector plate. We assume that the austenite is a sink for solutes such that once the Ni and X elements enter the austenite, they do not come out again*. We treat only the case for which $k^X>0$ (the austenite is stabilized by both Ni and X solutes). In this case the formation of

* The rough arguments with Miedema's heats of formation in section X.B.3.a. suggest that the chemical potential difference between the solute atoms in the martensite and solute atoms in the austenite is not large enough to justify the idea that the austenite acts as a perfect solute sink.

austenite of an arbitrary ternary composition could be limited by either Ni diffusion or by X diffusion. The maximum amount of austenite which is allowed to form, $V^{\gamma}$, when it must be diffusionally enriched with Ni and X solutes by the amounts $c_{Ni}^{\gamma} - c_{Ni}^{\alpha'}$ and $c_X^{\gamma} - c_X^{\alpha'}$ with respect to the depleted martensite in time $t$, is either limited by Ni diffusion:

$$V_{Ni}^{\gamma}(c_{Ni}^{\gamma} - c_{Ni}^{\alpha}) = \kappa\sqrt{D_{Ni}\, t}\,(c_{Ni})\,, \qquad \text{X-15}$$

or is limited by X diffusion:

$$V_X^{\gamma}(c_X^{\gamma} - c_X^{\alpha}) = \kappa\sqrt{D_X\, t}\,(c_X)\,. \qquad \text{X-16}$$

Here $c_{Ni}$ and $c_X$ refer to the average alloy concentration and $\kappa$ is a geometrical constant. The austenite will form most rapidly when $V_{Ni}^{\gamma} = V_X^{\gamma}$, so that both the diffusing species are simultaneously incorporated into the new austenite when they reach the $\alpha'-\gamma$ interface. (If we had the inequality $V_{Ni}^{\gamma} > V_X^{\gamma}$, the Ni atoms must wait for the X atoms to arrive at the $\alpha'-\gamma$ interface before more austenite of the stated composition is formed.) Equating $V_{Ni}^{\gamma}$ and $V_X^{\gamma}$ from equations X-15 and X-16:

$$\frac{\sqrt{D_{Ni}\, t}\,(c_{Ni})}{c_{Ni}^{\gamma} - c_{Ni}^{\alpha}} = \frac{\sqrt{D_X\, t}\,(c_X)}{c_X^{\gamma} - c_X^{\alpha}} \qquad \text{X-17}$$

At this point we can impose equation X-14 on equation X-17, and with some fairly non-critical estimates of the solute concentrations of the martensite, it would be possible to predict the Ni and X solute concentrations of the austenite in ters of the Ni and X diffusivities. However, since the Ni and X diffusivities are poorly known, I take the opposite tack and determine the ratio of diffusivities in terms of the measured chemical concentrations. With the austenite chemical concentration data of Figs. 44 and 45 for Ni and X solutes in 9Ni steel, and with reasonable estimates of the solute concentrations of the depleted martensite, I estimate that $\frac{D_X}{D_{Ni}} = 46$ at 550°C, $\frac{D_X}{D_{Ni}} = 8$ at 600°C, and $\frac{D_X}{D_{Ni}} = 4$ at 630°C. These diffusivity ratios were obtained by squaring ratios of uncertain chemical con-

centration differences, so they are at best semi-quantitative. They lead to a prediction that the difference between the activation energy for Ni diffusion and the activation energy for X diffusion is 30-40 kcal/mole, which seems rather large.

The large diffusive mobility of Mn should enhance the kinetics of austenite growth. In a Fe-9Ni-1.25Mn alloy tempered at 600°C, there is a total enrichment of Mn in the austenite which is about 50% as large as the enrichment of austenite by Ni. Since $k^{Mn}$ is about +1, this means that the austenite in the Fe-9Ni-1.25Mn alloy required only $\frac{2}{3}$ of the Ni enrichment as the austenite in a Fe-9Ni binary alloy. Therefore after the same tempering time there should be about $\frac{3}{2}$ times more austenite in the Fe-9Ni-1.25 Mn alloy than the Fe-9Ni binary alloy. This seems to be in reasonable agreement with the kinetics shown in Fig. 42. However, the assumption that the austenite behaves as a total sink for solute atoms causes an overestimation of the enhancement of austenite precipitation kinetics by the ternary addition. It will be suggested later that nucleation effects, or perhaps Mn-vacancy interactions may also contribute to the enhancement of austenite precipitation kinetics in the Fe-9Ni-1.25 Mn alloy.

### 3. Ni-X Covalent Bonding.

*Equilibrium Segregation of X Solutes.*

Now we briefly discuss the segregation of X elements to the austenite in terms of the chemical potentials of the X atoms themselves, and not from a phase stability standpoint. Table VIII suggests that Cr and Si are not particularly helpful in stabilizing the austenite, and Fig. 42 shows that they impede the kinetics of austenite formation with respect to a binary Fe-Ni alloy In spite of all this, both Cr and Si do segregate to the austenite to a qualitatively similar extent as Mn. It is now suggested that covalent bonding between Ni and Cr

atoms and Ni and Si atoms are partially responsible for the segregation of Cr and Si to the austenite. Ignoring the considerations of the previous section, we assume that the austenite has already formed with a Ni concentration of 20%. We consider only the equilibrium partitioning of the ternary X solutes between two phases which have different numbers of Ni-X bonds for each X atom.

An estimate of the energetic preference of the Ni-X bond over the Fe-X bond made with Miedema's heats of formation [267-271] of Fe-X and Ni-X alloys. For X=Mn, Cr, or Si, the Ni-X ordered alloys all have a heat of formation which is ~ 5 kcal/mole less than Fe-X alloys. Dividing this energy among 8 nearest neighbor bonds indicates an energy of a Ni-X bond which is ~0.03 eV less than the Fe-X bond. With an average of 0.48 Ni-X bonds per atom in the martensite (assumed to contain 6% Ni) and with an average of 2.4 Ni-X bonds in the austenite (assumed to contain 20% Ni), it is found that the equilibrium concentration of X in the austenite will be 2.2 times as large as in the martensite. This raio will be 2.3 and 2.1 at 550°C and 630 °C respectively. This estimate is very rough; the Ni-X bond energies are known only approximately, and except for the greater number of nearest neighbors in a fcc structure, it ignores the role of crystal structure in determining the chemical potentials of the X solutes. Nevertheless, the energetically favorable Ni-X bonding does appear to be a plausible driving force for the segregation of Mn, Cr, and Si atoms to the Ni-rich austenite.

*Effects on Diffusion.*

If the Ni and X atoms are attracted more strongly to each other than they are to Fe atoms, the atom-vacancy interchange frequencies responsible for solute diffusion can be altered. Altered solute diffusivities can change the kinetics of the $\alpha' \rightarrow \gamma$ reaction. An extreme example would occur if there were the formation of a stable complex of Ni atoms surrounding an X atom. If all Ni

atoms were bonded strongly enough to X atoms to be stable against a Ni-vacancy interchange at 600°C, the Ni diffusivity would be zero, and no austenite could form. However, this extreme example requires the Ni-X bond energy to be an unreasonable number of eV lower than the Fe-X bond energy. We now consider whether a reasonable estimate of the Ni-X attraction can predict an altered Ni diffusivity.

Consider a Ni atom which, in its diffusive travel, passes through a site which is a 1n.n. site of an X atom. If the X atom has no effect on the saddle point energy of the diffusive jump, the activation energy for the Ni atom to jump into this site is unaffected. However, because of the lower energy of the Ni-X bond, the Ni atom will spend more time in this site than it would if the X atom were an Fe atom. Since it is assumed that the presence of an X atom has no effect on the saddle point energy of the diffusive jump, the additional Ni-X bonding energy can be effectively added to the activation energy necessary for the Ni atom to jump out of this site. (This simply reflects the extra energy change associated with a diffusive jump which breaks one Ni-X bond and replaces it with one Fe-X bond.) The relevant energy difference was determined from Miedema's heats of formation in the previous sub-section to be ~0.03 eV. At 600°C the consequent change in Boltzmann factor indicates that the Ni jump frequency from this 1n.n. site of the X atom is $\sim\frac{2}{3}$ of what it would be if the X atom were replaced by an Fe atom. This is experimentally insignificant for Ni diffusion because only about 12% of all sites in a Fe-9Ni-1X alloy have an X atom as a first nearest neighbor. However, because Ni is much more plentiful, it is possible that X solute diffusivities could be slowed by Ni-X covalent bonding.

Further evidence that the Ni-X bonding does not have a substantial effect on Ni or X diffusion is that short-range-order does not evolve in Fe-9Ni-1X alloys. It is expected that such short-range-order should evolve in the Q-

treated Fe-9Ni-1X alloys after perhaps a few hundred diffusive jumps -- well before any austenite is formed. $^{57}$Fe atoms will be excluded from regions where Ni and X atoms have clustered so this short-range-order should be evident in Q - QT difference spectra as dips on the sides of the main $\alpha'$ absorption peaks which appear before an austenite peak is seen. I made a specific search for such effects in a series of low temperature isochronal temperings of both Fe-9Ni and Fe-9Ni-1Mn alloys. After accounting for the changes in the anisotropic hyperfine magnetic field perturbations, there were no peaks in the difference spectra which indicated Ni-X clustering (see section X.A.5.).

A second effect of Ni-X covalent bonding on diffusivities could occur if the Ni-X bonding alters the attraction of vacancies to the Ni or X solutes. This is discussed at the end of the next section.

**4. Solute-Vacancy Binding and Isomer Shifts.**

This section is concerned with how Ni and X diffusivities are affected by vacancy-solute interactions. Central to this problem are estimates of the strengths of vacancy-solute interactions. I offer a novel approach to these estimates which is based on measurements of localized isomer shifts at $^{57}$Fe nuclei near the solute atom.

The three vacancy-atom interchange frequencies: $\omega_{V-Fe}$, $\omega_{V-Ni}$, and $\omega_{V-X}$ [311,312], which determine the diffusion processes in the present alloys, may depend on the local environment around the vacancy. One such important local modification of the interchange frequencies occurs when there are attractive or repulsive interactions between vacancies and particular solute atoms [313,314]. The energy of interaction between a vacancy and an X atom, $E_{V-X}$, is defined as the difference in the total system energy when the vacancy is a nearest neighbor of an X atom and the total energy when the vacancy and X atom are well-separated. A detailed and complicated 3-dimensional picture of

the diffusion process is required if we want to consider the effects of vacancy-solute binding as specific local modifications of the interchange frequencies. Fortunately, since only effects on long-range diffusion are of interest in determining $\alpha' \rightarrow \gamma$ transformation kinetics, we can consider the modification of the diffusion process to depend on how the vacancy-solute interaction affects the fraction of time that the vacancies spend as nearest neighbors to the solute atom. From the altered activation energy required for the vacancy to leave these nearest neighbor sites, we expect that the vacancy will remain $\exp(-E_{V-X}/kT)$ times longer as a nearest neighbor of the solute atom than it would remain at a well-separated site. When we know the number of trapping sites and $E_{V-X}$, we can then predict the fractional change in the number of mobile vacancies, and hence the fractional change of diffusivities. We find it necessary to assume that all alloys have an equal density of vacancies -- a dubious but convenient assumption.

The major part of the solute-vacancy interaction energy is electrostatic in origin. (With Eschelby's results [315], C. P. Flynn has shown [316] that elastic energy changes associated with the relaxation of atoms around a vacancy that neighbors a solute are small — they will be especially small for our solutes which have atomic volumes similar to Fe atoms.) $E_{V-X}$ is determined by the interaction of the displaced charge around the vacancy, $\Delta\rho_V(\mathbf{r})$, and the displaced charge around the solute, $\Delta\rho_X(\mathbf{r})$:

$$E_{V-X} = \frac{1}{2}\int_{-\infty}^{\infty}\int_{-\infty}^{\infty} \frac{\Delta\rho_V(\mathbf{r})\,\Delta\rho_X(\mathbf{r}')}{|\mathbf{r}-\mathbf{r}'|}\, d^3r\, d^3r' \qquad \text{X-18}$$

The charge redistribution around the solute, $\Delta\rho_X(\mathbf{r})$, is identical to that used in section V.E. to evaluate the $\Delta i_j^X$ parameters. If there were an analogous relationship between $\Delta\rho_V(\mathbf{r})$ and the nuclear charge redistribution associated with the $^{57}$Fe isomer shift, a perfect correspondence would be expected between isomer shifts and solute-vacancy binding energies (i.e. solute-vacancy binding

energies could be evaluated from isomer shifts). The actual correspondence is imperfect but still useful.

Since $\Delta\rho_V(\mathbf{r})$ and $\Delta\rho_x(\mathbf{r})$ are peaked functions centered about the vacancy and solute sites, following Flynn [316] we separate $E_{V-X}$ into a sum of two independent terms: $E_s$, which is an integral of the overlapping solute and vacancy charge redistributions at the solute site, and Ev, which involves an analogous overlap integral at the vacancy site. The charge redistribution associated with the vacancy, $\Delta\rho_V(\mathbf{r})$, has three parts: 1.) the loss from the vacancy site of the nucleus and the electrons localized to it, 2.) the screening of the vacant site by the electrons of the host metal, and 3.) the repositioning of the atoms around the vacancy to further minimize the system energy. If all 26 of the electrons associated with a Fe atom were local to it, the removal of the Fe atom from its site would result in part 1 being zero. However, since some Fe valence electrons are donated to the metal bandstructure, the loss of the Fe atom with its localized electrons will remove more positive charge than negative charge. Part 1 is therefore negative. This perturbation will be screened by the conduction electrons to contribute part 2 of the $\Delta\rho_V(\mathbf{r})$. For our purposes the relaxation contribution of part 3 can be ignored; this should not qualitatively affect the proposed correspondence between localized isomer shifts and solute-vacancy binding.

The correspondence between localized isomer shifts and the $E_V$ part of the solute-vacancy interaction energies is a natural one. The charge perturbation associated with the vacancy, $\Delta\rho_V(\mathbf{r})$, is a constant of Fe metal. The sensitivity of the localized $^{57}$Fe isomer shift to electron density changes is a characteristic of the $^{57}$Fe atom. Like Ev, $\Delta i_1^z$ is proportional* to the electron charge

* An exception to this may occur if different solutes cause $3d$ and $4s$ charge redistributions to occur in different proportions. It may therefore be necessary to work with solutes from the same series of the periodic table in order to have a good correspondence between $E_V$ and $\Delta i_1^z$.

redistribution at 1n.n. sites of the solute atom. We expect that neither the charge perturbation associated with the vacancy, nor the sensitivity of the $^{57}$Fe isomer shift to the charge redistribution at the $^{57}$Fe site, are dependent on the type of neighboring solute atom. Unfortunately, without more detailed information about the charge perturbation associated with the vacancy, one can only suggest a proportionality between $\Delta i_1^z$ and Ev, and not an absolute relationship. Again, as in the case for $E_V$, the interesting charge redistribution determining $E_S$ is caused by the solute; the charge redistribution around the vacancy is a characteristic of the Fe host. When the solute and vacancy are separated by $r_j$, similar values of $\Delta\rho_V(0)\Delta\rho_X(r_j)$ and $\Delta\rho_V(r_j)\Delta\rho_X(0)$ ensure that $E_S$ will be comparable to $E_V$; Flynn finds that they are often almost identical. For convenience I assumed that $E_i = E_V$. Our relationship between $\Delta i_1^z$ and $E_V$is therefore equivalent to a relationship between $\Delta i_1^z$ and $\frac{1}{2} E_{V-X}$.

In dilute binary Fe alloys, first nearest neighbor Cr, Mn, Ni, and Si atoms result in local $^{57}$Fe isomer shifts, $\Delta i_1^X$, of -0.02, -0.016, +0.02, and +0.035 mm/sec, respectively [41,107]. With the assumption that $\Delta|\psi_{4s}|^2 = -1.2\Delta|\psi_{3d}|^2$, these data indicate a net gain of about +0.02, +0.02, -0.02, and - 0.03 4$s$ and 3$d$ electrons at a 1n.n. site of these Cr, Mn, Ni, and Si solutes, respectively. Twisting the point of a proportionality between $\Delta i_1^z$ and $\frac{1}{2} E_{V-X}$ a little, we assume that these electron density changes equal the electron density changes due to the solute at the vacancy site. Assuming an effective charge of $-\frac{1}{2}$ e at the vacancy site, these electron density changes predict (with the overlap integral for Ev) values of $E_{V-X}$ of about +0.05 eV, +0.05 ev, -0.05 eV, and -0.075 eV for Cr, Mn, Ni, and Si solutes, respectively. (Negative energies denote attractive solute-vacancy interactions, positive energies denote repulsion.)

Sadly, there are no good experimental data available for comparison with

the vacancy-solute binding energies predicted here. Vacancy experiments are very difficult to perform with bcc Fe alloys because the bcc structure is a low temperature phase; the experimenter cannot reliably obtain significant vacancy concentrations by quenching from a high temperature. The reported vacancy experiments with bcc Fe either do not study solute-vacancy interactions [317-319], or are subject to ambiguous interpretations [321-323]. Demangeat [324] has determined vacancy-solute binding energies in dilute bcc Fe alloys by calculating the electronic density of states for $3d$ and $4s$ electrons near vacancies and solute atoms. For Mn, Cr, and Ni in ferromagnetic bcc Fe, he found values of $E_{V-X}$ for 1n.n. separations between solute and vacancy of +0.05, +0.035, and -0.06 eV, respectively. The proportionality between these values of $E_{V-X}$ and the values of $E_{V-X}$ obtained from local isomer shift data is as good as can be expected, considering the isomer shift method neglected many details of the electron redistributions around vacancies and solute atoms. Demangeat found interaction energies for 2n.n. separations of +0.09, +0.02, and -0.17 eV, respectively. Accurate $\Delta i_2^X$ parameters are not available, but they are generally presumed to be less than the $\Delta i_1^X$ parameters. If $\Delta i_2^X < \Delta i_1^X$, then the localized isomer shift approach to vacancy-solute interactions will predict weaker 2n.n. vacancy-solute interactions than 1n.n. vacancy-solute interactions, in disagreement with some of Demangeat's calculations.

Vacancy-solute binding will slow the diffusion of all species because the binding reduces the number of mobile vacancies available for mechanisms of diffusion. At 600°C a binding energy of -0.075 eV between vacancies and 1n.n. Si atoms should reduce the number of mobile vacancies by about $\frac{1}{12}$ when $c_{Si} = 0.004$. This is in qualitative agreement with the observation that Si slows the $\alpha' \rightarrow \gamma$ transformation kinetics in Fe-9Ni-0.4Si alloys , but is an order of magnitude too small. On the other hand, a repulsive vacancy-solute interaction will

slow the diffusion of the solute in question, but will increase the effective number of mobile vacancies for the diffusion of atoms which are not neighbors of the repelling solute. When the repelling solute concentration is 1.25% and the repulsive 1n.n. vacancy-solute interaction energy is 0.1 eV or greater, at 600°C the available vacancies will hop between 90% of the lattice sites, increasing average diffusivities by about 10%. Although the relatively fast Mn diffusion implies that the Mn-vacancy repulsion is surmountable, the enhanced kinetics of the $\alpha' \rightarrow \gamma$ reaction in a Fe-9Ni-1.25Mn alloy may be due in part to a Mn-vacancy repulsion* which enhances the Ni diffusivity. However, we also should similarly expect a Cr-vacancy repulsion, but no enhancement of the $\alpha' \rightarrow \gamma$ reaction in Fe-9Ni-1.25 Cr alloys was found.

**5. Austenite Nucleation: Mechanical History and Solute Effects.**

Nucleation of the $\alpha' \rightarrow \gamma$ transformation is the rate limiting step for the formation of austenite at lower tempering temperatures (see section X.B.1.), but my Mössbauer spectrometry methods were incapable of direct studies of nucleation phenomena. (The Mössbauer spectra were insensitive to martensite chemistry changes in the very early stages of the $\alpha' \rightarrow \gamma$ transformation when less than 1% austenite formed.) However, some indirect information supplied by Mössbauer spectrometry concerning how microstructure affects the nucleation of austenite is now discussed.

In early experiments with the tempering of N.K.K. 9Ni steel, the $\frac{1}{2} - 1$ mil foils for transmission Mössbauer spectrometry work were prepared with an initial cold rolling. These rolled foils were then homogenized at 1000°C followed by

* Localized isomer shift data reported for Fe-X alloys were used to determine $E_{V-X}$. This $E_{V-X}$ is appropriate for Fe-X binary alloys, but the application of this $E_{V-X}$ to Fe-Ni-X alloys will be inappropriate if $\Delta i_1^X$ is significantly affected by Ni concentration. As suggested in section X.A.1., this should not be a problem for Cr and Si atoms. However, Ni-Mn covalent bonding may alter $\Delta i_1^{Mn}$ significantly, and I made no attempt to measure $\Delta i_1^{Mn}$ in ternary Fe-9Ni-1Mn alloys.

a Q treatment at 800°C, or were Q treated directly. The austenite in these specimens formed very slowly during subsequent temperings, up to 8 times more slowly than was observed (with backscatter Mössbauer spectrometry and x-ray diffractometry techniques) for material that was heat treated as thick plates of as-received commercial material. (Compare Figs. 42 and 43.) It was also found that foils subjected to less cold rolling had a more rapid austenite precipitation, although the austenite still formed about twice as slowly as it did in thick plates. These results were apparently independent of the final polished thickness of the specimen, so surface effects* were not these cause of the retarded precipitation kinetics.

It is unlikely that the defect structure introduced by cold rolling directly affected the diffusivity of solutes because this defect structure was removed by the solution treatment and the austenitizing treatment. However, the cold rolling will affect the size of the grains formed during austenitization, and therefore the morphology of the prior austenite grain boundaries and the martensite lath boundaries. The distribution of internal microstresses could be affected as well. With this circumstantial evidence, it is my conviction that austenite nucleation, and not mechanisms of solute transport, is the step in the $\alpha' \rightarrow \gamma$ reaction that was affected by the cold rolling. Furthermore, if the diffusivities of solutes were altered by the cold rolling, it is expected that the chemical balance of Ni and X in the precipitated austenite will also be affected. This was not observed upon visual comparison of the experimental spectra. I believe that these observations of an effect of very early cold rolling on austenite precipitation kinetics indicate that at 600°C the kinetics of austenite precipitation are

* In addition, in all later experiments with 9Ni steel, the specimens for tempering were prepared from previously Q-treated bulk material by cutting thin slices from it with an abrasive wheel saw under flood cooling. The austenite precipitation kinetics in these specimens were independent of specimen thickness, and virtually identical to the kinetics found by backscatter Mössbauer and x-ray experiments with thick specimens.

very sensitive to microstructural details. Such effects warrant further study, but these observations alone should encourage the use of very consistent practices for thermomechanical processing of 9Ni steel.

Plausible effects of ternary solutes on the mechanism of $\alpha' \rightarrow \gamma$ nucleation are now speculatively discussed. Although it is known that austenite crystals grow from boundaries between martensite crystals, it is not certain that the early nucleation process is as simple as the formation of a fcc crystal of equilibrium composition between two bcc crystals which have the equilibrium composition at their interface. If a solute atom has a substantial interaction with these internal surfaces, the surface depletion or enrichment of this solute may play an important role in austenite nucleation. In particular, Mn is known to be a grain boundary surfactant in steels [325-327]. Since Mn is also an austenite stabilizer, the more rapid austenite precipitation kinetics in Fe-Ni-Mn alloys than Fe-Ni, Fe-Ni-Cr, or Fe-Ni-Si alloys may be due to a more extensive austenite nucleation at martensite lath interfaces in these Mn-containing alloys.

The carbon content of 9Ni steel is 0.28 at.%, and carbon is extremely mobile at 600°C (see Fig. 1). It is possible that after only very short tempering times, or even during the heating cycle, nearly all of the carbon could have formed grain boundary carbides which would later facilitate austenite nucleation. Hyperfine magnetic field data for carbides in alloy steels [29-36] indicate that the expected 1% of the $^{57}$Fe atoms in carbide phases should give small, sharp peaks situated between the sextet of martensite peaks. The absence of any discerable carbide peaks in any of the carbon-containing alloys indicates that no more than one-third* of carbon was tied up in Fe-rich carbides. However, this could still be enough carbide to have a significant effect on austenite nucleation. Previous transmission electron microscopy work at Berkeley has

* This upper limit is based on the quality of counting statistics in a composite spectrum.

provided only scant evidence of carbides in 9Ni steel, but in recent work, H. J. Kim and H. Shin have found them after rapid thermal cycles.

**6. Thermal Stability of Austenite: Effects of Ternary Solutes.**

So far only the $\alpha' \rightarrow \gamma$ transformation has been considered. Now the $\gamma \rightarrow \alpha'$ transformation will be discussed, with emphasis on how the ternary solutes affect the thermal stability of the precipitated austenite. In this work I have obtained data on the amount of austenite present in 600°C tempered material at 500°C, at room temperature, and again at room temperature after the material was quenched to liquid nitrogen temperature (-196°C). The observed differences in thermal stabilities of austenite in different alloys were so large that even these limited data are quite informative.

Commercial 9Ni steel tempered less than 10 hours at 600°C had the most stable austenite; no thermally induced transformation of this austenite was observed, even after quenching to liquid nitrogen temperature. A very large amount of austenite (28%) was retained at room temperature in commercial 9Ni steel after the specimen was accidentally overheated in the glassblowing procedure and a black film was produced on its surface. It is believed that the unusual stability of this austenite was due to the addition of carbon to the material during the accident. Fe-9Ni-1Mn alloys also had very stable precipitated austenite; no transformation of the austenite was observed when this material was cooled to room temperature, and only a small amount of austenite could be transformed upon repeated quenchings in liquid nitrogen. On the other hand, only a small amount of the austenite that formed in the Fe-9Ni-1Cr alloys remained after cooling to room temperature. A qualitative summary of the austenite stability data is:

| TABLE VIII | |
|---|---|
| Austenite Thermal Stability | |
| Most Stable | burned N.K.K. 9Ni |
| | N.K.K. 9Ni |
| ↓ | |
| | Fe-9Ni-1Mn |
| | Fe-9Ni-0.3C |
| ↓ | |
| Least Stable | Fe-9Ni-0.4Si |
| | Fe-9Ni binary |
| | Fe-9Ni-1Cr |

These differences in austenite stability do not arise from "chemical stability" differences associated with the effects of different ternary solutes on the Gibbs free energy ($G = U - TS + PV$) of the austenite. For example, austenite in Fe-9Ni-1Mn and Fe-9Ni-1Cr alloys have markedly different stabilities. However, it has already been discussed how the internal energy differences (reflected in the term $U$) associated with Fe and Ni bonding to Cr and Mn atoms are very small. The mixing entropy difference and the vibrational entropy difference between austenites in Fe-Ni-Mn and Fe-Ni-Cr alloys should also be negligible. The macroscopic $P \cdot V$ term in the Gibbs free energy cannot be different for Fe-Ni-Mn and Fe-Ni-Cr alloys either, but perhaps there are differences in the microstresses, or perhaps there are $\gamma - \alpha'$ interfacial differences in Fe-Ni-Cr and Fe-Ni-Mn alloys which are responsible for their different austenite stabilities. That austenite stability may be affected by microstresses is suggested by the observation that the solute content of the austenite remains constant with tempering time, but the austenite thermal stability decreases with tempering time. Presumably this effect is related to the

size of the austenite crystals. Changes in microstresses with the growth of austenite crystals may facilitate the nucleation of the $\gamma \rightarrow \alpha'$ transformation.

It seems reasonable that nucleation effects could be important in determining austenite stabilities because the $\gamma \rightarrow \alpha'$ transformation is largely athermal*; athermal transformations are often a consequence of a large nucleation barrier. Perhaps the nucleation of the $\gamma \rightarrow \alpha'$ transformation involves dislocations moving into the austenite from the $\gamma - \alpha'$ interface. In this case it would seem reasonable that the segregation of Mn to this interface may effect changes in nucleation mechanisms that cause the nucleation barrier to be decreased.

**7. Mössbauer Spectrometry in Physical Metallurgy.**

In transmission electron microscopy (TEM), a macroscopic electron beam is precisely focused to reveal microstructural details; electron optical technique and specimen characteristics determine the lower limit of spatial information attainable. This contrasts with Mössbauer spectrometry, which inherently samples information on the atomic scale. In fact, the main thrust of the present work has been to interpret the observed hyperfine structure in terms of features outside the $^{57}Fe$ atom, but the largest scale of spatial information obtained was still less than 3A. However, the wide-ranging usefulness of TEM for problems in materials science is due to the wide-ranging ability of its contrast mechanisms to distinguish regions of material with microstructural differences. Unfortunately, in Mössbauer spectrometry many microstructural details do not cause distinct differences in the absorption energies of $^{57}Fe$ nuclei.

This section first sketches a concept of two levels of distinguishability of

* In a small test, some N.K.K. 9Ni steel which was tempered 240 hours at 600°C showed the same amount of $\gamma \rightarrow \alpha'$ transformation (about 6%) after immersion in liquid nitrogen for 0.1 sec, 100 sec, and $10^5$ sec.

local environments in Mössbauer spectra. On the simplest level, a Mössbauer spectrum can be resolved into non-overlapping, or otherwise clearly distinct spectra from $^{57}Fe$ nuclei in distinct local environments. This is a common situation in phase analysis. For example, if n distinct spectra are resolved, then quantitative measurements of n volume fractions may be made with precision. These n spectra are resolvable because they are associated with major differences in the mechanisms of nuclear energy level perturbations. A second level of information may be contained within these individual spectra; further structure in these spectra may arise due to small, local variations in these perturbations. When a diversity of local environments are present, and the number of these significant perturbations becomes large, we hope that their effects will combine in such a way that the detailed shape of Mössbauer peaks can be clearly dependent on trends in the local environment. For instance, in the case of Fe-Ni alloys I was able to correlate changes in Ni concentrations to changes in peak shapes even though the detailed local Ni perturbations were not resolved.

When individual local hyperfine field perturbations can be resolved and identified, the distinguishability of local environments by Mössbauer spectrometry can become solidly quantitative. Dilute solutions are particularly elegant in this regard because the only likely local environments for a $^{57}Fe$ nucleus involve zero neighboring solute atoms, or one neighboring solute atom. When an "X satellite" can be independently resolved, a probabilistic interpretation of its intensity can provide precise information on concentration changes of X solutes, or in other experiments the "X satellite" intensity may provide quantitative information on the local ordering of solutes around iron atoms.

It is often true that a large (>10%) solute concentration is required for Fe alloys to exhibit metallurgically interesting ordering reactions and the forma-

tion of new phases. The present work suggests that there is a certain category of non-dilute *ternary* alloys in which chemical composition analysis information can be provided by the elegant method of dilute solutions. In addition to the "X satellites" in our Fe-9Ni-1X alloys, it is suspected that useful satellite peaks due to "class L" solutes* may be seen in iron-based alloys that contain large concentrations of "class R" solutes. Fe-Co-V is a ternary alloy in this category. Ordering in Fe-Co alloys is affected by the presence of V. If the sets {f} and {g} do not depend strongly on Co content, a "V satellite" should be observable in Fe-Co-V alloys. It should be possible to accurately determine the ordering-induced changes in the number of Fe atoms nuclei with V neighbors. For instance, it should be possible to determine if a V atom attracts Co atoms as its first nearest neighbors, because the "V satellite" would be reduced in intensity if such short-range-order has developed.

Although there are many potential experiments in which conventional Mössbauer spectrometry could be used for studies of local chemistry or local order, there are probably even more experiments in which Mössbauer spectrometry will be of limited use because $^{57}$Fe hyperfine field information is insensitive to metallurgically distinct environments. When such a situation arises because of overlapping Mössbauer absorption energies, a further level of metallurgical distinguishability may be achieved by using the Mössbauer effect in conjunction with a second physical effect. There are many such experimental possibilities, but I complete this discussion by considering a technique that seems roughly analogous to the impressive capability of TEM combined with x-ray fluorescence spectrometry for obtaining microchemical information.

* "Class L" is a popular terminology for many elements to the left of Fe on the periodic table for which the significant $\Delta H_i^L$ are positive. On the other hand, the significant $\Delta H_i^R$ are negative. For these "class R" solutes the parameters {g} are positive and small, whereas for the "class L" solutes the parameters {g} are negative and large. The differing sign of $\{\Delta H_i\}$ for "class L" and "class R" solutes is largely due to the resulting differences in $\Delta H_{INL}$.

The 14.41 keV $\gamma$-rays used in $^{57}$Fe Mössbauer spectrometry have a wavelength of 0.86 Å, and are therefore practical for crystal diffraction experiments* [328-331]. I believe that the diffraction of $\gamma$-rays by $^{57}$Fe-containing crystals offers promise as a new type of micro-chemical analysis tool in materials science. In essence, a particular diffracted $\gamma$-ray beam can be chosen for study, thereby selecting a particular crystal structure in the material. A moving $\gamma$-ray source will allow a conventional Mössbauer spectrum to be collected with this diffracted $\gamma$-ray beam. Chemical analysis information could then be obtained from the Mössbauer spectrum of the selected crystal structure. Unique information could be obtained by taking a Mössbauer spectrum from small-angle-diffracted $\gamma$-rays that have interacted with small microstructural features such as Guinier-Preston zones. Such $\gamma$-ray diffraction experiments present serious experimental problems with counting statistics and reabsorptions in the specimen. An effect on the energy width of the Mössbauer peaks occurs, due to a decreased lifetime of the excited nuclear state of the $^{57}$Fe nuclei which constitute the diffracting crystal, and this will muddy the details in the hyperfine structure and hence the local chemistry information. In spite of these challenging problems, methods of $\gamma$-ray diffraction still appears to be an important direction for the growth of Mössbauer spectrometry in materials science because of its promise for further increasing the distinguishability of metallurgically distinct environments.

* In an early experiment in the 1960's [328] the ratio of the diffracted beam intensity capable of causing a Mössbauer absorption to the total diffracted beam intensity was measured. From this ratio the fraction of $\gamma$-rays that had undergone elastic coherent scattering by the crystal could be determined. More recently there have been many experiments in the Soviet Union (for a review see [331]) in which the diffracting crystal contains the Mössbauer isotope. The diffracted $\gamma$-ray wavefunction contains a contribution from the usual electronic scattering plus a contribution from the coherent scattering due to $\gamma$-ray reemissions from the Mössbauer nuclei. The resulting scattered intensity contains a cross term, or interference term, between the nuclear and electronic scattering process. This interference has been used to determine the phase of the electronic scattering factor.

# CHAPTER XI

# CONCLUSIONS AND SUMMARY

## A. Chemical and Phase Analyses.

The initial thrust of my experimental work was to develop techniques of Mössbauer spectrometry for quantitative microchemical and microphase analysis of Fe-9Ni and Fe-9Ni-1X alloys. Methods and calibrations for determining retained austenite contents in steels were already well-established before the start of this work. Nevertheless, I found that using the areas of austenite peaks in difference spectra simplified the determinations of austenite contents. Approximate corrections for thickness distortions were readily performed by using the intensities of difference spectra. A comparison of austenite peak intensities at 18°C and 500°C was made, and it showed that the recoil-free fractions of the austenite and martensite had the same temperature dependence, and I suggest that they are probably the same.

The development of methods and techniques to determine changes in the solute concentrations of martensite became the major thrust of this work. Many Mössbauer spectra of alloys with different compositions were obtained in a thorough "calibration" program. Chemical concentration calibration constants, $N_3^X$, were determined for X = Mn, Cr, and Si (and roughly for C) in different Fe-Ni host alloys at 18°C and 500°C. Similar, but more phenomenological, chemical concentration calibrations were also established for Ni concentration analyses at 18°C and 500°C. A difference spectrum procedure was implemented in which difference spectrum intensities on the high and low Doppler shift energy sides of the 18°C martensite peaks from Fe-Ni-X ternary alloys could be related to Ni and X solute concentration changes, respectively. Because of a small overlap of

these Ni and X difference spectrum intensities at 18°C, there were small uncertainties in the normalization of the starting spectra. These problems may have caused systematic errors when Ni and X concentration changes were determined simultaneously. The hyperfine fields at $^{57}$Fe nuclei near Ni atoms are markedly temperature dependent, and this causes the difference spectrum intensities associated with Ni and X concentration changes to become completely overlapping at 500°C. In general, independent Ni and X concentration information could not be obtained from 500°C spectra, but in situations where one was held constant, the change in the other could be found.

In some cases, inhomogeneous solute concentrations in the martensite directly affected the accuracy of Ni concentration measurements, and may have indirectly affected the accuracy of the X concentration measurements. Fortunately, diffusion profiles of the Ni had only small concentration variations, and so were not a serious problem. However, in some alloys an extensive transformation of precipitated austenite upon cooling created pockets of fresh martensite with large (≈20%) Ni concentrations; the mixture of this enriched martensite with the depleted martensite caused the average Ni concentration to be significantly in error. An increased overlap of Ni and X difference spectrum intensities from this inhomogeneous martensite also reduced the apparent concentration of X solutes. Consequently, only qualitative microchemical analyses were obtained from 18°C Mössbauer spectra from Fe-Ni and Fe-Ni-X alloys with thermally transformed austenite.

The hyperfine magnetic field perturbations at $^{57}$Fe nuclei near Ni atoms are not completely isotropic; there is some dependence of the magnitude of these perturbations on the angle, $\varphi$, between the magnetization direction and the direction of the Ni atom from the $^{57}$Fe nucleus. This anisotropic contribution appears to be only several percent of the total hyperfine magnetic field pertur-

bation due to the Ni atom, but changes in this anisotropic component caused effects in difference spectra which were comparable to to small Ni and X concentration changes. Such changes in the anisotropic hyperfine magnetic field perturbations could be mostly prevented by "locking" the magnetizations of the martensite crystals in the same orientations from run to run. This was accomplished by applying a saturating magnetic field to the specimens.

The methods that were developed for Ni and X concentration analyses of martensite suffered primarily from experimental difficulties and normalization problems. These problems are about equally serious, but I believe that it is more important to first solve the interrelated expermental problems of counting statistics and Doppler drive stability. I expect that solutions to the normalization problem may become clear when more accurate shapes of difference spectra are known. Nevertheless, the reproducibility and the precision of the present data were good. Ni concentration changes of the martensite as small as ±0.1% were detectable. For X solutes with $N_s^X = 14$, a remarkable sensitivity to ±0.03% concentration changes was achieved. Even higher sensitivities could probably be obtained with better quality experimental data.

**B. Electronic Structure.**

Although there are a number of electronic mechanisms whereby the $^{57}$Fe hyperfine magnetic field can theoretically be affected by neighboring solute atoms, in alloys of 3*d* transition metals the nonlocal solute effects can be mostly explained by an R.K.K.Y.-like response, presumably including local hybridization effects, of the 4*s* conduction electron spin density to the magnetic moments in the alloy, $\Delta\rho^S(\mathbf{r})$. There also appears to be a smaller effect (about 10% as large) due to a response of the conduction electron spin polarization to the solute valence. This valence effect can be explained by an electron spin susceptibility to a local charge perturbation that gives the electron

spin redistribution, $\Delta\rho^{SC}(\mathbf{r})$, of section V.E.4. For the procedures in this thesis, which measured areas in difference spectra, it was only necessary to consider effects that cause hyperfine magnetic field perturbations to change from experimentally insignificant to expermentally significant, or vice versa. Only large (> 4kG) changes in a $\Delta II_j^X$ parameter were of significance to the method of microchemical analysis, so the smaller valence effects and the atomic volume effects for Ni, Mn, Cr, and Si solutes could be neglected with impunity.

The hyperfine magnetic fields at $^{57}$Fe nuclei near solute atoms are adequately estimated with a semi-phenomenological model which parameterizes three ways that the $^{57}$Fe hyperfine magnetic field will respond linearly respond to the magnetic moments in the alloy ($H_L$, $H_{DNL}$, and $H_{INL}$). These three contributions to the $^{57}$Fe hyperfine magnetic field all arise from changes in the spin-polarization of the $s$ electrons at the $^{57}$Fe nucleus. The spin-polarization of each type of $s$ electron at the $^{57}$Fe nucleus will respond to any changes in the magnetic moment at the $^{57}$Fe atom itself through $H_L$. The spin-polarization of the delocalized 4$s$ electrons at the $^{57}$Fe nucleus, however, is also sensitive to the magnetic moment change at a nearby solute site when the solute atom is substituted for a Fe atom; the $H_{DNL}$ contribution is developed in this way. In non-concentrated alloys, most of the nearest neighbors of the $^{57}$Fe atom are Fe atoms, and changes in their magnetic moments caused by a nearby solute atom can also be responsible for affecting the 4$s$ spin-polarization at the $^{57}$Fe nucleus; this contribution is called the $H_{INL}$ term. The hyperfine magnetic field response parameter used for a nearest neighbor site in either the $H_{DNL}$ or the $H_{INL}$ term is the same, and these $\{f(r_j)\}$ are assumed to be intrinsic to the host metal.

With additional parameters that characterize the effects on Ni and X magnetic moments due to neighboring X and Ni atoms, the model of linear response

was formally extended to ternary Fe-Ni-X alloys. In the case when X is Si, and probably in the case when X is Cr, the model of linear response predicts no effect on the calibration constant $N_s^X$ for various Ni concentrations, in agreement with the experimental calibration work. However, in the case of $\Delta H_2^{Mn}$ for a *binary* Fe-Mn alloy, a propitious combination of $\Delta H_L$, $\Delta H_{DNL}$, and $\Delta H_{INL}$ is self-cancelling so that $\Delta H_2^{Mn}$ is nearly zero. It is argued that a large $g_{Ni}^{Mn}$ parameter upsets this balance (through $H_{DNL}$) to provide a $\Delta H_2^{Mn}$ which is is experimentally significant in ternary Fe-Ni-Mn alloys. Consequently, the chemical concentration calibration constant, $N_s^{Mn}$, changes from 8 to 14 when the host Ni concentration exceeds 3 or 4%.

The popular additivity assumption for $\Delta H_i^X$ parameters is not consistent with the model of linear response for non-dilute solutions when $g_X^{Fe} \neq g_X^X$. This inequality is important in Fe-Ni alloys, and with it the model of linear response explains why the skewness of Fe-9Ni Mössbauer peaks cannot be predicted with additive $\Delta H_i^{Ni}$ parameters. The correlation between the temperature dependence of the hyperfine magnetic field perturbation parameters, $\{\Delta H_i^{Ni}\}$ and $\{\Delta i_i^{Ni}\}$, is consistent with the model of linear response and other experimental data if the electron transfers associated with the significant $g_{Ni}^{Fe}(r_j)$ parameters become less localized and less polarized with increasing temperature.

The model of linear response of hyperfine magnetic fields to magnetic moments was consistent with the observed $\Delta H_j^X$ parameters, even for Fe-Ni-X alloys for which we might have expected the $\{f(r_j)\}$ parameters to differ from those of pure Fe. Nevertheless, I believe that more systematic experimental work is necessary to build confidence in this model. Hyperfine magnetic field systematics in ternary alloys are useful in this regard because Fe-X binary alloys of 3*d* transition metals have already been shown to be consistent with the model. A more detailed fundamental understanding of charge transfers and

spin-polarizations in transition metal alloys would also be useful in ascertaining the validity of the model of linear response.

**C. Metallurgy of Fe-Ni Alloys.**

The formation of austenite during tempering occurs primarily by a nucleation and growth mechanism. In binary Fe-9Ni alloys tempered at 600°C, the austenite forms with the equilibrium Ni concentration predicted by the Fe-Ni binary phase diagram. To the accuracy of my chemical analysis data, the austenite in all alloys maintains a steady composition as it grows.

Ternary elements in a Fe-9Ni matrix affect the kinetics of austenite precipitation, the solute concentrations of the austenite, and the thermal stability of the austenite against the martensite transformation. All four commercial solutes, Mn, Cr, Si, and C, segregate to the austenite, presumably because their chemical potential is lower in the austenite than the martensite. Their segregation does not ensure that the kinetics of austenite formation are enhanced, nor does their segregation ensure the stability of the austenite. On the one hand, the segregation of Mn appears to enhance both the kinetics of the austenite formation and the stability of the austenite against the martensite transformation. On the other hand, the segregations of Cr and Si to the austenite appear to diminish both the kinetics of formation and the thermal stability of the austenite.

In the case of Mn segregation in a Fe-9Ni-1.25 Mn alloy, and in the case of X element segregation in N.K.K. 9Ni steel, quantitative microchemical data were obtained which showed that the Ni in the austenite was effectively replaced by the Mn and X solutes. This appears to be a result of the austenite phase boundary moving to lower Ni concentrations as these solutes segregate to the austenite. A degree of freedom in Ni and X solute concentrations of the ausenite is permitted by the Gibbs phase rule. Consequently, diffusion kinetics of Ni

and X solutes have a free hand to choose the particular balance of Ni and X concentrations in the austenite formed at different temperatures. In these alloys it seems that the enhanced kinetics of austenite formation with respect to the Fe-9Ni binary alloy were due to Mn and X diffusivities being greater than the Ni diffusivity. Although an increased number of nucleation sites could account for some of the enhanced precipitation kinetics of N.K.K. 9Ni steel, an increased ratio of X diffusivity to Ni diffusivity is the best way to account for why the austenite in N.K.K. 9Ni steel becomes relatively more enriched in X solutes at lower tempering temperatures.

It was observed that there was a large reduction in the net activation energy for austenite formation at higher temperatures. This was shown to be consistent with a nucleation and growth mechanism having a constant activation energy for solute diffusion, but having a strongly temperature-dependent number of nucleation sites. The number of austenite nucleation sites is argued to be zero at $T_0$, to rise rapidly with small $+\Delta T$, and to become nearly temperature-independent at large $\Delta T$. I was unable to study the nucleation process directly, but circumstantial evidence indicated that it was quite sensitive to thermomechanical processing. It is suggested that the austenite precipitation is especially sensitive to the properties of the grain boundaries at which the austenite is known to nucleate.

**D. Miscellaneous.**

Short-range-order was detected in neither 9Ni steel nor Fe-9Ni-1Mn alloys after tempering. The local chemical environment appears to account for nearly all of the hyperfine structure of Fe-Ni-X martensite spectra. Internal stresses and defect structures of the martensite appear to be observable only through their effect on the magnetic anisotropy of the martensite. Changes in the magnetic anisotropy of the martensite in Fe-9Ni alloys were probably consequences

of internal stress relief during tempering.

The anisotropic hyperfine magnetic field perturbations at $^{57}Fe$ nuclei near the Ni atoms appear to have a different temperature-dependence than the isotropic part of the perturbation.

Localized isomer shift parameters, $\{\Delta i_i^N\}$, appear to be related to the electrostatic contribution to solute-vacancy binding energies.

# APPENDIX A

## Moments of the Binomial Distribution

The $N^{th}$ moment of the binomial distribution for $n$ trials can be determined from the $N-1^{th}$, $N-2^{th}$,... moments of the binomial distribution for $n-1$ trials. This recursive feature makes working with the binomial distribution particularly convenient. As an example, we develop the relation between the $3^{rd}$ moment of the binomial distribution for 14 trials in terms of the $2^{nd}$ and $1^{st}$ moments of the binomial distribution for 13 trials:

$$<x^3>_{14} \equiv \sum_{i=0}^{14} i^3 \frac{14!}{i!\,(14-i)!}\, c^i\,(1-c)^{14-i}$$

Note that the $i = 0$ term vanishes:

$$<x^3>_{14} = 14c \sum_{i=1}^{14} i^2 \frac{13!}{(i-1)!\,(13-(i-1))!}\, c^{i-1}\,(1-c)^{13-(i-1)}$$

Define $j \equiv i - 1$:

$$<x^3>_{14} = 14c \sum_{j=0}^{14} (j+1)^2 \frac{13!}{j!\,(13-j)!}\, c^j\,(1-c)^{13-j}$$

Define:

$$<x^N>_{13} \equiv \sum_{j=0}^{13} i^N \frac{13!}{j!\,(13-j)!}\, c^j\,(1-c)^{13-j}$$

So that:

$$<x^3>_{14} = 14c\,[<x^2>_{13} + 2<x>_{13} + 1]$$

With care and patience, all the higher moments of Table VII were evaluated with repeated applications of similar procedures.

## REFERENCES

[1] R. L. Mössbauer, Z. Physik 151 (1958) 124.

[2] R. L. Mössbauer, Naturwissenschaften 45 (1958) 538.

[3] R. L. Mössbauer, Z. Naturforsch. 14a (1959) 211.

[4] R. V. Pound and G. A. Rebka, Jr., Phys. Rev. Lett. 4 (1960) 337.

[5] R. V. Pound and G. A. Rebka, Jr., Phys. Rev. Lett. 4 (1960) 274.

[6] H. Y. Hay, J. P. Shiffer, T. E. Cranshaw, and P. A. Engelstaff, Phys. Rev. Lett. 4 (1960) 165.

[7] L. Grodzins and E. A. Phillips, Phys. Rev. 124 (1961) 774.

[8] S. L. Ruby and D. I. Bolef, Phys. Rev. Lett. 5 (1960) 5.

[9] F. E. Fujita in Mössbauer Spectroscopy Vol. 5, U. Gonser, ed., Springer-Verlag, New York (1975) 201.

[10] M. Ron in Applications of Mössbauer Spectroscopy Vol. II, R. L. Cohen, ed., Academic Press, New York (1980) 329.

[11] U. Gonser and M. Ron in Applications of Mössbauer Spectroscopy Vol. II, R. L. Cohen, ed., Academic Press, New York (1980) 282.

[12] L. H. Schwartz in Applications of Mossbauer Spectroscopy Vol. I, Chapter 2, R. Cohen ed., Academic Press, New York (1976).

[13] M. Ron, Int. Atomic Energy Agency Sm-159/32, Vienna (1973).

[14] R. D. Jones, Iron and Steel 46 (1973) 137.

[15] G. P. Huffman and F. E. Huggins "Applications of Physics in the Steel Industry", APS/AISI, Lehigh Univ. Oct., 1981.

[16] P. A. Flinn in Experimental Methods of Materials Research, H. Herman, ed. Wiley (Interscience), New York (1967) p. 163.

[17] B. S. Bokshtein, Yu. B. Voitkovskii, and A. B. Shvartsman, Zavod. Lab. 34 (1968) 34.

[18] U. Gonser in Introduction to Mossbauer Spectroscopy, L. May ed., Plenum Press, New York (1971) Chap. 8.

[19] U. Gonser, Mössbauer Spectroscopy, Springer-Verlag, Berlin and New York (1976).

[20] H. L. Marcus, L. H. Schwartz, and M. E. Fine, Trans. ASM 59 (1966) 468.

[21] B. W. Christ and P. M. Giles, Trans. AIME 242 (1968) 1915.

[22] H. Asano, Jour. Phys. Soc. Japan 27 (1969) 542.

[23] H. K. Chow, R. F. Weise, and P. A. Flinn, Report to USAEC Contract No. AT-(30-1)-4023; USAEC Rept. NSEC-4023-1 (1969).

[24] H. K. Chow and R. L. Bogner, Develop. Appl. Spectrosc. 8 (1970) 229.

[25] N. Abe and L. H. Schwartz, Mater Sci. Eng. 14 (1974) 239.

[26] K. J. Kim and L. H. Schwartz, Mater. Sci. Eng. 33 (1978) 5.

[27] B. Fultz, M.Sc. Thesis, University of California, Berkeley, (1978) LBL-7671.

[28] C. K. Syn, B. Fultz and J. W. Morris Jr., Met. Trans. A 9 (1978) 1635.

[29] P. M. Gielen and R. Kaplow, Acta. Met. 15 (1967) 49.

[30] M. Ron, H. Shechter, and S. Niedzwiedz, Jour. Appl. Phys. 39 (1968) 265.

[31] H. Ino, F. E. Fujita, Y. Maeda, Y. Ono, and Y. Inokuti, Jour Phys. Soc. Japan 25 (1968) 88.

[32] Z. Mathalone, M. Ron, J. Pipman, and S. Niedzwiedz, J. Appl. Phys. 42 (1971) 687.

[33] G. LeCaer, A. Simon, A. Lorenzo, and J. M. Genin, Phys. Stat. Solidi 6a (1971) K97.

[34] M. Ron and Z. Mathalone, Phys. Rev. B4 (1971) 774.

[35] D. L. Williamson, R. G. Schupmann, J. P. Materkowski, and G. Krauss, Met. Trans. 10A (1979) 379.

[36] D. L. Williamson, K. Nakazawa, and G. Krauss, Met. Trans. 10A (1979) 1351.

[37] H. L. Marcus, L. H. Schwartz, and M. E. Fine, Jour. Appl. Phys. 38 (1967) 4750.

[38] H. L. Marcus and L. H. Schwartz, Phys. Rev. 162 (1967) 259.

[39] A. Asano, Ph.D. Thesis, Northwestern Univ. (1974).

[40] R. Tahara, Y. Nakamura, M. Inagaki, and Y. Iwama, Phys. Stat Solidi 41 (1977) 451.

[41] I. Vincze and I. A. Campbell, Jour. Phys. F: Metal Phys. 3 (1973) 647.

[42] R. B. G. Yeo and O. O. Miller, "A History of Nickel Steels from Meteorites to Maraging", Sorby Centennial Symposium on History of Metallurgy, ASM, Cleveland, Ohio, Oct. 21-23, 1963.

[43] A. W. Pense and R. D. Stout, Welding Research Council Bulletin No. 205, 1975.

[44] R. Sergeson, Trans. Amer. Soc. Steel Treating (1932) 19,368.

[45] Metals Handbook Vol. 1, B. P. Bardes, ed., American Society for Metals (1978) p. 476.

[46] W. W. Cias, Austenite Transformation Kinetics of Ferrous Alloys, Climax Molybdenum Co. publication M291, p. 16.

[47] G. Krauss in Hardenability Concepts with Applications to Steel, D. Doane and J. S. Kirkaldy, eds., AIME Warrendale, Pennsylvania (1978) p. 229.

[48] F. B. Pickering, ibid., p. 179.

[49] J. I. Kim, Ph.D. Thesis, Univ. of Calif., Berkeley (1979) LBL-9956.

[50] N. S. Stoloff in Fracture Vol. 6, H. Liebowitz, ed., Academic Press, New York (1969) p. 7.

[51] J. W. Morris, Jr., J. I. Kim, and C. K. Syn in Proceedings of the Sagamore Conference, Lake George, New York, July 17-21, 1978, LBL-9435.

[52] C. K. Syn, S. Jin, and J. W. Morris, Jr., Met. Trans. A 7 (1976) 1827.

[53] S. Jin, J. W. Morris, Jr., and V. F. Zackay, Met. Trans. A 6 (1975) 141.

[54] S. Jin, S. K. Hwang, and J. W. Morris, Jr., Met. Trans. A 6 (1975) 1569.

[55] G. R. Brophy and A. J. Miller, Trans. ASM 41 (1949) 1185.

[56] T. N. Armstrong and G. R. Brophy, The American Society of Mechanical Engineers, Oct. 1947, The International Nickel Company, New York.

[57] C. W. Marschall, Ph.D. Thesis, Case Institute of Technology, Cleveland, Ohio (1961).

[58] C. W. Marschall, R. F. Hehemann, and A. R. Troiano, Trans. ASM 55 (1962) 135.

[59] T. Ōoka and K. Sugino, Jour. Japan Inst. Metals 30 (1966) 435.

[60] T. Ōoka, H. Mimura, S. Yano, K. Sugino and T. Toizumi, Jour. Japan Inst. Metals 30 (1966) 442.

[61] M. Kron, A. Constant, A. Clerc, J. Plateau, G. Henry, M.

Robert, and C. Crussard, Memories Scientifiques Rev. Metallurg. 58 (1961) 901.

[62] S. Yano, H. Sakurai, H. Mimura, N. Wakita, T. Ozawa, and K. Aoki, Trans. Iron and Steel Inst. Japan 13 (1973) 133.

[63] Japanese Patent Publication No. 46-13498 (1971); U. S. Patent No. 3619302 (9-11-1972).

[64] H. Haga, Trans. Iron Steel Inst. Japan 13 (1973) 141.

[65] A. G. Evans, private communication to B. Fultz during qualifying exam, Univ. of Calif., Berkeley, June, 1980.

[66] J. W. Morris, Jr., C. K. Syn, J. I. Kim, and B. Fultz, Proceedings of the International Conference on Martensite Transformations, MIT, 1979 Cambridge, Mass. p. 572.

[67] N. Yamada, presentation at 106$^{th}$ AIME annual meeting, Atlanta, Georgia, March 8, 1977.

[68] J. I. Kim and J. W. Morris, Jr., Met. Trans. A 12 (1981) 1957.

[69] J. I. Kim, unpublished results, University of California, Berkeley (1980).

[70] A. D. Romig, Jr. and J. I. Goldstein, Met. Trans. A 11 (1980) 1151.

[71] A. D. Romig, Jr. and J. I. Goldstein, Met. Trans. A 12 (1981) 243.

[72] C. J. Van Tyne, S. K. Tarby, and A. D. Romig, Jr., TMS-AIME paper A80-28, AIME, Warrendale, Pennsylvania.

[73] T. Funekoshi, Ph.D. Thesis, Tohuku Univ., Japan (1973).

[74] J. I. Kim and J. W. Morris, Jr., Met. Trans. A 11 (1980) 1401.

[75] P. B. Moon, Proc. Phys. Soc. 63 (1950) 1189.

[76] K. G. Malmfors in Beta- and Gamma-Ray Spectroscopy, K. Siegbahn, ed., North Holland, Amsterdam (1955) Chapter XVIII.

[77] S. C. Fultz, R. L. Bramblett, J. T. Caldwell, N. E. Hanson, and C. P. Jupiter, Phys. Rev. 128 (1962) 2345.

[78] J. Miller, C. Schuhl, G. Tamas and C. Tzara, Jour. Phys. Radium 21 (1960) 296.

[79] B. L. Berman and S. C. Fultz, Reviews of Modern Physics 47 (1975) 713.

[80] B. M. Spicer, Suppl. Nuovo Cimento 2 (1964) 243.

[81] H. J. Lipkin, Ann. Phys. 9 (1960) 332.

[82] H. Frauenfelder, The Mössbauer Effect, W. A. Benjanim, New York (1962) Chapter 2.

[83] R. L. Cohen, Applications of Mössbauer Spectroscopy Vol. 1, Academic Press, New York (1976) Chapter 1.

[84] C. Kittel, Quantum Theory of Solids, J. Wiley (1963) Chapter 20.

[85] G. K. Wertheim, The Mössbauer Effect: Principles and Applications, Academic Press, New York (1964).

[86] W. M. Visscher, Ann. Phys. 9 (1960) 194.

[87] D. S. Saxon, Elementary Quantum Mechanics, Holden Day, San Francisco (1968) p. 341-343.

[88] L. I. Schiff, Quantum Mechanics, McGraw - Hill, New York (1968) p. 44.

[89] B. D. Josephson, Phys. Rev. Lett. 4 (1960) 341.

[90] J. M. Blatt and V. F. Weisskopf, Theoretical Nuclear Physics, J. Wiley, New York (1952) Chapter 8.

[91] W. Heitler, Quantum Theory of Radiation, Clarendon Press, Oxford (1949).

[92] C. Fabry and A. Perot, Ann. de chim. et phys. 12 (1897) 459.

[93] Ch. Wali-Mohammed, Astrophys. Jour. 39 (1914) 185.

[94] W. Pauli, Naturwissenschaften 12 (1924) 741.

[95] H. E. White, Introduction to Atomic Spectra, McGraw - Hill, New York (1934) Chapter 18.

[96] S. DeBenedetti, G. Lang, and R. Ingalls, Phys. Rev. Lett. 6 (1961) 60.

[97] L. R. Walker, G. K. Wertheim, and V. Jaccarino, Phys. Rev. Lett. 6 (1961) 98.

[98] J. J. Spijkerman, Phys. Rev. Lett. 26 (1971) 323.

[99] C. E. Violet and D. N. Pipkorn, Jour, Appl. Phys. 42 (1971) 4339.

[100] O. C. Kistner and A. W. Sunyar, Phys. Rev. Lett. 4 (1960) 412.

[101] S. S. Hanna, J. Heberle, C. Littlejohn, G. J. Perlow, R. S. Preston, and D. H. Vincent, Phys. Rev. Lett. 4 (1960) 177.

[102] H. Frauenfelder, D. E. Nagle, R. D. Tailor, D. Cochran and W. M. Visscher, Phys. Rev. 126 (1962) 1065.

[103] P. A. Flinn and S. L. Ruby, Phys. Rev. 124 (1961) 34.

[104] M. B. Stearns, Phys. Rev. 129 (1963) 1136.

[105] G. K. Wertheim, V. Jaccarino, J. H. Wernick, and D. N. E. Buchanan, Phys. Rev. Lett. 12 (1964) 24.

[106] F. Van Der Woude and G. A. Sawatzky, Physics Reports 12 (1974) 335.

[107] I. Vincze and A. T. Aldred, Phys. Rev. B 9 (1974) 3845.

[108] I. Vincze and L. Cser, Phys. Stat. Sol. B 49 (1972) K99.

[109] I. Vincze and L. Cser, Phys. Stat. Sol. B 50 (1972) 709.

[110] I. Vincze and G. Grüner, Physical Review Letters 28 (1972) 178.

[112] G. Grüner, I. Vincze and L. Cser, Solid State Commun. 10 (1972) 347.

[113] I Vincze and I. A. Campbell, Sol. State. Comm. 15 (1974) 1495.

[114] T. E. Cranshaw, Jour. of Physics F 2 (1972) 615.

[115] T. E. Cranshaw, C. E. Johnson and M. S. Ridout, Physics Letters 21 (1966) 481.

[116] M. B. Stearns, Jour. Appl. Phys. 36 (1965) 913.

[117] M. B. Stearns, Phys. Rev. 147 (1966) 439.

[118] M. B. Stearns, Phys. Rev. B 4 (1971) 4069.

[119] W. E. Sauer and R. J. Reynik, Jour. Appl. Phys. 42 (1971) 1604.

[120] P. J. Schurer, K. W. Maring and F. Van der Woude, Int. J. Magnetism 4 (1973) 291.

[121] P. J. Schurer, G. A. Sawatzky and F. Van der Woude, Phys. Rev. Letters 27 (1971) 586.

[121.5] B. deMayo, D. W. Forester, and S. Spooner, Jour. Appl. Phys. 41 (1970) 1319.

[122] G. K. Wertheim, Phys. Rev B 1 (1970) 1263.

[122.5] D. Feldmann, H. R. Kirchmayer, A. Schmolz, and M. Velicescu, IEEE Transactions on Magnetics MAG-7 (1971) 61.

[123] J. I. Budnick, T. J. Burch, S. Skalski and K. Raj, Phys. Rev. Letters 24 (1970) 511.

[124] M. Rubenstein, G. H. Stauss, and M. B. Stearns, Jour. Appl. Phys. 37 (1966) 1334.

[125] M. Rubenstein, Phys. Rev. 172 (1968) 277.

[126] G. H. Stauss, Phys. Rev. B 4 (1971) 3106.

[127] L. D. Khoi, P. Veillet and I. A. Campbell, Jour. Phys. F: Metal Phys. 4 (1974) 2310.

[128] B. Fultz and J. W. Morris, Jr. in Nuclear and Electron Resonance Spectroscopies Applied to Materials Science, E. N. Kaufmann and G. K. Shenoy, eds., North Holland, New York (1980) p. 377.

[129] S. Wen (Chen), unpublished results, Univ. of Calif., Berkeley (1976).

[130] Metals Handbook Vol. 8, Taylor Lyman, ed., American Soc. for Metals (1973).

[131] D. deFontaine, Jour. Appl. Cryst. 4 (1971) 15.

[132] P. C. Gehlen and J. B. Cohen, Phys. Rev. 139 (1965) A 844.

[133] J. E. Gragg, M. Hayakawa, and J. B. Cohen, Jour. Appl. Cryst. 6 (1973) 59.

[134] W. J. Carr, Jr. in Magnetism and Metallurgy Vol. 1, A. Berkowitz and E. Kneller, eds., Academic Press, New York (1969) Chapter 2.

[135] W. Marshall and C. E. Johnson, Jour. Phys. Radium 23 (1962) 773.

[136] P. D. DeCicco and a. Kitz, Phys. Rev. 162 (1967) 486.

[137] E. Fermi, Z. Phys. 60 (1930) 320.

[138] E. Fermi and E. Segré, Rend. Accad. Nazl. Lincei 4 (1933) 18.

[139] E. Fermi and E. Segré, Z. Phys. 82 (1933) 729.

[140] R. M. Sternheimer, Phys. Rev. 86 (1952) 316.

[141] R. E. Watson and A. J. Freeman, Phys Rev. 123 (1961) 2027.

[142] A. J. Freeman and R. E. Watson in Treatise on Magnetism Vol. 2A, G. Rado and H. Suhl, eds., Academic Press, New York (1965) Chapter 4.

[143] R. E. Watson and A. J. Freeman in Hyperfine Interactions, A. J. Freeman and R. B. Frankel, eds., Academic Press, New York (1967) Chapter 2.

[144] L. I. Schiff, Quantum Mechanics, McGraw - Hill, New York (1968) section 47.

[145] J. C. Slater, Phys. Rev. 35 (1930) 210.

[146] V. Fock, Z. Phys. 61 (1930) 126.

[147] J. C. Slater, Phys. Rev. 81 (1951) 385; 82 (1951) 538; 91

(1953) 528.

[148] N. W. Ashcroft and N. D. Mermin, Solid State Physics, Holt, Rinehart and Winston, New York (1976) p. 337.

[149] S. S. Hanna, J. Heberle, G. J. Perlow, R. S. Preston, and D. H. Vincent, Phys. Rev. Lett. 4 (1960) 513.

[150] C. Song, J. Trooster and N. Benczer-Koller, Phys. Rev. B 9 (1974) 3854.

[151] K. J. Duff and T. P. Das, Phys. Rev. B3 (1971) 2294.

[152] J. Lindhard, Kgl. Danske Videnskab. Selskab Mat.-Fys. Medd. 28 (1954) No. 8.

[153] N. W. Ashcroft and N. D. Mermin op. cit. p. 343.

[154] C. Kittel, Quantum Theory of Solids, John Wiley, New York (1963) p. 89.

[155] B. B. Schwartz in Hyperfine Interactions in Excited Nuclei Vol. I, G. Goldring and R. Kalish, eds., Gordon and Breach, London (1971) 185.

[156] J. Friedel, Phil. Mag. 43 (1952) 153.

[157] J. Friedel, Adv. Phys. 3 (1953) 446.

[158] J. Friedel, Canadian Jour. of Physics 34 (1956) 1190.

[159] L. I. Schiff, op. cit., Section 19.

[160] J. Friedel, Ann. Phys. 9 (1954) 158.

[161] F. J. Blatt, Phys. Rev. 99 (1955) 1708; 100 (1955) 666.

[162] P. de Faget de Casteljau and J. Friedel, Jour. Phys. Radium 17 (1956) 27.

[163] J. Friedel in Theory of Magnetism in Transition Metals, W. Marshall, ed., Academic Press, New York (1967) p. 283.

[164] M. A. Ruderman and C. Kittel, Phys. Rev. 96 (1954) 99.

[165] T. Kasuya, Prog. Theor. Phys. 16 (1956) 45.

[166] K. Yosida, Phys. Rev. 106 (1957) 893.

[167] A. W. Overhauser, Jour. Appl. Phys. 34 (1963) 1019S.

[168] C. Zener, Phys. Rev. 81 (1951) 440; 83 (1951) 299.

[169] R. E. Watson and A. J. Freeman, Phys. Rev. Lett. 14 (1965) 695.

[170] R. E. Watson in Hyperfine Interactions, A. J. Freeman and R. B. Frankel, eds., Academic Press, New York (1967) Chapter 9.

[171] R. E. Watson and A. J. Freeman, Phys Rev. 178 (1969) 725.

[172] R. E. Watson and L. H. Bennett, Phys. Rev. B 15 (1977) 502.

[173] D. J. Kim, B. B. Schwartz and H. C. Praddaude, Phys. Rev. B 7 (1973) 205.

[174] D. J. Kim, H. C. Praddaude and B. B. Schwartz, Phys. Rev. Letters 23 (1969) 419.

[175] D. J. Kim, H. C. Praddaude and B. B. Schwartz, Jour. Appl. Phys. 41 (1970) 921.

[176] D. J. Kim and B. B. Schwartz, Phys. Rev. Letters, 28 (1972) 310.

[177] I. Sondhi, Jour. Chem. Phys. 62 (1974) 1385.

[178] M. B. Stearns and J. M. Norbeck, Phys. Rev. B 20 (1979) 3739.

[179] R. E. Watson and L. H. Bennett in Charge Transfer / Electronic Structure of Alloys, L. H. Bennett and R. H. Willens, eds., AIME, New York (1974) p. 1.

[180] R. E. Watson and L. H. Bennett, Phys. Rev. B 17 (1978) 3714.

[181] R. E. Watson and L. H. Bennett in Theory of Alloy Phase Formation, L. H. Bennett, ed., AIME, New York (1980) p. 425.

[182] P. W. Anderson and A. M. Clogston, Bull. Amer. Phys. Soc. 2 (1961) 124. P. W. Anderson, Phys. Rev. 124 (1961) 41.

[183] R. E. Watson, S. Koide, M. Peter and A. J. Freeman, Phys. Rev. 139 (1965) A167.

[184] J. S. Langer and S. H. Vosko, J. Phys. Chem. Solids 12 (1959) 196.

[185] O. Gunnarsson and B. I. Lundquist, Phys. Rev. B 13 (1976) 4274.

[186] K. S. Singwi, A. Sjolander, M. P. Tosi and R. H. Land, Phys. Rev. B 1 (1970) 1044.

[187] M. Gell-Mann and K. Brueckner, Phys. Rev. 106 (1957) 364.

[188] D. R. Hammon and A. W. Overhauser, Phys. Rev. 143 (1966) 183.

[189] C. Herring, Treatise on Magnetism Vol. 4, G. Rado and H. Suhl, eds., Academic Press, New York (1966).

[190] A. W. Overhauser, Phys. Rev. 128 (1962) 1437.

[191] D. A. Shirley and G. A. Westenbarger, Phys. Rev. 138 (1965) A170.

[192] D. A. Shirley, Physics Letters 25A (1967) 129.

[193] D. A. Shirley, S. S. Rosenblum and E. Matthias, Phys. Rev. 170

(1968) 363.

[194] G. N. Rao, A. K. Singhvi and K. K. Gupta, in International Conference on Hyperfine Interactions, E. Karlsson and R. Wappling, eds., Upplands Grafiska AB, Uppsula (1974) p. 150.

[196] C. E. Johnson in Hyperfine Fields in Excited Nuclei Vol. 3, G. Goldring and R. Kalish, eds., Gordon and Breach, London (1971) 803.

[197] F. M. Galperin, Phys. Stat. Solidi, 73 (1976) K73.

[198] M. B. Stearns, Physics Letters 34A (1971) 146.

[199] V. D. Kul'kov, Sov. Phys. Solid State 14 (1972) 557.

[200] E. J. Ansaldo and L. Grodzins, Phys. Lett. 34B (1971) 43.

[201] E. Daniel and J. Friedel, Jour. Phys. Chem. Solids 24 (1963) 1601.

[202] I. A. Campbell, Jour. Phys. C 2 (1969) 1338.

[203] A. Blandin in Theory of Magnetism in Transition Metals, W. Marshall, ed., Academic Press, New York (1967) p. 393.

[204] B. Caroli and A. Blandin, Jour. Phys. Chem. Solids 27 (1966) 503.

[205] P. Jena and D. J. W. Geldart, Solid State Communications 15 (1974) 139.

[206] P. Jena and D. J. W. Geldart, Phys. Rev. B7 (1973) 439.

[207] A. Blandin and I. A. Campbell, Physical Review Letters 31 (1973) 51.

[208] I. A. Campbell and I. Vincze, Phys. Rev. B 13 (1976) 4178.

[209] M. B. Stearns, Phys. Rev. B 13 (1976) 4180.

[210] C. C. M. Campbell, Jour. Phys. F: Metal Physics 5 (1975) 1931.

[211] D. A. Shirley, in Hyperfine Structure and Nuclear Radiations, E. Matthias and D. A. Shirley, eds., North Holland, Amsterdam (1967).

[212] I. Vincze, Phys. Rev. B 7 (1973) 54.

[213] N. F. Mott, Adv. Phys. 13 (1964) 325 section 7.

[214] T. M. Holden, J. B. Comly and G. G. Low, Proc. Phys. Soc. 92 (1967) 726.

[215] J. Friedel, Adv. Phys. 3 (1954) 446.

[216] M. B. Stearns, Phys. Rev. B 8 (1973) 4383.

[217] H. Bernas and I. A. Campbell, Solid State Communications 4 (1966) 577.

[218] S. Kobayashi, K. Asayama, and J. Itoh, Jour. Phys. Soc. Japan 21 (1966) 65.

[219] M. B. Stearns Phys. Rev. B 9 (1974) 2311.

[220] M. B. Stearns, Phys. Rev. B 13 (1976) 1183.

[220.5] M. B. Stearns and L. A. Feldkamp, Phys. Rev. B 13 (1976) 1198.

[221] M. B. Stearns, Phys. Rev. B 6 (1972) 3326.

[222] M. B. Stearns, J. Appl. Phys. 50 (1979) 2060.

[223] M. B. Stearns, Jour. Appl. Phys. 49 (1978) 1555.

[224] M. F. Collins and J. B. Forsyth, Phil. Mag. 8 (1963) 401.

[225] M. F. Collins and G. G. Low, Proc. Phys. Soc. 86 (1965) 535.

[226] I. A. Campbell, Proc. Phys. Soc. 89 (1966) 71.

[227] G. G. Low, Jour. of Appl. Phys. 39 (1968) 1174.

[228] Yu. A. Izyumov and R. P. Ozerov, Magnetic Neutron Diffraction, Plenum Press, New York (1970) Chapter 5.

[229] H. R. Child and J. W. Cable, Phys. Rev. B 13 (1976) 227.

[230] W. A. Rachinger, Jour. Sci. Instr. 25 (1948) 254.

[231] A. R. Stokes, Proc. Phys. Soc. London 61 (1948) 382.

[232] B. Fultz, J. I. Kim, and J. W. Morris, Jr., University of California (1979-80) to be published.

[233] R. L. Miller, Trans. ASM 57 (1964) 892.

[234] R. L. Miller, Trans. ASM 61 (1968) 592.

[235] B. Fultz and J. W. Morris, Jr., Rev. Sci. Instr. 49 (1978) 1216.

[236] T. R. McGuire and P. J. Flanders, Magnetism and Metallurgy Vol. 1, A. E. Berkowitz and E. Kneller, eds., Academic Press, New York (1969) part B.

[237] B. Fultz and J. W. Morris, Jr., Nucl. Instr. and Methods 188 (1981) 197.

[238] B. Fultz, private communication to L. H. Schwartz, Nov. 3, 1981.

[239] A. H. Muir, Jr., Atomics International Report AI-6699; important graph is given in: H. Frauenfelder, The Mössbauer Effect, W. A. Benjamin, New York (1962) p. 48.

[240] J. de Launay in Solid State Physics Vol. 2, F. Seitz and D. Turnbull, eds., Academic Press, New York (1956).

[241] Y. Tanji, Jour. Phys. Soc. Japan 30 (1971) 133.

[242] N. DeCristofaro and R. Kaplow, Scripta Metallurgica 9 (1975) 781.

[243] L. H. Schwartz and K. J. Kim, Met. Trans. A 7 (1976) 1567.

[244] S. Margulies and J. R. Ehrman, Nucl. Instr. and Methods 12 (1961) 131. S. Margulies, P. Debrunner and H. Frauenfelder, Nucl. Instr. Methods 21 (1963) 217.

[245] G. A. Bykov and P. J. Hien, Soviet Physics JETP 16 (1963) 646.

[246] D. P. Johnson and J. G. Dash, Phys. Rev. 172 (1968) 983.

[247] J. Heberle, Nucl. Instr. and Methods 58 (1968) 90.

[248] M. C. Dibar Ure and P. A. Flinn, Mössbauer Effect Methodology Vol. 7, I. J. Gruverman, ed., Plenum Press, New York (1971).

[249] R. C. Singleton, Comm. ACM 10 (1967) 647.

[250] A. D. Romig, Jr. and J. I. Goldstein, Met. Trans. A 9 (1978) 1599.

[251] N. DeCristofaro, R. Kaplow and W. S. Owen, Met. Trans. A 9A (1978) 821.

[252] V. N. Gridnev, G. G. Gavrilyuk, V. V. Nemoshkalenko, Y. A. Polushkin and O. N. Razumov, Fiz. Metal. Metalloved 32 (1977) 582.

[253] F. E. Fujita and C. Shiga, Proceedings of the First JIM International Symposium on New Aspects of Martensitic Transformation, Kobe May 10-12 1976, Pub. by Japan Institute of Metals (1976) 287.

T. Moriya, Y. Sumitomo, H. Ino, and F. E. Fujita, Jour. Phys. Soc. Japan 35 (1973) 1378.

[254] P. G. de Gennes, Jour. Phys. Rad. 23 (1962) 630.

[255] V. Heine, Phys. Rev. 153 (1967) 673.

[256] R. E. Watson and L. H. Bennett, Phys. Rev. B 18 (1978) 6439.

[257] R. E. Watson and L. H. Bennett, Jour. Phys. Chem. Solids 39 (1978) 1235.

[258] R. E. Watson, J. Hudis, and M. L. Perlman, Phys. Rev. B 4 (1971) 4139.

[259] J. Friedel in The Physics of Metals Vol.I, J. M. Ziman, ed., Cambridge Univ. Press, Cambridge (1969).

[260] W. A. Harrison, Physical Review B 23 (1981) 5230.

[261] F. Ducastelle and F. Cyrot-Lackmann, Jour. Phys. Chem. Solids

31 (1970) 1295.

[262] F. Gautier, J. van der Rest and F. Brouers, Jour. Phys. F: Metal Phys. 5 (1975) 1884.

[263] J. van der Rest, F. Gautier and F. Brouers, Jour. Phys. F: Metal Phys. 5 (1975) 995.

[264] J. van der Rest, F. Gautier and F. Brouers, Jour. Phys. F: Metal Phys. 5 (1975) 2283.

[265] F. Brouers, M. Cyrot and F. Cyrot-Lackman, Phys. Rev. B 7 (1973) 4370.

[266] F. Gautier, F. Ducastelle and J. Giner, Phil. Mag. 31 (1975) 1373.

[267] A. R. Miedema, F. R. de Boer, and P. F. deChatel, Jour. Phys. F 3 (1973) 1558.

[268] A. R. Miedema, Jour. Less Common Metals 32 (1973) 117.

[269] R. Boom, F. R. de Boer, and A. R. Miedema, Jour. Less Common Metals 45 (1976) 237 ; 46 (1976) 271.

[270] A. R. Miedema, F. R. de Boer, and R. Boom, Jour Less Common Metals 41 (1975) 283 ; 46 (1976) 67.

[271] A. R. Miedema and P. F. de Chatel in Theory of Alloy Phase Formation, L. H. Bennett, ed., AIME publication, Warrendale, Pa. (1980) p. 344.

[272] H. Ehrenreich and L. M. Schwartz, Solid State Phys. 31 (1976) 149.

[273] H. Hasegawa and J. Kanamori, Jour. of the Phys. Soc. of Japan 31 (1971) 382.

[274] H. Hasegawa and J. Kanamori, Jour. Phys. Soc. Japan 33 (1972) 1607.

[275] H. Hasegawa and J. Kanamori, Jour. Phys. Soc. Japan 33 (1972) 1599.

[276] J. W. Cable and E. O. Wollan, Phys. Rev. B 7 (1973) 2005.

[277] J. W. Cable and H. R. Child, Phys. Rev. B 10 (1974) 4607.

[278] T. Jo, Jour. Phys. Soc. Japan 40 (1976) 715.

[279] T. Jo and H. Miwa, Jour. Phys. Soc. Japan 40 (1976) 706.

[280] Y. Kitoaka and K. Asayama, Jour. Phys. Soc. Japan 40 (1976) 1521.

[281] P. Chardhuri and R. K. Moitra, Phys. Rev. B 18 (1978) 6694.

[282] L. M. Falicov and F. Yndurain, Phys. Rev. B 12 (1975) 5664.

[283] B. Kolk, Jour. Appl. Physics 50 (1979) 7551.

[284] K. Aoi, H. Deuling and K. H. Bennemann, Phys. Rev. B 10 (1974) 1975.

[285] H. Miwa and N. Hamada, Jour. Appl. Phys. 49 (1978) 1532.

[286] I. A. Campbell, Jour Phys. C: Solid St. Phys. 3 (1970) 2151.

[287] Y. Calvayrac and M. Fayard, Mater. Res. Bull. 7 (1972) 891.

[287.1] M. Diana and G. Mazzone, Phys. Rev. B 9 (1974) 3898.

[288] V. Jaccarino, L. R. Walker, and G. K. Wertheim, Phys. Rev. Lett. 13 (1964) 752.

[289] R. A. Tawil and J. Callaway, Phys. Rev. B 7 (1973) 4242.

[290] K. J. Duff and T. P. Das, Phys. Rev. B 3 (1971) 192.

[291] R. E. Watson, A. J. Freeman, and S. Koide, Phys. Rev. B 186 (1969) 625.

[292] I. Vincze, L, Cser, D. L. Nagy, Proceedings of the Conference on the Application of the Mössbauer Effect, Tihany 1969, I. Dezsi, ed., Budapest (1971) p. 389.

[293] F. van der Woude and G. Boom, Rev. Sci. Instr. 36 (1965) 800.

[294] D. M. Edwards, J. Phys. F 6 (1976) L185.

[295] G. J. Perlow, C. E. Johnson and W. Marshall, Phys. Rev. 140 (1965) A875.

[296] C. D. Graham, Jr. in Magnetism and Metallurgy Vol. 2, A. E. Berkowitz and E. Kneller, eds., Academic Press, New York (1969) Chapter 15.

[297] J. C. Slonczewski in Treatise on Magnetism Vol. 1, G. Rado and H. Suhl, eds., Academic Press, New York (1963) Chap. 5.

[298] J. Barton, E. Wieser and M. Muller, Phys. Stat. Sol. 39 (1977) 259.

[299] U. Gonser, M. Ron, H. Ruppersberg, W. Keune, and A. Trautwein, Phys. Stat. Solidi a 10 (1972) 493.

D. L. Nagy, Appl. Phys. 17 (1978) 269.

[300] Welding Handbook Vol. 1, C. Weisman, ed., American Welding Society publication, Miami, Fla. (1976) p. 226.

[300] H. Kessler and W. Pitsch, Acta. Met. 15 (1967) 401.

[301] H. I. Aaronson, J. K. Lee, and K. C. Russell in Precipitation Processes in Solids, K. C. Russell and H. I. Aaronson, eds., AIME

publication, Warrendale, Pa. (1978) p. 31.

[302] J. W. Morris, Jr., J. I. Kim, and C. K. Syn, "Advances in the Heat Treatment of Steels", Office of Naval Research Rept. no. 9 for contract no. N00014-69-A-0200-1062, July, 1979.

[303] G. Horvay and J. W. Cahn, Acta Metallurgica 9 (1961) 695.

[304] F. S. Ham, Jour. Phys. Chem. Solids 6 (1958) 335.

[305] C. Atkinson, K. R. Kinsman, H. B. Aaron, and H. I. Aaronson, Met. Trans. 4 (1973) 783.

[306] H. B. Aaron and H. I. Aaronson Acta. Met. 16 (1968) 789.

[307] A. D. Brailsford and H. B. Aaron, Jour. Appl. Phys. 40 (1969) 1702.

[308] Metals Handbook Vol. 8, T. Lyman, ed. ASM publication (1973) p. 304.

[309] C. J. Smithells, Metals Reference Book Vol. 2, Butterworths, Washington (1962) p. 594.

[310] Diffusion and Defect Data, F. H. Wohlbier, ed., vols. 1 - 25, (1967 - 1981).

[311] P. G. Shewmon, Diffusion in Solids McGraw-Hill, New York (1963) Chap. 2.

[312] J. R. Manning in Diffusion, H. I. Aaronson, ed. ASM publication (1973) Chapter 1.

[313] A. B. Lidiard, Phil. Mag. 4 (1960) 1171.

[314] R. E. Howard and J. R. Manning, Phys. Rev. 154 (1967) 561.

[315] J. D. Eshelby, Jour. Appl. Phys. 25 (1954) 255.

[316] C. P. Flynn, Phys. Rev. 125 (1962) 881.

[317] F. Ichikawa, K. Yamakawa, F. E. Fujita, Scripta Metallurgica 6 (1972) 929.

[318] G. Hettich, H. Mehrer and K. Maier, Scripta Metallurgica 11 (1977) 795.

[319] M. Kiritani, H. Takata, K. Moriyama and F. E. Fujita, Phil. Mag. A 40 (1979) 779.

[320] H. Schultz, Scripta Metalurgica 8 (1974) 721.

[321] T. H. Youssef and G. Grais, Scripta Metallurgica 9 (1975) 603.

[322] W. Glaeser and H. Wever, Phys. Stat. Sol. 35 (1969) 367.

[323] V. Irmer and M. F. Kniepmeier, Phil. Mag. 25 (1972) 1345.

[324] C. Demangeat, Phil. Mag. 31 (1975) 323.

[325] H. J. Lee, Ph.D. Thesis, University of California, Berkeley June, 1982.

[326] R. O. Ritchie, Met. Trans. A 8 (1977) 1131.

[327] T. Inoue in Grain Boundaries in Engineering Materials, J. L. Walters, J. H. Westbrook, and P. A. Woodford, eds. proceedings of the Fourth Boulton Landing Conference (1974) p. 553.

[328] P. J. Black and P. B. Moon, Nature 188 (1960) 481.

[329] K. Gabathuler and H. J. Leisi in Hyperfine Interactions in Excited Nuclei, Vol. 3, G. Goldring and R. Kalish, eds., Gordon and Breach, London (1971) 821.

[330] J. P. Hannon and G. T. Trammel, Phys. Rev. 186 (1969) 306.

[331] V. A. Belyakov, Sov. Phys. Usp. 18 (1975) 267.

## FIGURE CAPTIONS

1) a. Binary Fe-Ni equilibrium phase diagrams:
solid line from ref.[72,250]
broken line from ref.[308]
b. Estimated diffusion lengths after 0.1 hr for solutes in martensite.
c. The most complicated sequence of thermal treatments for a specimen foil in the vacuum furnace of the Mössbauer spectrometer. Spectra were collected during constant temperature intervals marked "S". Calibration checks with the pure Fe foil are indicated by "FeS", and occur only at the beginning and end of the entire sequence.

2) A. Bright field TEM micrograph of N.K.K. 9Ni steel tempered 28 hrs at 600°C as a thick plate
B. Corresponding dark field TEM micrograph of austenite (002) reflection with [110] austenite zone axis
a. and f. are characteristic STEM x-ray spectra taken from austenite and martensite, respectively.

3) Energy level diagram for a $^{57}Fe$ nucleus in a ferromagnetic metal

4) Block diagram of Mössbauer spectrometer (transmission geometry with the vacuum furnace)

5) top: Ar + $CH_4$ gas-filled proportional counter for transmission geometry spectra
bottom: Time exposure of amplified detector pulses during spectrum collection, showing pulses coincident with single channel analyzer output on right.

6) Spectrometer timing diagrams
top: Synchronization of Doppler drive and data collection
bottom: Detected pulses are switched between counter A and counter B for alternate data channels.

7) top: Assembled vacuum furnace
left: Bifilar heating element
right: Specimen package

8) top: Detector count rate precision is seen in inverted and overlayed peaks no. 6 from a Fe-9Ni-0.4C alloy:

+ unprocessed peak from positive acceleration cycle
o unprocessed peak from negative acceleration cycle
bottom: Differences of peaks nos. 1 and 6 from a pure Fe foil collected on different days. The peaks that were differenced had dips larger than the Fe-9Ni-0.4Si peaks above.

9) Comparison of backscatter and transmission geometry Mössbauer spectra. Note the similarity of the (Mn+Cr)-induced intensity on the low Doppler shift energy side of peaks nos. 1 and 6.

10) Austenite content analysis with a backscatter spectrum. Note that the areas of the stripped martensite Lorentzians were slightly too small.

11) General effects of Ni on the martensite sextet. Purity of the Fe was only 99.92%. There is some systematic printer error in the relative velocities of the two spectra. The Fe-8.9Ni specimen was in the vacuum furnace and hence displays some intensity near 0 mm/sec.

12) General effects of the other alloy elements in 9Ni steel. There is some systematic printer error in the relative velocities of the two spectra. All spectra were obtained from specimens in the vacuum furnace.

13 - 14) Calibration of effects of Ni concentration changes on differences of spectra at 18°C (Fig. 13) and at 500°C (Fig. 14). Spectra were shifted only a few tenths of a data channel at their ends to compensate for known changes in the Doppler drive. Before differencing, the starting spectra were height normalized for peak no. 1.

15 - 18) Mössbauer peaks nos. 1 and 6 from Fe-Ni alloys at 18 C (Figs. 15 and 16), and at 500°C (Figs. 17 and 18). All spectra were height normalized for peak no. 1 (in Figs. 15 and 17), and peak no. 6 was taken from the same printout of the entire spectrum. All specimens were approximately 0.0003 in. thick. All peaks were shifted a few tenths of a data channel to compensate for changes in the Doppler drive. 500°C spectra were shifted comparable amounts to correct for differences in the furnace temperature.

19) Temperature dependence of peaks nos. 1 and 6 from Fe-9Ni

Mössbauer spectra. 18°C and 500°C spectra were taken from Figs. 15 - 18. 600°C spectra were taken from a specimen which formed only about 4 % austenite during data collection. The 600°C peaks were shifted to compensate for errors in the Doppler drive only.

20) Thickness distortion corrections for the data of Fig. 17. $\sigma_A(E)$ is the thickness distortion corrected peak shape with the source linewidth deconvolved. Convolving the source lineshape back into $\sigma_A(E)$ provides the expected peak shape from an infinitesimally thin absorber.

21) 18°C parameters of Fe-Ni hyperfine structure
top: Mean isomer shift and mean hyperfine magnetic field perturbation of Fe-Ni alloys with respect to pure Fe
bottom: Additional FWHM of Fe-Ni peaks nos. 1 and 6 with respect to pure Fe

22) $N^{th}$ moments of peak no. 1 from 18°C spectra of Fe-Ni alloys to the 1/N power. The variable "v" is actually the data channel number. All moments were numerically calculated with the same range of integration and the same ranges for baseline determination.

23) Search for effects of carbon on the shape of peaks nos. 1 and 6 from Fe-9Ni-X-0.3C alloys.

24) Search for effects of carbon on the Mossbauer spectrum of Fe-9Ni-0.3C after tempering for 3 hrs at 600°C. Before differencing, starting spectra were shifted 0.1 - 0.2 data channels more than suggested by the Doppler drive calibration spectra in order to overemphasize the intensity of the "C satellite" change.

25) See text section IX.A.2.

26) Effects of differences in Cr and Mn concentrations on difference spectrum intensity for a Fe-8.9Ni host at 500°C. Problems with the spectrum shifting procedure are evident to the author.

27 - 28) 18°C "Cr satellites" (Fig. 27), and "Mn satellites" (Fig. 28) from thin, untempered Fe-Ni-0.75X alloys. Starting peaks were either "RMS tail normalized", or were "height normalized" after correcting for shifts of the "unperturbed" part of the

hyperfine magnetic field, and known shifts of the Doppler drive. All starting peaks nos. 1 shown in these figures are normalized to have approximately the same area.

27a) Fe-0.75Cr

top: excess difference spectrum shift = +0.3 channels

middle: excess difference spectrum shift = 0 channels

bottom: excess difference spectrum shift = -0.3 channels

27b) Fe-3.0Ni-0.75Cr

27c) Fe-6.0Ni-0.75Cr

27d) Fe-8.9Ni-0.75Cr

27e) Fe-12.0Ni-0.75Cr

28a) Fe-0.75Mn

28b) Fe-3.0Ni-0.75Mn

28c) Fe-6.0Ni-0.75Mn

28d) Fe-8.9Ni-0.75Mn

28e) Other differences between starting peaks of 28d with the same heights, but shifts of +1.0 and -1.0 with respect to 28d.

29 - 41) Spectra were folded and compressed. "Peak no.1 height normalization" was used for all except Fig. 36, for which "peak no.1 area normalization" was used. Many starting spectra were shifted before differencing, but no other data processing was performed.

29) 600°C tempering sequence of Fe-8.9Ni alloy. All spectra were taken with the specimen in the vacuum furnace; top: 500°C, bottom: 18°C. Before differencing, shifts of starting spectra were determined by matching high Doppler shift energy sides of peaks nos. 1 and 6 to give differences like Fig. 14. The specimen was not allowed to cool below 500°C until after 34 hrs of tempering.

30) 600°C tempering sequence of Fe-8.9Ni-1.25Mn alloy. Spectra were taken at 18°C during the thermal cycle of Fig. 1c, and these data collections alternated between the collection of spectra of Fig. 31. Pure Fe calibration spectra were only collected before and after the entire sequence, so shifts of spectra were necessarily determined, at least in part, by the author's discretion. Note that the author's discretion favored smoother

changes in X concentration (Fig. 45), than in Ni concentration (Fig. 44).

31) 600°C tempering sequence of Fe-8.9Ni-0.75Mn alloy. 500°C spectra were from the same specimen in the tempering sequence used for the data of Fig. 30. Shifts were determined by high energy tail matching.

32) 600°C tempering sequence of Fe-8.9Ni-1.25Cr alloy, 18°C spectra. Same procedures as Fig. 30.

33) Same 600°C tempering sequence of Fe-8.9Ni-1.25Cr alloy as Fig. 32, but 500°C spectra. Same procedures as Fig. 31.

34) Sequence of one hour low-temperature temperings of Fe-8.9Ni alloy.

35) Differences of spectra from a Fe-8.9Ni specimen in different states of magnetization. Top spectrum is from a specimen that was never exposed to any magnetic field during preparation. "Magnetized" spectrum was obtained after stroking the specimen with a permanent magnet. "Magnetized with external field" spectrum was obtained with the specimen in the spectrometer magnet. No shifts of starting spectra were necessary to correct for changes in the Doppler drive.

36) "Peak no. 1 area normalized" difference spectra from data used for Fig. 38. Doppler drive had shifted only 0.1 data channels at peaks nos. 1 and 6 during the entire tempering sequence.

37 - 41) The specimens were not in the vacuum furnace, so the shifts of the starting spectra before differencing were generally determined within 0.1 data channels from the many pure Fe calibration spectra. The author's discretion was necessary only about one time out of four in order to determine shifts which could not be unequivocally determined in this way from the calibration spectra. Without uncertainties of the shifts of the Doppler drive, and without uncertainties due to "unlocked" directions of magnetization, these five sequences of difference spectra are the most quantitative sequences in this thesis.

40) See text section IX.B.

41) See text section IX.B.

42) Austenite formation kinetics at 600°C from specimens rolled into foils after their solution treatment, but before the "Q" treatment. Curves 1 - 3 were obtained from 18°C spectra. Dotted lines indicate austenite content after immersion in liquid nitrogen. Curve 6 was obtained from the 500°C binary Fe-8.9Ni data of Fig. 29. An Fe-8.9Ni-0.4Si alloy had about 1 % austenite at 18°C after 3 hrs of tempering at 600°C.

43) Kinetics of austenite formation in a plate of N.K.K. 9Ni steel at various tempering temperatures. All spectra for these data were obtained at 18°C. The 600°C specimen was accidentally overheated during glassblowing after the 9 hr tempering datum. The austenite content of the material tempered 243 hrs at 590°C ranged from 15 % to 20 %.

44) Author's discretion was necessary for data of the Fe-8.9Ni-1.25Mn alloy; see caption of Fig. 30.

45) Author's discretion was necessary for data of the Fe-8.9Ni-1.25Mn alloy; see caption of Fig. 30.

46) Notation and description of symbols used in Figs. 47 - 50. See text section X.A.1.

47 - 50) Magnetic moment changes and consequent hyperfine magnetic field perturbations in Fe-Ni-X alloys. See text section X.A.1.

51) Heating and cooling TTT diagrams. See text section X.B.1.

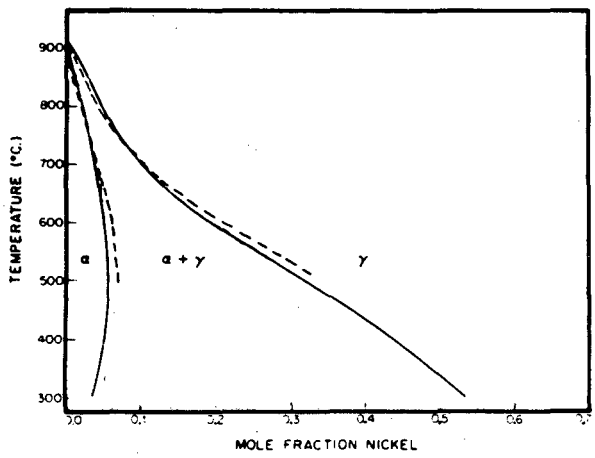


IRON - NICKEL PHASE DIAGRAM

A

B

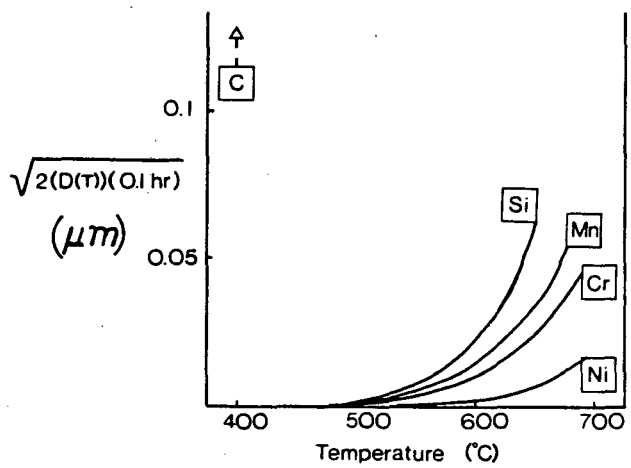


C

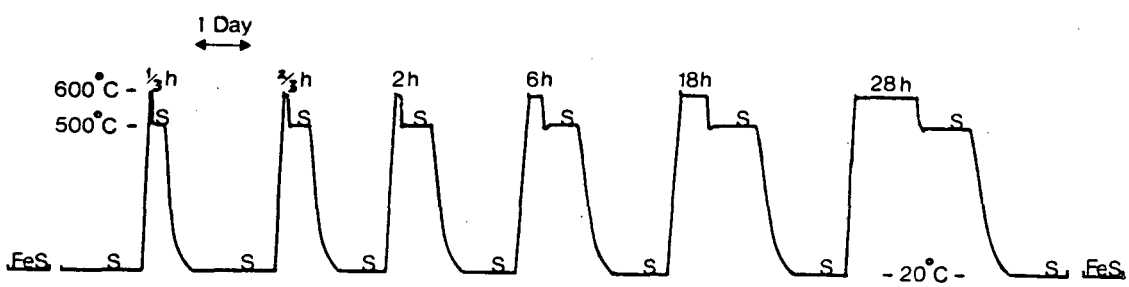


XBL 818-11197

Figure 1

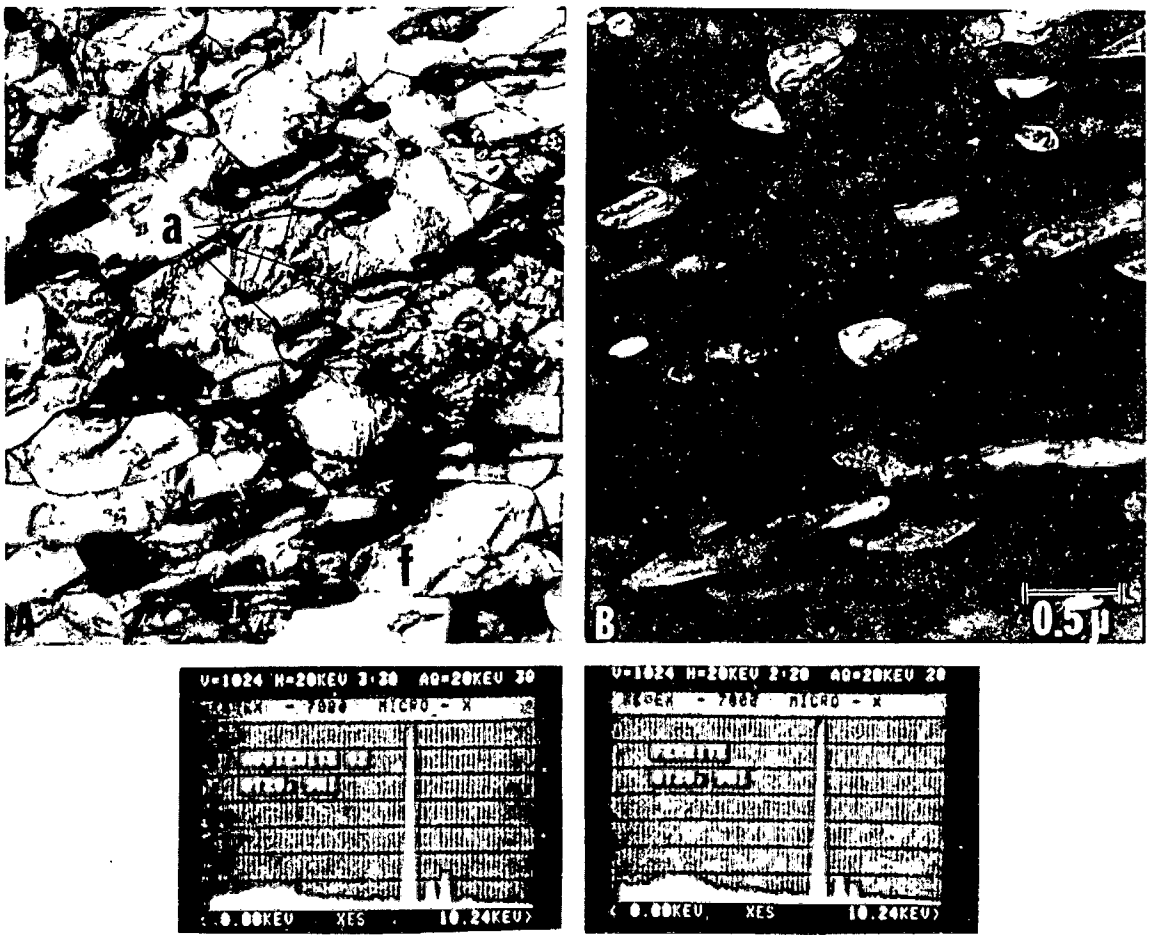


(a) (f)

CBB 806-7622

Figure 2

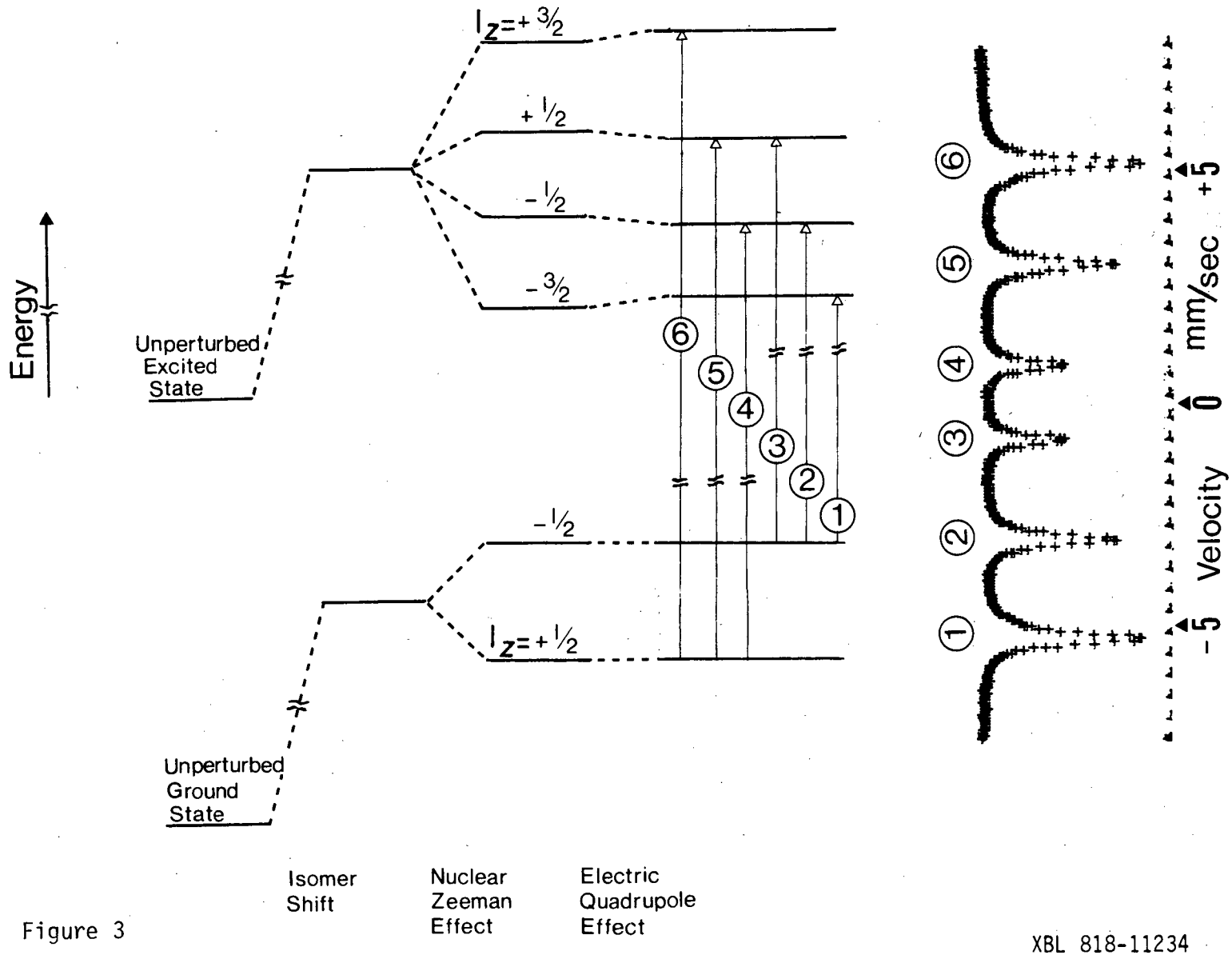


Figure 3

XBL 818-11234

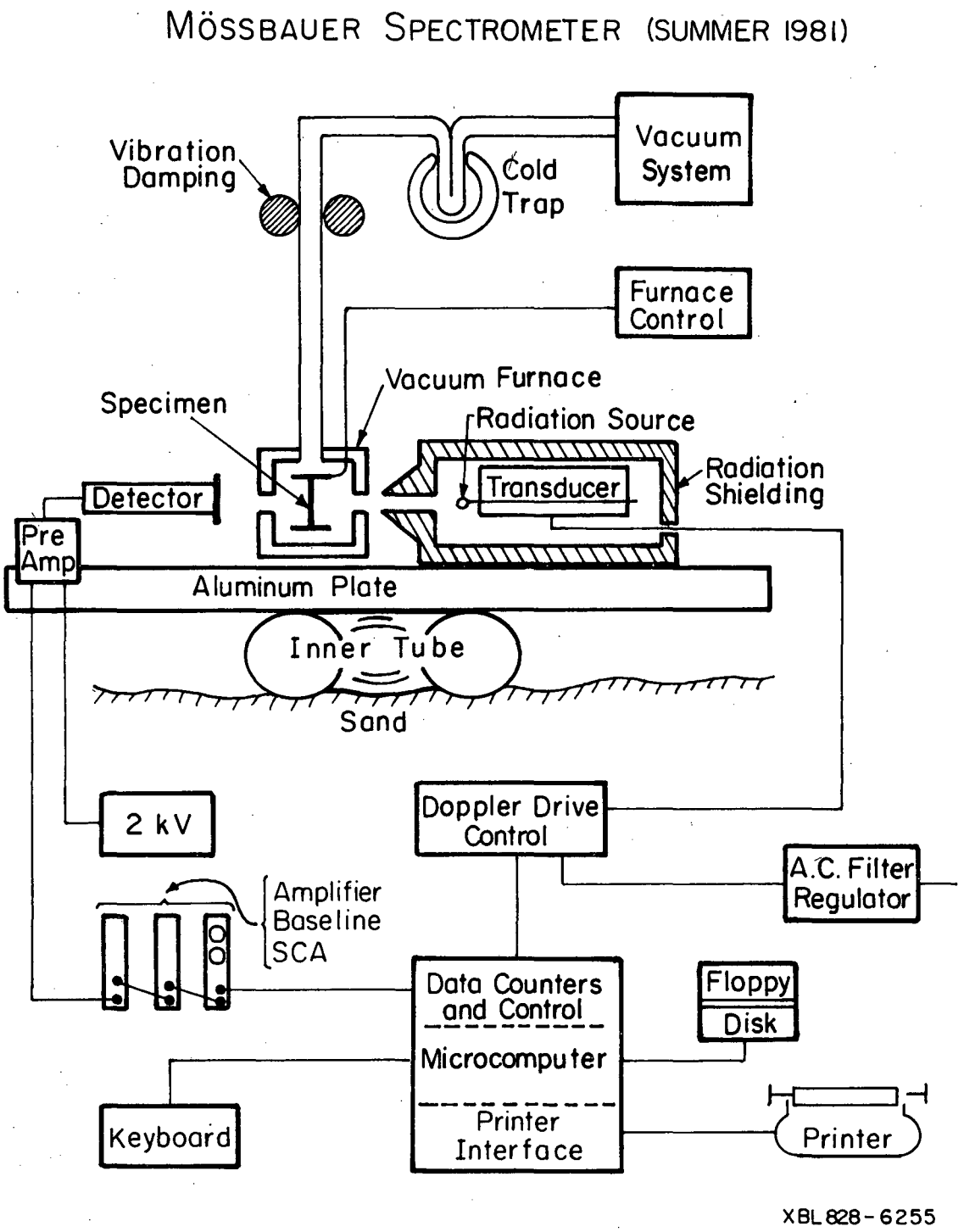
MÖSSBAUER SPECTROMETER (SUMMER 1981)
Vibration Damping
Cold Trap
Vacuum System
Furnace Control
Vacuum Furnace
Specimen
Radiation Source
Radiation Shielding
Transducer
Detector
Pre Amp
Aluminum Plate
Inner Tube
Sand
2 kV
Doppler Drive Control
A.C. Filter Regulator
Amplifier
Baseline
SCA
Data Counters and Control
Microcomputer
Printer Interface
Floppy Disk
Keyboard
Printer
XBL 828-6255

Figure 4

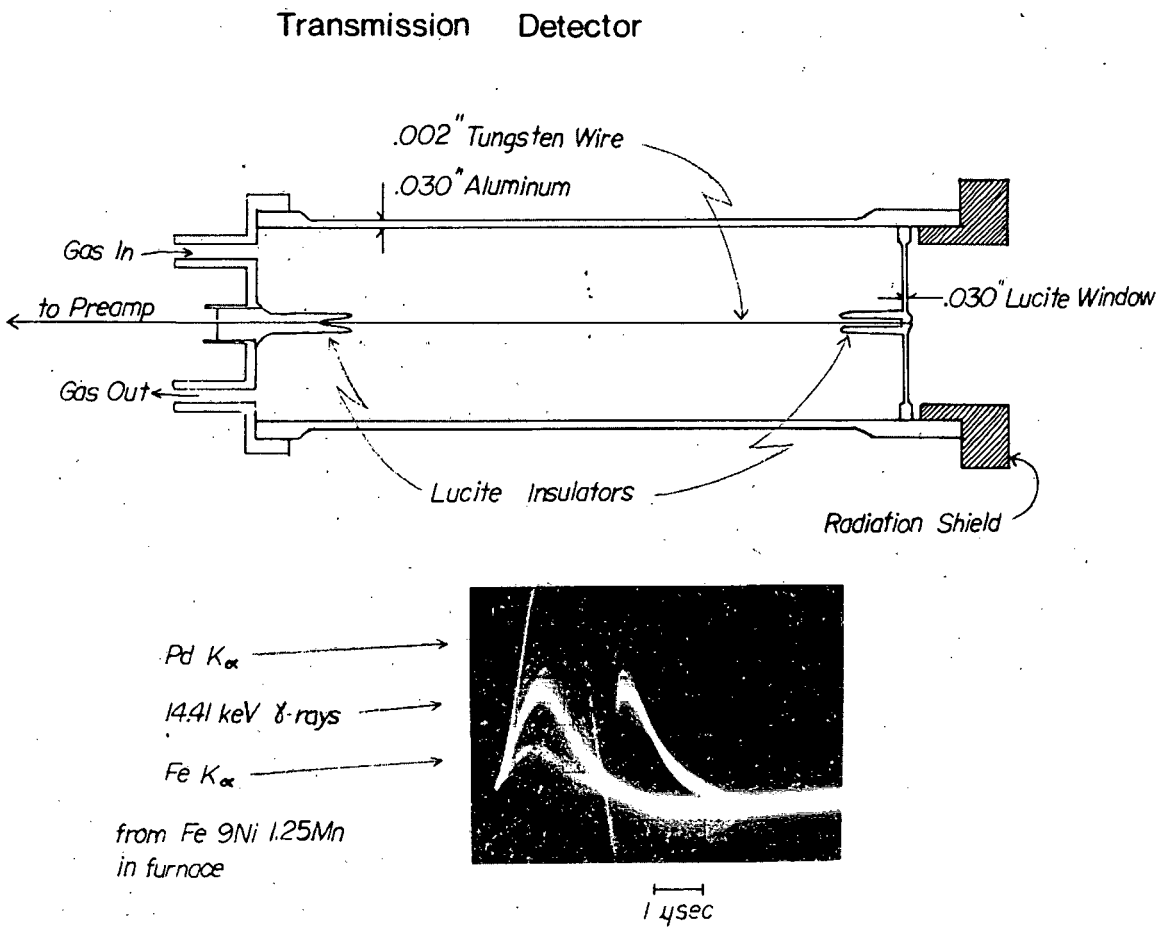


XBB 827-6539

Figure 5

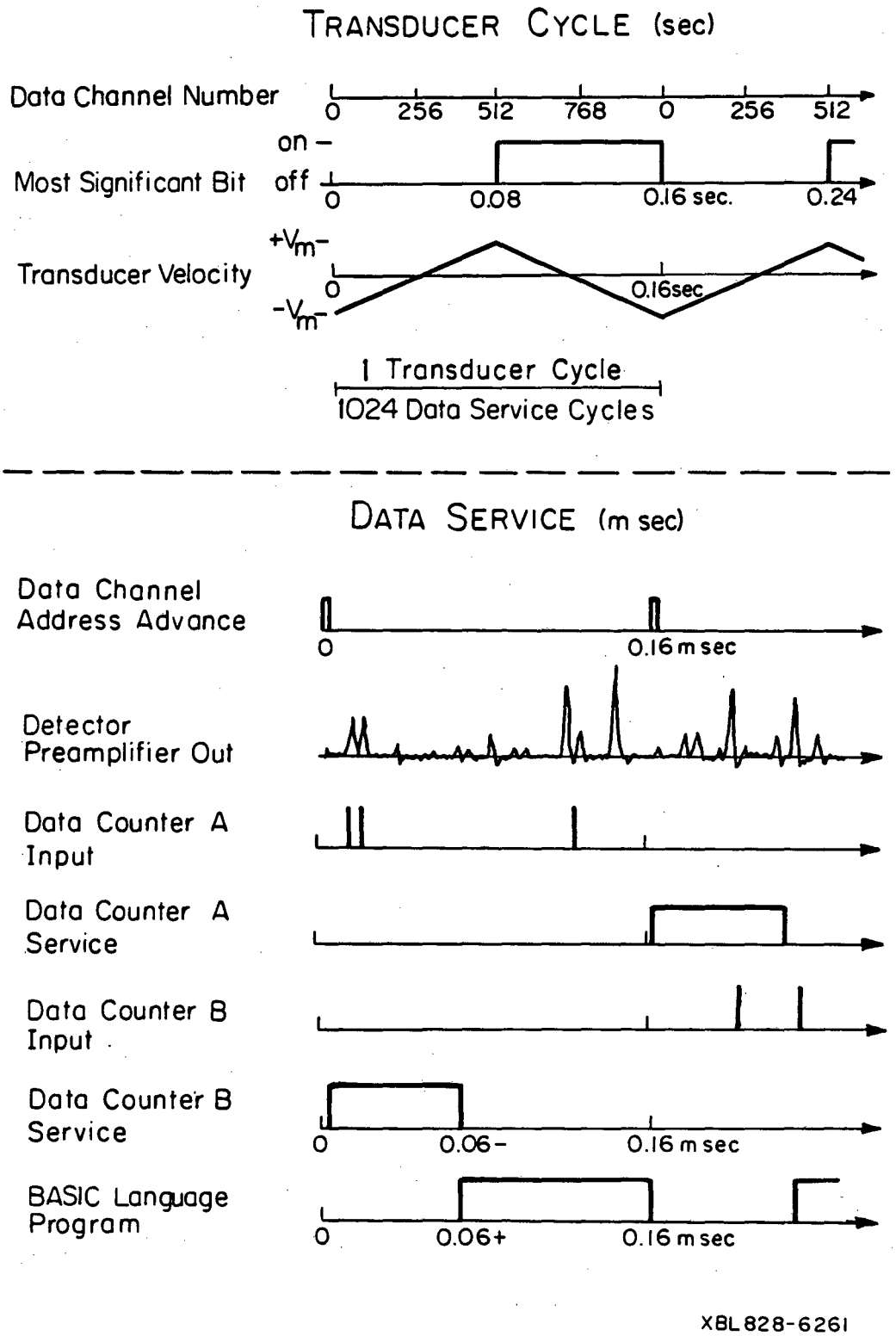
TRANSDUCER CYCLE (sec)
Data Channel Number
0
256
512
768
0
256
512
on –
Most Significant Bit
off
0
0.08
0.16 sec.
0.24
+Vm–
Transducer Velocity
0
0.16sec
–Vm–
1 Transducer Cycle
1024 Data Service Cycles
DATA SERVICE (m sec)
Data Channel Address Advance
0
0.16 m sec
Detector Preamplifier Out
Data Counter A Input
Data Counter A Service
Data Counter B Input
Data Counter B Service
0
0.06–
0.16 m sec
BASIC Language Program
0
0.06+
0.16 m sec
XBL 828-6261

Figure 6

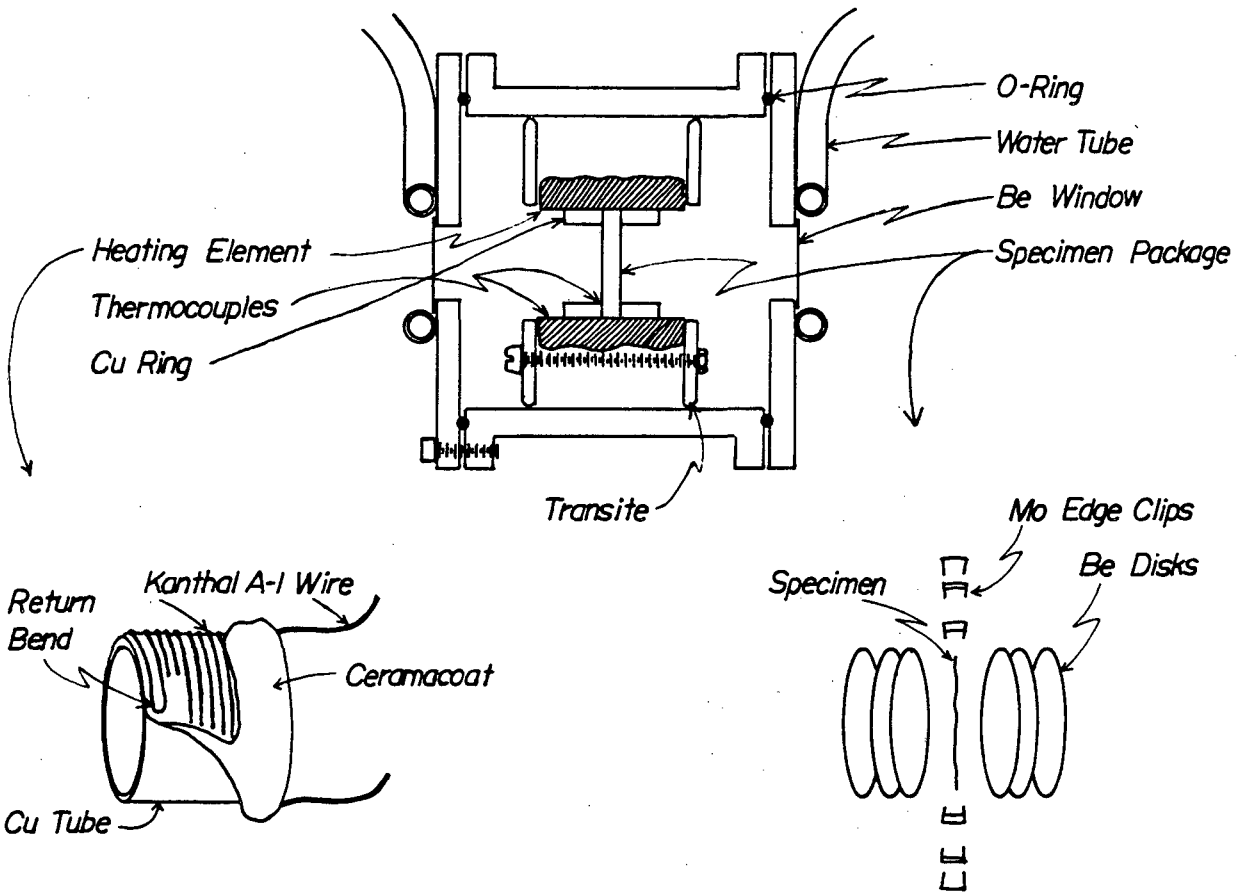


Vacuum Furnace

XBL 828-10832

Figure 7

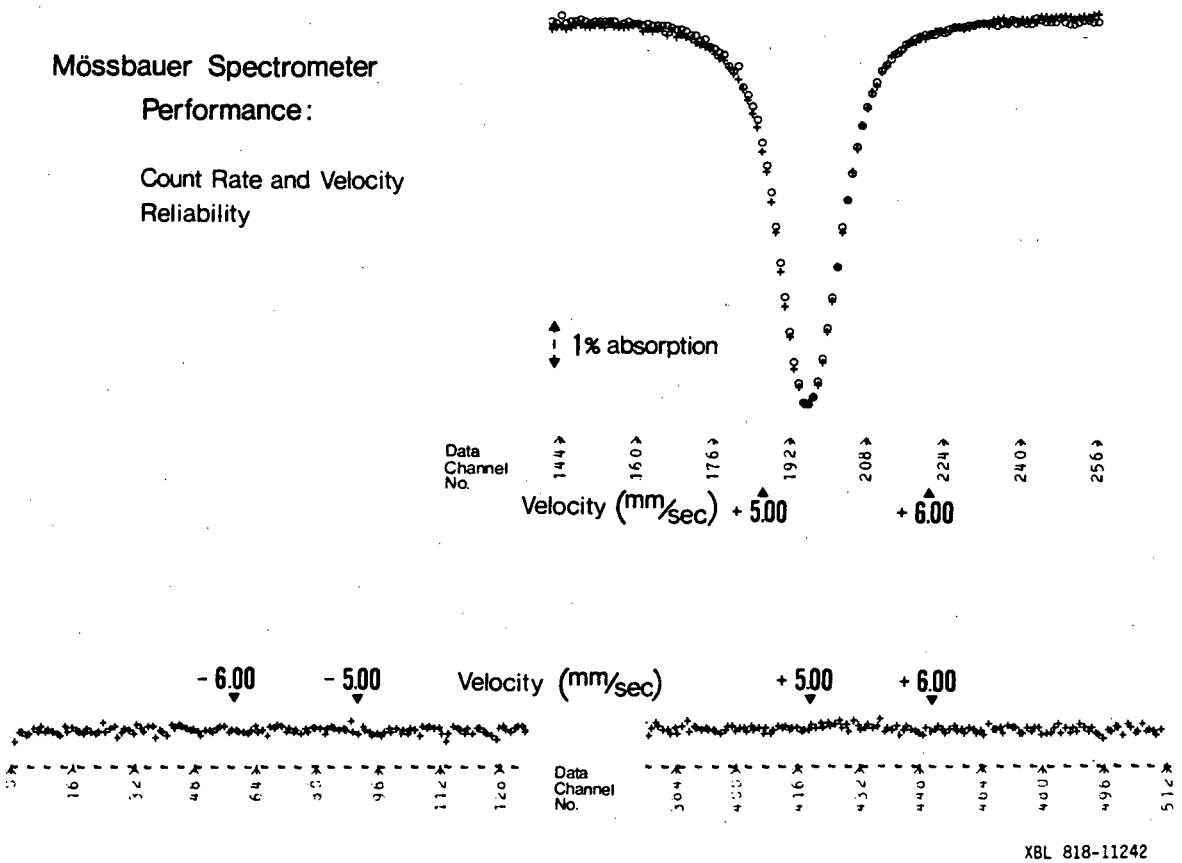
Mössbauer Spectrometer
Performance:
Count Rate and Velocity
Reliability
1% absorption
Data
Channel
No.
144
160
176
192
208
224
240
256
Velocity (mm/sec)
+ 5.00
+ 6.00
- 6.00
- 5.00
Velocity (mm/sec)
+ 5.00
+ 6.00
Data
Channel
No.
XBL 818-11242

Figure 8

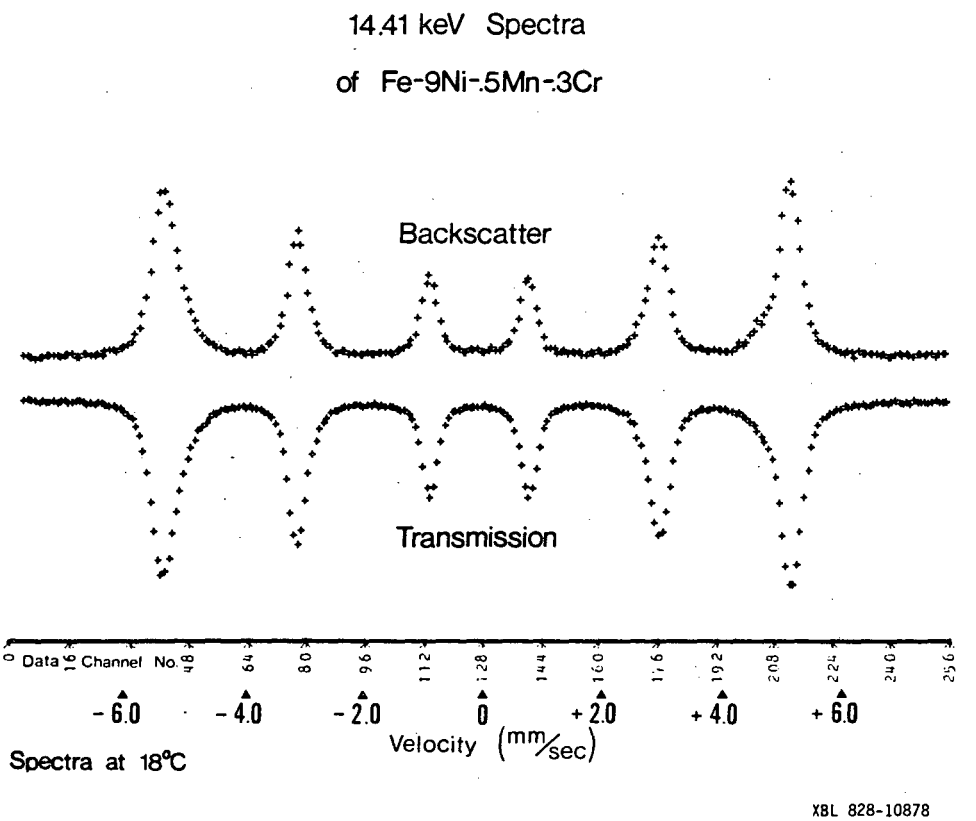
14.41 keV Spectra
of Fe-9Ni-.5Mn-.3Cr
Backscatter
Transmission
0 Data 16 Channel No. 48 64 80 96 112 128 144 160 176 192 208 224 240 256
- 6.0
- 4.0
- 2.0
0
+ 2.0
+ 4.0
+ 6.0
Velocity (mm/sec)
Spectra at 18°C
XBL 828-10878

Figure 9

# 14.41 keV Backscatter Austenite Analysis

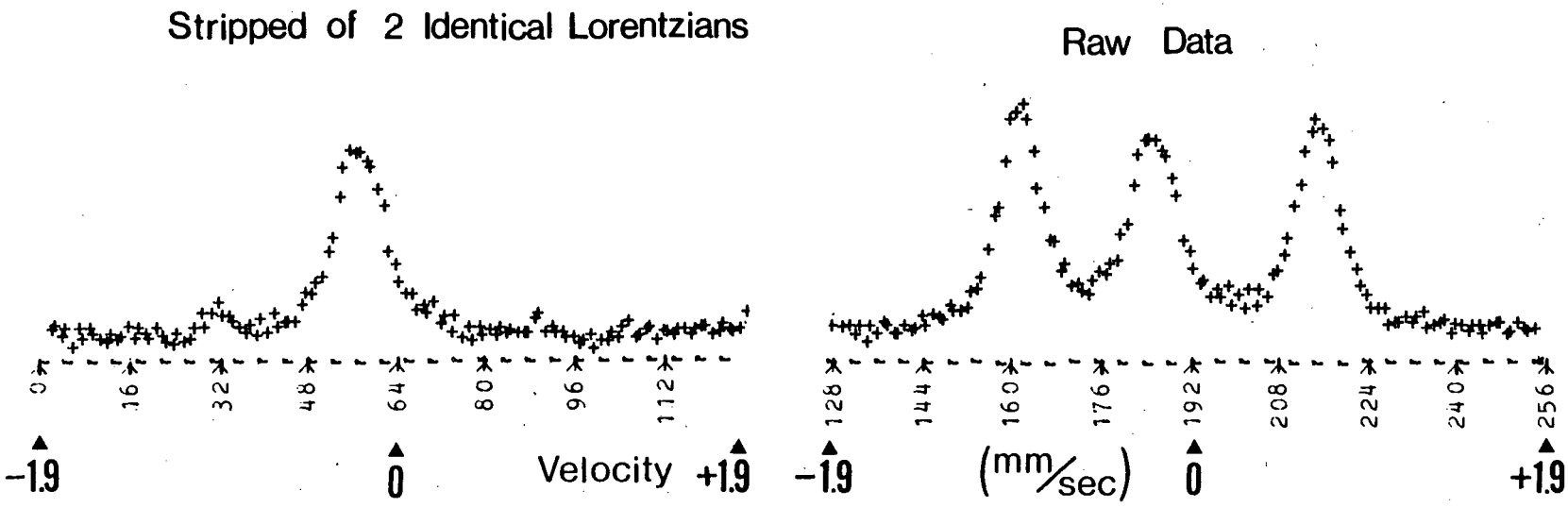


N.K.K. 9Ni Steel with 9.0 vol.% Austenite

XBL 828-10834

Figure 10

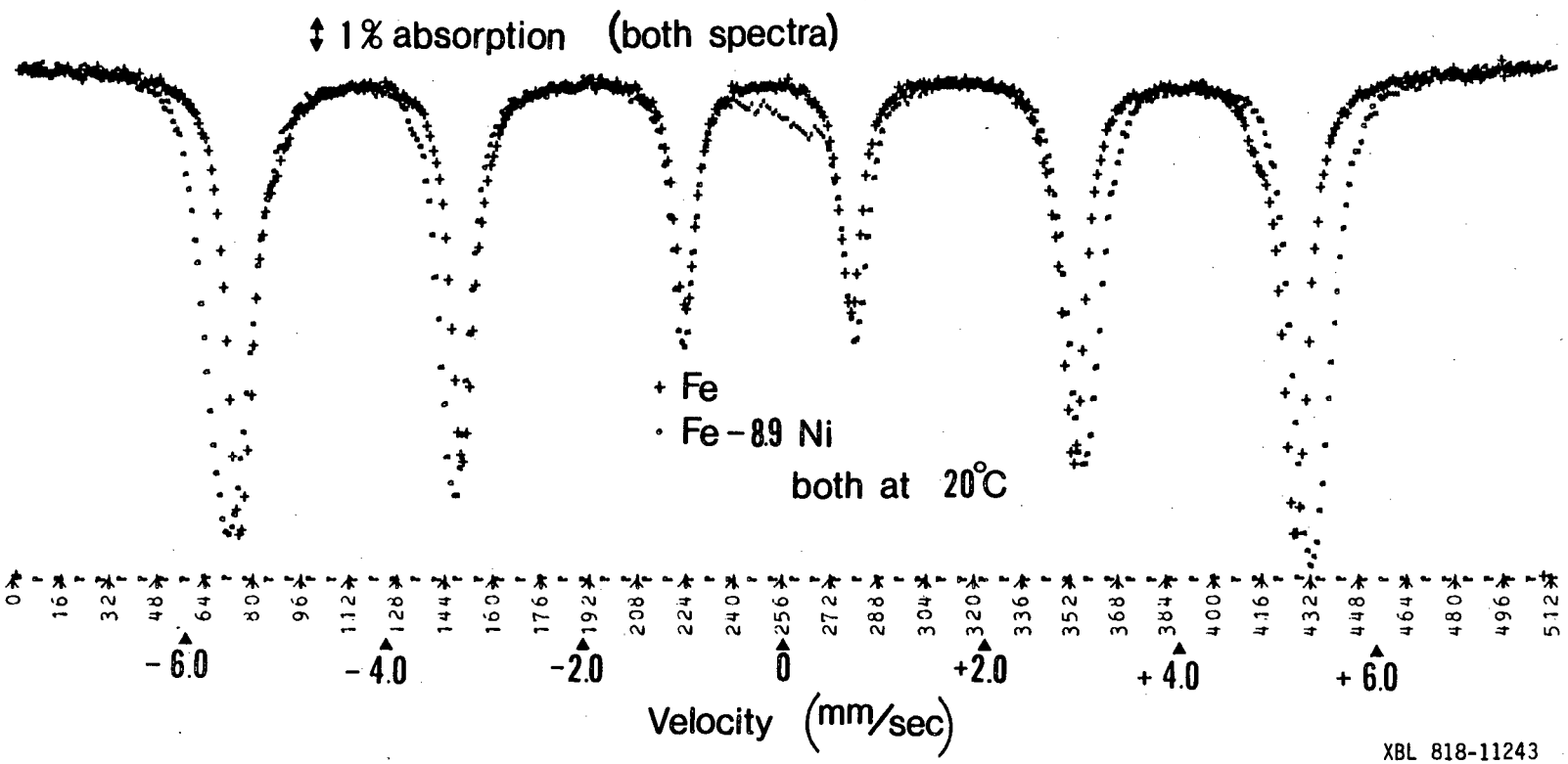


XBL 818-11243

Figure 11

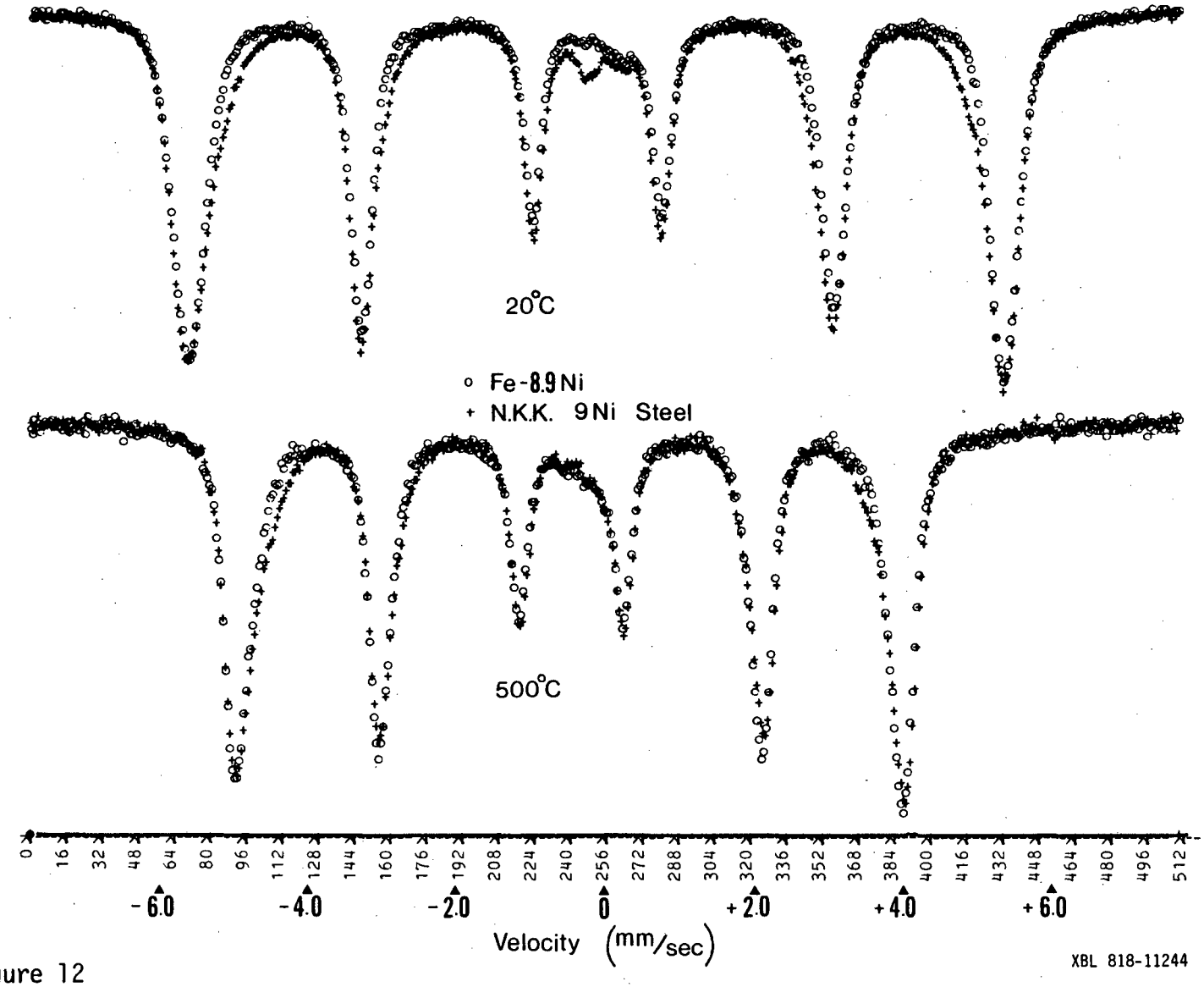
20°C
o Fe-8.9Ni
+ N.K.K. 9Ni Steel
500°C
0 16 32 48 64 80 96 112 128 144 160 176 192 208 224 240 256 272 288 304 320 336 352 368 384 400 416 432 448 464 480 496 512
-6.0 -4.0 -2.0 0 +2.0 +4.0 +6.0
Velocity (mm/sec)
XBL 818-11244

Figure 12

Calibration of Fe-Ni Difference Spectra 500°C

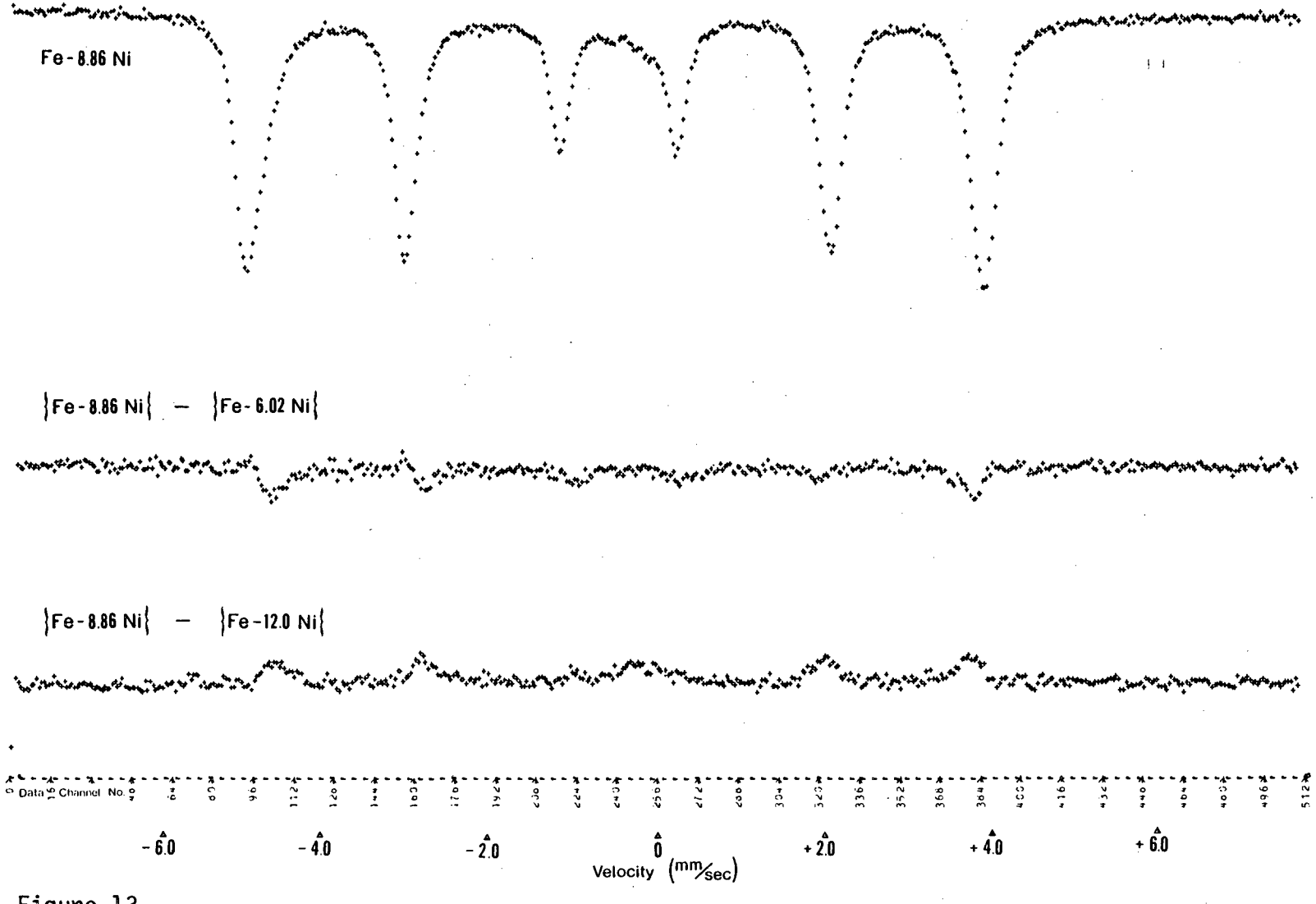


Figure 13

XBL 828-10885

Calibration of Fe-Ni Difference Spectra 18°C

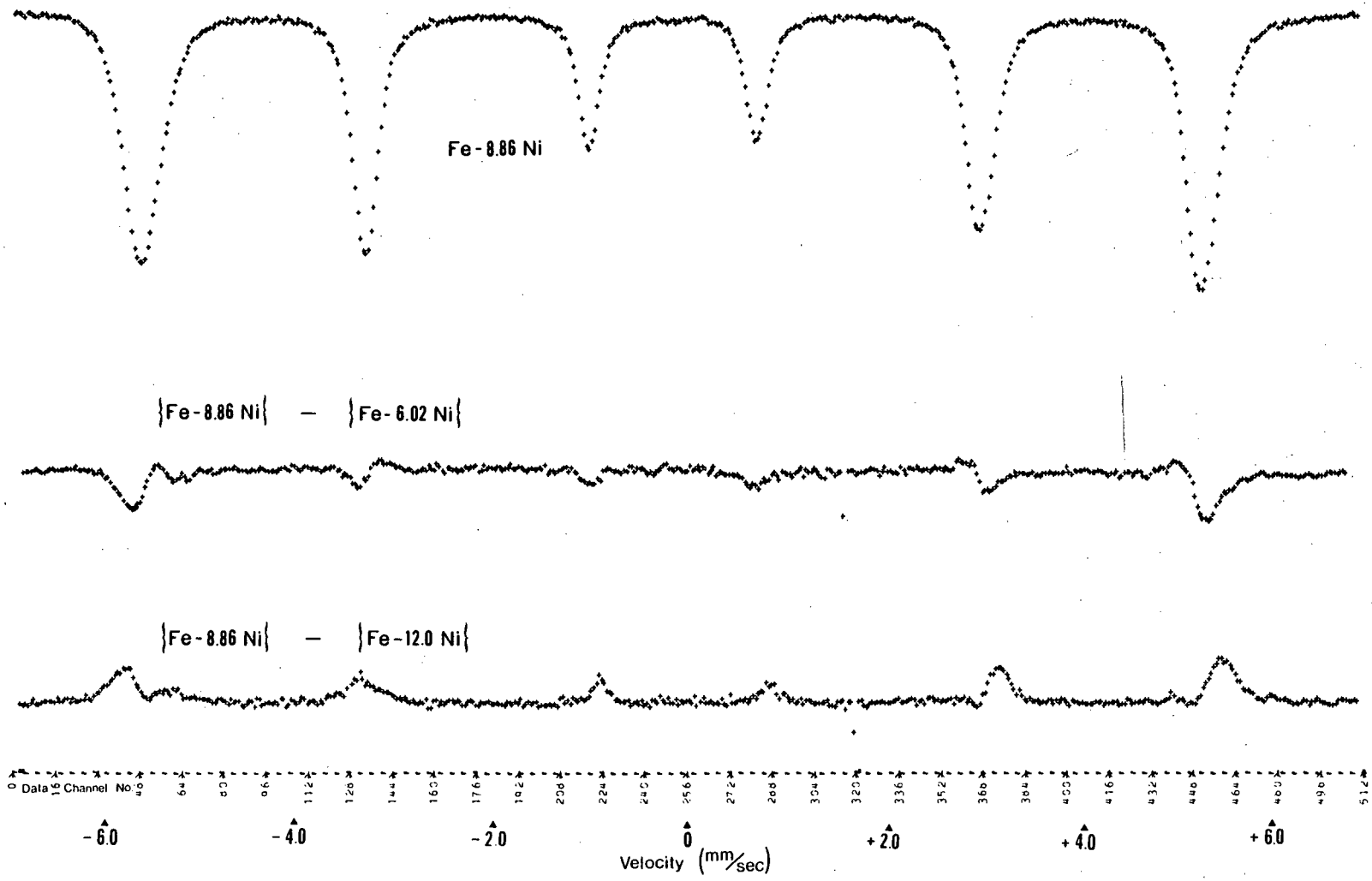


Figure 14

XBL 828-10886

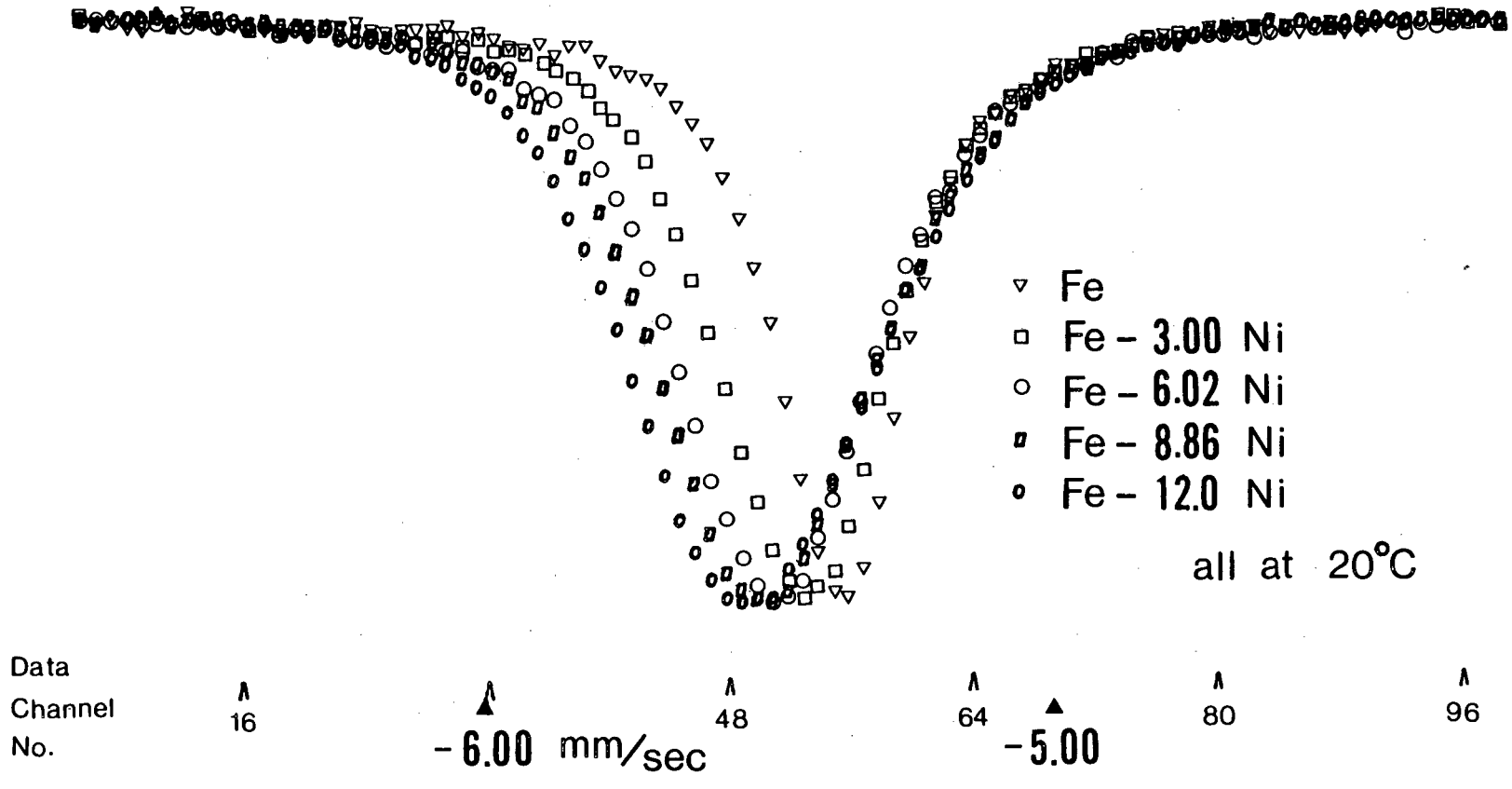


XBL 818-11240

Figure 15

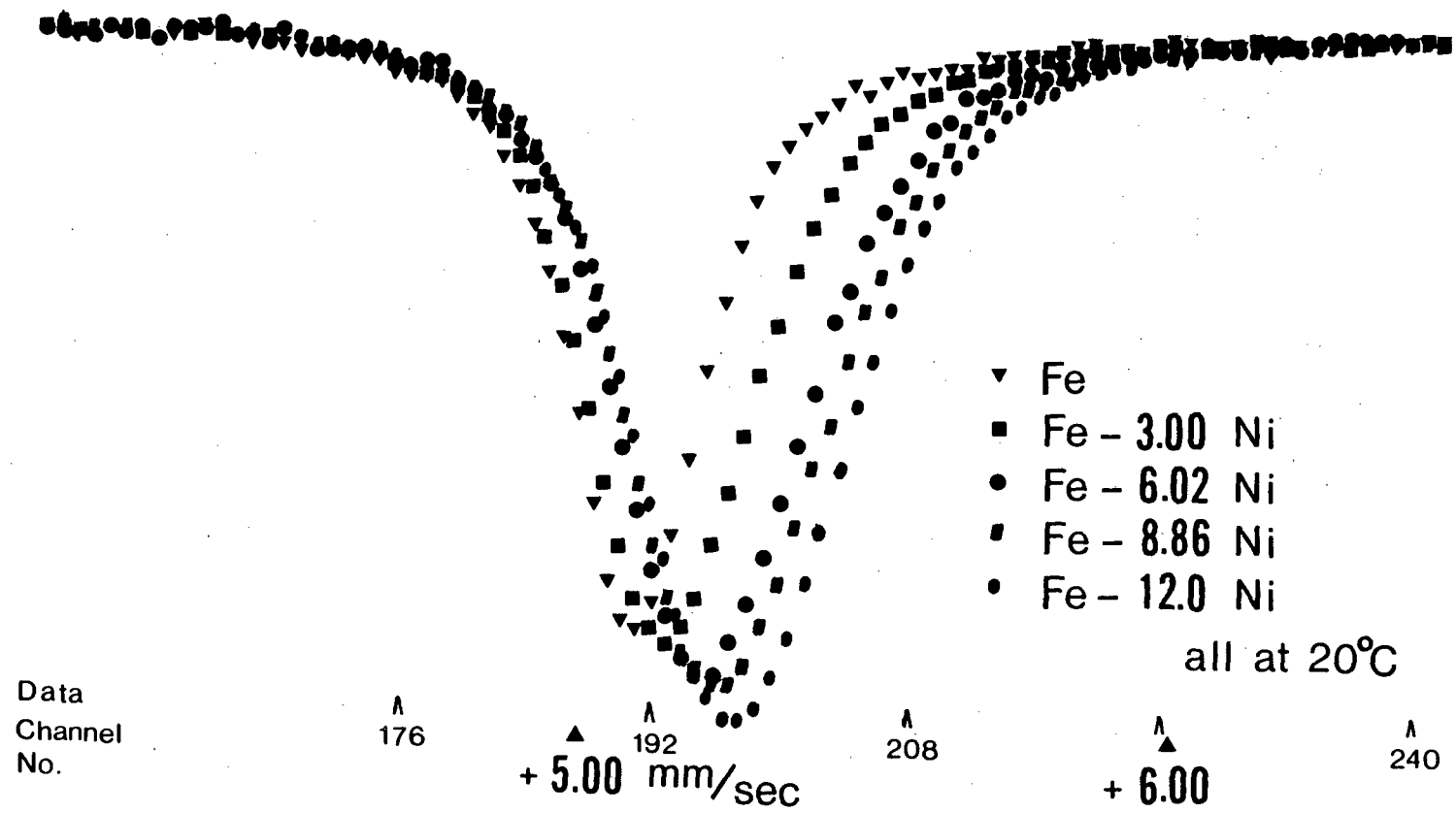


Figure 16

XBL 818-11241

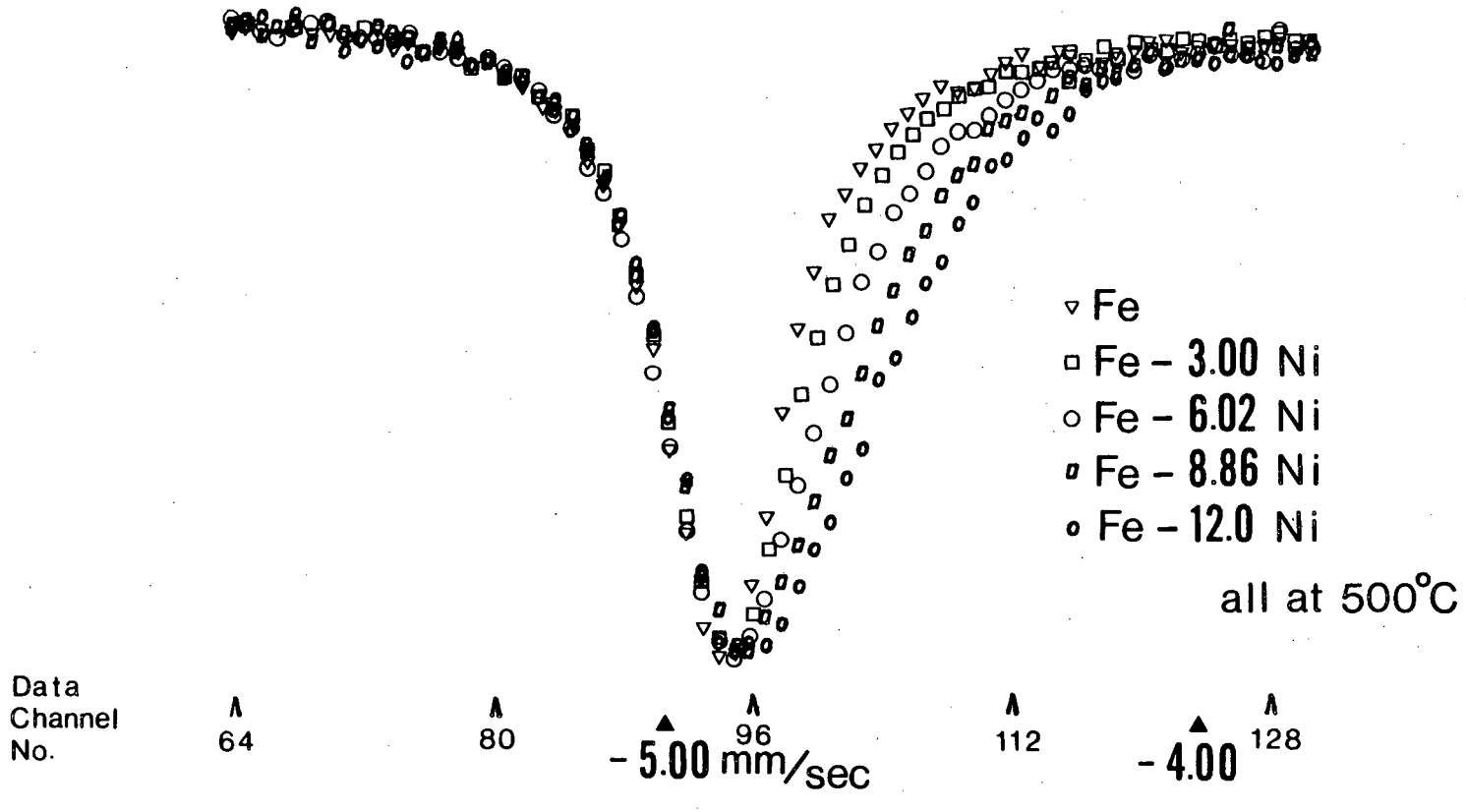


XBL 818-11238

Figure 17

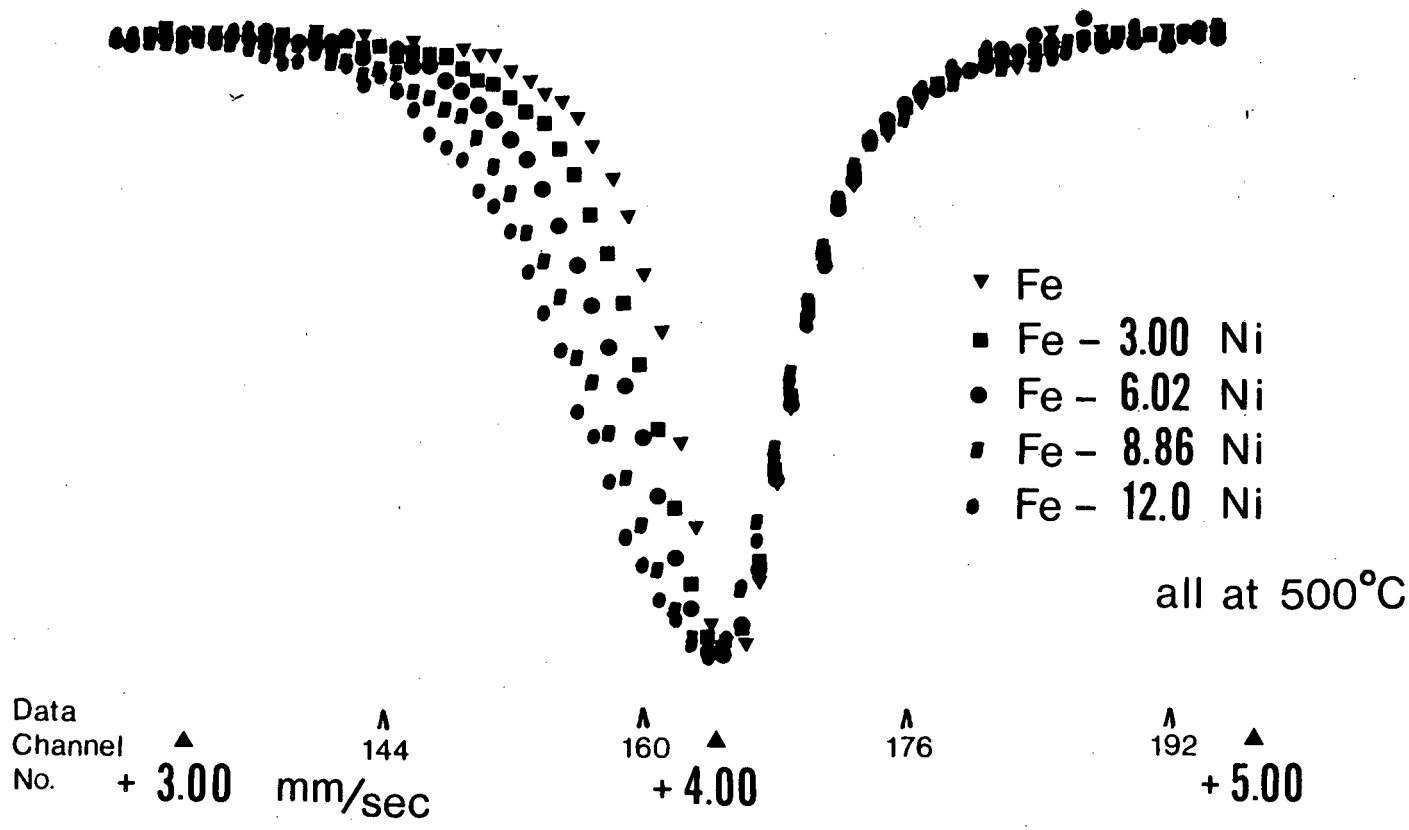


XBL 818-11239

Figure 18

Temperature Dependence of Spectra from Fe-9Ni

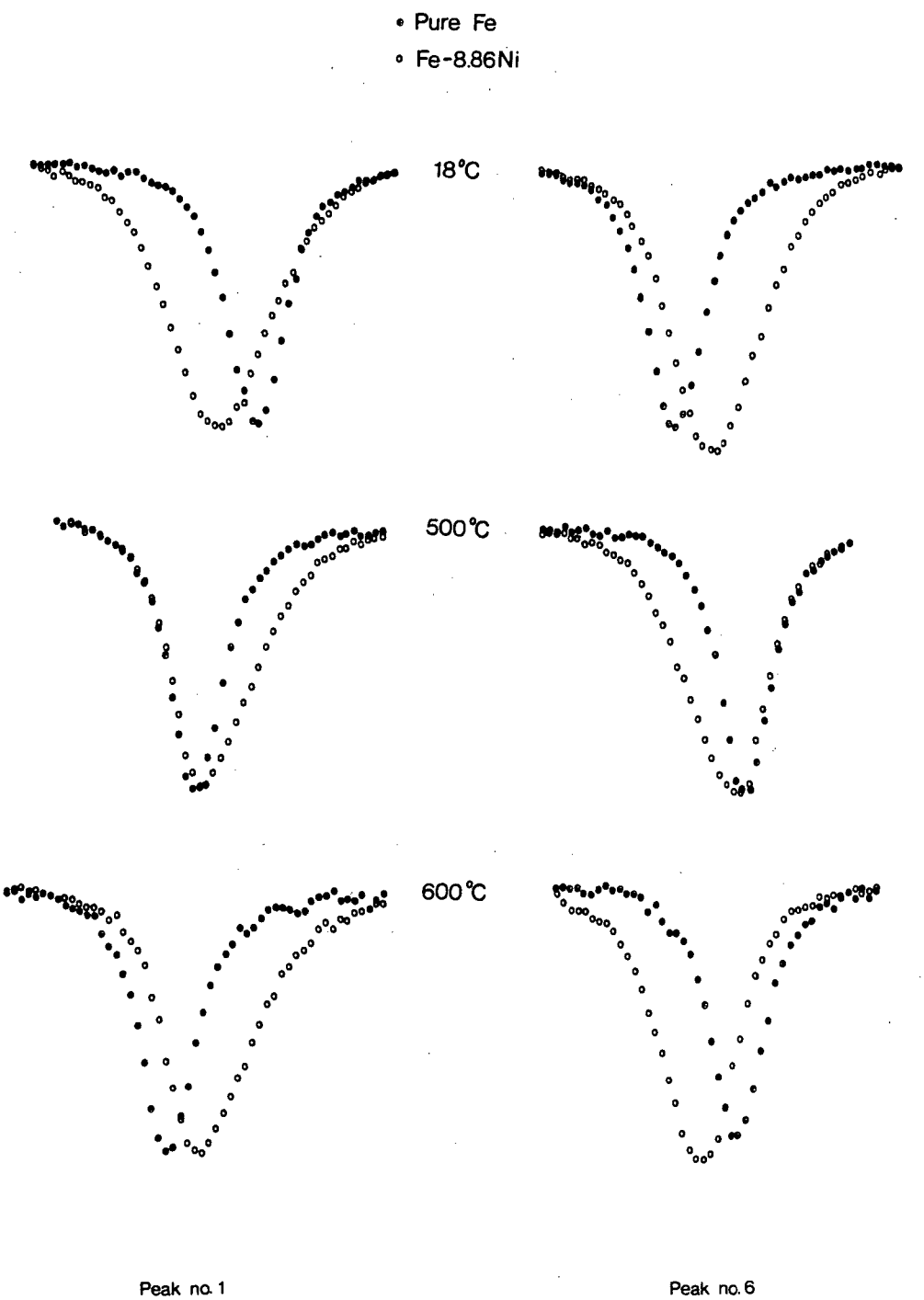


XBL 828-10887

Figure 19

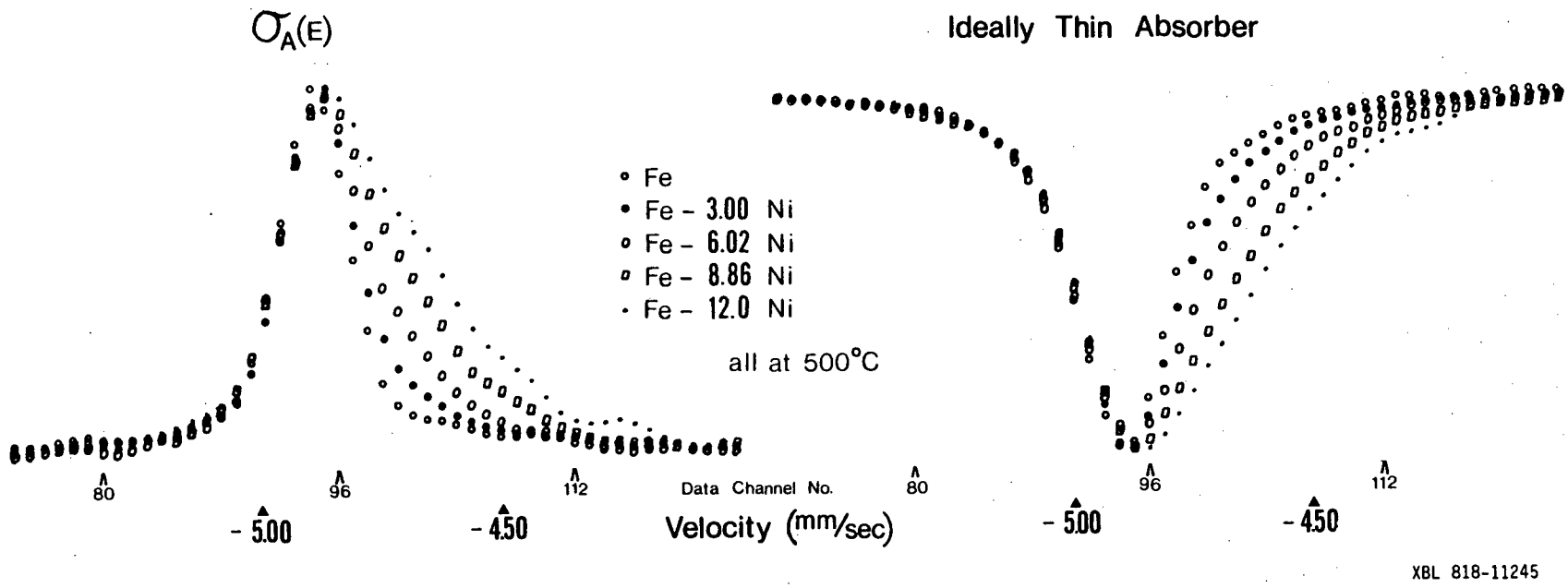
$\sigma_A(E)$
Ideally Thin Absorber
Fe
Fe - 3.00 Ni
Fe - 6.02 Ni
Fe - 8.86 Ni
Fe - 12.0 Ni
all at 500°C
80
96
112
Data Channel No.
80
96
112
- 5.00
- 4.50
Velocity (mm/sec)
- 5.00
- 4.50
XBL 818-11245

Figure 20

Hyperfine Structure in Binary Fe-Ni Alloys

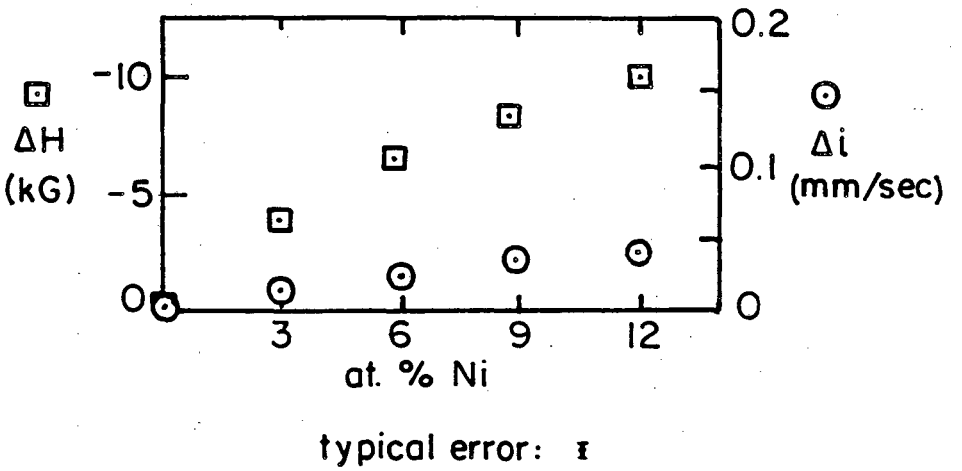


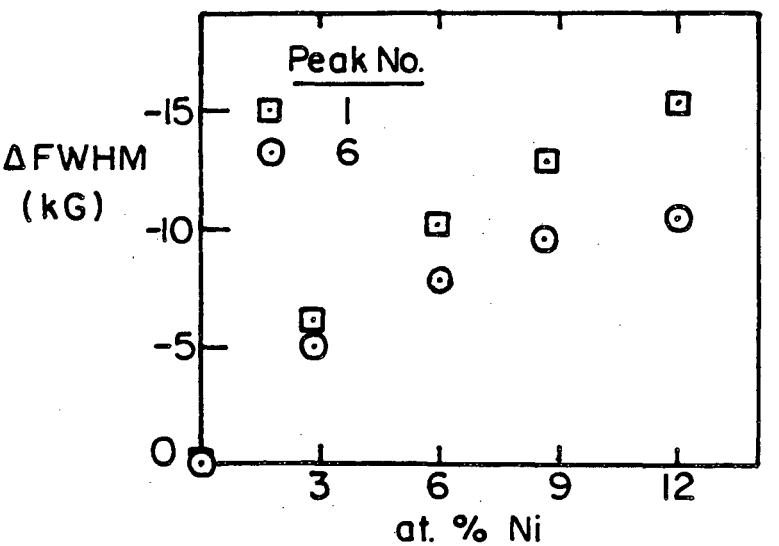


XBL 828-6424

Figure 21

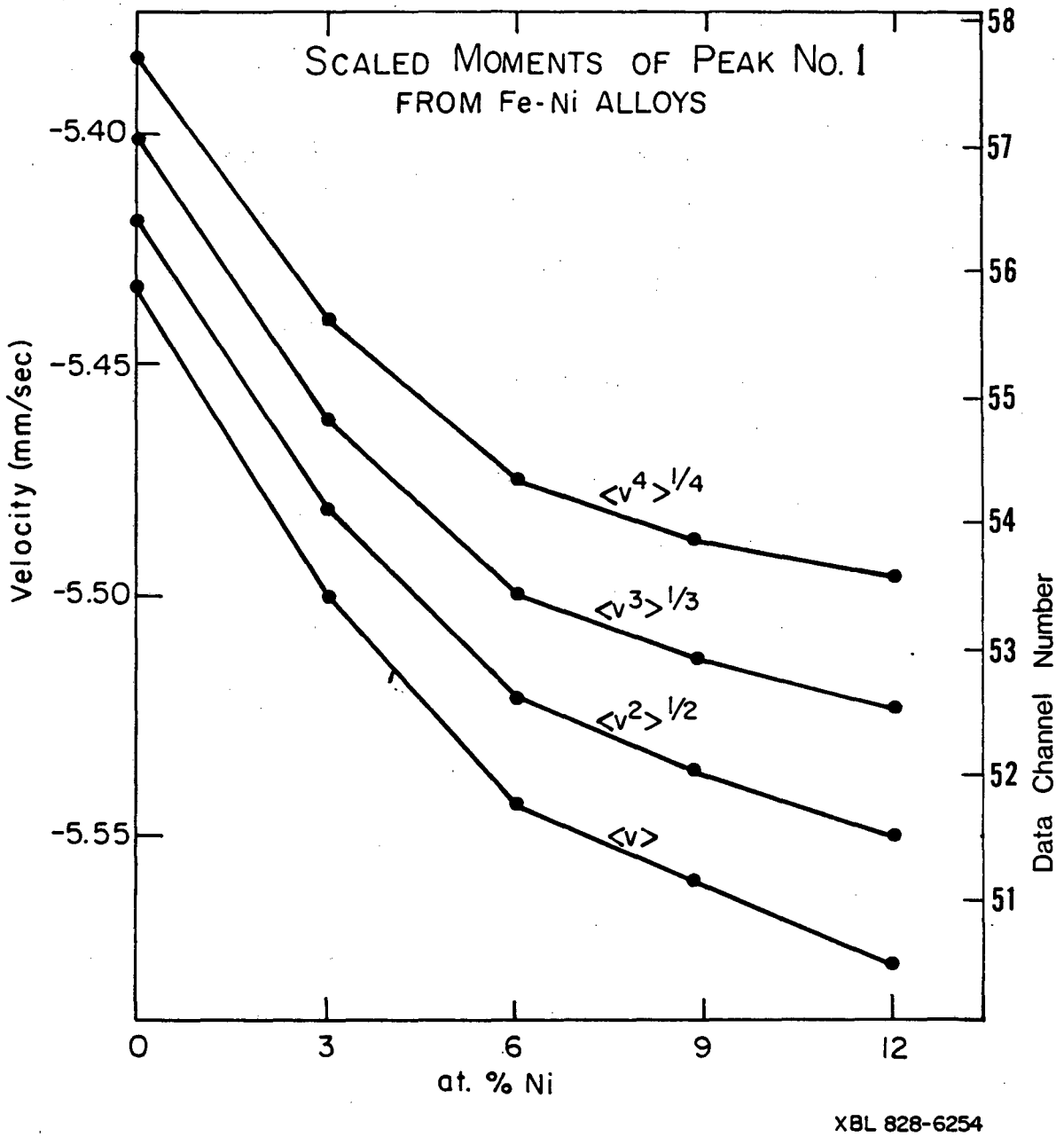
SCALED MOMENTS OF PEAK NO. 1
FROM Fe-Ni ALLOYS
-5.40
-5.45
-5.50
-5.55
Velocity (mm/sec)
58
57
56
55
54
53
52
51
Data Channel Number
<v4>1/4
<v3>1/3
<v2>1/2
<v>
0
3
6
9
12
at. % Ni
XBL 828-6254

Figure 22

Carbon Effects in

Backscatter 14.41 keV Spectra

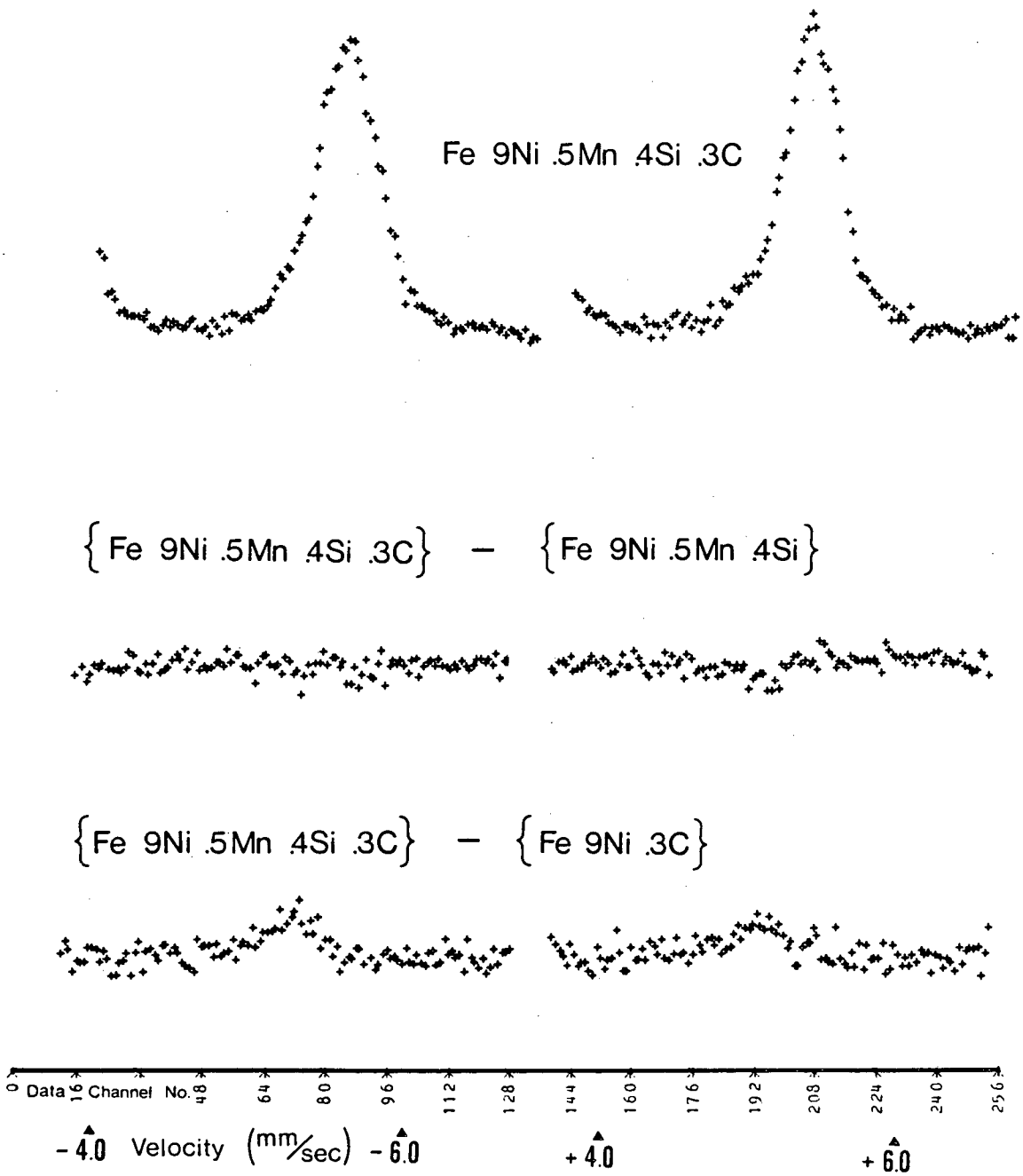


Spectra at 18°C

XBL 828-10879

Figure 23

Carbon Effects in Fe 9Ni .3C

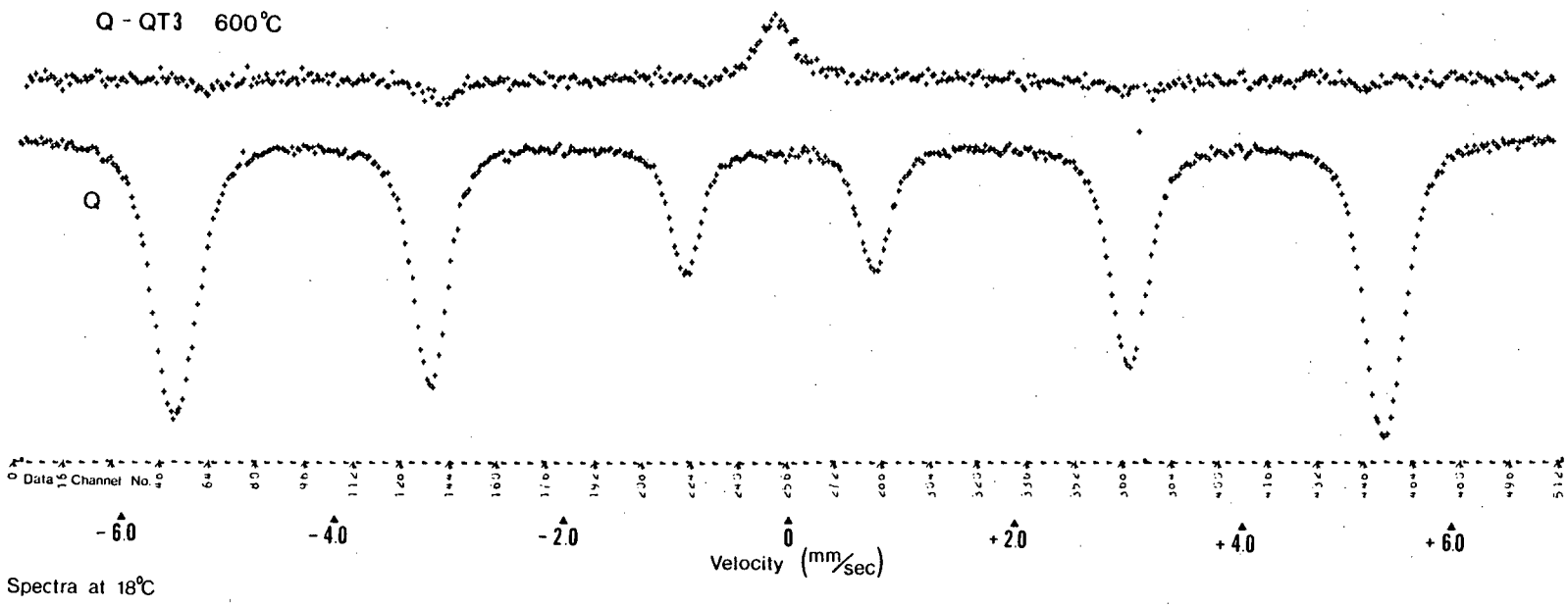


Spectra at 18°C

XBL 828-10884

Figure 24

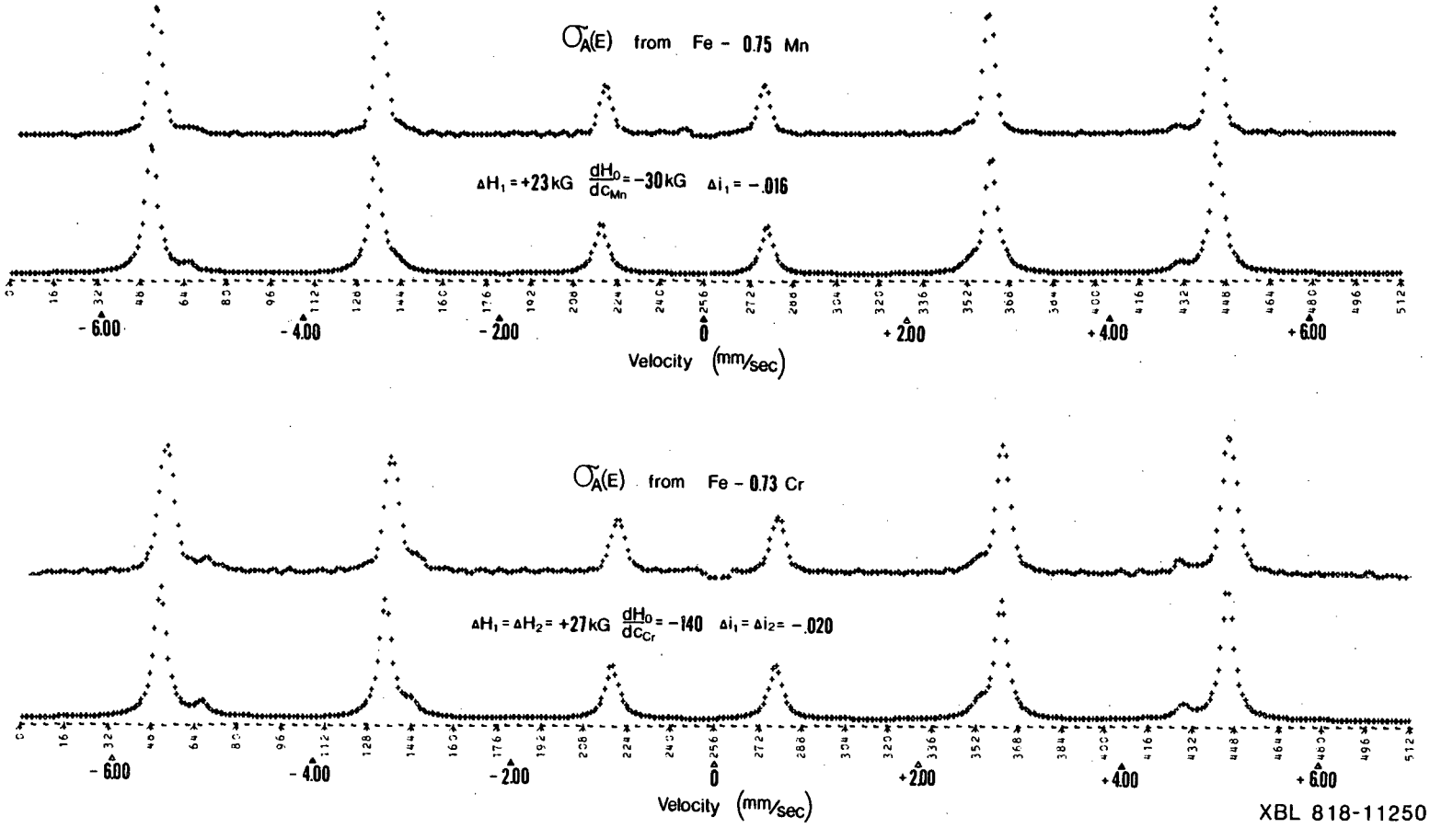


XBL 818-11250

Figure 25

"CR AND MN SATELLITES" FE - 8.9 Ni AT 500°C

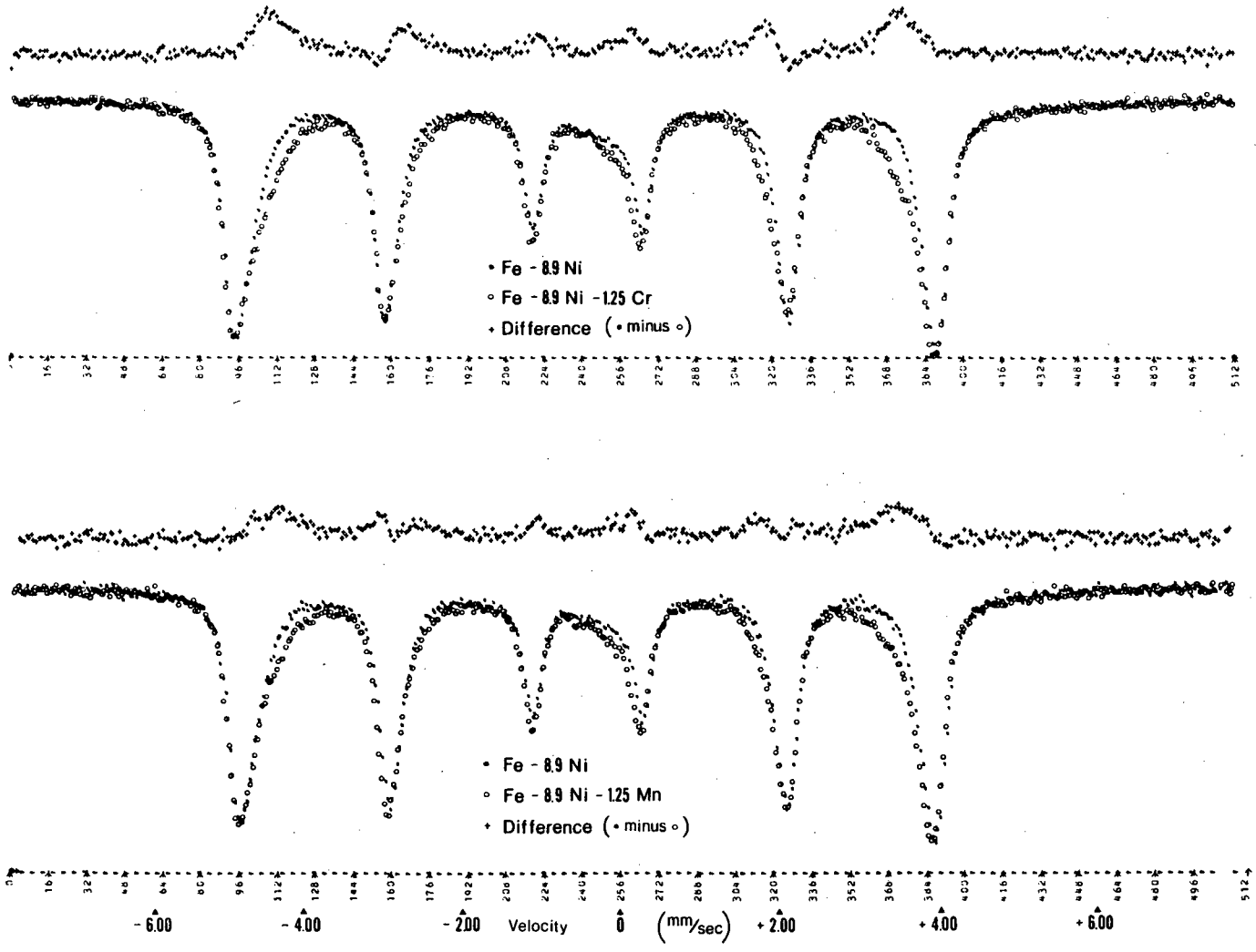


XBL 818-11251

Figure 26

"Cr Satellites" from Fe-X Ni-0.75 Cr

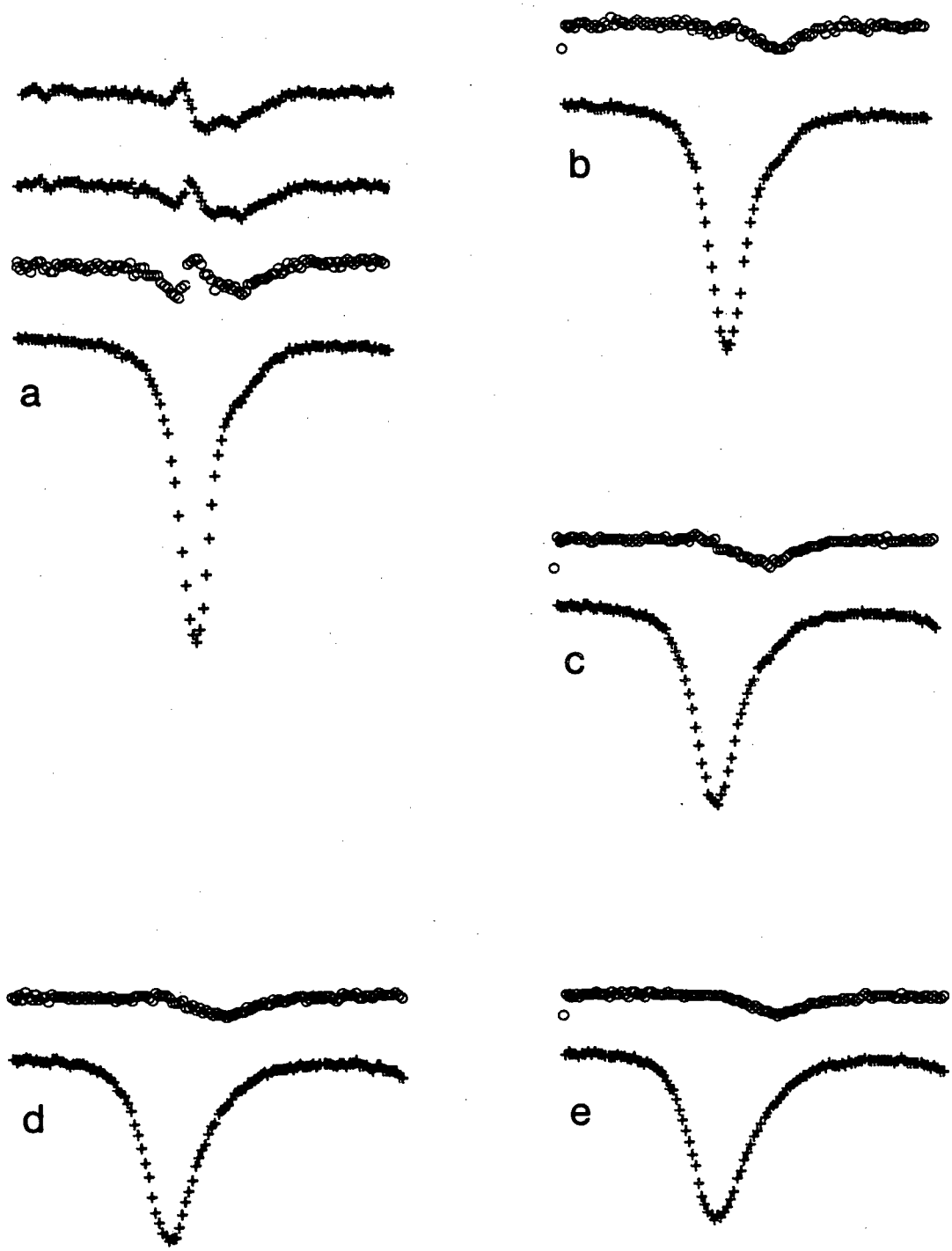


XBL 818-11236

Figure 27

"Mn Satellites" from Fe-X Ni-0.75 Mn

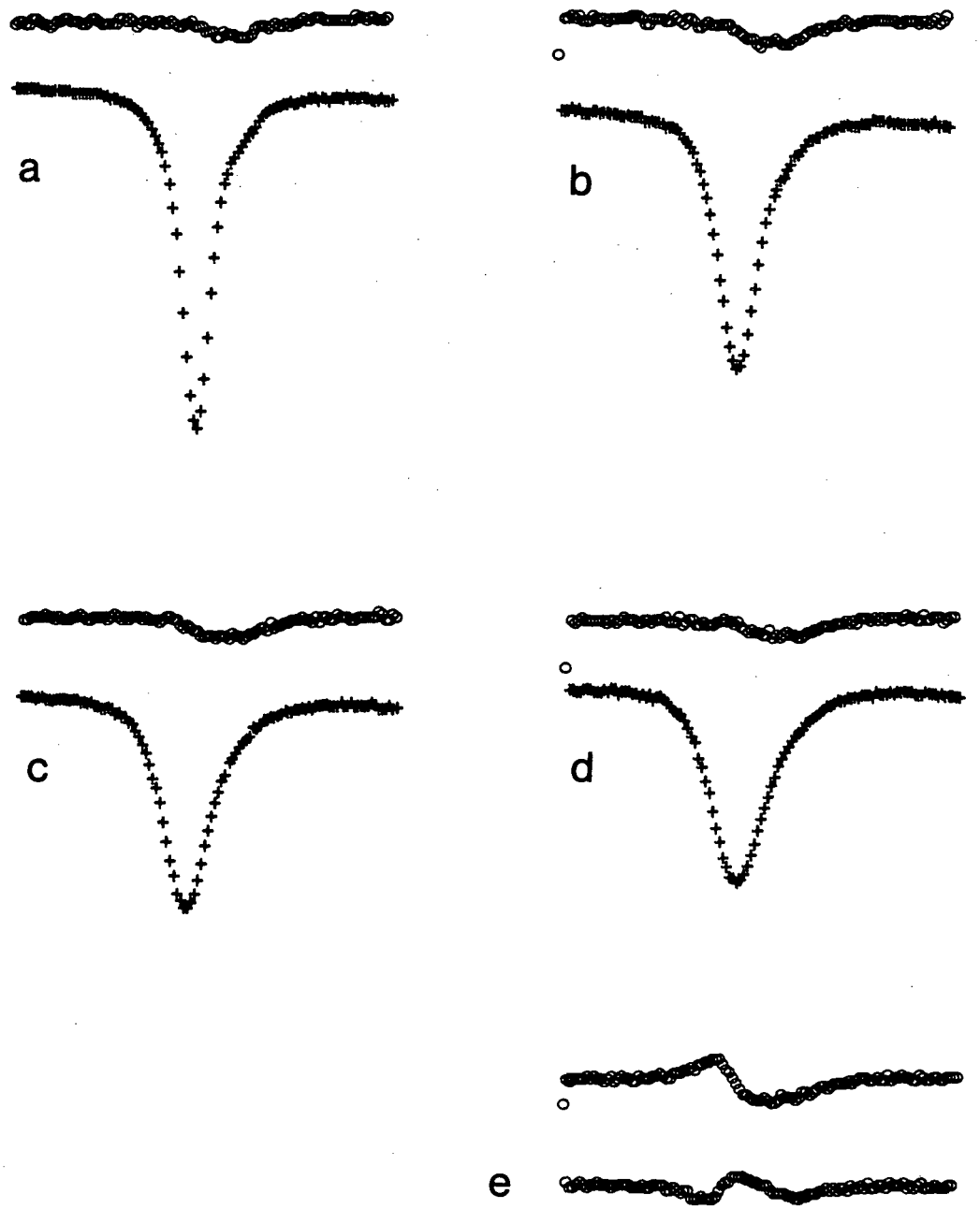


XBL 818-11237

Figure 28

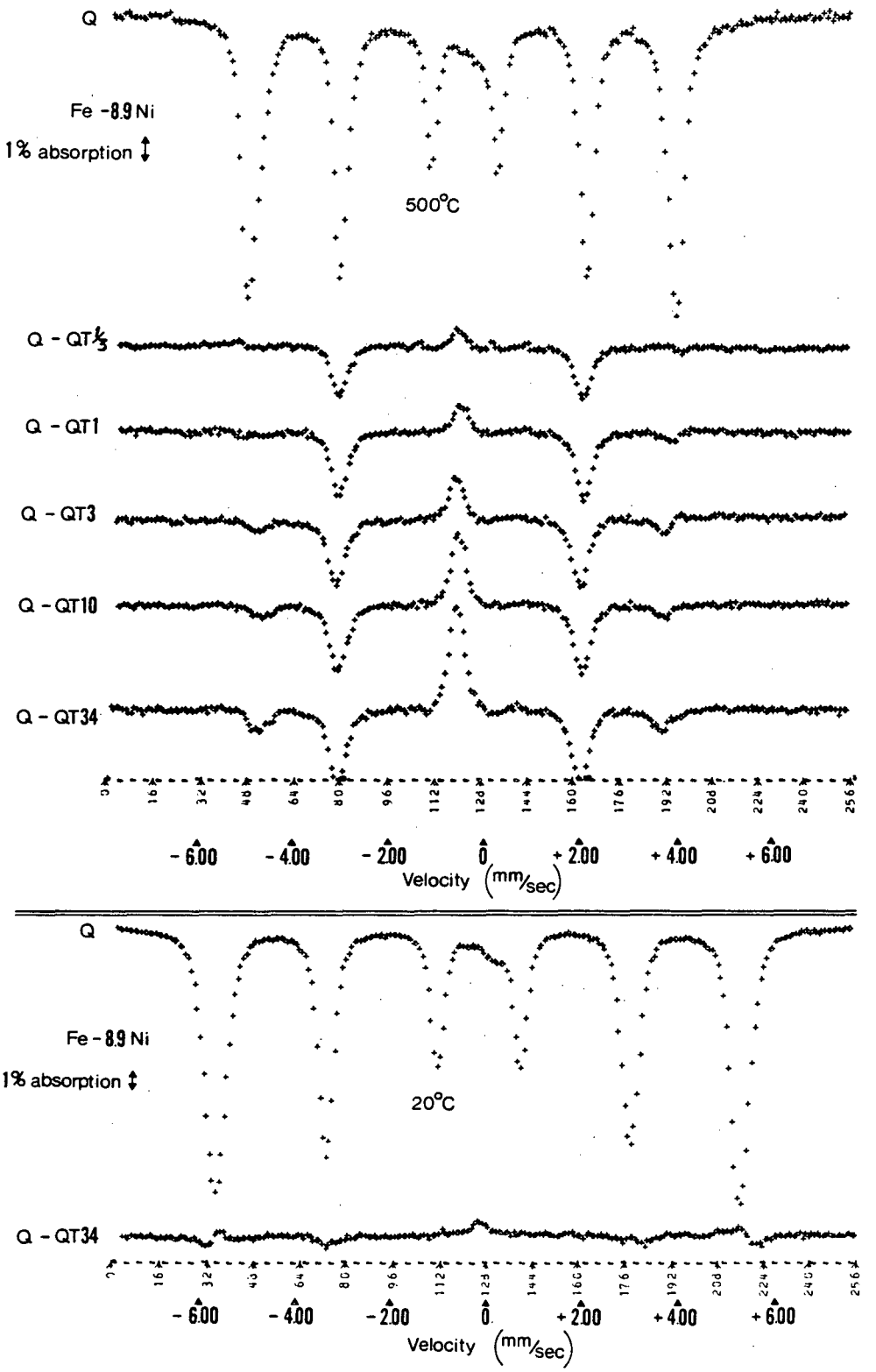


XBL 818-11252

Figure 29

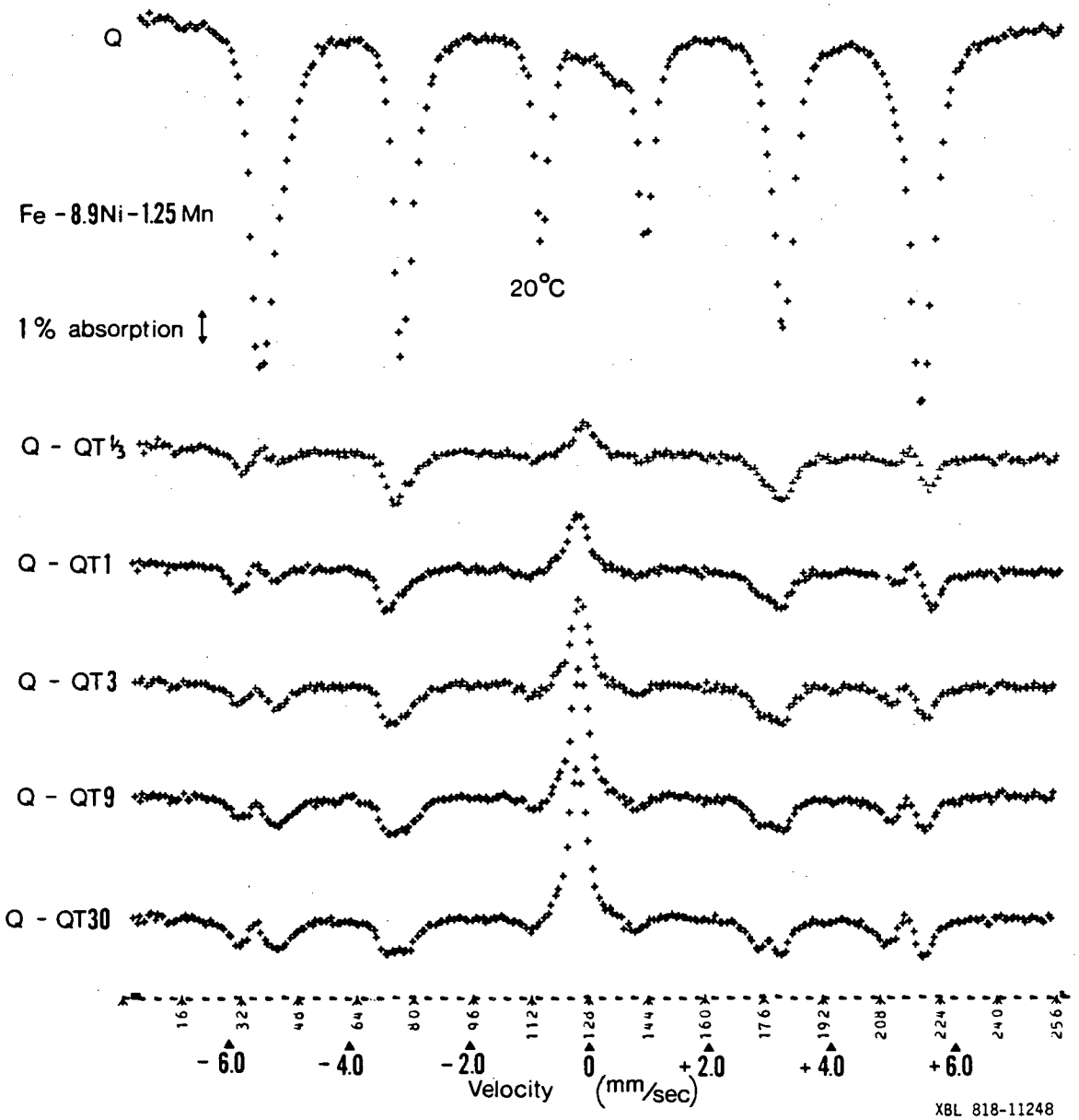
Q
Fe - 8.9Ni - 1.25 Mn
20°C
1 % absorption
Q - QT⅓
Q - QT1
Q - QT3
Q - QT9
Q - QT30
16
32
48
64
80
96
112
128
144
160
176
192
208
224
240
256
- 6.0
- 4.0
- 2.0
0
+ 2.0
+ 4.0
+ 6.0
Velocity (mm/sec)
XBL 818-11248

Figure 30

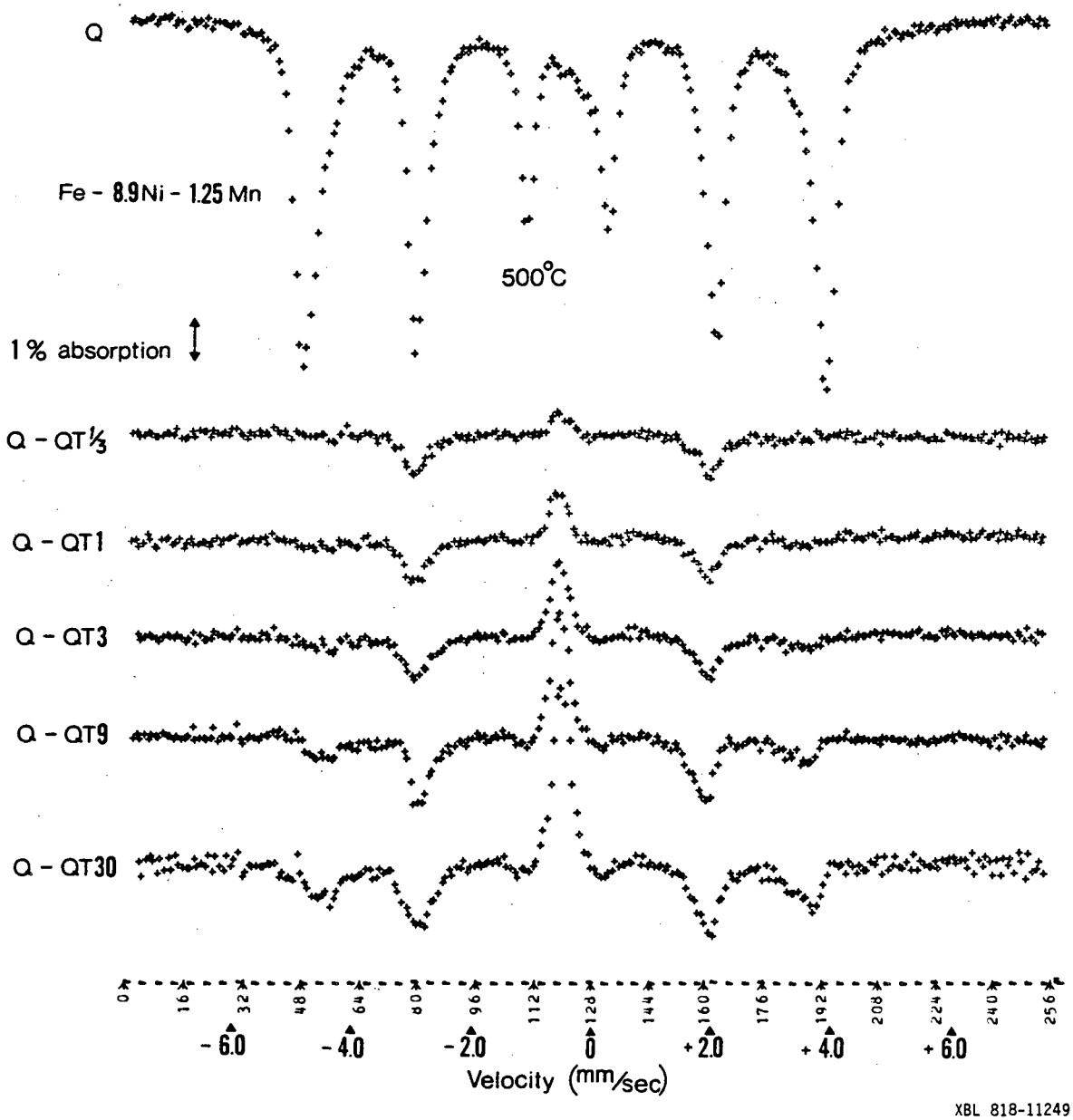
Q
Fe - 8.9Ni - 1.25 Mn
500°C
1 % absorption
Q - QT⅓
Q - QT1
Q - QT3
Q - QT9
Q - QT30
0
16
32
48
64
80
96
112
128
144
160
176
192
208
224
240
256
- 6.0
- 4.0
- 2.0
0
+ 2.0
+ 4.0
+ 6.0
Velocity (mm/sec)
XBL 818-11249

Figure 31

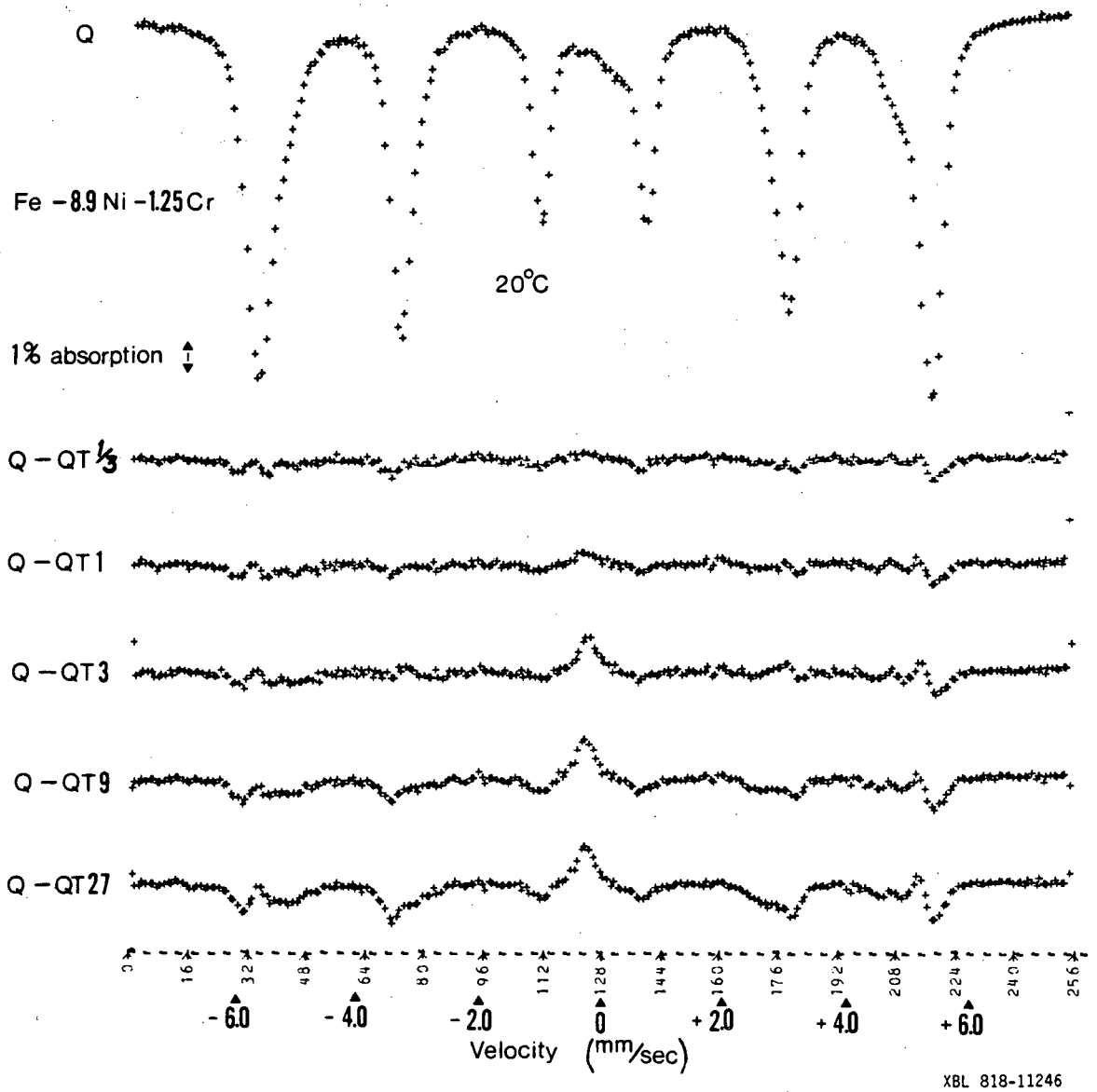
Q
Fe -8.9 Ni -1.25 Cr
20°C
1% absorption
Q - QT 1/3
Q - QT 1
Q - QT 3
Q - QT 9
Q - QT 27
0
16
32
48
64
80
96
112
128
144
160
176
192
208
224
240
256
- 6.0
- 4.0
- 2.0
0
+ 2.0
+ 4.0
+ 6.0
Velocity (mm/sec)
XBL 818-11246

Figure 32

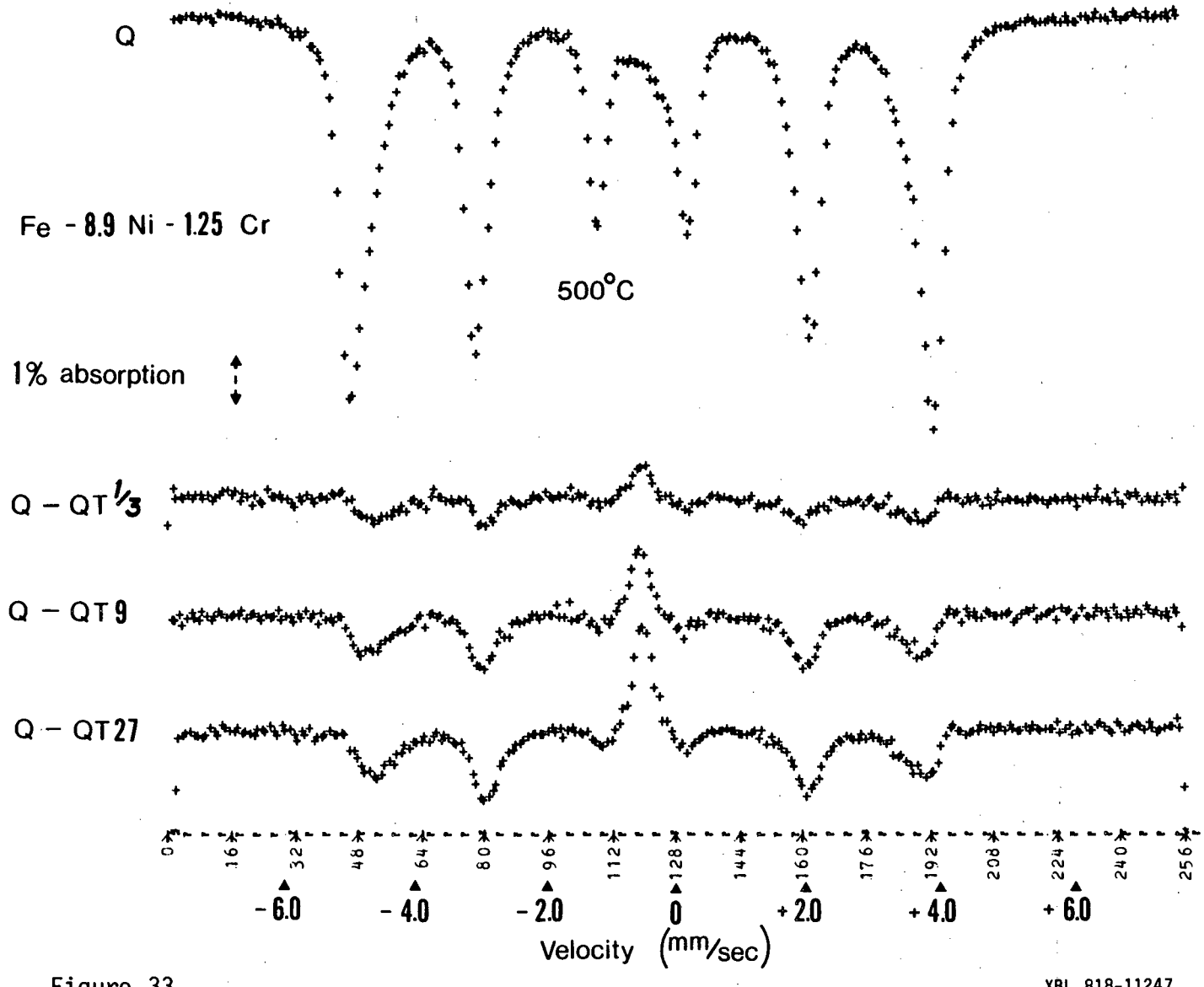


Figure 33

XBL 818-11247

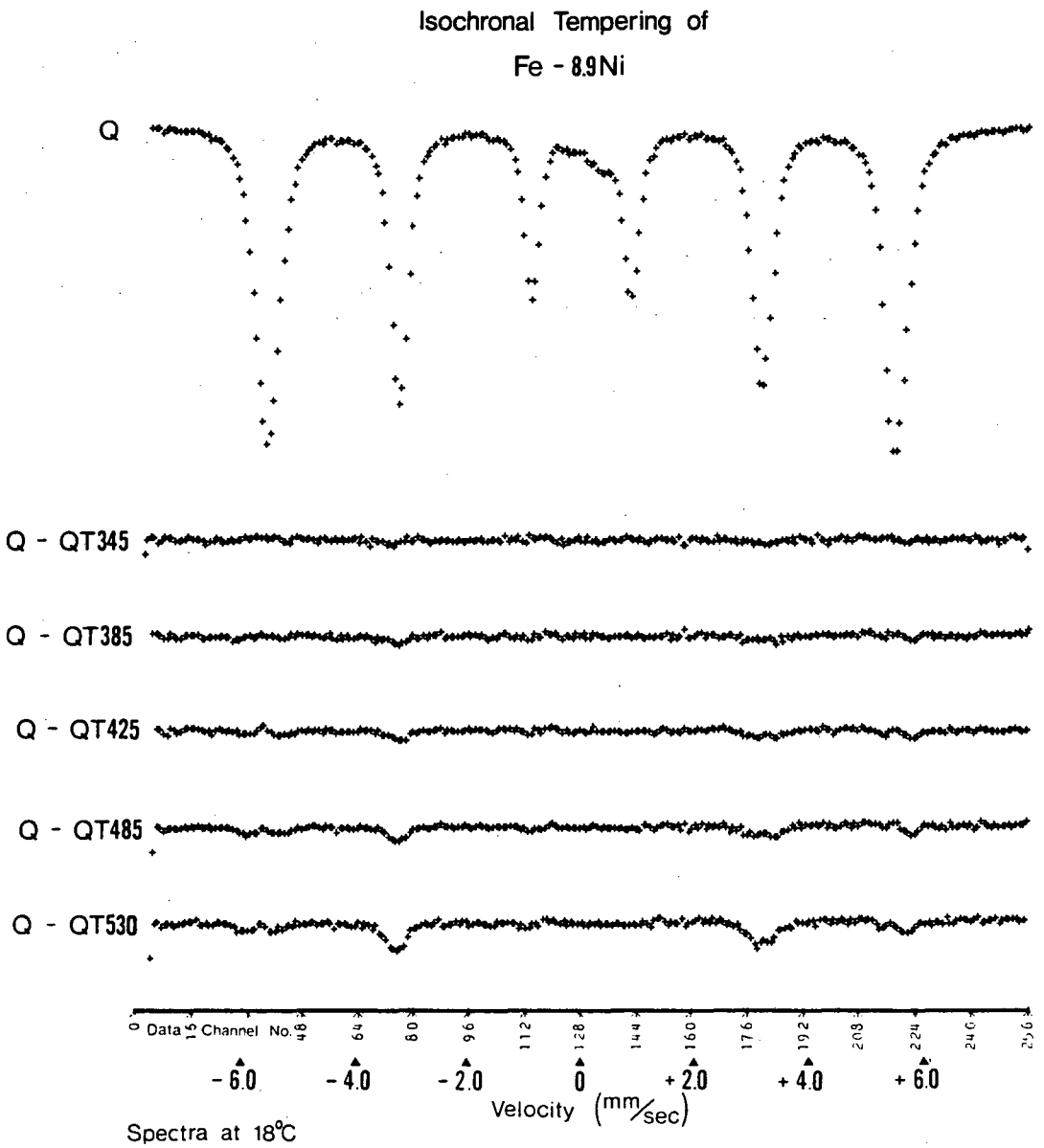


XBL 828-10875

Figure 34

Magnetic Orientation and

Anisotropic Hyperfine Magnetic Field Perturbations

in Fe - 8.9 Ni

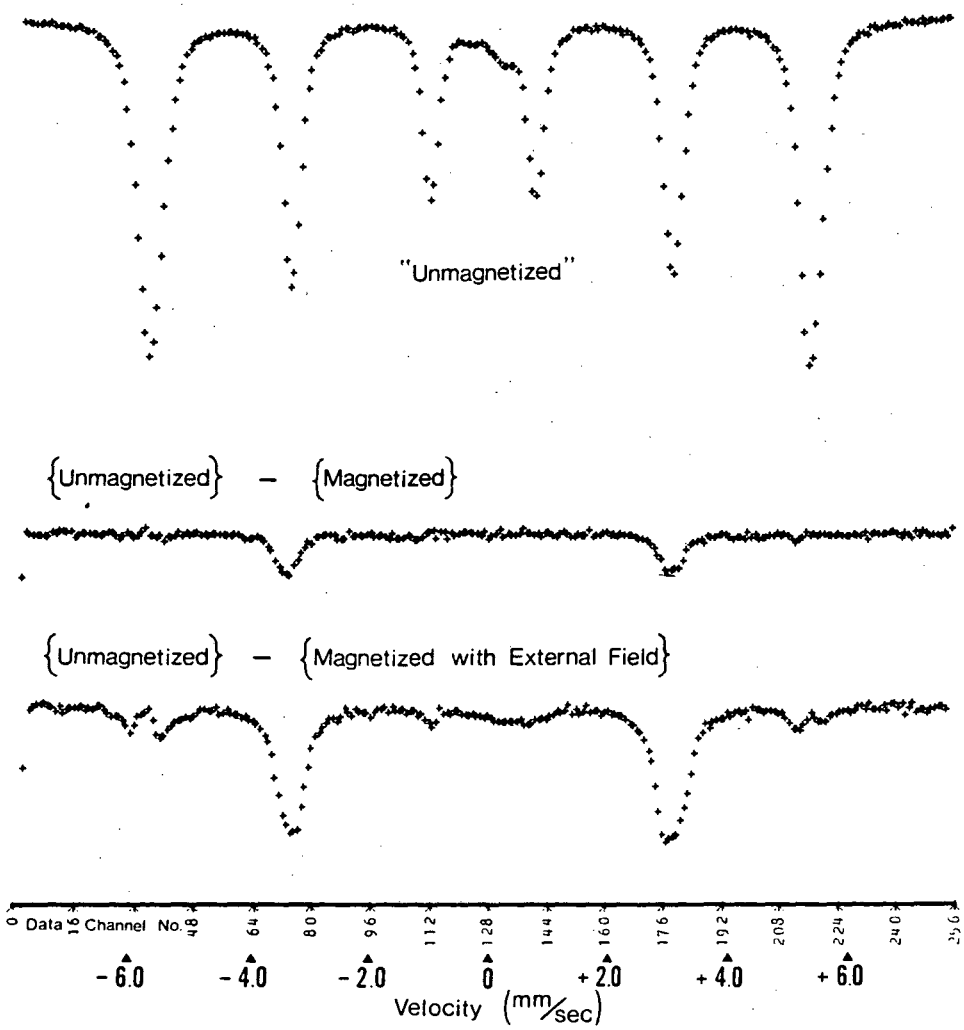


Spectra at 18°C

XBL 828-10876

Figure 35

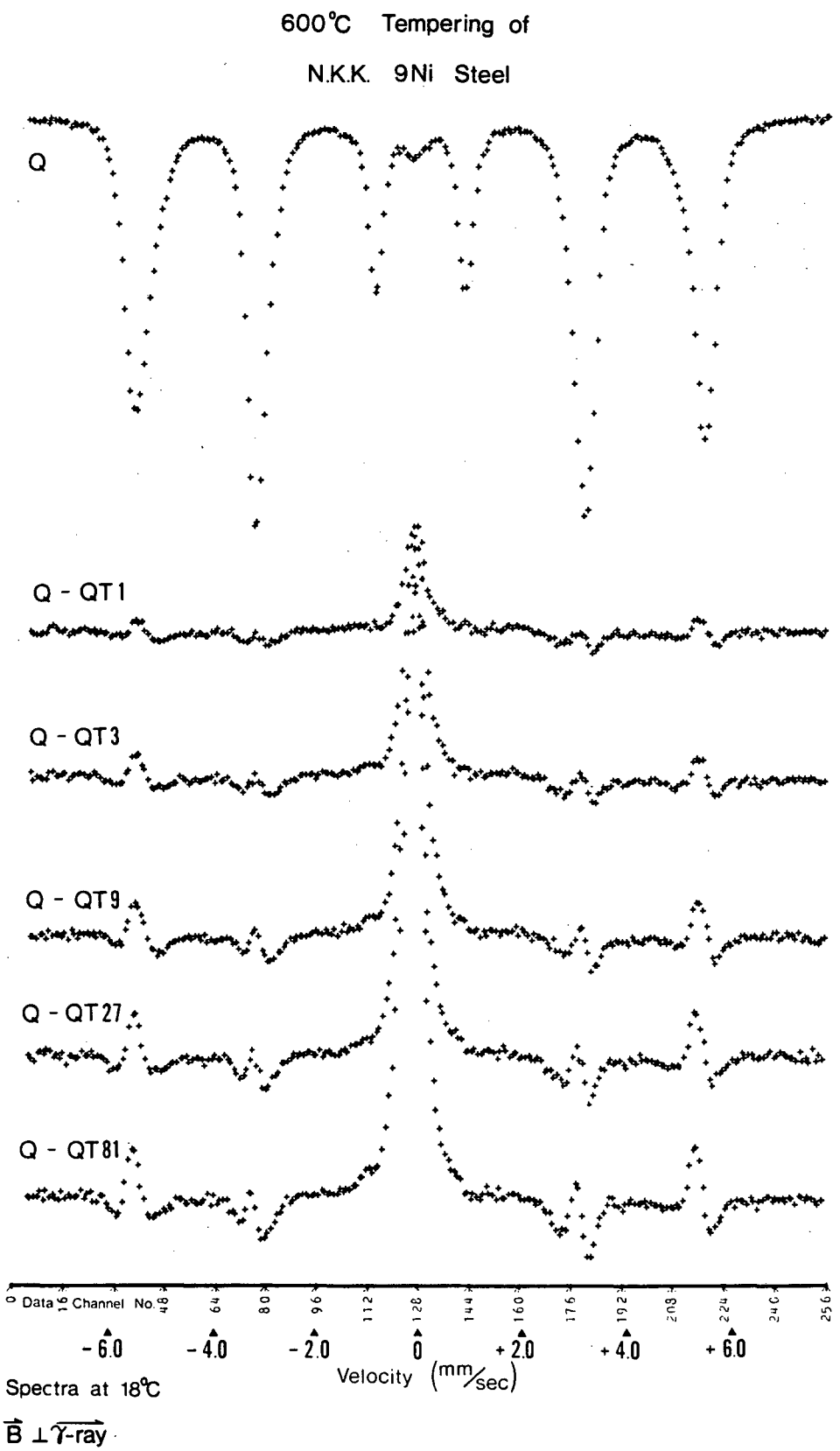


XBL 828-10871

Figure 36

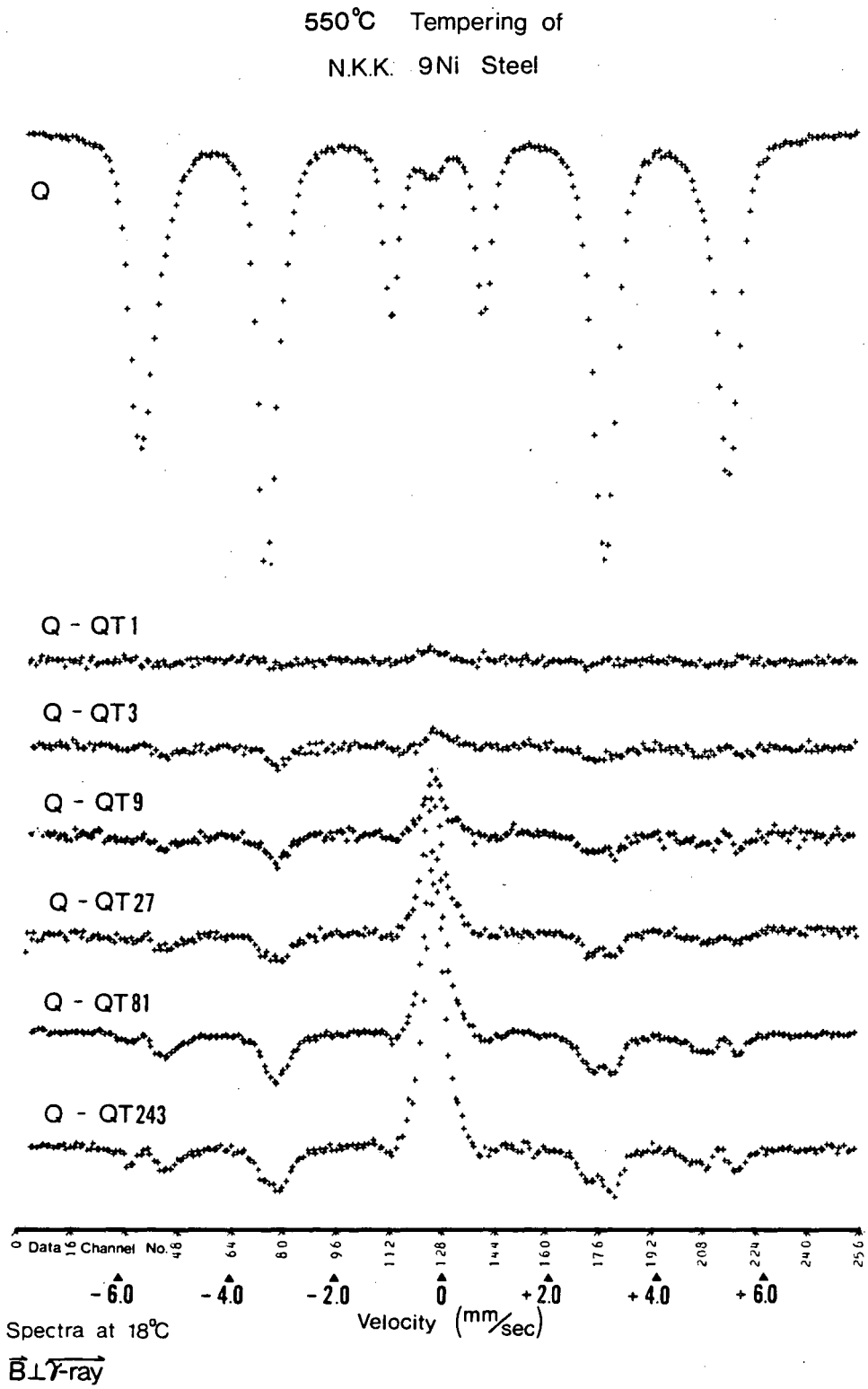


XBL 828-10870

Figure 37

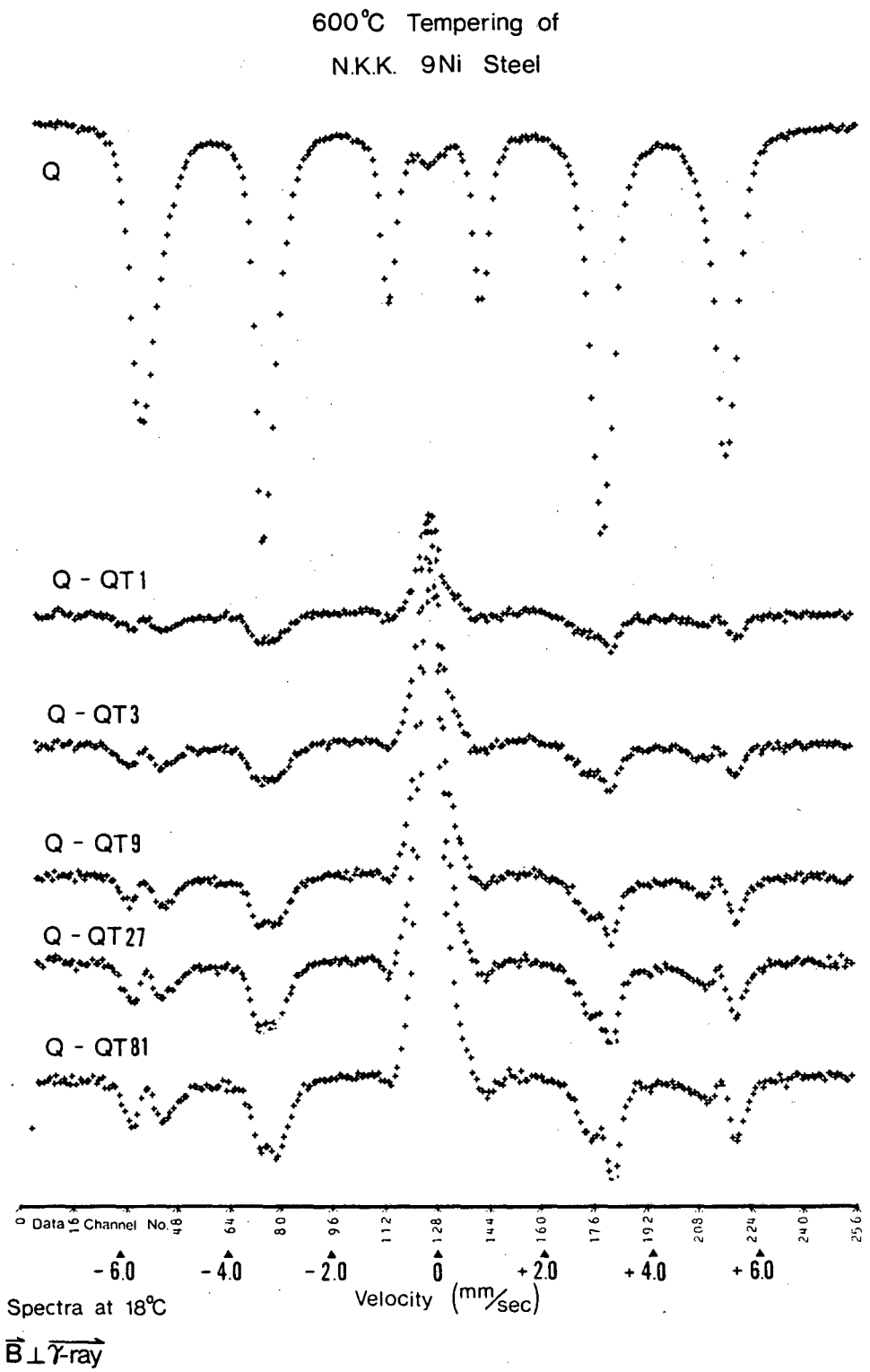
600°C Tempering of
N.K.K. 9Ni Steel
Q
Q - QT1
Q - QT3
Q - QT9
Q - QT27
Q - QT81
0 Data 16 Channel No. 48 64 80 96 112 128 144 160 176 192 208 224 240 256
-6.0 -4.0 -2.0 0 +2.0 +4.0 +6.0
Velocity (mm/sec)
Spectra at 18°C
B⊥γ-ray
XBL 828-10872

Figure 38

630°C Tempering of

N.K.K. 9Ni Steel

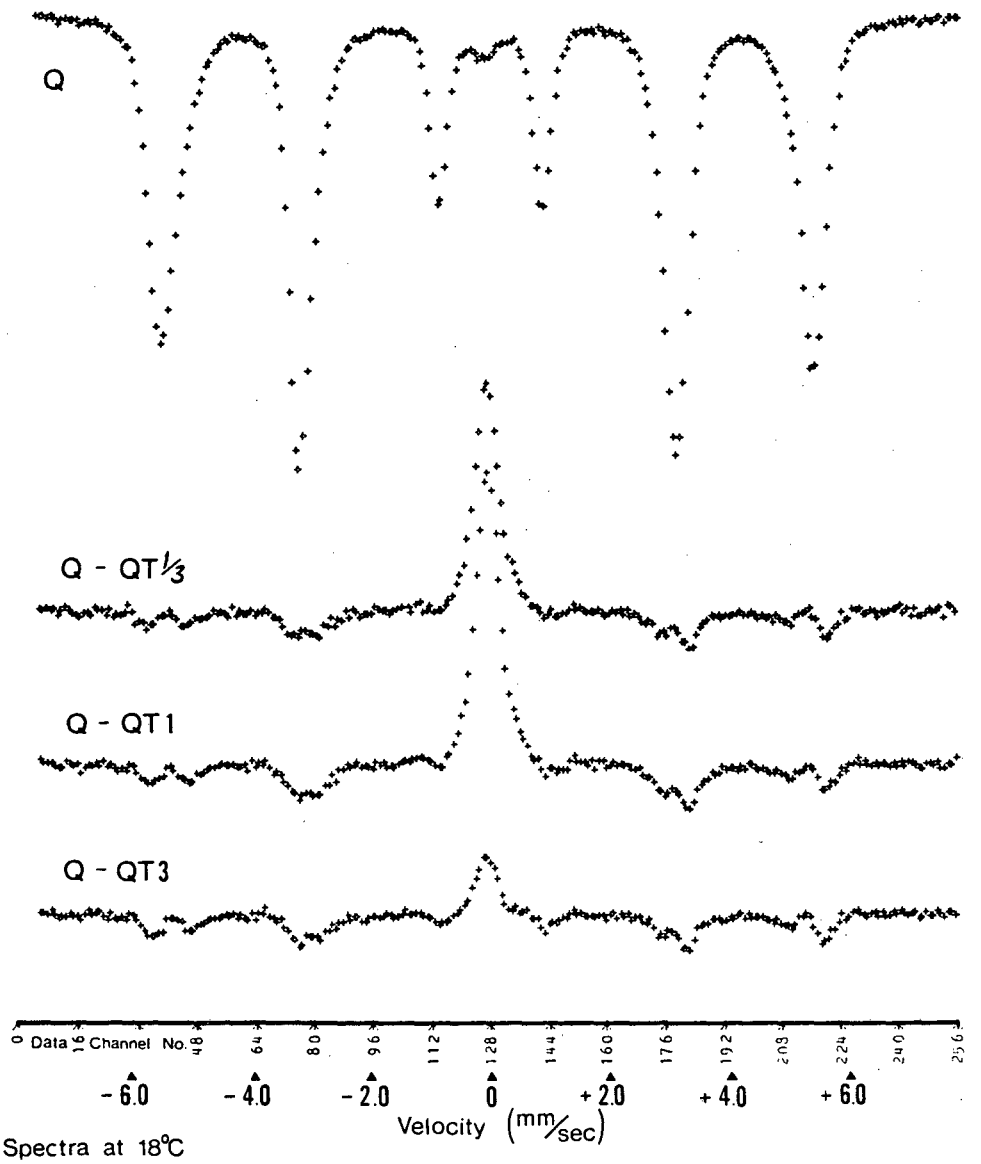


Spectra at 18°C

$\vec{B} \perp \vec{\gamma}$-ray

XBL 828-10873

Figure 39

Tempering of N.K.K. 9Ni Steel

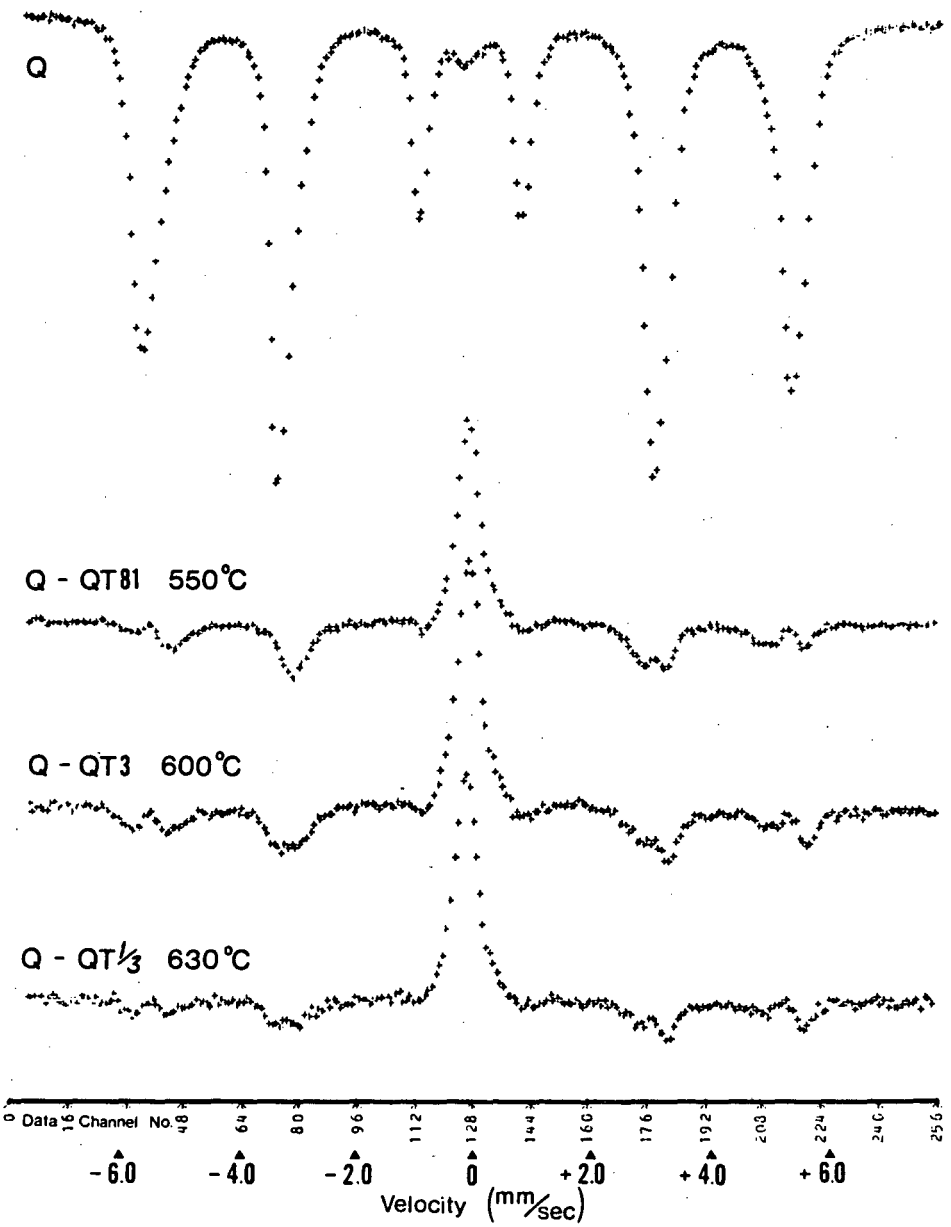


Spectra at 18°C

$\vec{B} \perp \vec{\gamma}$-ray

XBL 828-10874

Figure 40

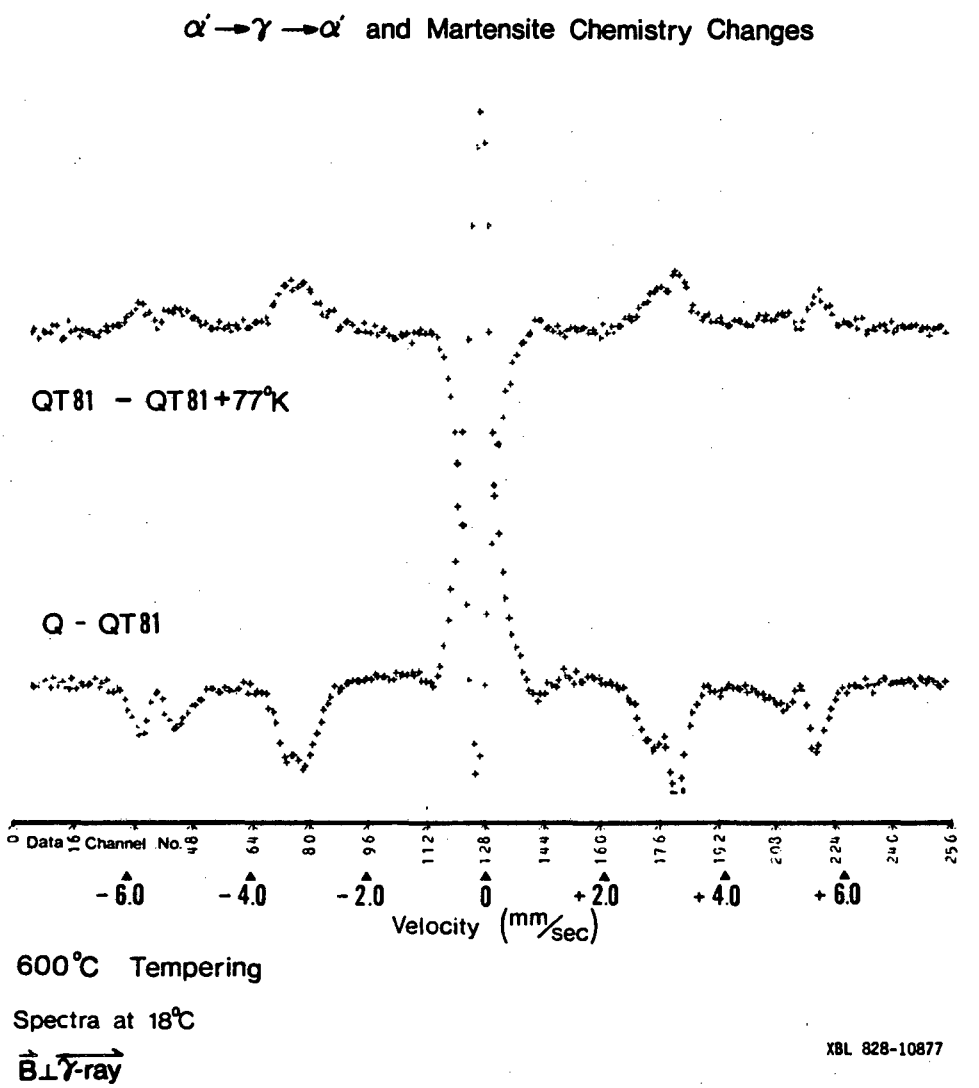
α′→γ→α′ and Martensite Chemistry Changes
QT81 − QT81+77°K
Q - QT81
0 Data 16 Channel No. 48 64 80 96 112 128 144 160 176 192 208 224 240 256
-6.0 -4.0 -2.0 0 +2.0 +4.0 +6.0
Velocity (mm/sec)
600°C Tempering
Spectra at 18°C
B⊥γ-ray
XBL 828-10877

Figure 41

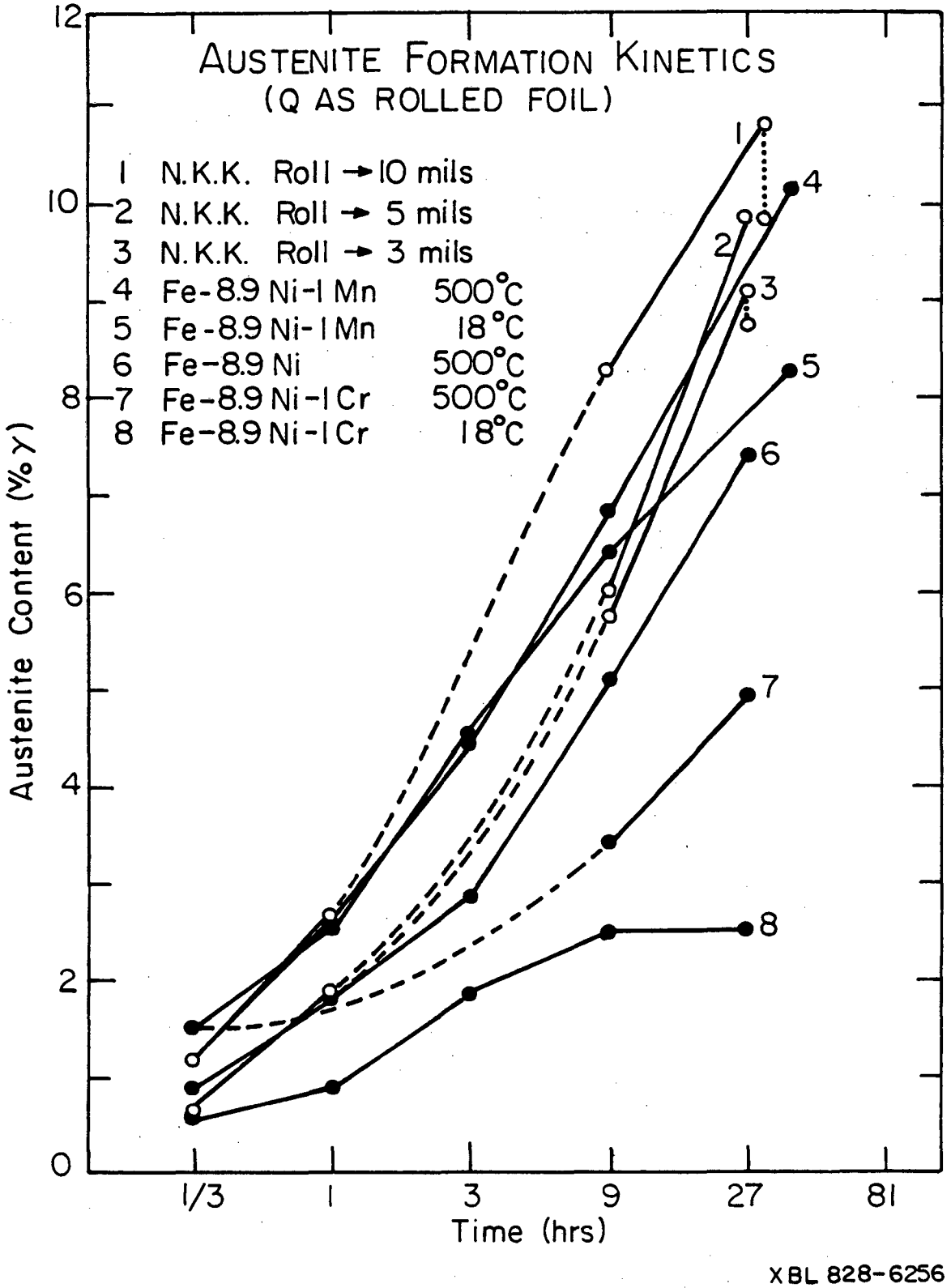
AUSTENITE FORMATION KINETICS
(Q AS ROLLED FOIL)
1 N.K.K. Roll → 10 mils
2 N.K.K. Roll → 5 mils
3 N.K.K. Roll → 3 mils
4 Fe-8.9 Ni-1 Mn 500°C
5 Fe-8.9 Ni-1 Mn 18°C
6 Fe-8.9 Ni 500°C
7 Fe-8.9 Ni-1 Cr 500°C
8 Fe-8.9 Ni-1 Cr 18°C
Austenite Content (% γ)
0
2
4
6
8
10
12
1/3
1
3
9
27
81
Time (hrs)
XBL 828-6256

Figure 42

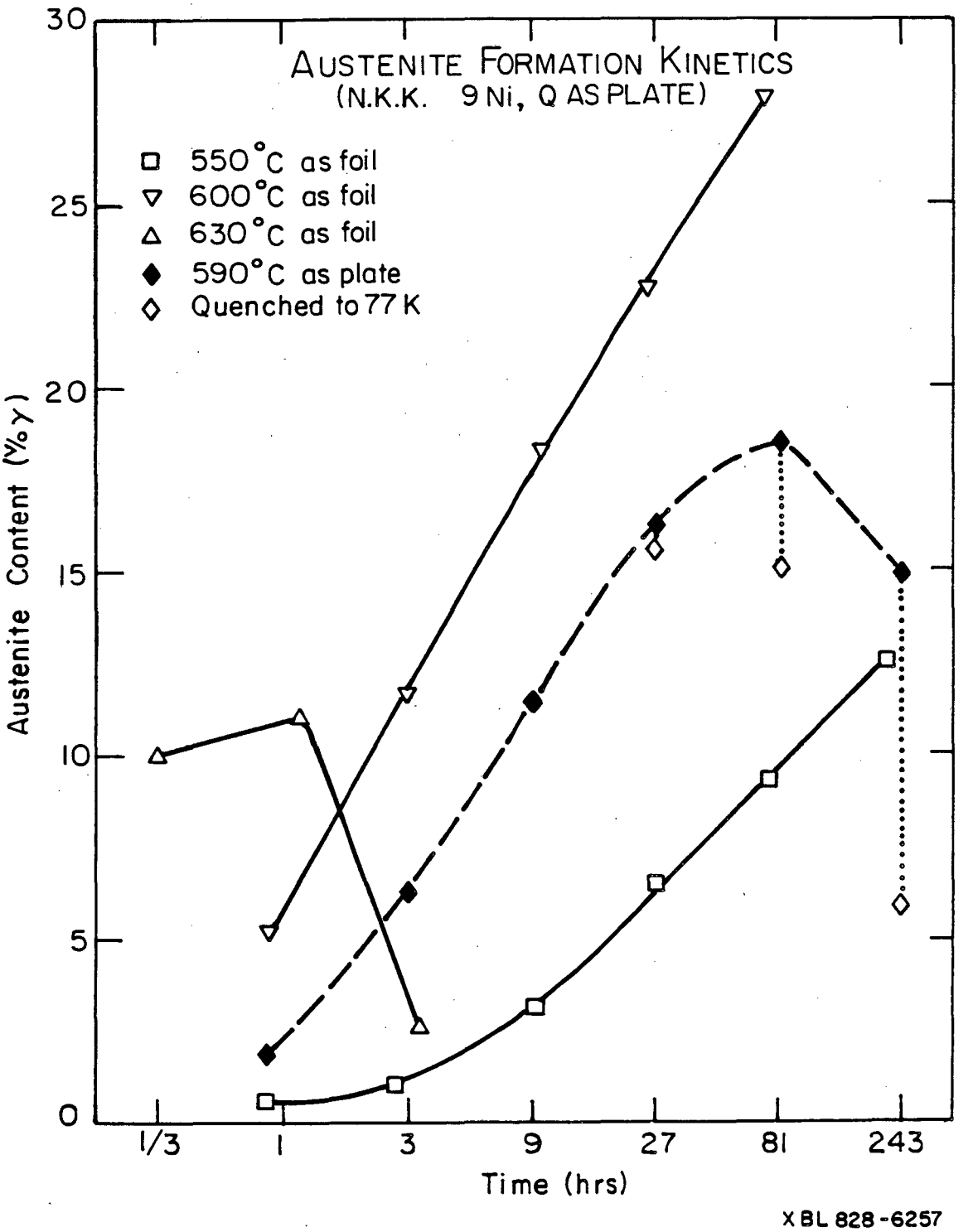
AUSTENITE FORMATION KINETICS
(N.K.K. 9 Ni, Q AS PLATE)
550°C as foil
600°C as foil
630°C as foil
590°C as plate
Quenched to 77 K
Austenite Content (% γ)
30
25
20
15
10
5
0
1/3
1
3
9
27
81
243
Time (hrs)
XBL 828-6257

Figure 43

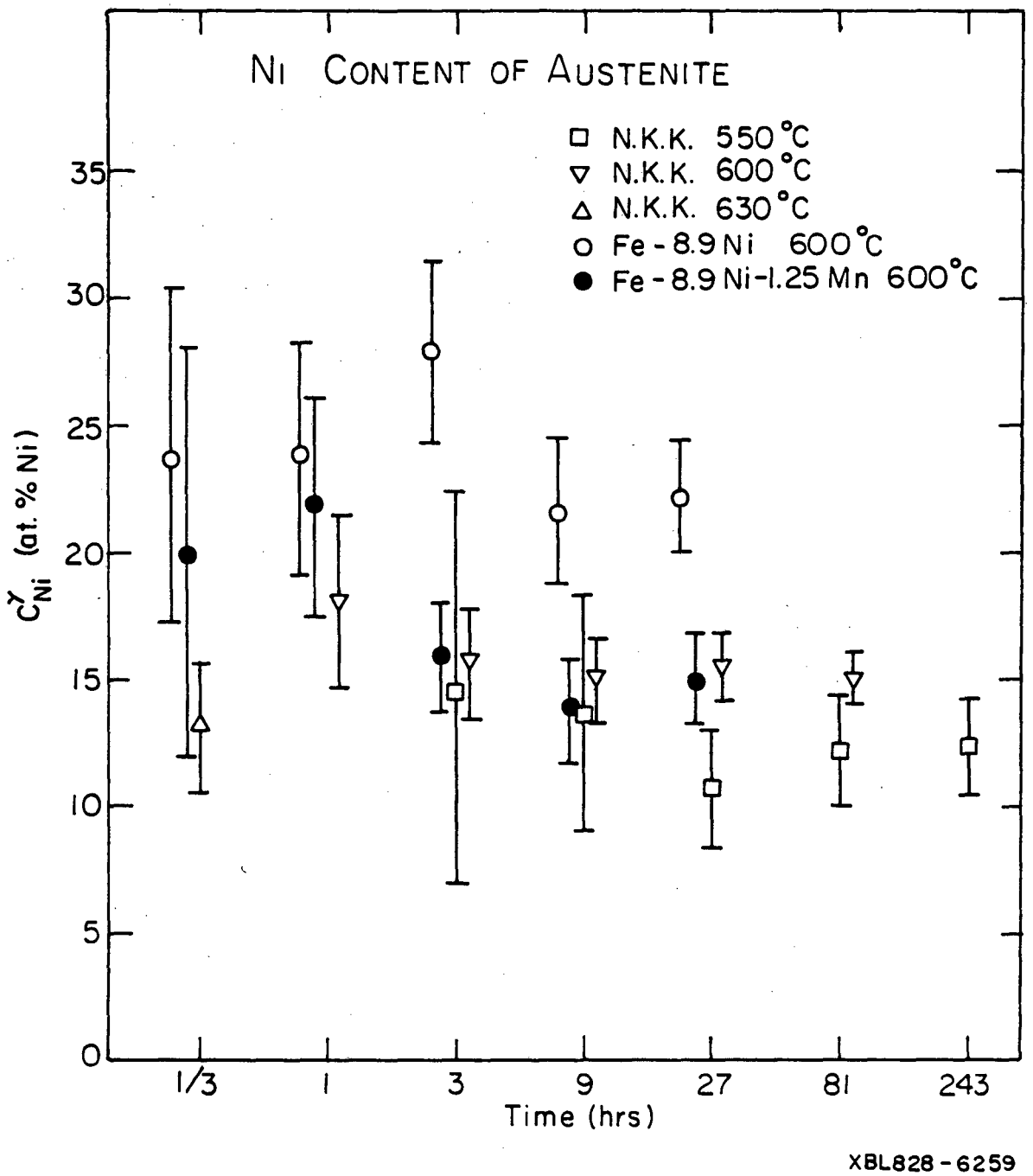
Ni Content of Austenite
N.K.K. 550°C
N.K.K. 600°C
N.K.K. 630°C
Fe-8.9 Ni 600°C
Fe-8.9 Ni-1.25 Mn 600°C
$C^{\gamma}_{Ni}$ (at. % Ni)
0
5
10
15
20
25
30
35
1/3
1
3
9
27
81
243
Time (hrs)
XBL828-6259

Figure 44

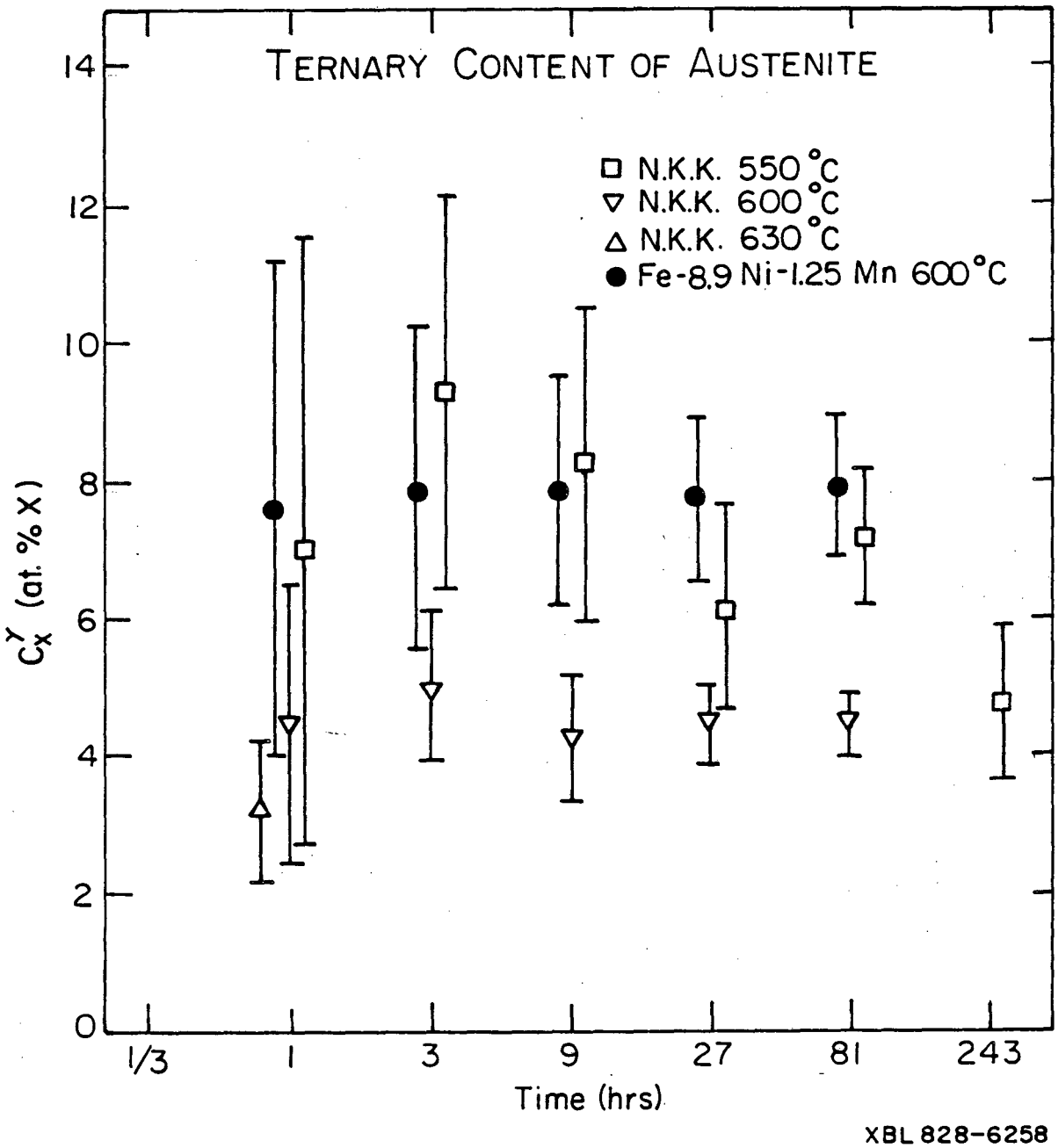
TERNARY CONTENT OF AUSTENITE
N.K.K. 550 °C
N.K.K. 600 °C
N.K.K. 630 °C
Fe-8.9 Ni-1.25 Mn 600 °C
$C_X^\gamma$ (at. % X)
0
2
4
6
8
10
12
14
1/3
1
3
9
27
81
243
Time (hrs)
XBL 828-6258

Figure 45

## NOTATION

Example: Fe 3d states

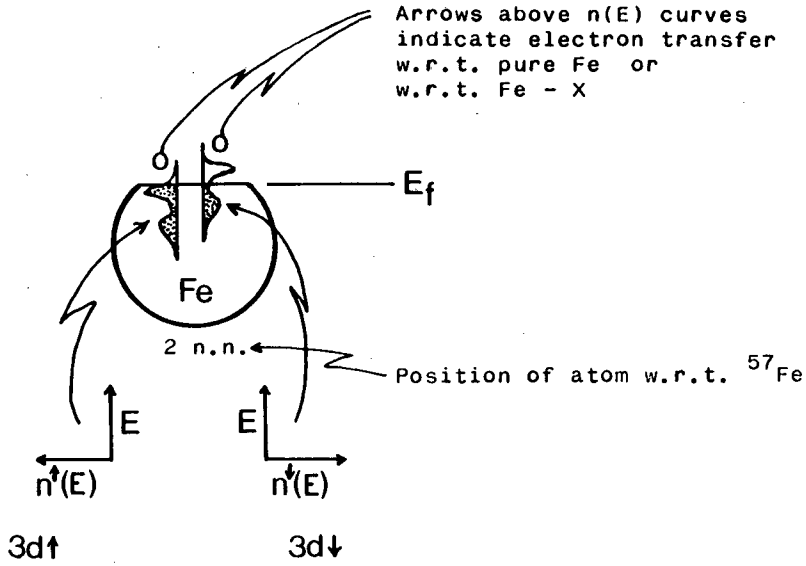


## NOTATION

Structure:

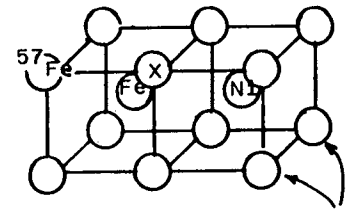


All these atoms are Fe

Structure as Drawn in Figures:

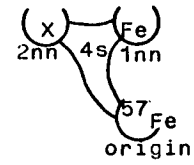


Fe - X

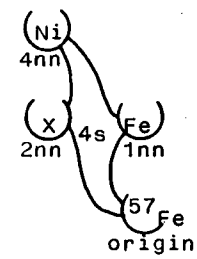


Fe - Ni - X

$\Delta H$, $\Delta i$ are w.r.t. pure Fe

$\delta H$, $\delta i$ are w.r.t. Fe - X

Figure 46

XBL 828-10880

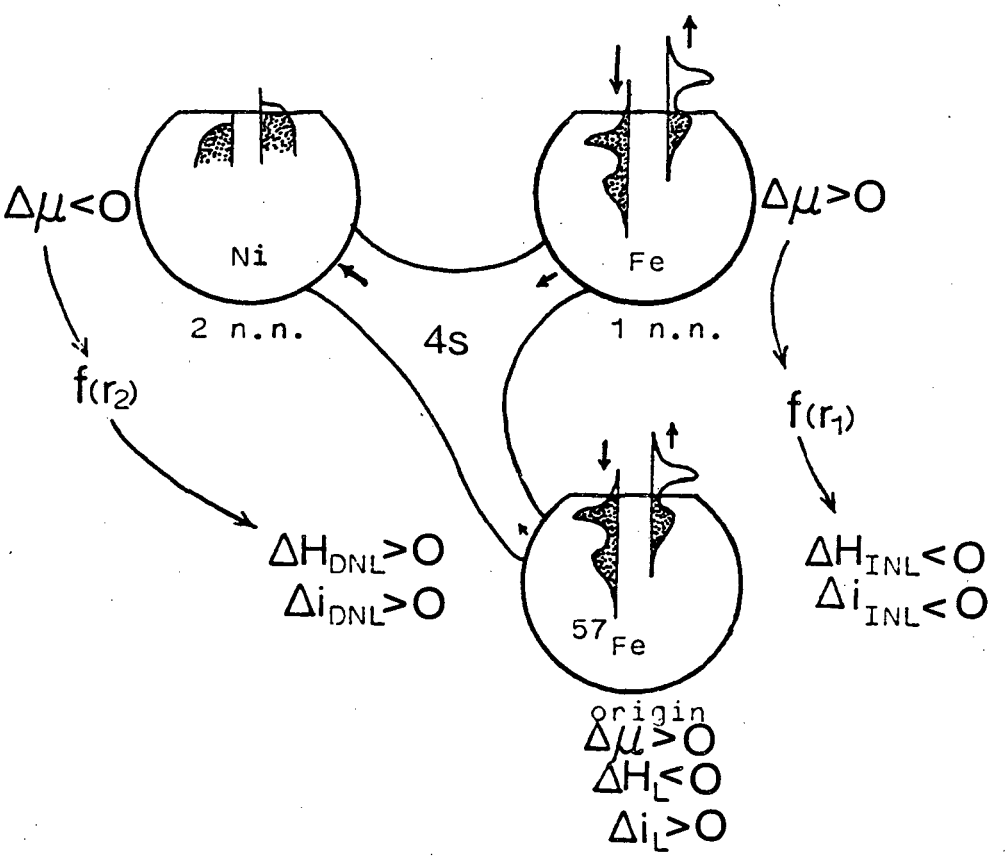


XBL 828-10833

Figure 47

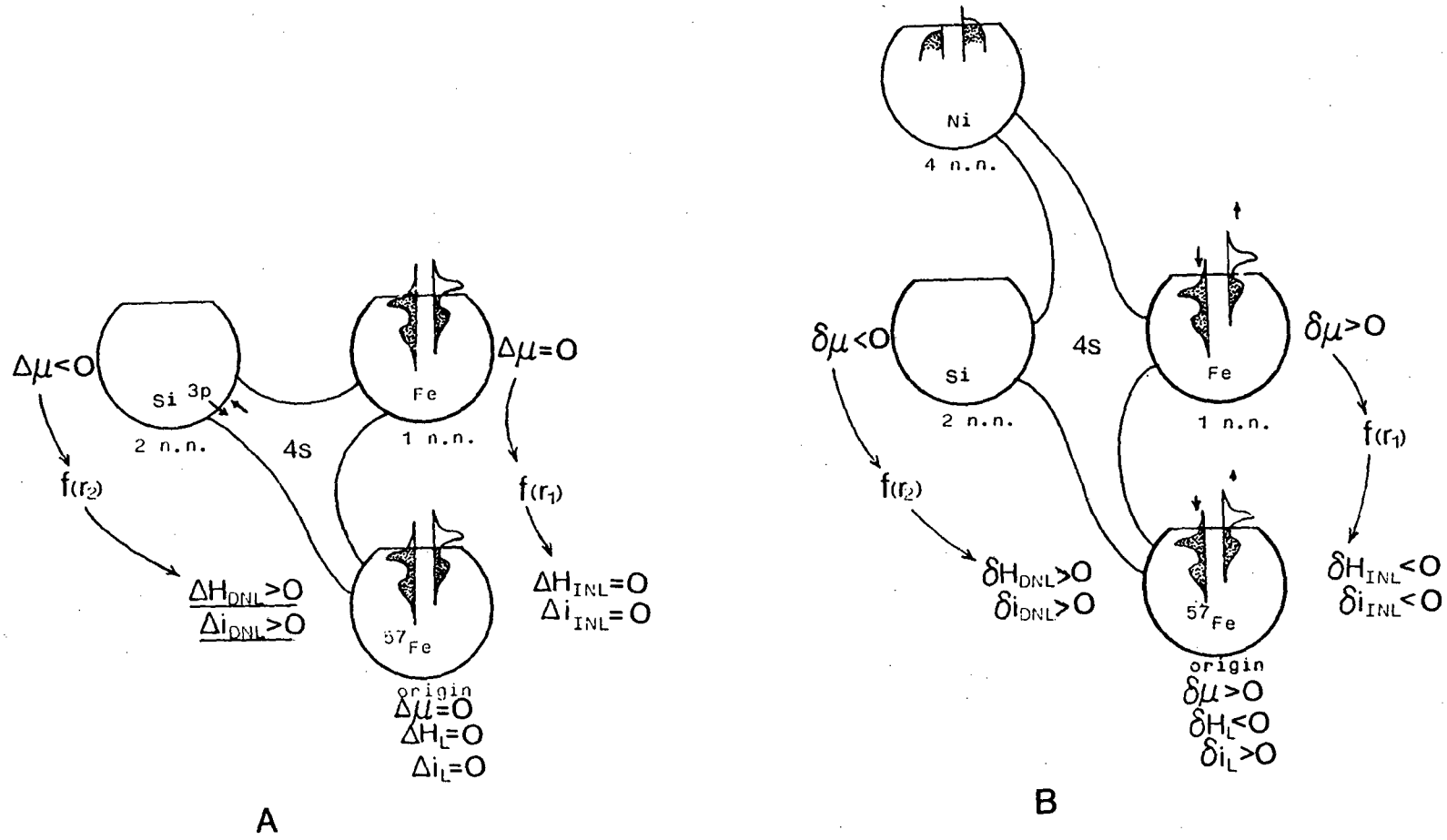


XBL 828-10881

Figure 48

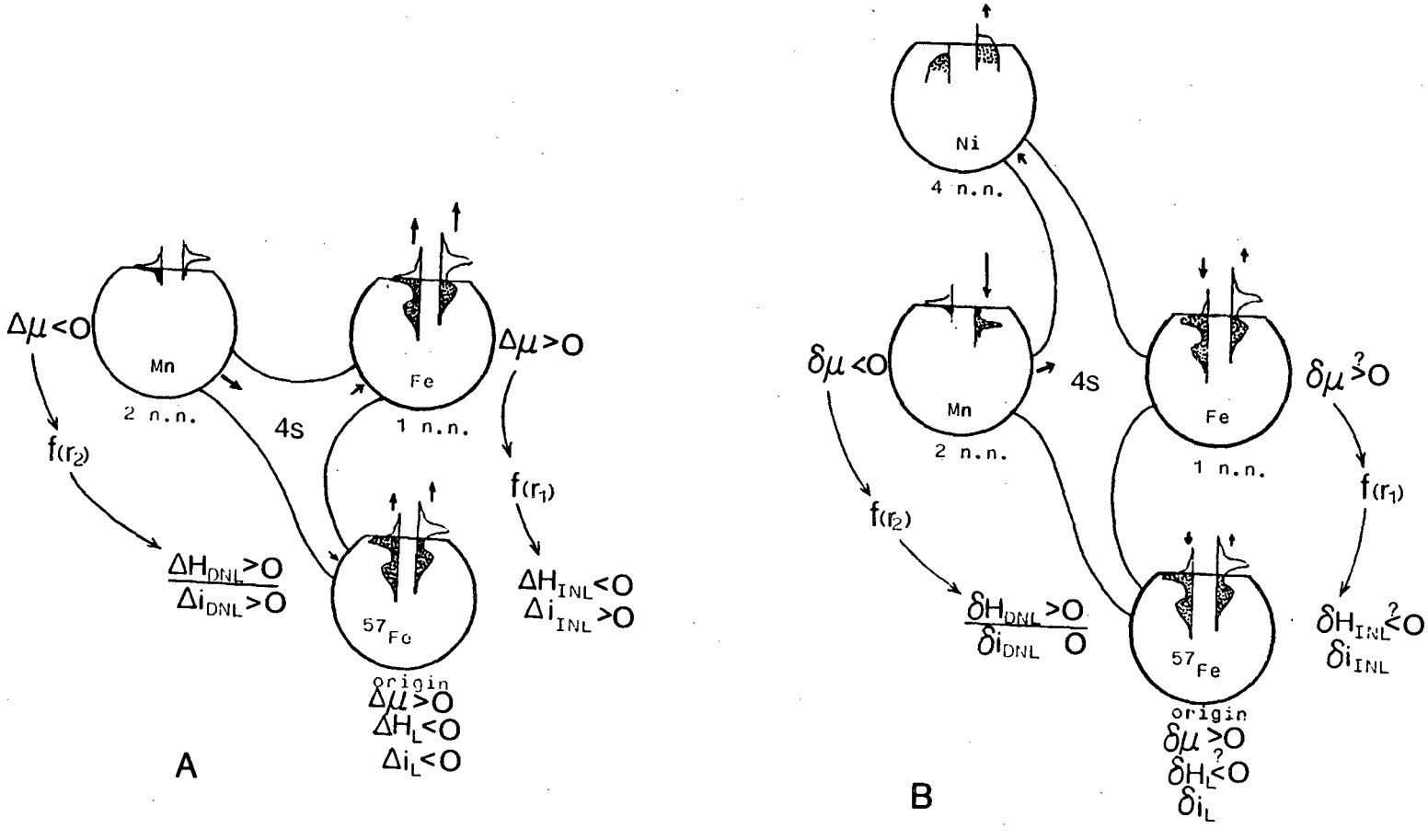


Figure 49

XBL 828-10882

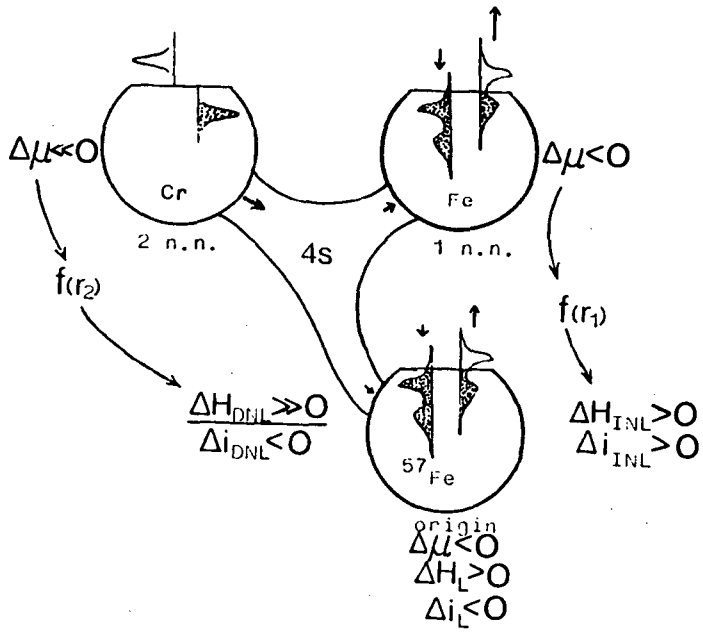


A

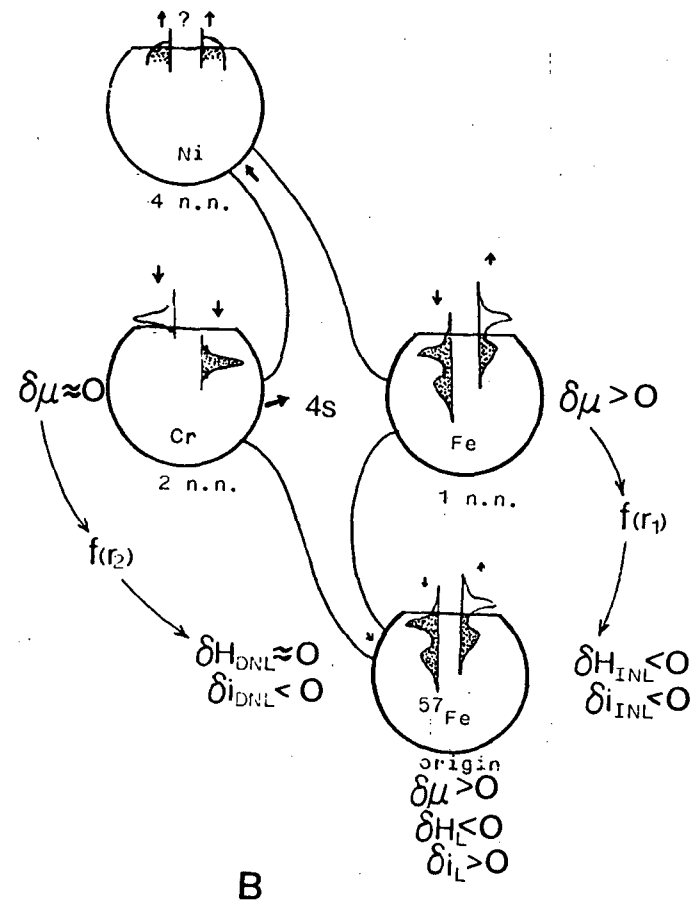


B

XBL 828-10883

Figure 50

# TTT DIAGRAMS

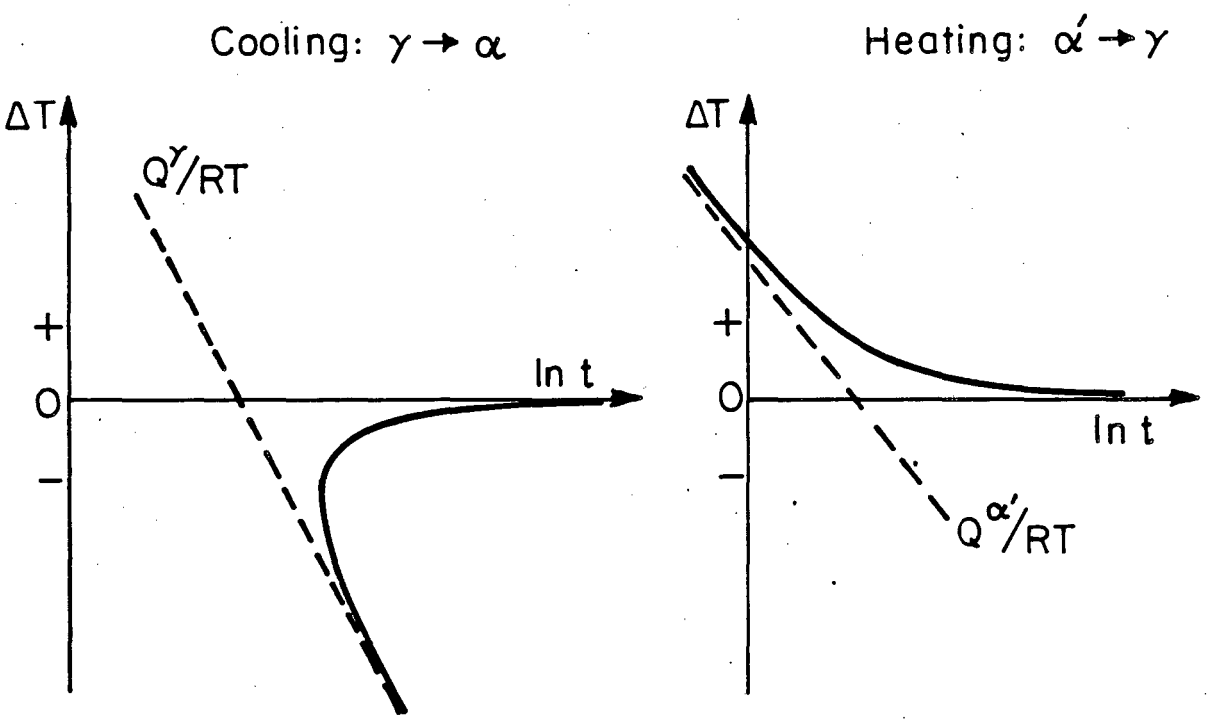


$m < 0$

XBL828-6260

Figure 51

This report was done with support from the Department of Energy. Any conclusions or opinions expressed in this report represent solely those of the author(s) and not necessarily those of The Regents of the University of California, the Lawrence Berkeley Laboratory or the Department of Energy.

Reference to a company or product name does not imply approval or recommendation of the product by the University of California or the U.S. Department of Energy to the exclusion of others that may be suitable.

*TECHNICAL INFORMATION DEPARTMENT*
*LAWRENCE BERKELEY LABORATORY*
*UNIVERSITY OF CALIFORNIA*
*BERKELEY, CALIFORNIA 94720*